A GEOPHYSICAL AND GEOLOGICAL INVESTIGATION OF EXTENSIONAL STRUCTURES, GREAT BASIN, WESTERN UNITED STATES

by

Craig Howard Jones

B.S. California Institute of Technology
(1981)

Submitted to the Department of Earth, Atmospheric, and Planetary Sciences
in Partial Fulfillment of the Requirements of the
Degree of

DOCTOR OF PHILOSOPHY

in

GEOPHYSICS

at the

MASSACHUSETTS INSTITUTE OF TECHNOLOGY

October 1987

Signature of Author_____
Department of Earth, Atmospheric and Planetary Sciences
October, 1987

Certified by_____
Peter H. Molnar
Thesis Supervisor

Accepted by_____
William F. Brace
Chairman, Departmental Committee on Graduate Students

A GEOPHYSICAL AND GEOLOGICAL INVESTIGATION OF EXTENSIONAL STRUCTURES, GREAT BASIN, WESTERN UNITED STATES

by

Craig H. Jones

Submitted to the Department of Earth, Atmospheric, and Planetary Sciences in partial fulfillment of the requirements of the degree of Doctor of Philosophy in Geophysics

ABSTRACT

Over the past twenty years, geologic work in the Great Basin of the western United States has emphasized the importance of low-angle normal faults and "décollements" in accommodating Cenozoic extension at several localities. Most of the discussion of these highly controversial structures has centered on examinations of exhumed, inactive examples of these structures. This thesis includes three investigations of regions inferred to contain active or recently active low-angle normal faults: Panamint Valley, California; the Hansel Valley region of northern Utah; and the southwestern portion of the Great Basin in California and Nevada.

Gravity, electrical, magnetotelluric, and seismic information gathered in the northern Panamint Valley by the 1985 MIT Field Geophysics Course indicate that most of the valley is underlain by less than 300 m of Plio-Pleistocene sediment. The thin accumulation of sediment should permit the detection at the base of the sediments of any body magnetized like the ~4-m.y.-old basalt exposed at the valley margins. Magnetic profiles across the valley, however, indicate that no such rock underlies 5 to 9 km of the width of the valley. The absence of basalt from beneath most of northern Panamint Valley suggests that the valley was created by slip on a low-angle normal fault; balancing a topographic profile across the valley indicates that the fault lies between 0.5 and 3 km beneath the valley floor.

Results from a microearthquake survey in northern Utah and southeastern Idaho were scrutinized both for systematic errors and for tectonic implications. Arrival times from more than 330 earthquakes were inverted for both earthquake locations and a one-dimensional (1-D) velocity structure; uncertainties of the velocities of the best-fit 1-D structure, termed M8, were about ±4%. Earthquakes recorded by more than 11 stations and located using structure M8 were estimated to have epicenters and depths with uncertainties of about 300 m and 1 km, respectively; these uncertainties reflect both noise in the arrival times and uncertainties in the velocity structure, assuming the velocity structure is one-dimensional. Relocating these events using a best-fit three-dimensional (3-D) velocity structure, M3D, produces differences between the 1-D and 3-D locations and velocities greater than those estimated using the 1-D structure and far in excess of the standard errors. The large differences of locations are due to several systematic errors caused by the assumption of a 1-D structure, several of which might be anticipated: For example, epicenters are closer to regions with laterally lower velocities using M3D, and depths of earthquakes differ in proportion to the mean 1-D structure near the earthquake. One error, not easily anticipated, results in errors in the depths of earthquakes increasing with the number of stations recording the events; the depth changes of the 1-D locations compensate for the greater lateral heterogeneity sampled by rays from the better-recorded events. Focal mechanisms are most sensitive to the location of an earthquake relative to a strong velocity gradient with depth. Focal mechanisms of earthquakes with a lower P-wave velocity at the calculated than at the true hypocenter will have too large a component of strike-slip; mechanisms of events with a

higher P-wave velocity at the calculated than at the true hypocenter will have too great a component of dip-slip.

Several features in the seismicity of the Hansel Valley--Pocatello Valley region were found to be inconsistent with a simple horst-and-graben structure in the region. Seismicity occurred not only under mountains near Hansel Valley but also under Pocatello Valley farther north; a vertical discontinuity existed in the seismicity south of about 41.82°N at a depth of about 4-5 km; and a sparsely distributed group of earthquakes occurred near a depth of 4-5 km with mechanisms consistent with slip on a low-angle normal fault. At about 41.82°N the seismicity is characterized by oblique-normal, right-lateral slip on a west-northwest striking, north-Dipping plane; this seismicity lies at the northern edge of the vertically discontinuous seismicity and at the southern edge of a lateral low-velocity region that has P- and S-wave velocities 10-15% lower than the regions to the north or south. The existence of a low-angle normal fault at a depth of 4-5 km beneath the Hansel Mountains and Hansel Valley is compatible with these observations and the regional geology of the region to the west; this fault is considered to lie at a greater depth north of a "step" at about 41.82°N. This step and its associated oblique-normal, right-lateral sense focal mechanisms appear to be the down-plunge continuation of the offset of the trace of the low-angle faults east of the Albion Mountains to those east of the Raft River Mountains. Hence the seismicity observed in the Hansel Valley--Pocatello Valley region is consistent with the presence of an active low-angle normal fault within the seismically active portion of the crust.

Finally, while relatively rapid and large-scale extension occurred in the Death Valley region of California during Neogene time, little or no shallow extension occurred in the adjacent Sierra Nevada. This contrast in tectonic history has often been extrapolated to include the entire lithosphere, but geophysical and geologic observations indicate that more extension of the mantle lithosphere has occurred under the Sierra than under the Death Valley region. Upper mantle seismic velocities observed beneath the High Sierra are lower than those observed in other regions with comparable surface heat flow. This discrepancy could be resolved if the mantle lithosphere beneath the High Sierra had become warmer, presumably by tectonic thinning, in the last 10 m.y. Upper mantle seismic velocities, averaged topography, and Bouguer gravity anomalies all are consistent with the presence of thinner mantle lithosphere beneath the High Sierra than beneath the California portion of the Basin and Range Province to the east. This suggests that extension of the crust near Death Valley might be accommodated at a deeper level by thinning of the mantle lithosphere beneath the Sierra Nevada.

The extension in the crust of the California Basin and Range Province and the thinning of the mantle lithosphere under the High Sierra appear to share the same bounds in time and space. The uplift of the High Sierra occurred over the past 9 m.y., which coincides with most of the extension that occurred in the California Basin and Range Province. Because the orientation of extension in the California Basin and Range Province is inferred to be approximately N60°W from geologic, geodetic, and in situ stress measurements, the northern and southern edges of the Death Valley extensional subprovince may extend N60°W from the inferred northern and southern limits of west dipping low-angle normal faults of the Death Valley region. Pronounced changes in the averaged topography and Bouguer gravity anomaly across these two bounds both in the Basin and Range Province and in the Sierra Nevada support a connection between the tectonics of both regions. The geomorphic history of the southern Sierra suggests an up-to-the-north warp of the Sierra across this southern bound during latest Cenozoic time. Hence extension near Death Valley may be localized in the crust and may be laterally connected to thinning of the mantle lithosphere beneath the Sierra Nevada. This geometry requires extended crust to overlie unextended mantle lithosphere near Death Valley and virtually unextended crust to overlie tectonically thinned mantle lithosphere in the High Sierra Nevada.

Thesis Supervisor: Peter H. Molnar
Title: Senior Research Scientist (formerly Professor of Geophysics)

ACKNOWLEDGMENTS

It is impossible to do graduate work for six years without incurring a number of debts; the number increases dramatically with the diversity of the work attempted and the amount of time spent in the field. Hence I cannot hope to acknowledge all those who provided assistance, guidance, or encouragement. To all those I do not specifically mention (and there are many), my most gracious thanks.

For six years Peter Molnar and I have disagreed on food, cities, preferred mountain ranges, and the English language (most of the prepositions in this thesis are his, I think). Through this time, though, he and I have agreed to prefer mountains to oceans. Although I chose to work on the wrong continent, Peter has been very supportive. The guidance, encouragement, numerous edits of sloppy drafts, and constant insistence on stating the uncertainties always present has had a strong affect on the way I do science. It has been fun, and I thank Peter for all he's done.

I have probably pestered most of the faculty and staff at one time or another; certain individuals, however, suffered most. Clark Burchfiel is one of those rare individuals who quickly and easily reduces a terrifying mass of field data into a comprehensible structural picture; I've tried and failed to surprise him with bizarre exposures in the field. Time and discussions with Ted Madden have been very enjoyable, both for the original views and the pure curiosity he brings to everything. Steve Roecker has survived me with good humor in the field and in the office; he has earned both my thanks and a combat ribbon. I owe a special debt to those who worked to make several field camps possible: Jean Titilah, Judith Stein, Sheila Gardner, and Lyle Hodgson. Through his longstanding support of our camps, Bill Brace made it possible for me to never set foot in Cambridge in January.

This whole experience was unmeasurably enriched by the numerous graduate students (and a few postdocs) who also toiled here. Mike Nelson and I arrived together (in my car), worked on one project together, shared an office for the past six years, and will complete our studies at nearly the same time. Mike's wide-ranging interests and straightforward criticism have created numerous discussions that relieved the monotony of narrower science. Numerous exploits with other denizens of the seventh floor cannot be recounted, but their names (in no particular order) can: "Mr. Fixit" Steve Hickman, the indescribable Kaye Shedlock, "astronaut" Steve Bratt, "Wall Drug" Dave Olgaard, subdued Helene Lyon-Caen, "muscles" Carol Bryan, turbocharged Joanne Friedrich, "Mr. Cigm" Randy Hay, "Softball is [or was] better than sex" Rob McCaffrey, rock-squeezer Yves Bernabe, "CARE package" Lind Gee, grizzled Geoff Abers, and novel-mutilator Rafael Benites. Of the many inhabitants of the other floors I am most indebted to Scott Phillips, Doug Walker, Dave Klepatcke,

Randy Mackie, Roger Buck, the tenth floor "Clones" and their successors, and the numerous glee-filled veterans of the fifth floor computer wars.

The completion of a marathon like a thesis requires support outside the ivory tower (or at least the department) as well as within it. I have had the extreme good fortune of having two great friends in Jean Titilah and Emilio Falco, who could absorb lots of frustration and help me move on to better things. Prem Kumar, with whom I shared an apartment for several years, provided the good humor and easygoing style that made life in New England a little more enjoyable. Two other housemates (both biologists), Wendy Katz and Peter Drain, and my landlady of five years, Laura Villemure, provided greatly needed perspective. In the final crunch, Anne Sheehan made life a little easier and more pleasant while suffering my constant complaints.

All of this would not have been possible, beyond the obvious reasons, without my mother. Her unstinting support, neverending concern, and boundless love made it easy for me to pursue an academic career; the open door and bountiful table she maintained made some poorly funded field work a reality.

Dedicated to
my mother,
who provided
a home and a source
of unwavering support
when both were needed.

TABLE OF CONTENTS

INTRODUCTION

In the late nineteenth century, geologists accompanying the governmental surveys of the western United States began to describe and analyze the structures found in the Great Basin province between the Rocky Mountains and the Sierra Nevada. The single strongest conclusion to come from this work, generally attributed to G. K. Gilbert, was that the mountain ranges within this province were created by slip on normal faults that bound them [Gilbert, 1874, 1875, 1928]. These "fault-block" mountains seemed to contrast strongly with the "fold-belt" mountains previously examined, the Appalachians and the Alps being the most eminent examples. The concept of a class of mountains formed by slip on high-angle normal faults and whose form was principally structural and not erosional was one of the more important contributions of nineteenth-century American geology to tectonic theory.

Through ensuing decades, continued work in the region revealed other structures not easily placed in Gilbert's framework. As early as 1910, Ransome et al. [1910] described a group of gently-dipping low-angle faults in the southern Great Basin; later workers added other enigmatic structures, often labeling them as "thrusts" [e.g., Noble, 1941; Ransome, 1931; and Hewett, 1956]. Longwell [1945] suggested that similar faults in southern Nevada were normal faults, and he labeled them "low-angle normal faults." Both Hunt and Mabey [1966] and Wright and Troxel [1973] reinterpreted the "Amargosa Thrust" of Noble [1941] as a fault accommodating extension of the crust; Anderson [1971] interpreted the geology in part of southeastern Nevada to have been formed by motion on a low-angle normal fault. To the north, many other gentle faults that removed stratigraphic section were initially considered to be related to Mesozoic thrust-faulting; as the recognized number of these faults grew, they came to be seen as a separate class of faults and were termed "denudational" faults by Armstrong [1972].

During the 1960s and 1970s evidence accumulated indicating that "metamorphic core complexes," ranges of metamorphic rock separated from overlying extended, unmetamorphosed rock by a relatively thin fault or mylonite zone, were created in Tertiary time (see a summary in Coney [1980]). Different workers emphasized differing aspects of these features, but the juxtaposition of metamorphosed and unmetamorphosed rock suggested that a large portion of the crust had been removed (articles in Crittenden et al. [1980]). Among the structures discussed in Crittenden et al. [1980] were low-angle normal faults, to which Davis et al. [1980] assigned great importance in the Whipple Mountains of southeastern California.

With perceptible, if perhaps unintended, irony, Brian Wernicke titled his 1981 paper "Low-angle normal faults in the Basin and Range Province--Nappe tectonics in an extending orogen" [Wernicke, 1981]; the irony lay in his suggestion that nappe structures, which were now seen to be fundamental to the understanding of the creation of the "fold-belt" mountains, might have been equally important in forming G. K. Gilbert's block-faulted mountain ranges. By extrapolating low-angle normal faults from the upper crust to the Moho, Wernicke provided a unifying explanation for the structures in both metamorphosed and unmetamorphosed parts of metamorphic core complexes; ductile fabrics overprinted by brittle structures in the lower plate indicate the upward motion of the lower plate. Thinning and translation of the upper plate provides the space for the lower plate to rise to the surface.

Most of the debate in this decade has centered on interpretations of exhumed, inactive structures; both low-angle normal faults and subhorizontal "décollements" have been advanced to explain the juxtaposition of faulted, unmetamorphosed rock with mylonitized, metamorphic rock [e.g., Bartley and Wernicke, 1984; Davis, 1983; Gans et al., 1985; Lee et al., 1987; Reynolds and Spencer, 1985]. Very few studies discuss active features analogous to these exhumed structures, and some workers have suggested that low-angle normal faults were active only before 5 m.y. ago [e.g., Zoback et al., 1981; Eaton, 1982].

Most geophysical work to date that encompasses the whole lithosphere does not examine structures more complicated than one-dimensional structures [e.g., Lachenbruch and Sass, 1978; McKenzie, 1978; Eaton, 1982; Sonder et al., 1987] thus limiting its impact on resolving the structures in the Great Basin. The possibility of seismic slip on low-angle normal faults has been the most closely examined geophysical manifestation of such faults; after reviewing the literature, Jackson [1987] concluded that no large earthquake initiated on such a fault.

The goal of the work presented in this thesis was to document, if possible, some characteristics of active low-angle normal faults. Three studies were pursued: A geophysical investigation of northern Panamint Valley, a microearthquake survey of northern Utah and southeastern Idaho, and a review of geophysical and geological information within the southwestern Great Basin. In a sense, these three studies are ordered by increasing depth: the first discusses a low-angle normal fault near its outcrop, the second discusses the possible presence of such a fault perhaps 40 km downdip from its exposure and 4-8 km deep, and the third considers the possibility of such a sense of shear throughout the lithosphere.

The first chapter presents an argument based upon geophysical observations made in northern Panamint Valley that the valley is floored by a low-angle normal fault and that slip on this fault created this part of Panamint Valley. Both flanks of Panamint Valley were covered by basalt flows about 5 m.y. ago; these flows presumably covered every exposed

surface in between at that time. The amount of extension across the valley since then can be estimated from the width of the valley not underlain by basalt. We found this to be between 5 and 9 km, far greater than that expected or possible if high-angle normal faults created the basin. Using this estimate of the increase in width of the valley over the past 5 m.y., we use the volume of the valley to estimate the depth of the fault that created the valley to be between about 1 and 3 km beneath the valley floor.

The second and third chapters are the results of observations of earthquakes in northern Utah and southeastern Idaho using a temporary array of seismometers. The second chapter details several systematic errors that were found to be present in earthquake locations and focal mechanisms; these errors are caused mostly by errors in the velocity structure used in determining the locations and mechanisms. Focal mechanisms will be in error if the earthquakes from which they were derived are located incorrectly relative to strong velocity contrasts. In general, mechanisms of events located within part of the velocity structure that has velocities higher than those of the material at the true hypocenter will tend to have too great a dip-slip component of motion; conversely, mechanisms of those events mislocated in material with erroneously low velocities will have too great a component of strike-slip. Earthquake hypocenters determined with an incorrect velocity structure can be in error by several times the standard error computed from a linearized inversion. These errors need not affect all events in a small region equally: relative locations are nearly as susceptible to error as absolute locations. The description of these errors and their inferred causes suggests a strategy for locating earthquakes while minimizing the risk of significant systematic errors that might bias any interpretation of the results.

Using the estimates of uncertainties and errors presented in Chapter 2, Chapter 3 explores the tectonic significance of the earthquakes observed in the Hansel Valley--Pocatello Valley region of northern Utah and southeastern Idaho. The seismicity was observed to fall in a band trending north-northeast from the Hansel Mountains in the south to Pocatello Valley in the north. Lateral variations of certain characteristics of the seismicity seem inconsistent with a simple "horst-and-graben" structure: the northern seismicity lies under a valley and appears to be continuous to a depth of about 8 km; the southern seismicity lies under mountains and is discontinuous at a depth of 4 to 5 km. The two regions are separated by a zone within which many earthquakes have focal mechanisms with a strike-slip component of motion. Both seismicity and focal mechanisms within this zone appear to define a west-northwest striking, north-dipping, oblique-slip normal fault with a right-lateral component of strike-slip. This fault lies at the northern edge of the vertically discontinuous seismicity and at the southern edge of a low-velocity region in the center of the array. We suggest that the seismicity is compatible with a low-angle normal fault at about 5 km depth under the southern part of the

array and below 8 km depth in the northern part of the array; the region with the oblique-slip fault represents a step (or "transfer fault") of the low-angle normal fault. This geometry is consistent with the geology in the vicinity of the Raft River Mountains to the west, and hence we suspect that this low-angle normal fault is the eastward extension of the low-angle normal faults at the east edge of the Raft River--Albion mountains metamorphic core complex. If this interpretation is correct, then an active low-angle normal fault would lie entirely within the seismically active portion of the crust.

The final chapter explores geophysical and geologic information bearing on the possibility that extension in the lithosphere is offset horizontally with increasing depth in the southwestern part of the Great Basin. Seismic velocities determined for the top of the mantle beneath the Sierra Nevada south of about 38°N are as low or lower than those beneath the adjacent Basin and Range to the east, suggesting that the mantle lithosphere beneath the Sierra Nevada is warmer, and hence thinner, than that to the east beneath the extended crust of the Death Valley region. The timing and north-south extent of extension in the Death Valley region is similar to that of the uplift of the Sierra Nevada; the southern boundary of this deformation is of particular interest because topographic and gravity gradients do not parallel the structure of the Sierra Nevada batholith but instead appear to lie on the extrapolation of the southern edge of known low-angle normal faults of the Death Valley region. These gradients and a history inferred from geomorphic evidence in the southern Sierra Nevada indicate that the southern end of the topographically-defined "High Sierra" also marks the southern end of most of the Neogene uplift of the range; this inference does not appear to be consistent with the hypothesis that the Sierran uplift is due to a thick, Mesozoic crust beneath the range. Hence I suggest that the uplift of the High Sierra was caused by extension of the sub-Sierran mantle lithosphere and that this extension is the downward continuation of the extension of the crust documented in the Death Valley region.

RESPONSIBILITIES

This thesis, perhaps more than most, is an anthology of published papers and papers in preparation for submission for publication. Chapters 1 and 4 have been published and are essentially unchanged from the published papers; titles and authorships have been reproduced here as in the published versions. Chapters 2 and 3 have yet to be submitted for publication; I have indicated the anticipated authorship and possible titles to be consistent with the other chapters, but these are subject to change as is the text.

The work presented in this document is that of many workers, as the authorship of two of the chapters indicates. Chapter 1 was the product of the 1985 MIT Field Geophysics Course,

taught by Peter Molnar and Ted Madden; Mike Nelson and I were the teaching assistants for the course. All members of the course (the four just named and Carrie Decker, Jeff Hegley, Rich Herrmann, Matt Kohn, Ram Manikkalingam, Joe Matarese, Deborah Meinholz, and Carolyn Ruppel) and Geoff Abers gathered and reduced the data. After completion of the course, I oversaw and helped draft the figures, prepared the manuscript, and drew the final interpretations presented in the paper (many of which had been discussed during the course). Peter Molnar and Ted Madden corrected and revised the manuscript as we prepared it for publication.

Chapters 2 and 3 are the product of a microearthquake survey conducted by MIT, the University of Utah, Université Scientifique, Technologique et Médicale de Grenoble (France), Cambridge University (United Kingdom), and the University of Wisconsin. The instruments were deployed and maintained by Harley Benz, Denis Hatzfeld, Suzette Jackson, myself, Geoff King, Rob McCaffrey, Kaspar Renggli, Martha Savage, and Nancy Threlfall under the supervision of Peter Molnar, R. B. Smith, and Steve Roecker. We were greatly aided by the assistance and generosity of the inhabitants of the area, who provided us with workspace, access, keys, advice, and an occasional tow out of some very deep mud. I picked all of the arrival times and first-motion polarities used in these studies; R. B. Smith arranged for the transfer of the digital seismograms from the field tapes to reel-to-reel tapes for our use. I executed all the inversions and reductions of the data; Steve Roecker, Peter Molnar, Kaye Shedlock, and Rob McCaffrey all provided guidance and suggestions through this work. Although the interpretations and conclusions of both chapters are my own, the existence of the second chapter is largely due to Peter's unending requests for greater clarity and definition of the uncertainties in our results.

The fourth and final chapter, because of its somewhat broader scale, reflects numerous discussions with many individuals, none of whom can be held responsible for any errors or mistaken attributions. In particular, Peter Molnar helped focus this paper from a more nebulous mass of observations; Clark Burchfiel, Brian Wernicke, and Doug Walker all freely offered observations and comments that proved useful in establishing the structural framework proposed in the paper.

REFERENCES

Anderson, R. E., Thin skin distension in Tertiary rocks of southeastern Nevada, *Geol. Soc. Am. Bull.*, *82*, 43-58, 1971.

Armstrong, R. L., Low-angle (denudation) faults, hinterland of the Sevier orogenic belt, eastern Nevada and western Utah, *Geol. Soc. Am. Bull.*, *83*, 1729-1754, 1972.

Bartley, J. M., and B. P. Wernicke, The Snake Range Décollement interpreted as a major extensional shear zone, *Tectonics*, *3*, 647-657, 1984.

Coney, P. J., Cordilleran metamorphic core complexes: An overview, *Mem. Geol. Soc. Am.*, *153*, 7-31, 1980.

Crittenden, M. D., Jr., P. J. Coney, and G. H. Davis (Eds.), Cordilleran Metamorphic Core Complexes, *Mem. Geol. Soc. Am.* , *153*, 490 pp., 1980.

Davis, G. A., J. L. Anderson, E. G. Frost, and T. J. Shackelford, Mylonitization and detachment faulting in the Whipple-Buckskin-Rawhide Mountains terrane, southeastern California and western Arizona, *Mem. Geol. Soc. Am.* , *153*, 79-130, 1980.

Davis, G. H., Shear-zone model for the origin of metamorphic core complexes, *Geology*, *11*, 342-347, 1983.

Eaton, G. P., The Basin and Range Province: Origin and tectonic significance, *Ann. Rev. Earth Planet. Sci.*, *10*, 409-440, 1982.

Gans, P. B., E. L. Miller, J. McCarthy, and M. L. Ouldcott, Tertiary extensional faulting and evolving brittle-ductile transition zones in the northern Snake Range and vicinity: New insights from seismic data, *Geology*, *13*, 189-193, 1985.

Gilbert, G. K., U. S. Geog. and Geol. Surveys W. 100th Mer. Progress Rept, 1872, 1874.

Gilbert, G. K., Report on the geology of portions of Nevada, Utah, California, and Arizona, examined in the years 1871 and 1872, *U.S. Geog. and Geol. Surveys W. 100th Mer. Rept.*, *3*, 1875.

Gilbert, G. K., Studies of basin-range structure, *U. S. Geol. Surv. Prof. Pap.*, *153*, 92 pp., 1928.

Hewett, D. F., Geology and mineral resources of the Ivanpah quadrangle, California and Nevada, *U. S. Geol. Surv. Prof. Pap.*, *275*, 1-172, 1956.

Hunt, C. B., and D. R. Mabey, Stratigraphy and structure, Death Valley, California, *U. S. Geol. Surv. Prof. Pap.*, *494-A*, 1-162, 1966.

Jackson, J. A., Active normal faulting and continental extension, Continental Extensional Tectonics, edited by M. P. Coward, J. F. Dewey, and P. L. Hancock, *Spec. Publ. Geol. Soc. Lond.*, *28*, 3-17, 1987.

Lachenbruch, A. H., and J. H. Sass, Models of an extending lithosphere and heat flow in the Basin and Range province, *Mem. Geol. Soc. Am.*, *152*, 209-250, 1978.

Lee, J., E. L. Miller, and J. F. Sutter, Ductile strain and metamorphism in an extensional tectonic setting: A case study from the northern Snake Range, Nevada, USA, in

Continental Extensional Tectonics, edited by M. P. Coward, J. F. Dewey, and P. L. Hancock, *Spec. Publ. Geol;. Soc. Lond.*, *28*, 267-298, 1987.

Longwell, C. R., Low-angle normal faults in the Basin-and-Range province, *Eos Trans. AGU*, *26*, 107-118, 1945.

McKenzie, D. P., Some remarks on the development of sedimentary basins, *Earth Planet. Sci. Lett.*, *40*, 25-32, 1978.

Noble, L. F., Structural features of the Virgin Spring area, Death Valley, California, *Geol. Soc. Am. Bull.*, *52*, 941-1000, 1941.

Ransome, F. L., W. H. Emmons, and G. H. Garrey, Geology and ore deposits of the Bullfrog district, Nevada, *U. S. Geol. Surv. Bull.*, *407*, 1-130, 1910.

Ransome, F. L., Geological reconnaissance of the revised Parker route through the Whipple Mountains, Consulting report to the Metropolitan Water District of Southern California, 10 pp., 1931.

Reynolds, S. J., and J. E. Spencer, Evidence for large-scale transport on the Bullard detachment fault, west-central Arizona, *Geology*, *13*, 353-356, 1985.

Sonder, L. J., P. C. England, B. P. Wernicke, and R. L. Christiansen, A physical model for Cenozoic extension of western North America, Contentental Extensional Tectonics, edited by M. P. Coward, J. F. Dewey, and P. L. Hancock, *Spec. Publ. Geol. Soc. Lond.*, *28*, 187-201, 1987.

Wernicke, B., Low-angle normal faults in the Basin and Range Province--Nappe tectonics in an extending orogen, *Nature*, *291*, 645-648, 1981.

Wright, L. A., and B. W. Troxel, Shallow-fault interpretation of basin and range structure, in *Gravity and Tectonics*, edited by K. A. DeJong and R. Scholten, pp. 397-407, John Wiley, New York, 1973.

Zoback, M. L., R. E. Anderson, and G. A. Thompson, Cainozoic evolution of the state of stress and style of tectonism of the Basin and Range province of the western United States, *Phil. Trans. R. Soc. Lond.*, *A300*, 407-434, 1981.

CHAPTER 1
A GEOPHYSICAL INVESTIGATION OF THE NORTHERN PANAMINT VALLEY, INYO COUNTY, CALIFORNIA: EVIDENCE FOR POSSIBLE LOW-ANGLE NORMAL FAULTING AT SHALLOW DEPTH IN THE CRUST[1]

MIT 1985 Field Geophysics Course[2]
Department of Earth, Atmospheric, and Planetary Science,
Massachusetts Institute of Technology, Cambridge

Shawn Biehler
Department of Earth Sciences, University of California, Riverside

Abstract. Gravity, magnetic, seismic refraction, electrical resistivity, and magnetotelluric measurements in northern Panamint Valley indicate that the alluvial and pluvial fill in the basin is thin and that basement under the valley floor lies at a shallow depth. Contours of the Bouguer gravity anomaly field do not define a low over the valley and do not mimic the mapped boundaries of alluvial fill. Electrical resistivity and seismic refraction measurements indicate that the playa in northern Panamint Valley is underlain by no more than about 200 m of sediment. This is consistent with the absence of any local lows in the Bouguer gravity anomaly field over the valley exceeding about 15 mGal in amplitude. There are no anomalies more than 50 nT in amplitude along an east-west magnetic profile across the valley floor. In contrast, upward continuations of magnetic profiles measured across basalt outcrops present at the valley margins still contain anomalies exceeding 75 nT in amplitude at heights of 300 m. Because the inferred thickness of sediment under a width between 5 and 9 km of the valley is less than 300 m, it is insufficient to conceal the signal expected from such magnetized basalt buried under the sediment. We interpret this finding as indicating that the valley is not underlain by basalt except at its margins, which implies that the west side of the valley has moved between 6 and 10 km away from the Panamint Range, in a direction parallel to the Hunter Mountain fault (~N55°W). A balanced cross section across the valley

---

[1]Originally published in *Journal of Geophysical Research*, *92*, 10427-10441, 1987.
[2]Craig H. Jones, Michael R. Nelson, Geoffrey Abers, Carrie Decker, Jeffrey Hegley, Richard Herrmann, Matthew Kohn, Theodore Madden, Ramanujam Manikkalingam, Joseph Matarese, Deborah Meinholz, Peter Molnar, and Carolyn Ruppel.

constrains the required low-angle normal fault to be between 0.5 and 3 km beneath the valley floor.

INTRODUCTION

The hypothesis that much of the crustal extension in the Basin and Range province has occurred by slip on low-angle ($\delta < 30°$) normal faults [e.g., Anderson, 1971; Armstrong, 1972; Davis et al., 1980; Longwell, 1945; Wernicke, 1981] has stimulated a renewed interest in Cenozoic deformation in the area (e.g., articles in the works edited by Crittenden et al. [1980] and Frost and Martin [1982]). Most of this research has focused on exhumed terrains where inactive low-angle normal faults are exposed; less emphasis has been placed on the geometry of active normal faults, most of which dip at steep angles at the surface ($\delta \approx 50°$-70°). Because virtually all fault plane solutions of earthquakes in regions of crustal extension indicate slip on planes dipping more steeply than 30° [Jackson, 1987], there is some question concerning the extent to which low-angle normal faulting occurs at present, to which it occurs seismically, and to which it has occurred at all. What is missing is a study of a region where low-angle normal faulting is active or has recently been active and where such a fault has not been warped and tilted or faulted, as so often is the case in exhumed terrains. To explore such a region requires both geologic study of the surficial rocks and geophysical constraints on the deeper structure.

With these thoughts in mind and as one of a series of investigations, the MIT Field Geophysics Course conducted a geophysical survey of northern Panamint Valley in January 1985. Concurrently with this study, Burchfiel et al. [1987] mapped in detail selected areas of the bedrock surrounding the valley. One of their primary goals was to determine the amount, direction, and age of extension. Our chief goal was to place constraints on the deep structure of the basin, which in turn would provide bounds on the amount of extension and the style of extensional deformation within the basin. This paper presents the salient results of the geophysical study, and a companion paper by Burchfiel et al. [1987] describes the new geological results.

OVERVIEW OF THE GEOLOGY

Panamint Valley trends generally north-northwest, subparallel to both Owens Valley to its west and the central part of Death Valley to its east (Figure 1-1). Within the area studied, the Panamint Mountains rise precipitously from an elevation of 450 m at the east side of the playa on the floor of Panamint Valley to a maximum of about 2500 m elevation. The Darwin Plateau on the west side of the valley rises less steeply to a series of hills and alluviated flats

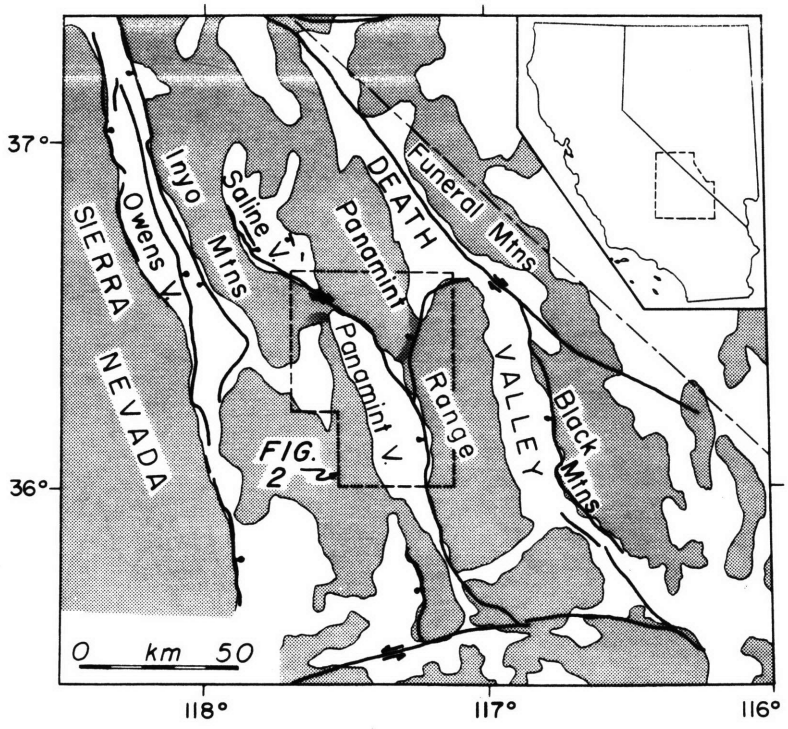

Fig. 1-1. Location map of northern Panamint Valley. Heavy lines are principal faults; mountain ranges are shaded.

at an elevation of about 1600 m, with peaks of the Nelson and Argus ranges to the north and south, respectively. Although deep ravines exist in these ranges, the range summits are mostly part of a gentle pediment of late Pliocene age [Maxson, 1950], suggesting a Quaternary age of the valley.

The geology of the region is described in greater detail by Burchfiel et al. [1987] and is illustrated in Figure 1-2. Most important for this study is the presence of 4-m.y.-old basalts both on the Darwin Plateau west of the valley and on the Panamint Range east of the valley. These are apparently the same basalts [Hall, 1971; Larson, 1979; Schweig, 1985]; hence they predate the creation of the valley. The degree to which these basalts are present under northern Panamint Valley is crucial to understanding the structures that formed the valley.

Paleozoic rocks crop out on both the east and west side of the northern playa (Figures 1-2 and 1-3). Hall [1971] inferred the eastern exposure, Lake Hill, to be a slide block. West of the playa there is a small exposure of bedrock, and north of SR 190 a borehole reached Paleozoic limestone under 111 m of unconsolidated sands, clays, and gravels (Panamint number 2 of Smith and Pratt [1957]) (Figure 1-3). Thus there are suggestions that the bedrock does not lie deep below the playa and that the basalt caps exposed on the Darwin Plateau and the Panamint Range do not cover the basement beneath the valley fill.

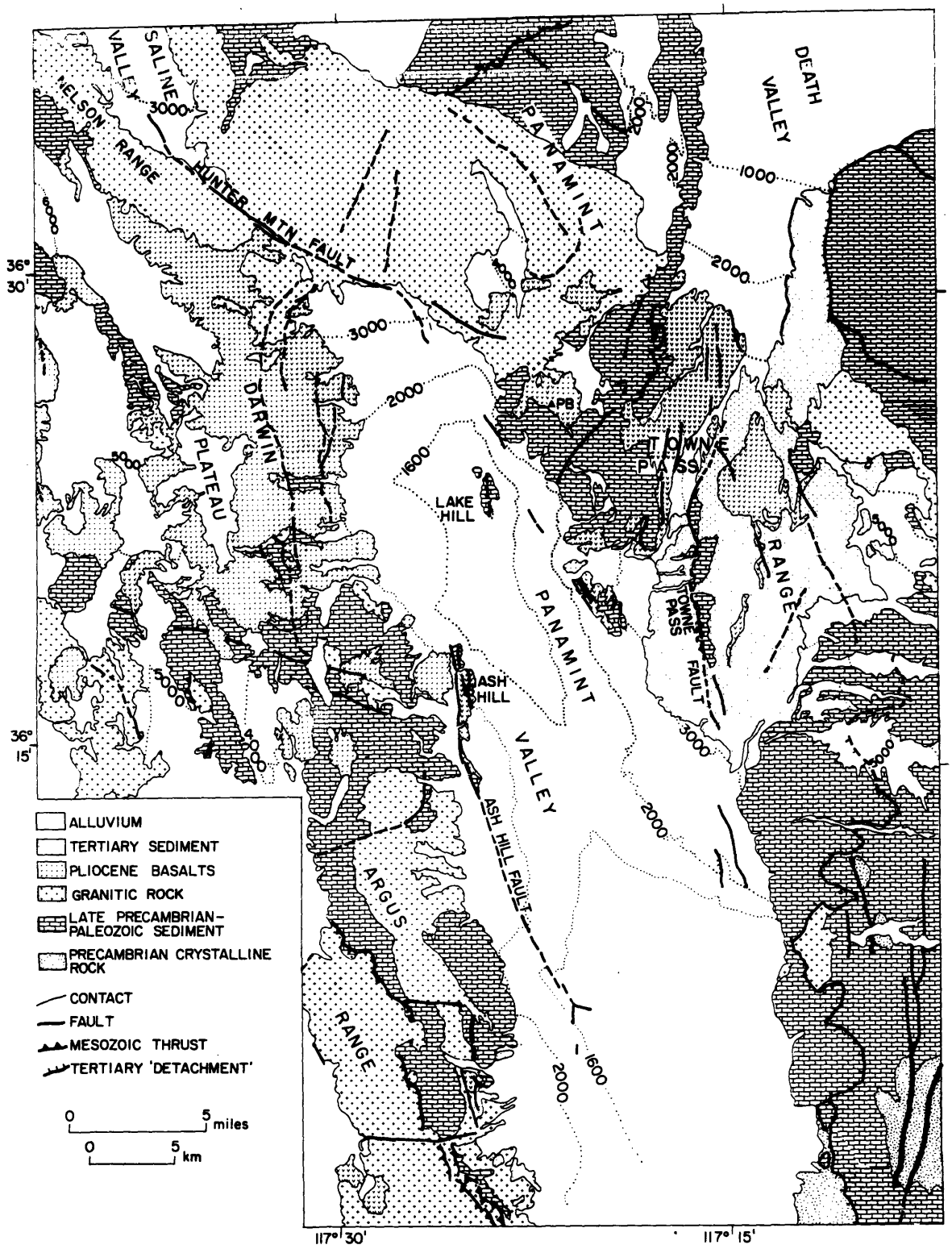

Fig. 1-2. Generalized geology of northern Panamint Valley and vicinity. Modified from Streitz and Stinson [1974]. Location PB is Panamint Butte. Elevation contours in feet.

THICKNESS OF SEDIMENTS IN NORTHERN PANAMINT VALLEY

Gravity, seismic refraction, electrical, and magnetotelluric measurements provide insight into the geologic structure both of the bedrock beneath Panamint Valley and of the sediments that fill the valley. A detailed description of the methods used in acquiring and reducing this data are presented in microfiche Appendix 1-A[1] with a fuller interpretation of the geophysical anomalies. The analysis that follows is concerned with the structure of the late Cenozoic sediments filling northern Panamint Valley.

Gravity

The gravity measurements that we interpret here were drawn from three sources. Published data for the region [Snyder et al., 1981a,b; Chapman et al., 1973] were modified slightly as described in microfiche Appendix 1-A. One survey of 188 sites, directed by one of us (S. Biehler) in the early 1960s, concentrated on the valley floor. The other survey, made by the rest of us in 1985, included 386 sites spanning both the valley and the surrounding mountains. Overall uncertainties of the Bouguer anomalies probably are as high as a few milligals in the high mountains but less than 1 mGal in the valley.

Although local gravity lows are present in the valley (Figure 1-4), there are no prominent gravity gradients and a rather poor correlation of the anomalies with the topography. Some of the most pronounced gravity features are not along the margins of the valley but entirely over bedrock; note the steady rise from west to east near Towne Pass and the -130 mGal highs in the Darwin Plateau area. The lack of a broad negative anomaly clearly identifiable with sediments in the valley places an upper bound of a few hundred meters on the thickness of the valley fill.

Seismic refraction

Two reversed seismic refraction lines were shot within the southern half of the dry lake bed in northern Panamint Valley. The longer profile runs 4570 m (15000 ft) S32°E from

---

[1]Appendices A and B are available with entire article on microfiche. Order from American Geophysical Union, 2000 Florida Avenue, N.W., Washington DC 20009. Document B87-009; $2.50. Payment must accompany order. (These appendices appear at the end of this chapter, a savings of $2.50!).

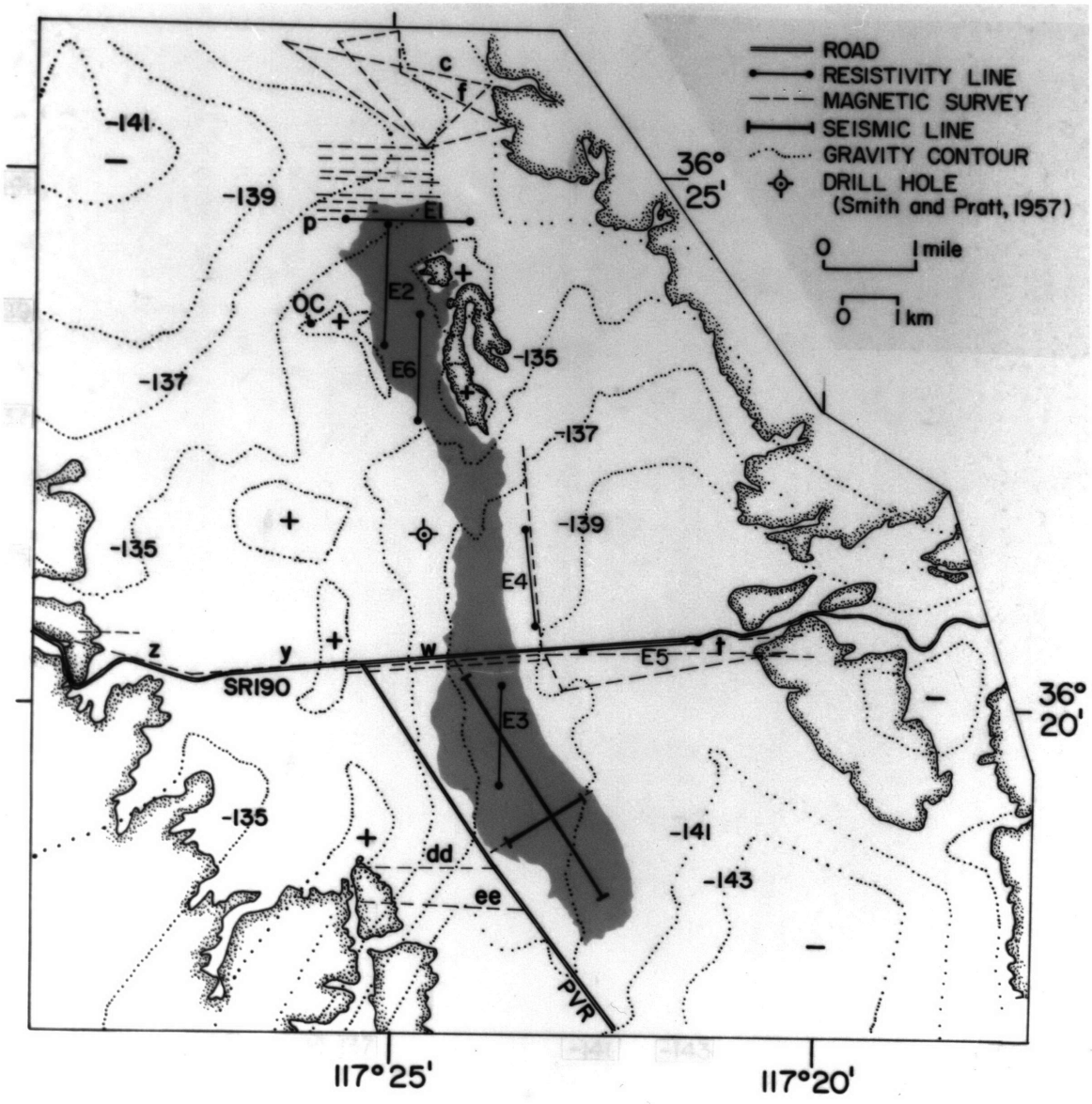
ROAD
RESISTIVITY LINE
MAGNETIC SURVEY
SEISMIC LINE
GRAVITY CONTOUR
DRILL HOLE
(Smith and Pratt, 1957)
0 1 mile
0 1 km
36° 25'
36° 20'
117°25'
117°20'
-141
-139
-137
-135
-143
E1
E2
E3
E4
E5
E6
p
c
f
OC
z
y
w
t
dd
ee
SR190
PVR

about 200 m south of SR 190, and the shorter profile, with a length of 1580 m (5200 ft), crosses the long profile perpendicular to it 2900 m from its northern end (Figure 1-3).

The observed travel time paths are well fit by a series of linear segments, as illustrated by the preferred fit in Figure 1-5 and Table 1-1. Combining the extreme fits allowed for each segment in all possible combinations produces the family of multilayered structures described by the range of values listed in Table 1-1.

These layers may be interpreted geologically with knowledge both of the rocks comprising surrounding ranges and of seismic velocities typical of different rock types [e.g., Press, 1966]. The upper layer is almost certainly unconsolidated alluvium. The compositions of the middle three layers are difficult to identify solely from their velocities, but Smith and Pratt's [1957] borehole log allows us to infer that layer 2 is primarily alluvial sands and silts and that layer 3 is reworked or disrupted Paleozoic sedimentary rocks. These inferences are supported by studies of electrical resistivity and of magnetic anomalies. The velocities of the three lower layers allow several explanations. The increasing velocity with depth could reflect either a decrease in weathering or faulting of the Paleozoic sedimentary rocks; the bottom layer (layer 5) with a velocity of 5.3 km/s would be the least disturbed. Alternatively or complementarily, the increase in velocity could be due to variations in composition, and the bottom layer could be disrupted crystalline rock.

Resistivity

We made 10 electrical resistivity profiles using a Schlumberger configuration and one with a dipole-dipole configuration in and around northern Panamint Valley. Measured apparent resistivities were interpreted by direct comparison with standard curves for the Schlumberger technique [La Compagnie Générale de Géophysique, 1955]. In a first step, all variation in apparent resistivity (ρ_a) was attributed to vertical variations of resistivity. Measurements in the valley were made to study the structure and thickness of the sedimentary fill. Two attempts to determine the electrical structure under Lake Hill probably failed because of three-dimensional topographic effects and structure to the side of the profile. Of the remaining eight Schlumberger configurations, four were on the playa, two on the alluvial fans to its east, and two on bedrock. Because our direct measurements on basalt

---

Fig. 1-3 (previous page). Detail of northern Panamint Valley with locations of seismic, electrical, and magnetic profiles. An outcrop of Paleozoic limestone is designated OC, the playa is solid gray, and outcrop is bounded by shaded edges. Gravity stations are located on Figure 1-4; contour interval is 2 mGal. Panamint Valley Road is designated PVR.

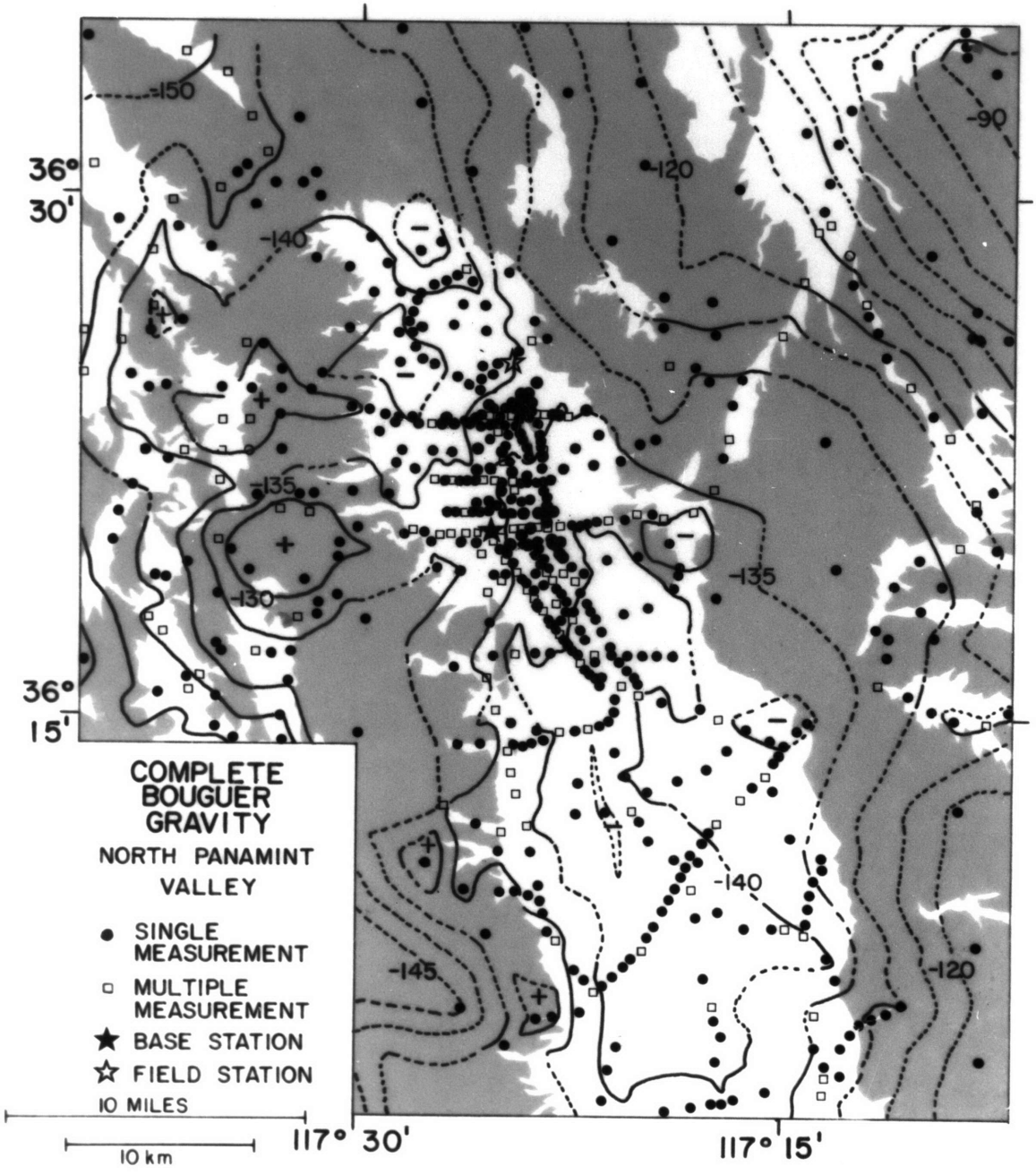
-150
-140
-135
-130
-120
-90
-135
-140
-145
-120
36° 30'
36° 15'
117° 30'
117° 15'
COMPLETE BOUGUER GRAVITY
NORTH PANAMINT VALLEY
SINGLE MEASUREMENT
MULTIPLE MEASUREMENT
BASE STATION
FIELD STATION
10 MILES
10 km

TABLE 1-1. Velocity Structure Under Seismic Arrays

Main Profile

Layer	Velocity km/s	Depth of Layer Top, m, at North End	Cross Line	South End
1	0.98 (0.81-1.11)			
2	1.71 (1.38-2.28)	53 (14-90)	38 (19-86)	29 (22-84)
3	3.16 (2.82-3.28)	120 (90-160)	112 (72-141)	108 (62-130)
4	3.95 (3.52-4.11)	354 (304-415)	329 (236-390)	314 (197-375)
5	5.33 (4.64-5.58)	838 (685-1051)	846 (622-1039)	850 (585-1032)

Cross Profile

Layer	Velocity km/s	Depth of Layer Top, m, at East End	Main Line	West End
1	1.07 (0.90-1.22)			
2	2.59 (2.55-2.81)	49 (38-59)	46 (36-65)	61 (52-90)*
3	3.38 (3.28-3.45)	119 (101-152)	149 (109-183)	185 (119-220)

Fit shown on Figure 1-5 is first value of each entry; figures in parentheses represent possible range of value of the parameter.
*Depth of the interface between layers 1 and 2 at the western end of the cross profile includes an 18-m increase in depth west across a fault(?) near x = 1330 m.

and Paleozoic sedimentary rocks yielded resistivities in excess of 100 Ω m, a value much greater than that of the alluvial sediments, electrical basement was treated as infinitely resistive. The remaining six profiles are interpreted here.

All four profiles from the playa can be closely approximated by standard curves calculated for three horizontal layers (Figure 1-6). The corresponding structures uniformly include a resistive cap over a conductive layer resting on a very resistive half-space. Because high conductivity is likely to be caused by fluid saturation, the resistivity in the conductive layer is probably the same everywhere. Thus an effort was made to find curves with an identical resistivity of the middle layer, which turned out to be near 1.0 Ω m. This proved successful for three profiles, but fitting the measurements from profile E6 required a higher resistivity (Figure 1-6).

The resulting layers are interpreted as dry resistive sediment overlying damp, conductive sediment that in turn overlies more resistive rock. The surface layer varies in thickness from

Fig. 1-4 (previous page). Complete Bouguer anomalies of northern Panamint Valley and vicinity; contour interval is 5 mGal. Pre-Quaternary exposures are shaded.

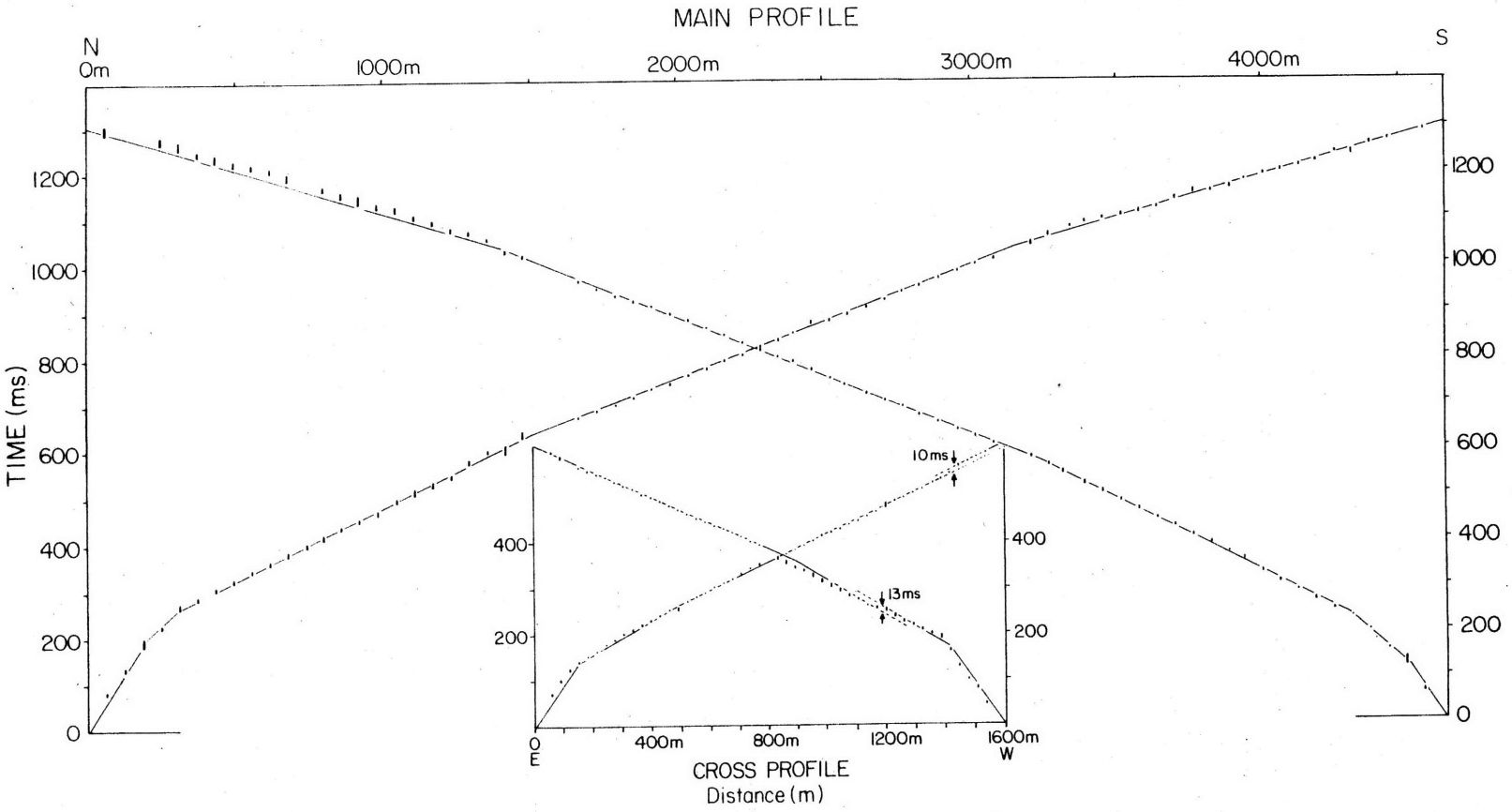
MAIN PROFILE
N
0m
1000m
2000m
3000m
4000m
S
TIME (ms)
0
200
400
600
800
1000
1200
10ms
13ms
0
E
400m
800m
1200m
1600m
W
CROSS PROFILE
Distance (m)

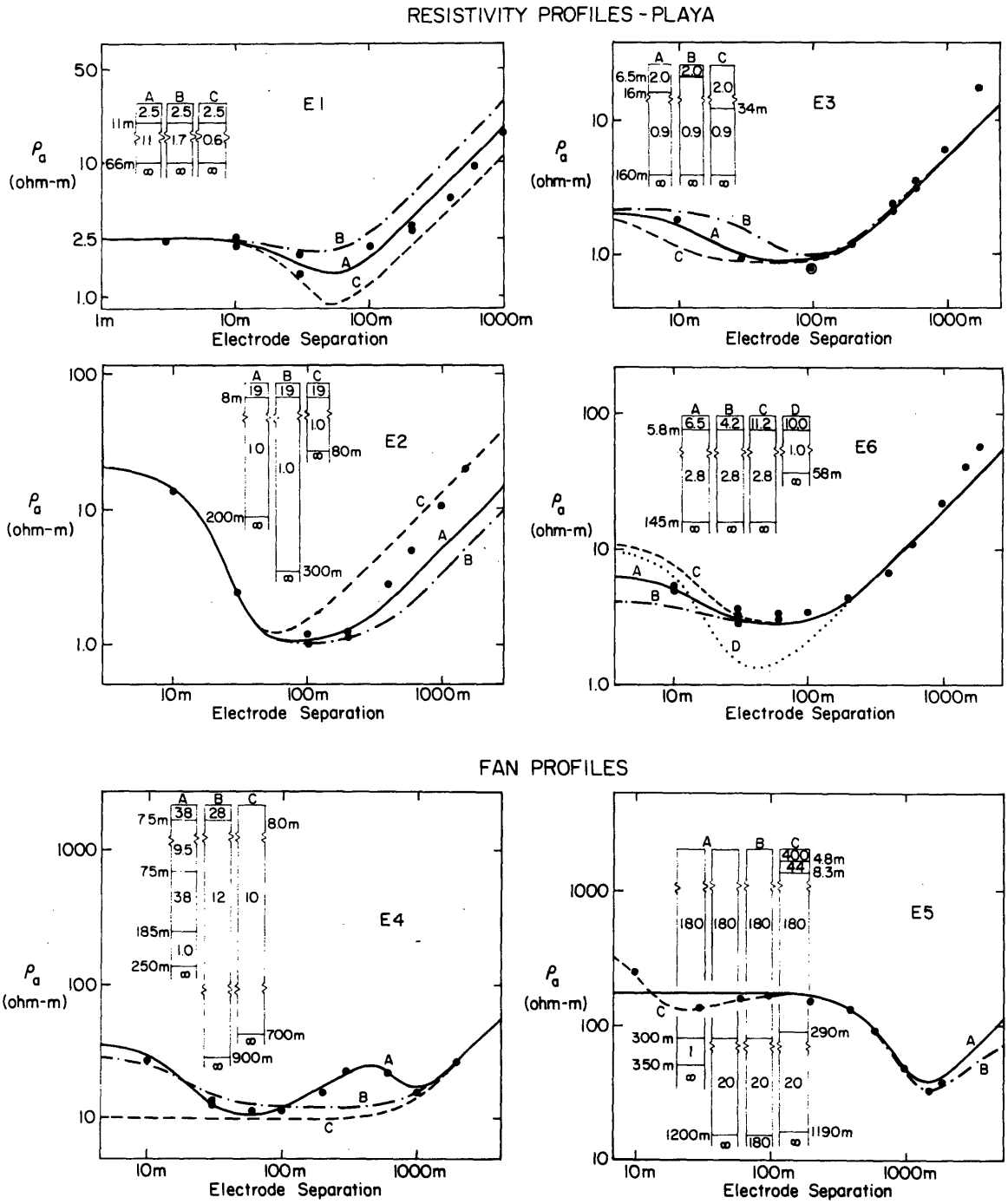

Fig. 1-6. Plots of apparent resistivity (ρ_a) in ohm meters versus electrode separation (x) in meters. Each plot illustrates the effect of a single parameter on the theoretical curves. Electrical resistivities are in ohm meters.

Fig. 1-5 (opposite page). Travel time curves of first arrivals for main seismic profile (top scale) and cross profile (center bottom).

about 5 to 15 m, and its resistivity varies from 2 to 20 Ω m. The inferred depth to the resistive third layer (basement) varies from 66 to 200 m, with a depth of about 150 m for the two best defined interfaces (profiles E3 and E6). Profile E3 is important because it was measured along the main seismic profile; the inferred depth of the top of the electrical basement at 160 m is very close to that of the second interface of the seismic structure, which is near a depth of 115 ± 35 m (Table 1-1). The apparent resistivities at large electrode spacings (> ~500 m) show some effects of coupling (electromagnetic or leakage), and we cannot make a very good determination of the minimum resistivity of the third layer. We estimate this minimum value to be 20 Ω m, which leaves the identification of this layer as bedrock somewhat ambiguous if based solely on the electrical measurements. The similar depth both of Paleozoic limestone in the drill hole of Smith and Pratt [1957] and of seismic layer three suggests that this more resistive layer is probably bedrock or largely derived from bedrock. Continuing investigation with more recently acquired data may resolve this problem.

The two arrays E4 and E5 deployed on the alluvial fans failed to define a resistive basement; neither profile shows a linear proportionality of ρ_a with electrode separation (Figure 1-6). If we assume that the slight upturn in ρ_a for $x > 1000$ m is due to a resistive basement, however, a minimum depth to such a basement can be estimated. For profile E4, this minimum depth is about 200 m. Because the array was deployed only 6 m above the playa surface, the resistive basement must therefore be at least 30 m below the depth inferred for the nearest arrays on the playa (E3 and E6). The minimum depth to basement is more poorly defined at array E5, 140 m above the playa. Basement probably is no shallower than 350 m below the profile, or 50 m below the basement under the playa, and could be much deeper.

Magnetotelluric measurements

Magnetotelluric (MT) measurements were made at 11 sites to place additional constraints on the resistivity structure of the valley. We followed the field and analytical techniques described in an earlier investigation [MIT Field Geophysics Course, 1985]. The final result is an impedance tensor Z, relating the electric field (E) and the time derivative of the magnetic field ($\dot{H}$) by the equation

$$E(\tau) = Z \cdot \dot{H}(\tau) \qquad (1\text{-}1)$$

where τ is time.

Because of the channeling of current by lateral variations in structure, it is usually difficult to use the size of the MT ellipse (representing the tensor Z) to bound the conductivity structure where such channeling occurs. In places away from the valley margin, where the valley structure can be considered two-dimensional, however, the electric field perpendicular to the valley axis can be used to estimate the total conductance of highly conductive sediments in the valley. Using the same regional crustal conductance of 7 mhos and regional telluric field in our frequency band of 750 (mV/km)/(nT/s) as was assumed in an earlier study [MIT Field Geophysics, 1985], we can calculate the product of average conductivity and thickness of the conductive sedimentary cover from MT measurements. The absence of any nearby outcrop and the orientation of the ellipse at site MT6 (located at the east end of the seismic cross profile, Figure 1-3) indicates that this site probably most closely fits the requirements for this calculation. Assuming the resistivity of $0.9 \pm 0.2\ \Omega$ m for the sedimentary fill obtained for resistivity profile E3, we use the computed valley conductance of 110 ± 10 mhos to estimate the thickness of the conductor to be 100 ± 30 m. This estimate is consistent with the 130-m thickness inferred from resistivity profile E3, especially if one recalls that the combined thickness of the first and second seismic layers at profile E3 is about 10 m greater than it is at site MT6 (Table 1-1 and Figure 1-3). At site MT1 east of Lake Hill the inferred conductance was 22 ± 2 mhos. We lack resistivity data to constrain the resistivities, but using $10\ \Omega$ m, a value observed in profiles away from the playa, one estimates a 220-m thickness for the conductive sediments. Thus the magnetotelluric measurements are consistent with the thin layer of highly conductive material in the valley inferred from electrical and seismic measurements.

MAGNETIC ANOMALIES AND THE ABSENCE OF BASALT BENEATH NORTHERN PANAMINT VALLEY

The widespread exposures of basalt flows around Panamint Valley led us to measure several profiles of the total magnetic field on the ground in the valley (Figure 1-3). Our hope was to use magnetic anomalies to infer the extent and depth of basalt flows beneath the valley fill. Two GeoMetrics G-816 portable proton magnetometers were used to measure the total field at spacings normally between 15 m (50 ft) and 120 m (400 ft), depending on the lateral variation of the magnetic field. Each measurement is the average of a minimum of three readings made 2-3 m apart. A virtually identical recording magnetometer was used to measure variations of the field with time at a fixed location in our base camp. Because of the quantity of the measurements and because of the low amplitude (<40 nT) and long period (>

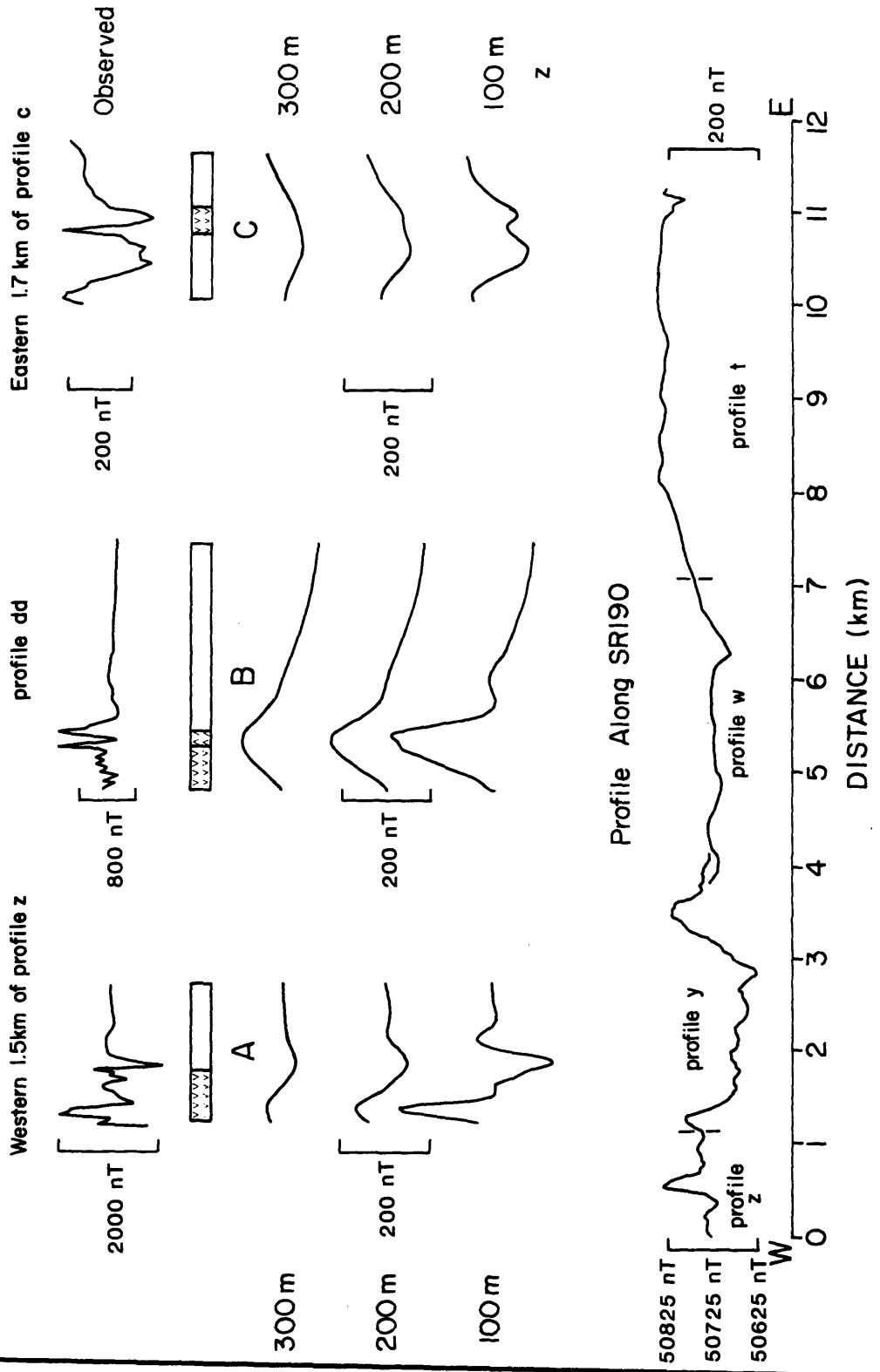

Fig. 1-7. Magnetic profiles. Columns A, B, and C are profiles across (A and B) and near (C) basalt exposures. Observed profiles are at top (note differing scales), while upward

6 hours) of the variations of the magnetic field during each day, we neither corrected the data for daily variations nor subtracted the regional field.

Our profiles fall into two sets: profiles across exposures of basalt at the margins of the valley and longer lines across the valley (Figure 1-2). The two sets are very different. Those across the basalt outcrops show large anomalies, in some cases thousands of nanoteslas, with short wavelengths (hundreds of meters and shorter), but those over the valley are of low amplitude (<200 nT) and long wavelengths (kilometers) (Figures 1-7 and 1-8). Some of the short-wavelength (<30 m) signal observed on the basalt is probably due to remagnetization of the near-surface basalt by lightning strikes, but the bulk of the anomaly is due to some combination of a characteristic magnetization acquired as the basalt cooled, a viscous remagnetization probably aligned with the modern dipole field, and an induced magnetization aligned with the modern magnetic field. Because these magnetizations should be relatively constant laterally within the basalt, the observed anomalies permit two obvious explanations: either there are only small variations in magnetization beneath the valley fill (no basalt) or any strongly magnetized sources are deep. Rather than model the magnetic anomalies using a few of the infinity of possible structures, we chose to use the profiles of magnetic anomalies across basalt outcrops as reliable examples of how the magnetization of basalt can affect the measured field. We then compared these profiles and upward continuations of them with profiles measured across the valley. Such comparisons allow us to draw inferences about the magnetization of material beneath the valley and in particular about both the depth of material with high magnetization and the maximum values of magnetization.

Upward continuation of a profile was accomplished first by multiplying the Fourier transform of the profile by e^{-kz} and then by plotting the inverse transform, where k is the wave number and z the height of the continuation. Multiplying by the quantity e^{-kz} drastically reduces the short wavelength anomalies prominent at the surface, leaving the longer wavelengths to dominate for values of z as low as 50 m (Figures 1-7 and 1-8). For some profiles shown in Figures 1-7 and 1-8 only a portion of the entire profile is shown, but before truncation the entire profile was processed as described above.

continuations to elevation z (in meters) are below and at a uniform scale. Geologic bar diagrams separate the observed profiles from the upward continuations; symbols as in Figure 1-1 with the addition of inverted "v"s indicating basalt exposures within 100 m of, but not on, the profile. At bottom, at the same scale as the upward continuations, is the profile across Panamint Valley composed of individual segments as indicated. All distance scales are identical. Profiles are located on Figure 1-3.

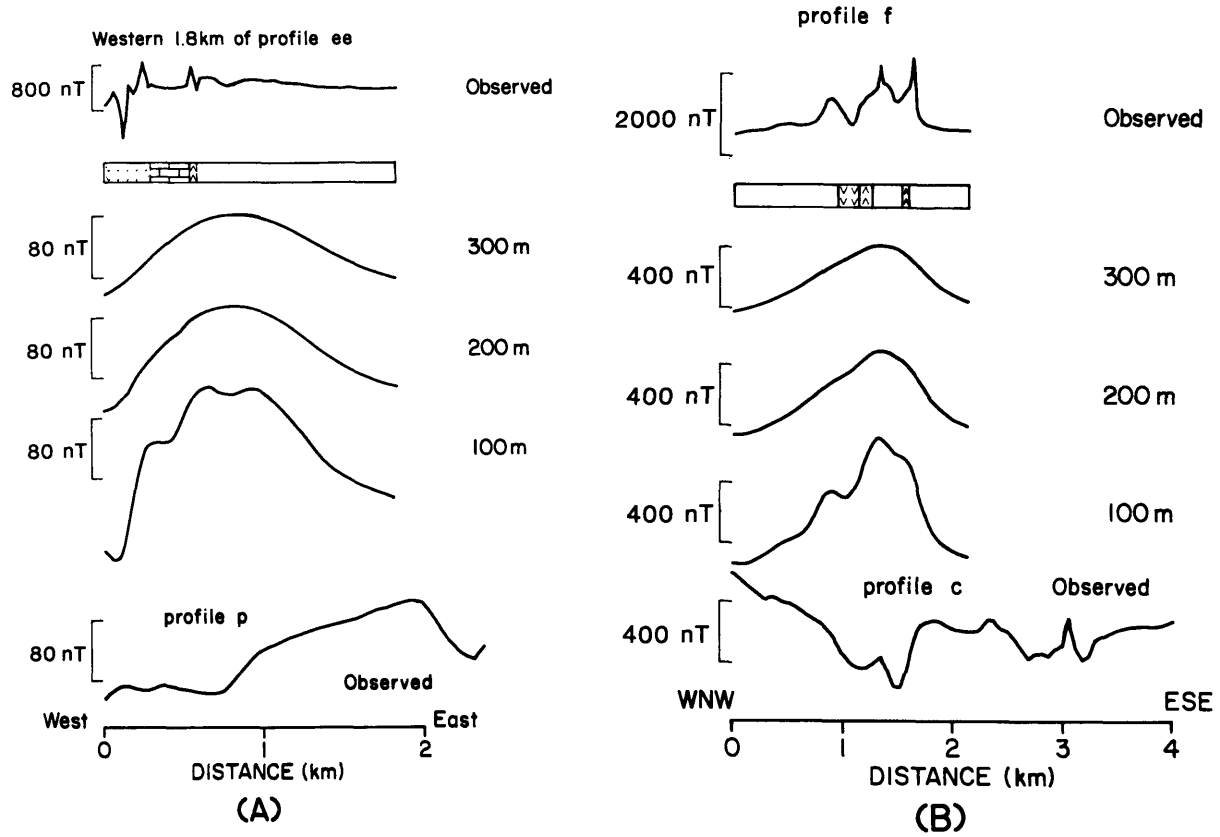

Fig. 1-8. Magnetic profiles, layout similar to Figure 1-7. Bottom profiles: (a) across the northern end of the playa; (b) 2.5 km north of the playa.

The upward continuation of profiles by this procedure is based on the assumptions that the field is two dimensional, varying only vertically and along the profile, and that the profile was measured along a horizontal line, assumptions that probably are false in places and only approximately correct in others. For two reasons, however, we think that the horizontal variation of the field perpendicular to the profile is not serious. First, if the field varied in both horizontal directions with a similar spectrum, the upward continuation of it to a height z would attenuate a given wave number by the same amount as the upward continuation of a one-dimensional profile to a height of $\sqrt{2} \cdot z$. For the comparison that we make here, a 50% error in the heights, or inferred depths below the sediment in the basin, is not important. Second, the similarity of the profiles that we made over the edge of the basin suggests that the anomalous field there is roughly two dimensional, and upward continuations of profiles over the edge of the basin, both of those that cross exposures of basalt and of those along which basalt is not exposed, are very similar. This can be seen by comparing the upward continued profiles in Figure 1-8b and profile C in Figure 1-7, where basalt was not exposed along the profile but did crop out tens of meters from it, with the remaining three upward continued

profiles in Figures 1-7 and 1-8, which crossed linear edges of basalt outcrops at nearly right angles. Given the qualitative nature of the inferences drawn below, the errors introduced by the simple application of upward continuation to the profiles will not be important.

We then compared directly the upward continued profiles with the observed profiles across the valley, and we used this comparison to infer the depth of any basaltic body under the valley fill, assuming that the valley fill is not magnetized. Although we did not measure any magnetizations for this study, magnetizations for sands and silts are usually orders of magnitude below those typical of basalt [e.g., Telford et al., 1976, p. 121]. In places the valley sediments are conglomerates with basalt cobbles; these sediments may have unusually high magnetizations, but we expect that anomalies from the gradual facies changes to finer, less magnetic sediments are inconsistent with the wavelengths and amplitudes characteristic of anomalies from buried or exposed edges of basalt sheets.

On the long profile across Panamint Valley (Figure 1-7) there are two candidates for strongly magnetized zones (basalt) below the sediment, at distances of about 1 and 3.5 km. The anomalies around 0.4 and 1.2 km are narrow, suggesting, by comparison with the upward continuations of profiles A and B of Figure 1-7, a rather shallow (<150 m) depth for the source. The shape of the anomalies resembles that over the edges of a tabular, magnetized body with a slight eastward dip and with its edges near 0.5 and 1.2 km. The amplitudes of the anomalies are half that of the very similarly shaped anomaly A (Figure 1-7) upward continued to z = 100 m. We infer that a tabular body equal in magnetization to the basalt lies to the south of the profile, mostly concealed by a Pleistocene fanglomerate. This body is probably a portion of the volcanic sequence exposed west of the valley.

Both the width and amplitude of the other anomaly near 3.5 km are much greater than those of the anomaly near 1 km. Its shape and amplitude are both similar to the upward continuations of curves A and B to z = 200 m (Figure 1-7). We suspect that the anomaly near 3.5 km is due to basalt between the depth of 100 and 300 m. It could represent the western edge of a sheet extending under the valley, but the field to the east is nearly featureless. Such a sheet would have to underlie the valley to its eastern edge without any significant fault offset or variation in magnetization for it to fail to produce an obvious signal. Because we measured differences in magnetic intensity of thousands of nanoteslas at sites only hundreds of meters apart on the Darwin Plateau and because there is no significant anomaly over the valley to the east, we suspect that the signal near 3.5 km is due to a small body extending from about 3.0 to 3.5 km and buried 200 ± ~100 m and that a uniformly magnetized sheet does not underlie the central and eastern parts of the valley. Its western boundary is almost certainly the Ash Hill fault, and the source is probably a northward continuation of the basalt from Ash Hill (Figure 1-1).

The lack of any large anomaly to the east of x=4 km can be explained by three hypotheses: either (1) no significant amount of basalt lies under the valley, (2) the amount of sedimentary fill in the valley is sufficiently great to prevent detection of magnetic anomalies produced by magnetization of the basement, or (3) basalt under the valley is substantially less magnetic than that exposed at the valley's margins. We infer from the upward continuations of profiles across the margins that any magnetic sources like those produced by the basalt at the valley margins must be buried more than about 300 m for them to go undetected (Figures 1-7 and 1-8). Based on the interpretation of seismic, electric, and Bouguer gravity data already presented, we doubt that the pre-Tertiary basement is deeper than 150 m under the playa (segment w of Figure 1-7). Hence at least 5 km of the profile across the valley lacks a strongly magnetized basement immediately beneath the valley fill.

The basement may be deeper under the eastern part of the profile, which crosses the fan east of the playa, and we cannot eliminate the possibility that basalt is buried within or beneath the great thickness of sediment (> ~350 m) inferred from resistivity profile E5. The uncertainty in the age of these sediments beneath resistivity profile E5 prevents any conclusive finding about the easternmost segment of the cross-valley profile; hence we infer that at least 5 km and possibly as much as 9 km of the roughly 11.5 km width of the valley is underlain by basement whose uppermost part lacks material magnetized as strongly as the basalt on the margins.

No other profile crosses the entire valley, but two other segments (profiles p and c) can be compared with upward continuations of profiles across the margins (Figure 1-8). Magnetic anomalies along profile p (Figure 1-8a) are too small for any but deep (>300 m) sources similar to the basalt at the valley margin. This profile coincides with resistivity profile E1, for which the basement appears to be at a depth of only 130 m. Therefore strongly magnetized rock, like basalt, cannot be near the top of basement under this area, but some more weakly magnetized rock might be present at the east end of the profile. Profile c (Figure 1-8b) passes south of basalt exposures near x = 3 km, and the signal near x = 3 km is similar to another from 1.0 to 1.5 km. The amplitudes of both of these magnetic anomalies are much smaller than those of profiles over outcropping basalt. The narrow widths of these anomalies requires that the source be near the surface (z < 100 m; compare with upward continuations of Figures 1-7 and 1-8), but the low amplitudes require that the sources under the profiles either be less strongly magnetized than outcropping basalt or extend laterally less than about 100 m from the profile. The presence of small blocks of volcanic rock (hundreds of meters) near the surface at 1.3 and 3.0 km might account for the observed anomalies. The impressive gradient at the west end of this profile is not defined enough to infer a unique origin.

The smooth variations in the magnetic anomalies over the basin seem to indicate that basalt is absent under the valley. Were there variations in magnetization as large as those that occur in and near the basalt along the margins of the valley, they would generate much larger anomalies than those that we observe, unless they were at depths of 300 m or more. The evidence that basement is at a depth of only 100-200 m eliminates the latter possibility. Only if the basalt beneath the valley lost its magnetization through some process that did not destroy the magnetization of exposed basalt could there be basalt beneath the valley that does not generate a signal of 50 nT or more.

We have made profiles over only a small portion of the valley, and thus we cannot eliminate the possibility that there are areas underlain by basalt. From the profile along State Highway SR 190, however, we infer that at least 5 km of the width of the valley, and perhaps 9 km, are not underlain by basalt.

GEOLOGIC INTERPRETATION

A combination of gravity, electrical, magnetic, and seismic investigations imply that northern Panamint Valley is essentially a shallow basin. Probably subcrop beneath alluvial sediments in most of the valley, like the rare exposures of bedrock, is Paleozoic carbonate rock, possibly with granite of the Hunter Mountain pluton in the north, but with less dense Pliocene sediment on the east side of the valley southeast of Lake Hill. The structure of the northern valley is probably characterized by a complex assemblage of north to north-northwest trending horsts and grabens (see Appendix 1-A). Such structure is consistent with the magnetic profile north of Ash Hill and the electrical and gravity data collected near Lake Hill.

A section of the subsurface is best constrained under the playa. In the upper 100-150 m of material, P wave velocities are below 3 km/s and electrical conductivities are about 1 Ω m. These are typical values for brine-saturated, unconsolidated sediment. Under these sediments, P wave velocities range from 3.1 to 4.0 km/s and resistivities exceed about 20 Ω m. This material probably is Paleozoic carbonate rock similar to that at the bottom of Smith and Pratt's [1957] drill hole. The P wave velocities seem low for well-indurated carbonate rock; this layer might be either a well-indurated, probably calcified fanglomerate or tectonic chaos similar to the Amargosa chaos to the east [Wright and Troxel, 1973]. Both would have appropriate values of velocity and resistivity. This layer is inferred to be about 700 m thick from our seismic profile. The similarities of the resistivity and density of this material to those of Paleozoic sedimentary rock prevent us from estimating the lateral extent of this

layer. Seismic basement, with a P wave velocity of about 5.3 km/s, could be less disrupted Paleozoic sedimentary rock.

In the valley the magnetic field shows little variation (<50 nT) over distances less than about 3 km. Since variations as large as 2000 nT occur over distances of 100 m or so at the margins where basalt is exposed, the simplest explanation is that the basalt is absent beneath about 50-90% of the valley floor.

Low-angle normal faulting

The similarity of the basalt in the Darwin Plateau and in the Panamint Range, and its apparent absence in Panamint Valley, suggests a large displacement of the sides of the valley. This inference is yet more strongly supported by Burchfiel et al.'s [1987] measured offsets of piercing points on opposite sides of the Hunter Mountain strike-slip fault connecting Panamint and Saline valleys; the offset is 9 ± 1 km. If the apparent absence of basalt beneath a 5-9 km width of Panamint Valley were due to displacement of the Darwin Plateau away from the Panamint Range in a direction parallel to the Hunter Mountain fault, the offset would be between about 6 and 10 km. The shallow depth of the basement beneath northern Panamint Valley and the apparent absence of basalt thus imply that 4 m.y. ago the basalt on the eastern margin of the Darwin Plateau was continuous with the basalt on the Panamint Range and that slip has occurred at a very shallow depth on a fault dipping at a very gentle angle to the west (Figure 1-9). Were the extension to have occurred on a series of steep faults, there should be remnants of basalt left behind in the valley floor. For a fixed amount of slip on a low-angle normal fault, if the fault were deeper, the basin would be deeper than it is. If only one major fault had been active and if the average plunge of slip on it were as steep as 20° or 30°, then for 8 km of slip, the elevation of the basalt on the Darwin Plateau would be 3-5 km lower than the basalt on the Panamint Range. Thus the amount of horizontal slip (9 km), the apparent absence of basalt, the shallow depth of the basement beneath the basin, and the comparable elevation of the Darwin Plateau and the Panamint Range together require a gently dipping fault or system of faults along which the upper few kilometers of the crust beneath the Darwin Plateau were stripped from what is now the basement of Panamint Valley.

Because the inferred total extension across Panamint Valley essentially matches the displacement suggested by Burchfiel et al. [1987] for the Hunter Mountain fault, the low-angle normal fault need not be older than either the Hunter Mountain fault or northern Panamint Valley. Because 4-m.y.-old basalts predate the formation of the northern valley and are apparently absent from beneath the valley floor, the faults bounding northern

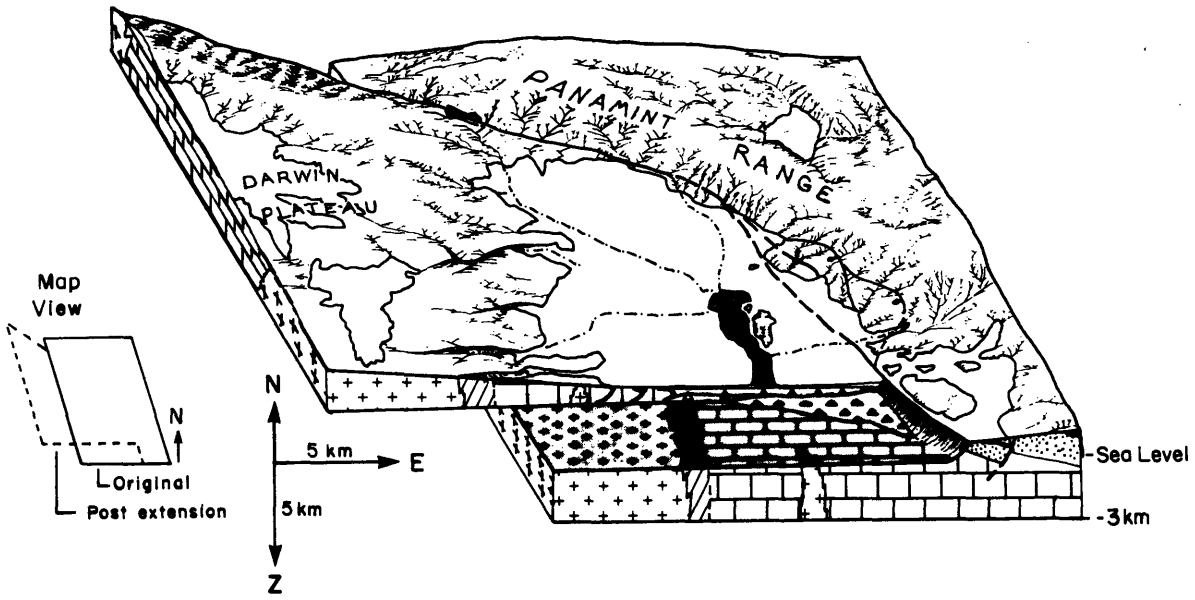

Fig. 1-9. Isometric block diagram of northern Panamint Valley illustrating structures inferred from this study. View is down 30° to due north. Symbols on block margins as in Figure 1-10 except for solid black, denoting basalt, and triangles, denoting tectonic breccia. Note that no coherent upper plate material underlies most of Panamint Valley. No vertical exaggeration or perspective.

Panamint Valley that merge downward with this low-angle normal fault must be younger than 4 m.y.

Implications of low-angle normal faulting for features in the gravity and magnetic fields

Mabey [1961] associated the Hunter Mountain pluton with two prominent geophysical anomalies on the Darwin Plateau: several Bouguer gravity highs over the dense, metamorphosed rock immediately adjacent to the pluton, and a large (~1000 nT) aeromagnetic high over the pluton. Because the pluton has very steep contacts with the country rock [Burchfiel et al., 1987], the pluton probably extends roughly vertically to or below the depth of the inferred low-angle normal fault. The geophysical anomalies that should be produced by the beheaded portion of the pluton provide an additional test of the existence of the low-angle normal fault.

The gravity anomalies that Mabey [1961] inferred to be due to high-density metamorphic rock lie on the Darwin Plateau north-northwest from the -130+ mGal high at about 36°20'N, 117°32'W (Figure 1-4). If the gravity highs of the Darwin Plateau were due to density contrasts in the upper plate, then when restored, the areas of high density should lie over the lower plate at the west margin of the modern valley, roughly in the north-south portion of the

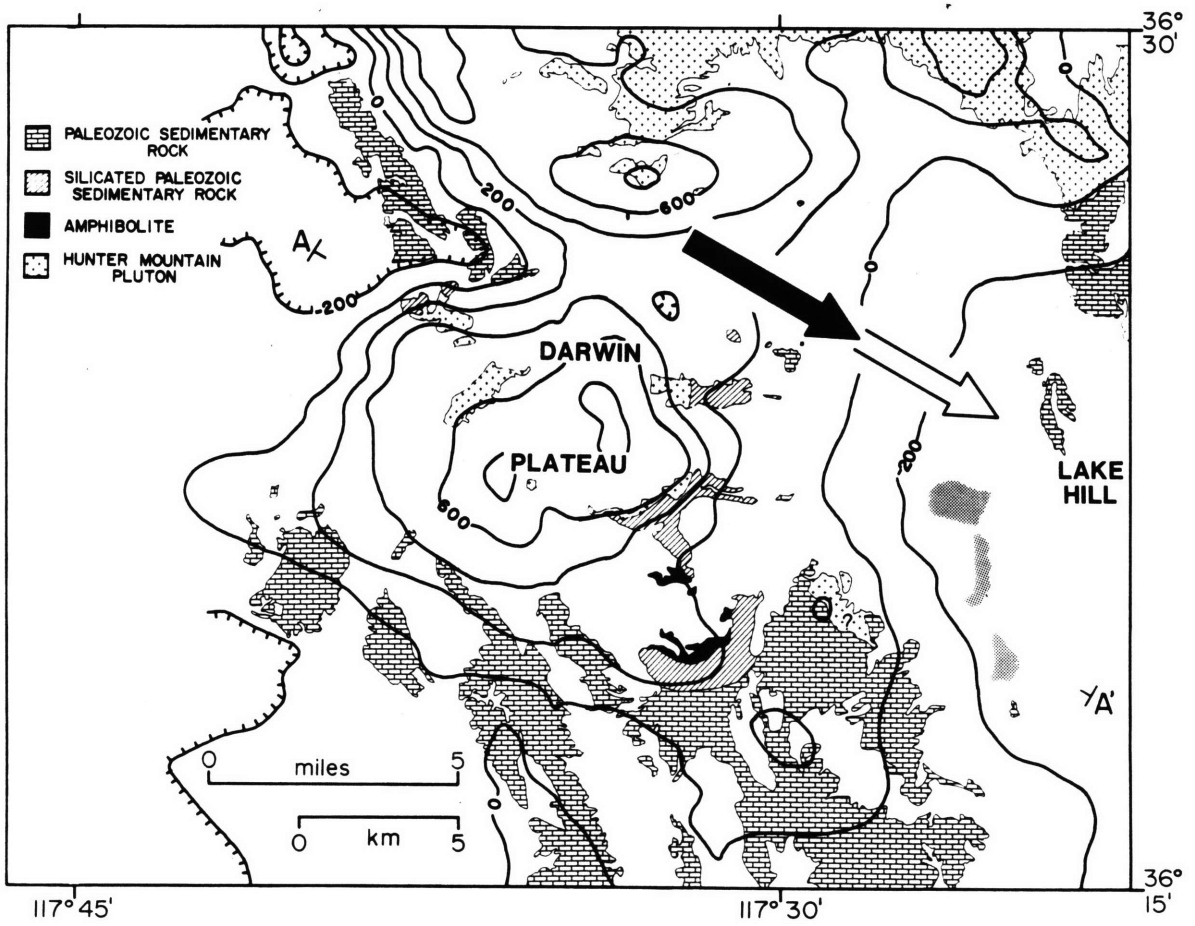
36° 30'
PALEOZOIC SEDIMENTARY ROCK
SILICATED PALEOZOIC SEDIMENTARY ROCK
AMPHIBOLITE
HUNTER MOUNTAIN PLUTON
A
A'
0
200
600
-200
DARWIN
PLATEAU
LAKE HILL
0 miles 5
0 km 5
117° 45'
117° 30'
36° 15'

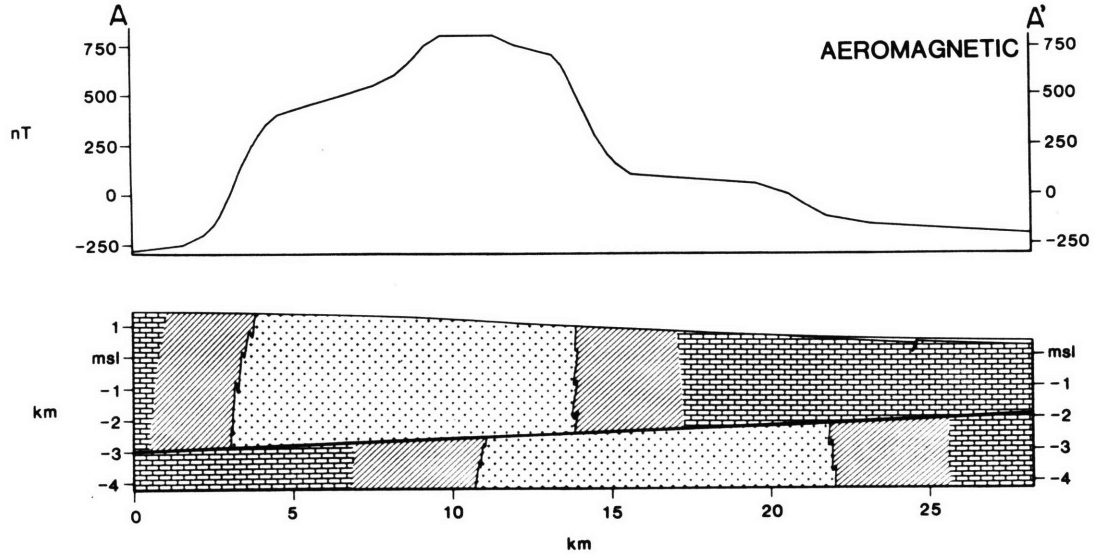
A
A'
AEROMAGNETIC
nT
750
500
250
0
-250
km
1
msl
-1
-2
-3
-4
0
5
10
15
20
25
km

-135 mGal gravity high between about 36°18'N and 36°23'N (Figures 1-3 and 1-4). The gravity anomaly over this edge of the valley seems high, especially if the 100-300 m depth to the basalt just west of Panamint Valley Road is correct and if gravity increases regionally eastward. Thus the sources of both highs might be the same high density metamorphic rock that later was sliced by a gently dipping fault. If this explanation were correct, then the amphibolite and silicated metamorphic rock exposed in the Darwin Plateau might also underlie the western margin of the valley.

The aeromagnetic anomalies in the vicinity of the Hunter Mountain pluton can also be explained as the disruption of a single magnetized body. The increase in the magnetic field across the western edge of the pluton is 1000 nT. The decrease across the eastern edge in the Darwin Plateau however, seems to occur across two steps, with a steep western drop of about 500-750 nT at the east edge of the Darwin Plateau and with a gentler eastern drop of about 200-400 nT about 8 km southeast of the Darwin Plateau (Figure 1-10). If the first decrease were caused by contrasts in magnetization within the upper plate and the second from those in the lower plate, then restoration of the postulated slip on the low-angle normal fault would superimpose these gradients as indicated by the arrow on Figure 1-10. This restoration would also restore the contact of the intrusion with the metamorphic country rock as described by Burchfiel et al. [1987].

This proposed correlation of these gravity and magnetic signatures suggests that the inferred offset of the Mesozoic Hunter Mountain pluton might be about equal to the inferred opening of northern Panamint Valley. Because the Mesozoic Hunter Mountain pluton would then not be offset, this reconstruction would eliminate the possibility of any large displacement on the underlying low-angle normal fault predating the creation of northern

---

Fig. 1-10. Geophysical anomalies associated with the Hunter Mountain pluton. Aeromagnetic contour interval 200 nT, from U.S. Geological Survey [1982]. Shaded areas are alluviated areas in Panamint Valley with Bouguer anomalies greater than -133 mGal (compare with Figure 1-3). Arrows indicate minimum (solid) and maximum (open) movement of the Panamint Range relative to the Darwin Plateau inferred from the area in the valley not underlain by basalt. Silicated Paleozoic sedimentary rock is not separated from Paleozoic sedimentary rock east of 117°30'W. The relation of the queried intrusion to the pluton is uncertain. Geology modified from Hall and MacKevitt [1962] and Hall [1971]. Cross-section line is drawn parallel to the Hunter Mountain fault; the schematic geologic cross section indicates the approximate geometry for the Hunter Mountain pluton for 8 km of extension parallel to the Hunter Mountain fault.

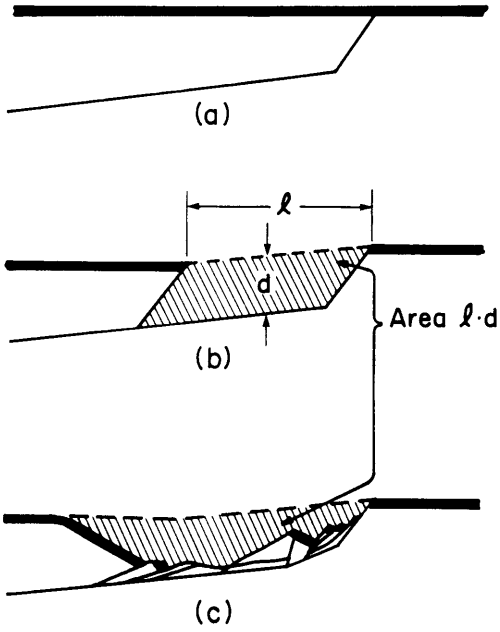

Fig. 1-11. Cartoon illustrating relation of the cross-sectional area of Panamint Valley to the displacement (l) and depth (d) of the low-angle normal fault. (a) Before faulting, (b) idealized after faulting with no deformation of the upper plate, and (c) idealized after faulting with more realistic deformation of the upper plate.

Panamint Valley. Hence the low-angle normal fault is probably not a reactivated fault but rather a feature created about 4 m.y. ago when northern Panamint Valley began to form.

The depth of the low-angle normal fault

The depth of the fault is of special interest because its position below the basalt cap of the Panamint Range closely approximates its depth at its inception. One possible estimate of this depth is given by assuming that the top surface of the layer with a velocity of 5.3 km/s defines the upper surface of the lower plate of the fault. This places the fault at depth of about 800 m below the playa (Table 1-1) or about 2.5 km below the basalt cap to the east. Another estimate can be made if the 400-nT aeromagnetic gradient is assumed to mark the edge of the Hunter Mountain pluton in the lower plate; the 2-4 km half width of this gradient in an east-west direction is consistent with the source being about 2-8 km below the flight line, which was flown at an elevation of 2100 m, about the same as the basalt cap of the Panamint Range. This range is similar to that of 3.8-10.2 km below the flight line obtained from the amplitudes of the anomalies, described in Appendix 1-B.

A simple geometrical argument provides the most reliable method for estimating the depth of the low-angle normal fault underlying the valley and the Darwin Plateau. In cross section the area left vacant by the motion of the upper plate equals the product of the displacement of the undeformed upper plate (l) and the mean depth of the low-angle surface below a line parallel to the low-angle normal fault from where it crops out (d, Figure 1-11). The relatively thin layer of sediments, the closed basin of northern Panamint Valley, and the undissected nature of the surrounding ranges suggests that erosion has not removed much

material from the section line and that this simple calculation is reasonable. Topographic cross sections were constructed across the valley near SR 190 and at the north end of the playa. We estimated the cross-sectional area of the valley below a line connecting basalt exposed high in the Panamint Range with basalt exposed just west of the pronounced flexure between the Darwin Plateau and Panamint Valley. These estimates range from 17.6 to 25.5 km^2. The larger calculated area includes some deformation clearly associated with the older Towne Pass fault system at the east end of SR 190. Eliminating this effect leaves an estimate for the area of 19 ± 2 km^2. For between 5 and 9 km of east-west extension across the valley, the mean depth of the fault would be 3.0 ± 1.2 km beneath a surface at an elevation of 1800 m (6000 ft) or 1.7 ± 1.2 km beneath the playa.

CONCLUSIONS

Complete Bouguer anomalies obtained within and around northern Panamint Valley display no steep gradients within the valley or near its margin. The most pronounced low within the valley, of 15 mGal, suggests that the maximum thickness of Tertiary sediment is less than 1.2 km and that much of the valley is probably underlain by much thinner Tertiary cover. A 5-10 mGal high on the Darwin Plateau to the west is probably caused by high-density amphibolitic rocks exposed over the same area. Much of the variation in the gravity field over Panamint Valley could be due to similar density variations in the basement beneath it and not to variations in the thickness of Tertiary and Quaternary sediments.

Two seismic profiles, one along and one across the valley's northern playa, yielded first arrivals of P waves consistent with a velocity structure with four gently dipping, and possibly flat, interfaces (Table 1-1). The velocities of the upper two layers are less than 2.8 km/s, and their combined thickness increases to the west-northwest from a minimum of about 108 m to a maximum of about 185 m. The P wave velocities of the two deeper layers are 3.2 and 4.0 km/s, and the interfaces dip gently to the north. The depth to the base of these layers is about 840 m. Seismic basement at that depth has a velocity of 5.3 km/s.

Six of 10 electrical profiles measured using a Schlumberger configuration were interpreted in terms of a vertically varying resistivity structure. Four profiles measured on the playa are consistent with similar three-layer structures: a resistive layer with a thickness of 5-12 m and with a resistance of 2-20 Ω m overlies a more conductive layer generally extending to a depth of 70-200 m and with a resistivity near 1 Ω m, which in turn overlies a half-space with a resistivity of 20 Ω m or more. Two profiles measured on the fans east of the playa show much thicker intermediate layers. Minimum estimates of the depth to resistive

basement are 200 m just east of the playa and range between 200 m and 1 km beneath the elevation of the playa about 3 km east of it.

Ellipses representing impedance tensors, which were calculated from magnetotelluric measurements made in and around the valley, generally reflect the existence of a conductive channel provided by the valley. The magnitude of the minor axes for a midvalley measurement yields an estimate of the product of the mean conductivity with the thickness of the surficial conductor consistent with a thickness of 100 m for this conductor, an estimate similar to that derived from a nearby resistivity profile.

These data allow us to infer that the thickness of the low-density, low-velocity, and highly conductive sediments in the valley is only 100-200 m under the playa, an inference supported by the existence of Paleozoic limestone found at a depth of 111 m in a borehole under the valley floor [Smith and Pratt, 1957].

Measurements of the magnetic field made along profiles across the valley floor exhibit low variations (<50 nT) of the magnetic field over distances less than about 3 km, but profiles across edges of exposures of basalt (Figures 1-7 and 1-8) show very large amplitudes (up to 2000 nT) over distances of only 100 m or so. Because of the subdued field over the valley, if basalt underlay the valley, it would have to lie deeper than several hundred meters. The amplitude (>75 nT) of anomalies calculated by upward continuations of the profiles across the basalt outcrops to a height of 300 m is greater than what we observed in the valley; yet the thickness of the sediment is less than 200 m over most of the valley. Thus we infer that basalt is absent under 50-90% of the valley floor along SR 190. The large uncertainty in this estimate arises because in the area east of the playa the thickness of the sedimentary cover could exceed 400 m.

The absence of basalt under a 5-9 km wide area of the valley floor can be explained by tectonic denudation of the initially regionally extensive flows that still cover much of the Darwin Plateau and the Panamint Range. Our estimate of between 6 and 10 km of northwesterly displacement of the Darwin Plateau on a shallow, gently west dipping normal fault is consistent with Burchfiel et al.'s [1987] inference of 9 ± 1 km of right-lateral strike-slip displacement on the Hunter Mountain fault connecting Panamint and Saline Valleys.

Acknowledgments. We thank B. P. Luyendyk of the University of California at Santa Barbara, E. Silver of the University of California at Santa Cruz, and G. Thompson of Stanford University for the loan of equipment; Beno, Ron, and Tanya Atwater for the loan of a jeep; B. Gilman, S. Wild, M. Prang, and S. Park for vital assistance in carrying out the seismic refraction study; and L. McKenna, A. Michael, S. Park, C. Stork, and others for weekend assistance. R. Simpson and G. Thompson made many useful comments in

reviewing this paper. We also thank the Ridgecrest office of the Bureau of Land Management for their assistance and cooperation. We are particularly grateful to B. C. Burchfiel and K. V. Hodges for their advice and recommendations and for sharing their results. L. Ardrey drafted the figures. Finally, we thank N. Hourihan, S. Neustadtl, and B. Stuntebeck for managing our camp so well.

APPENDIX 1-A
COLLECTION, REDUCTION, AND FURTHER INTERPRETATION OF GEOPHYSICAL DATA GATHERED IN NORTHERN PANAMINT VALLEY[1]

INTRODUCTION

Panamint Valley lies in the California Basin and Range midway between Death Valley and Owens Valley (Figure 1-1). Bedrock of the surrounding ranges is largely Mesozoic granite that has intruded late Precambian to earliest Mesozoic sedimentary rocks [e.g., Dunne et al., 1978]. One such pluton, the Hunter Mountain pluton (north of about 36°20'N on Figure 1-2), has metamorphosed its wallrocks locally into amphibolites. As described by Burchfiel et al. [1987] northern Panamint Valley formed in the last 4 m.y. Unlike many valleys of the Basin and Range Province, Panamint Valley has some exposures of pre-Cenozoic rock near its center (Lake Hill and OC on Figure 1-3); Lake Hill was previously considered to be a block that slid out onto the valley floor [Hall, 1971].

We gathered gravity, seismic, electrical (resistivity and magnetotelluric), and magnetic measurements in and near northern Panamint Valley in order obtain constraints on the structure of the subsurface beneath the valley floor. Gravity measurements were made to define the thickness of Quaternary sediment in the basin and to investigate bedrock structures that could bias this estimate. Two reversed seismic refraction profiles, one along the valley and 4.6 km in length and the other across the valley and 1.5 km in length, were shot to constrain the depth to basement and its dip at one locality. Electrical resistivity measurements were made for a similar purpose and to define the electrical properties of the sediments. Magnetotelluric data permit a gross interpretation of shallow conductors and help to constrain the subsurface structure near Lake Hill. The principal results of these investigations are presented in the published article. This appendix contains a more detailed summary of both the acquisition of and reduction of these data. We also discuss the occurrence and possible origin of several anomalies not discussed in the main paper.

---

[1] Initially published as a microfiche appendix to "A Geophysical Investigation..." (Document number B87-009 of the American Geophysical Union). Figure numbers refer to figures in the main text (except Figure A1).

Table 1-A1. Apparent Velocities (v_a) and Intercept Times (t_i) for Line Segments Fitting Observed First Arrivals from Seismic Refraction Profiles

		Main Profile				
		Forward			Reversed	
Segment		v_a(km/s)	t_i(ms)		v_a(km/s)	t_i(ms)
1		0.76-1.04			0.85-1.19	
2		1.22-2.24	30-130		1.66-2.33	49-97
3		3.15-3.39	166-184		2.99-3.19	128-137
4		4.00-4.33	262-280		3.64-3.93	190-230
5		5.39-5.65	449-498		4.67-5.52	356-477
		Cross Profile				
		Forward			Reversed	
Segment		v_a(km/s)	t_i(ms)		v_a(km/s)	t_i(ms)
1		0.79-1.22			1.01-1.22	
2		2.51-2.66	72-82	x>1190m	2.63-3.44	110-135
				x<1190m	2.59-2.99	85-118
3	x<1340m	3.23-3.35	117-124	3.38-3.55	149-170	
	x>1340m	3.24-4.02	122-209			

SEISMIC REFRACTION

The two seismic refraction profiles shot in northern Panamint Valley are shown on Figure 1-3. Explosive charges weighing from 4.5 to 23 kg were buried and detonated at depths from 2.5 to 5.5 m. Timing was controlled via radio. Two 24-channel analog recording units (RS-44 and PS-19) formed the recording array. Geophones were placed at intervals of 60 m (200 ft) on the long profile and 30 m (100 ft) on the short one. The travel time curves (Figure 1-5) are well defined because first arrivals were strong and clear.

The observed travel time curves are fit well by a series of linear segments, as illustrated by the prefered fit of Figure 1-5. Note that two of the segments defined for the cross profile have been offset. The westward delay of about 10 ms for the forward profile and 13 ms for the reverse profile is interpreted to be the result of an offset in the interface between layers 1 and 2 near x = 1330 m. Hence these segments were fit separately on both sides of the observed time offset. To gauge the uncertainties in the slopes and intercepts of these lines, we determined the most extreme lines that could fit most of the data within a given segment. Each line is defined by

$$t = x/v_a + t_i \qquad (1\text{-A1})$$

where the apparent velocities, v_a, and intercept times, t_i, are listed in Table 1-A1, and t and x are the time and distance from the source, respectively. Combining the extreme fits allowed for each segment in all possible combinations produces the family of multi-layered structures described by the range of values listed in Table 1-1.

The dips of the interfaces are generally to the north and west, but those of individual interfaces are difficult to constrain tightly. The top layer probably thickens from southeast to northwest while the second layer probably thickens more from east to west. The step observed in the travel time curves of the cross profile appears to be due to an offset of about 18 ± 10 m in the layer 1--layer 2 boundary, since this is the only velocity contrast sampled by rays from both sources. The down-to-the-west offset of this boundary may represent the subsurface expression of a fault similar in slip direction to the Ash Hill Fault to the west. Alternatively, it might represent a facies transition from higher velocity playa or lacustrine deposits to lower velocity coarse clastic deposits in the upper part of seismic layer 2. The abrupt offset is more consistent with a fault than a facies transition.

The deepest interfaces were not detected on the short profile, and for them only the north-northwest to south-southeast component of dip can be determined. Although any individual interface could dip southeast, the mean velocity of the upper 0.75 km of the crust must be slower under the northwest than under the southeast part of the line. This observation is important because this dip is opposite to that implied by the gravity observations made on and near the seismic profile, which we discuss below. The lack of any simple correlation between trends in gravity and dips of these seismic layers probably is more a reflection of the shallowness of the basin than of peculiarities in the constituent rocks in the basin.

Two boreholes in northern Panamint Valley confirm that the two upper layers are comprised of Quaternary sediment. As noted in the text, a borehole north of SR 190 went through sand and silt before reaching bottom in Paleozoic carbonate rock at 111 m [Smith and Pratt, 1957]. Because of the distance between the seismic line and this drillhole (Figure 1-3), a lithologic interpretation of the difference between the first and second layers based on this drillhole would be tenuous. Motts and Carpenter [1968] reported the log from another hole drilled somewhat northwest of the southern shotpoint of the main seismic profile. This hole reached a depth of 49.4 m (162 ft); the upper 20 m is predominately silts and silty clays, the next 17 m is clay with only minor amounts of silt, and the bottom 12 m is interbedded sand and clay. A sharp increase in the measured soil moisture occurs at 12 m and again near 33 m depth. We tentatively identify the upper seismic layer as silt, sand, and silty clay; the second layer is probably comprised of the clay found in the lower portion of the drillhole.

Thickness variations of the upper two seismic layers agree very well with an interpretation of the subsurface information made by Smith [1976]. He suggested that the

coarser clastic units in this area are deposits of a delta headed in Darwin Canyon (roughly along SR 190 at the west edge of Panamint Valley). Our finding that the upper seismic layer increases in thickness toward the northwest is consistent with Smith's suggestion and our correlation. The east-to-west thickening of the second layer probably reflects the pre-Quaternary topography; this may be related to the structures beneath the Quaternary units, because the increasing thickness to the west is consistent with the down-to-the-west offset on the fault inferred from the cross profile. Smith [1976] correlated the clay layer in Motts and Carpenter's [1968] southern drillhole with his Gale stage pluvial event, which he inferred to have concluded 48,000 ± 10,000 years ago. If this age approximates the age at which the seismic layer 1--layer 2 boundary formed, then the mean slip rate of the inferred fault under the western end of the cross profile is 0.37 +0.37/-0.23 mm/yr over the last 48,000 years. If this offset of the travel-time curve is indeed due to faulting, then this rate probably is a minimum estimate of the rate when the fault was active because we observed no evidence for an active fault at the surface.

ELECTRICAL RESISTIVITY

Six of the ten Schlumberger profiles that we deployed yielded results that can be interpreted in terms of the electrical structure of the sediments in northern Panamint Valley. The simple one-dimensional interpretations are summarized in the published paper and are illustrated in Figure 1-6. For the four playa profiles, we interpret the top resistive layer to be dry sediment and the middle conductive layer to be brine-saturated sediment. The dry nature of the upper several meters was confirmed by the holes drilled for the seismic charges. Motts and Carpenter [1968] also reported soil moisture contents from three drillholes on the playa in northern Panamint Valley. They found a sharp increase in soil moisture content at about 13 m near the south end of our seismic profile and at about 8 m both near the north end of profile E3 and near the middle of profile E6 (Figure 1-3). These depths are very close to the depths that we inferred for the base of the resistive surface layer.

Unfortunately several of the resistivity profiles in the valley show evidence of either elecromagnetic or leakage coupling which prevent an accurate determination of the properties of electrical basement. The evidence for unwanted coupling is seen especially strongly in profile E2, where the slope of the apparent resistivity versus distance indicates a constant signal level versus distance for electrode spacings beyond about 300 m. This result can be caused by leakage, which is always a matter of concern with Schlumberger arrays because of the proximity of the transmitting and receiving equipment to each other. It can also be caused by current channeling due to the presence of vertical resistivity boundaries. Since E2

and E6 were run alongside the Lake Hill outcrop, the steep slopes of the apparent resistivity curves might be caused by such current channeling. The constant signal level signature develops at shorter separations on profile E2 than on profile E6, thus suggesting that leakage coupling is a significant problem since E6 is closer than E2 to Lake Hill. This does not preclude the possibility of current channeling occurring, but it cannot be confirmed by these resistivity profiles. In the future, based on these experiences, we recommend using resistivity measurement geometries that minimize coupling effects when the area is very conductive.

Profile E4 is very complex; the best fitting curve that we could find (curve A) is an approximation made by joining two separate curves, each constructed for a three layer structure. The vertically varying resistivities probably reflect an intertonguing of conductive playa sediments with more resistive conglomerates and fanglomerates. In any case it seems unlikely that basement is shallower than about 200 m. Since the array was deployed where the fan is only 6 m above the playa surface, the resistive basement must therefore be at least 30 m below the depth inferred for the nearest arrays on the playa (E3 and E6).

Array E5 was deployed much higher on the fan than E4, at an elevation about 140 m above the playa. A thick resistive layer caps a more conductive one with only the barest hint of a resistive basement (Figure 1-6). We think that the thick resistor is dry, porous fanglomerate, which might include some of the Pliocene sediments exposed to the east. The increase in conductivity below it might reflect increasing saturation or the presence of finer grained Pliocene sediments. Because the resistivity of this more conductive region is poorly constrained, the depth to the more resistive material underneath is also. The two structures illustrated for curve A (Figure 1-6) are probably representative of the extreme values of the depth to resistive basement. Hence the top of the electrical basement at site E5 could lie from 50 m to more than 800 m below that under the playa. This inferred increase of more than 190 m in the thickness of sediment east of the playa could be the source of the gravity low at the east side of the valley (Figure 1-4).

MAGNETOTELLURIC MEASUREMENTS

Magnetotelluric (MT) measurements were made at eleven sites to place additional constraints on the resistivity structure of the valley. We followed the field and analytic techniques described in an earlier investigation [MIT Field Geophysics Course, 1985]. The impedance tensor Z (1-1) is presented as an ellipse at each site (Figure 1-A1 and Table 1-A2).

The long axes of the ellipses are generally parallel to the main direction that current flows beneath the site, and the measured ellipses are in accord with the structure of the valley outlined above. The ellipses at sites MT6 and MT7 are parallel to the valley axis, which is

Table 1-A2. Principal Axes of Magnetotelluric Impedence Tensors

Array I.D.	Major Axis Amplitude	Major Axis Orientation	Minor Axis Amplitude	Minor Axis Orientation
MT1	2030 ± 750	352° ± 2°	241 ± 14	262° ± 2°
MT2	1870 ± 770	187° ± 3°	457 ± 23	277° ± 3°
MT3	310 ± 100	331° ± 10°	265 ± 110	241° ± 10°
MT4	398 ± 170	323° ± 20°	178 ± 52	233° ± 20°
MT5	4650 ± 1500	274° ± 7°	695 ± 400	184° ± 7°
MT6	698 ± 270	336° ± 1°	49 ± 4	246° ± 1°
MT7	741 ± 410	338° ± 2°	109 ± 10	248° ± 2°
MT8	1132 ± 450	317° ± 23°	535 ± 120	227° ± 23°
MT9	1818 ± 290	282° ± 13°	613 ± 200	192° ± 13°
MT10	2300 ± 260	295° ± 5°	702 ± 160	205° ± 5°
MT11	6770 ± 400	296° ± 6°	1250 ± 420	206° ± 6°

Units of amplitude are (mv/km)/(nT/sec). Directions clockwise from due north. Locations on Figure 1-A1 except MT10 and MT11, 2.7 km and 2.9 km north of SR190 on the Saline Valley road on the Darwin Plateau. Amplitude uncertainties represent difference between calculating Z by postmultiplying by E or H.

expected since the valley provides a conductive channel through more resistive bedrock. The orientations of the ellipses of the two pairs of sites MT1-MT2 and MT8-MT9 may reflect deflection of current around obstacles: Lake Hill for the first pair and Ash Hill for the second. The deflections imply that the rocks of Lake Hill are either in contact with bedrock or are underlain by a thinner section of young sediments than lies in the valley on either side. The east-west elongation of the ellipse at site MT5 may reflect a deflection of current around a continuation of the Ash Hill Fault or simply a channeling of current into the valley from the margins, possibly toward the valley fill that produces the gravity low at the east side of the valley. The ellipses at sites MT3 and MT4 are somewhat puzzling and may record structural complications if current diverges at this point. Measurements at sites MT10 (36°22.32'N, 117°37.84'W) and MT11 (36°22.46'N, 117°37.95'W) on the Darwin Plateau illustrate higher impedances than those observed in the sediment-filled valley.

GRAVITY MEASUREMENTS

Collection and Reduction

In our surveys at least three readings were made at each site, and these were tied daily to a field base station where five readings were taken in both the morning and the evening. The measurements were tied to the gravity base station in northern Panamint Valley described

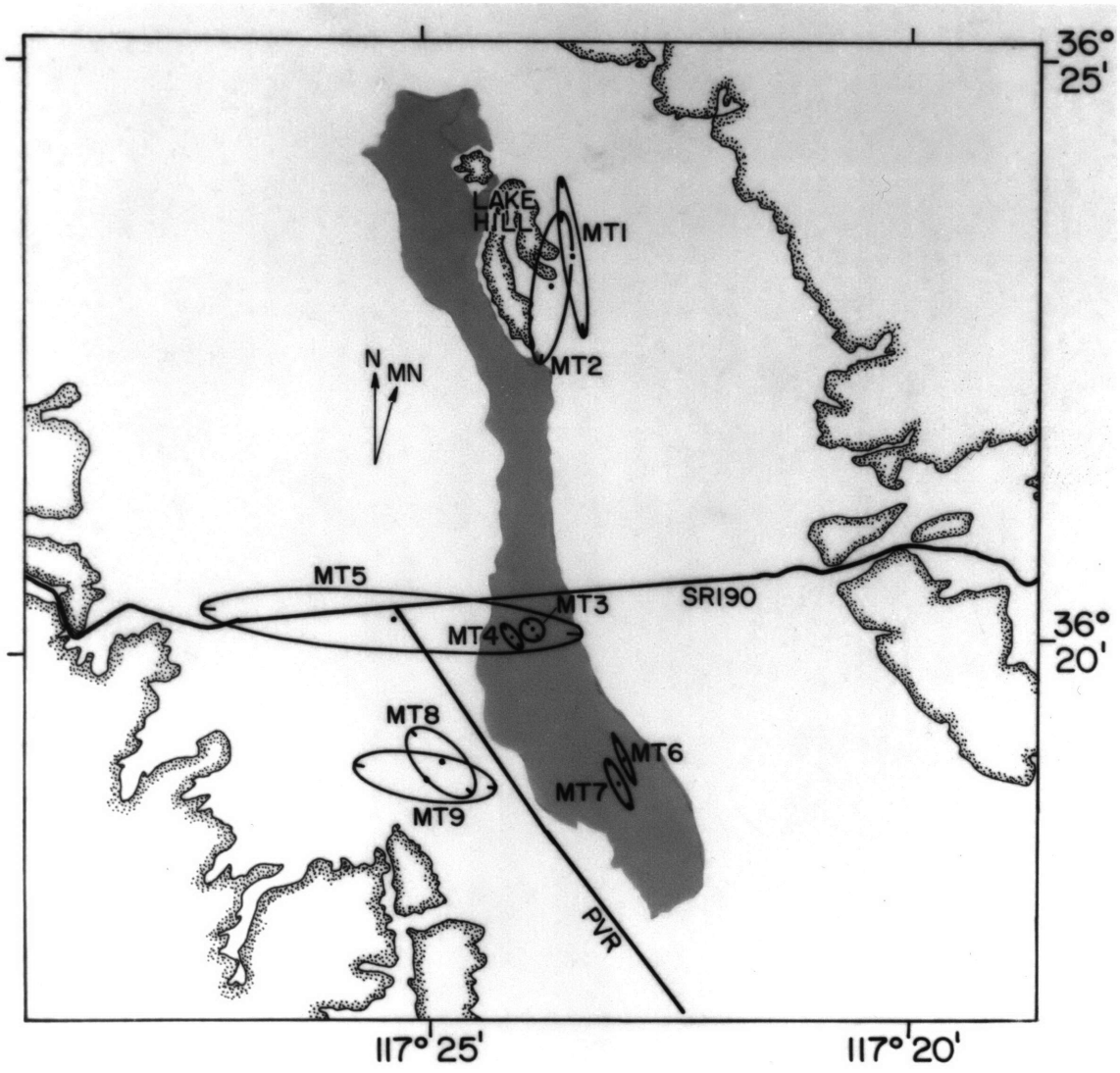
36°
25'
LAKE
HILL
MT1
MT2
N
MN
MT5
MT3
SR190
MT4
36°
20'
MT8
MT6
MT7
MT9
PVR
117°25'
117°20'

below. Most locations were plotted on U.S. Geological Survey 15 minute series maps in the field, and elevations were taken from benchmarks, from elevations printed on the maps, and by interpolation between contours. Some locations were determined on newer 7 1/2 minute USGS orthophotoquads and then transferred to the 15 minute maps. Uncertainties in most elevations are under 6 m and many are under 1 m. Errors in locations rarely exceed 100 m, and many are less than 20 m.

Measurements at each site were corrected for earth tides, for drift, and for latitude using the 1967 GRS formula [International Association of Geodesy, 1971]. Standard free air and simple Bouguer corrections were made. Terrain corrections for the 1985 survey were obtained using a Hammer chart [Dobrin, 1976] out to zone F and then extended to 167 km using a USGS computer program based on the method of Plouff [1966, 1977]. In the earlier survey, terrain corrections were calculated using Hammer charts to 40 km. It was inexpedient to extend these corrections using the USGS computer program, so earlier terrain corrections for these sites were discarded and recalculated on the computer. Because most of these sites are in locally gentle topography, the error in the corrections for inner zones introduced by the finite topographic grid available to the computer program should have been small (usually <0.1 mGal). This was verified by comparison of terrain corrections calculated for sites occupied by both surveys. A final correction for earth curvature yielded the complete Bouguer anomalies discussed below. We used a reduction density of 2.67 g/cm^3 for both terrain and Bouguer corrections. Overall uncertainties of the Bouguer anomalies probably are as high as a few milliGals in the high mountains but less than 1 mGal in the valley.

Both of the gravity surveys that we ran have been tied to the California Division of Mines and Geology (CDMG) base station network [Chapman, 1966] at the Panamint Valley station. This base station, number 231, is described by Chapman [1966] as being "about 2^1/$_2$ miles east of Panamint Springs in Panamint Valley on State Highway 190 on the north side of the highway just west of the junction with a dirt road leading southeast. Reading taken on ground 0.5' below disc" of USGS benchmark 13-D. The dirt road, now paved, is the Panamint Valley road. The latitude is 36°20.39' north; the longitude is 117°25.39' west; the elevation is 1575.6 feet (480.2m).

We use the GRS 67 gravity formula [International Association of Geodesy, 1971] and IGSN 71 gravity base values [Morelli, 1974]. Converting the base station to this system using the new ties to eastern California stations [Oliver et al., 1980] should yield the observed

---

Fig. 1-A1 (opposite). Magnetotelluric impedence ellipses near playa (shaded). Outcrop within shaded edges. Scaling of ellipses is linear.

gravity value of 979616.5 mGal of Snyder et al. [1981b]. Our data may be compared with surveys based on the old standards by adding 2.1 mGal to the values presented here.

When we merged our data with preexisting gravity measurements some discrepencies required correction. Our copy of the pre-existing data had already been corrected to the new standards, contrary to the documentation of Snyder et al. [1981a]. When comparing readings at stations we reoccupied we found some systematic differences. Stations with identifiers of the form Bxxx, where xxx is a number, were found to be 2.1 mGal lower than our measurements west of about 117°35'W. This includes the Saline Valley base station (number 232, Chapman [1966]), and we suspect that this reflects a problem in the tie between the two base stations. We added 2.1 mGal to the Bxxx stations west of 117°35'W because this appears to be the dividing line between stations tied to the different base stations. For the same reason we added 1.7 mGal to stations with an identifier of 2xxx-, where - is a blank in our listing. East of 117°35' this same series of measurements seems 0.46 mGal too high and we have subtracted this value from the preexisting measurements.

Terrain corrections also proved a problem. Although our data and the USGS data are supposed to contain corrections for terrain out to 166.7 km distance, some of the latter terrain corrections clearly cover a smaller area. Hence we recomputed the total terrain correction for stations with identifiers of 2xxx-, 3xxx-, 5xxx-, and 8xxx-. We left other terrain corrections unaltered because they appeared accurate and we suspected that the computer generated inner zone terrain corrections would increase any error.

Interpretation

Gravity anomalies over bedrock exposed in the Darwin Plateau are instructive in interpreting the gravity field over the valley (Figures 1-3 and 1-4). High gravity values extend northward from the Argus Range for about 20 km, the most prominent lying at about 117°35'W, 36°20'N (Figure 1-4). Mabey [1961] interpreted these high values as a reflection of high density metamorphic rock at the margin of the Hunter Mountain pluton. He also considered the largest gravity anomaly to be about 10 mGals in amplitude superimposed on the regional west to east increase in Bouguer anomalies from the Sierra Nevada to Death Valley. Our measurements further refine Mabey's gravity high to be between 5 and 15 mGal high (the -130 mGal closed contour on Figure 1-4) located over Hall and McKevett's [1962] mapped exposure of amphibolite.

Because the amplitudes and wavelengths of the anomaly field observed on bedrock and over northern Panamint Valley are similar, any interpretation of the gravity anomalies in the valley must consider both the alluvial fill and the basement structure beneath the fill as

possible sources for these anomalies. Since no observed gradient is steep enough to rule out the possibility that its source is a density contrast within the basement, we are unable to infer reliably the thickness of valley fill from the gravity data alone.

The large westward decrease in the Bouguer gravity anomaly across the region (Figure 1-4) is probably due to regional variations in the thickness of the crust or in the density of the upper mantle. Removal of an eastward increasing regional gradient similar to that described by Mabey [1961] enhances the gradient across the playa and reduces the gradient near Towne Pass. Removal of such a regional gradient would also enhance the local gravity low centered near exposures of Pliocene sedimentary rock (Figure 1-2). From deflection of the gravity contours around these exposures (Figure 1-5), we deduce that the low is between 5 and 15 mGal in amplitude. If the density contrast between sediments and underlying basement were 0.3 g/cm3, then the thickness of these Pliocene sediments would be roughly between 400 and 1200 m. This magnitude for the thickness of the Pliocene sediments is corroborated somewhat by our interpretation of resistivity profile E5.

Upon subtraction of a linear, regional gradient exceeding about 0.8 mGal/km, gravity highs west of the playa and within the valley exceed gravity values measured on Paleozoic sedimentary rocks northeast of the valley. As bedrock is not exposed at these highs, we suspect that there is a lateral density contrast below the valley fill creating these highs. This is supported by the greater thickness of sediment inferred to lie toward the north-northwest along the main seismic line; this inference would be in conflict with the 4 mGal increase in the Bouguer anomaly from south-southeast to north-northwest were there no density contrasts beneath the sediments. As we discuss in the text, we infer this suballuvial density contrast to be the metamorphic rock at the margin of the Hunter Mountain pluton within the lower plate of the low-angle normal fault inferred to underlie northern Panamint Valley.

INTERPRETATION AND CONCLUSIONS

In addition to the results presented in the main text, electrical, magnetotelluric, seismic, and gravity measurements in northern Panamint Valley also provide constraints on several geologic features in and around the valley.

Magnetotelluric measurements made near Lake Hill indicate that the rock beneath Lake Hill is, on average, more resistive than that either under the playa or under the fan to the east. Magnetotelluric ellipses near Lake Hill are deflected in a manner consistent with a resistive anomaly beneath Lake Hill. We suspect that this is because Lake Hill is an outcrop of bedrock and so lacks any Cenozoic sediment beneath it, but we cannot eliminate the possibility that a thin layer of Cenozoic sediment underlies Lake Hill.

Similar anomalies elsewhere in the valley suggest that there is substantial complexity to the relief of the bedrock surface beneath the valley fill. Magnetotelluric ellipses are deflected near Ash Hill, supporting identification of it as exposure of bedrock. Other anomolous magnetotelluric ellipses near the valley center suggest the presence of complicated current paths and hence complicated electrical structure, but our data are insufficient to identify the cause.

The seismic refraction cross profile on the playa in northern Panamint Valley shows evidence for fault offset of the bedrock surface. An 18 ± 10 m down-to-the-west offset of the base of the uppermost seismic layer could be either a fault or a facies change in the valley fill. Because of the abrupt nature of the offset, we assume that it is due to faulting. We believe that the boundary at the base of seismic layer 1 is the contact between clastic deposits forming layer 1 and clays forming layer 2. Accepting Smith's [1976] estimate of the age of this horizon as 48,000 ± 10,000 years, then the average slip rate since that time has been 0.37 +0.37/-0.23 mm/yr.

Although gravity measurements could only restrict the maximum amount of sediment in the valley, these measurements did reveal some anomalies of importance. The removal of any linear regional gravity field increasing by more than about 0.8 mGal/km from west to east results in higher residual gravity anomalies within the western third of Panamint Valley than on the bedrock immediately to the west. Because these relatively high values are found on alluvial fill that we infer to be at least 100 m thick from magnetic anomalies described in the published paper, we infer these high gravity values to be caused by a relatively dense mass within the bedrock beneath the western part of Panamint Valley. The inconsistency between the increasing thickness of sediment and increasingly positive Bouguer anomaly south to north along the main seismic profile can also be explained by a density anomaly within the bedrock. We suggest that the source of this anomaly might be a body of metamorphic rock similar to those that cause the positive gravity anomalies on the Darwin Plateau [Mabey, 1961]. The importance of this tentative correlation is discussed in the published paper.

Bouguer gravity lows observed at the eastern margin of Panamint Valley and west and south of Towne Pass are probably produced by low density Pliocene sedimentary rock. It is difficult to separate the effect of these rocks from the large regional gradient observed in the area, but we infer that a 5 to 15 mGal negative anomaly is associated with these rocks. Because the lowest gravity values in the valley are observed near exposures of these Pliocene rocks, we suggest that rock correlative to these exposures underlies part of the eastern part of Panamint Valley south of Towne Pass. If this is correct, then the latest Pliocene and

Quaternary alluvial fill is probably less than about 300 m thick across the entire northern Panamint Valley.

APPENDIX 1-B
CALCULATION OF THE DEPTH OF A LOW-ANGLE NORMAL FAULT FROM MAGNETIC ANOMALY AMPLITUDES

The relative magnitudes of the magnetic anomalies that are presumed to be caused by the magnetization of the Hunter Mountain pluton in the upper and lower plates of the low-angle normal fault suspected to underlie the Darwin Plateau can be used to estimate the depth of the fault. The peak magnetic intensity of a uniformly magnetized, bottomless vertical slab of width w occurs over its center, if the generating field is parallel to the sides of the slab. At an elevation d above such a bottomless slab the total field anomaly F has a maximum value of

$$F_{max} = 4 \cdot k \cdot F_o \cdot \sin^2 I \cdot \tan^{-1} \frac{w}{(2 \cdot d)} \qquad (1\text{-}B1)$$

where F_o and I are the intensity and inclination of the earth's field and k is the magnetic susceptibility of the slab [Telford et al., 1976, p. 189]. If the slab extends to a depth D then

$$F_{max} = 4 \cdot k \cdot F_o \cdot \sin^2 I \cdot \{\tan^{-1} \frac{w}{(2 \cdot d)} - \tan^{-1} \frac{w}{(2 \cdot D)}\}. \qquad (1\text{-}B2)$$

For simplicity let us assume that the Hunter Mountain pluton was truncated on a flat fault, then the ratio r of the peak magnetic anomaly over the upper plate to that of the lower plate is

$$r = \frac{\tan^{-1} \frac{w}{2 \cdot d} - \tan^{-1} \frac{w}{2 \cdot D}}{\tan^{-1} \frac{w}{2 \cdot D} - \tan^{-1} \frac{w}{2 \cdot B}} \qquad (1\text{-}B3)$$

where d is the flight elevation above the pluton's upper surface, D is the flight elevation above the fault, and B is the flight elevation above the bottom of the magnetized part of the pluton. Solving for D we find

$$D = w / \left[2 \cdot \tan \left(\frac{\tan^{-1} \frac{w}{2 \cdot d} + r \cdot \tan^{-1} \frac{w}{2 \cdot B}}{1 + r} \right) \right]. \qquad (1\text{-}B4)$$

From the mapped area of the pluton (Figure 1-2), we estimate w to be 9 ± 1 km, and from the amplitudes of the magnetic anomalies in Figure 1-9, we estimate r to be 2.5 ± 1.0. With d = 500 m, we find D to be 4.9 ± 1.1 km for B = 10 km, D = 6.8 ± 2.0 km for B = 20 km, and D = 7.7 ± 2.5 km for B = 30 km. Note that the corresponding depths of the fault below the Darwin Plateau, given by D - d, would be 4.4 ± 1.1, 6.8 ± 2.0, and 7.7 ± 2.5, respectively. If the Curie temperature of the magnetic carrier were 550° C, then using the background heat flow of 2 HFU reported by Combs [1980] for the area to the southwest, the maximum value of B would probably be about 20 km. Even this value of B is too high if any other low-angle normal faults or Mesozoic thrusts cut the Hunter Mountain pluton at a depth shallower than 20 km. Clearly, given the simple assumptions of a vertical, two-dimensional, uniformly magnetized body used to infer D, the uncertainties in D quoted above should be increased. Nevertheless, the simple analysis presented here shows that the anomalies over the Hunter Mountain pluton and over the northwest edge of Panamint Valley are consistent with the pluton being decapitated at a shallow depth of a few kilometers.

REFERENCES

Anderson, R. E., Thin skin distension in Tertiary rocks of southeastern Nevada, *Geol. Soc. Am. Bull.*, *82*, 43-58, 1971.

Armstrong, R. L., Low-angle (denudation) faults, hinterland of the Sevier orogenic belt, eastern Nevada and western Utah, *Geol. Soc. Am. Bull.*, *83*, 1729-1754, 1972.

Burchfiel, B. C., K. V. Hodges, and L. H. Royden, Geology of Panamint Valley--Saline Valley pull-apart system, California: Palinspastic evidence for low-angle geometry of a Neogene range-bounding fault, *J. Geophys. Res.*, *92*, 10422-10426, 1987.

Chapman, R. H., The California Division of Mines and Geology gravity base station network, *Calif. Div. Mines and Geol. Spec. Rept.*, *90*, 49 pp., 1966.

Chapman, R. H., D. L. Healey, and B. W. Troxel, Death Valley sheet, Bouguer gravity map of California, 8 pp. plus 1 sheet, Calif. Div. of Mines and Geol., Sacramento, 1973.

Combs, J., Heat flow in the Coso Geothermal Area, Inyo County, California, *J. Geophys. Res.*, *85*, 2411-2424, 1980.

Crittenden, M. D., Jr., P. J. Coney, and G. H. Davis (Eds.), Cordilleran Metamorphic Core Complexes, *Mem. Geol. Soc. Am.* , *153*, 490 pp., 1980.

Davis, G. A., J. L. Anderson, E. G. Frost, and T. J. Shackelford, Mylonitization and detachment faulting in the Whipple-Buckskin-Rawhide Mountains terrane, southeastern California and western Arizona, Cordilleran Metamorphic Core Complexes, edited by M. D. Crittenden Jr., P. J. Coney, and G. H. Davis, *Mem. Geol. Soc. Am.* , *153*, 79-130, 1980.

Dobrin, M. B., *Introduction to Geophysical Prospecting*, 630 pp., McGraw-Hill, U.S.A., 1976.

Dunne, G. C., R. M. Gulliver, A. G. Sylvester, Mesozoic evolution of rocks of the White, Inyo, Argus, and Slate Ranges, eastern California, *Mesozoic Paleogeography of the Western United States*, edited by D. G. Howell and K. A. McDougall, Pacific Sec. Soc. Econ. Paleontologists and Minerologists, Pacific Coast Paleogeography Symp. 2, p. 189-208, 1978.

Frost, E. G., and D. L. Martin (Eds.), *Mesozoic-Cenozoic Tectonic Evolution of the Colorado River Region, California, Arizona, and Nevada*, 608 pp., Cordilleran Publishers, San Diego, Calif., 1982.

Hall, W. E., Geology of the Panamint Butte Quadrangle, Inyo County, California, *U.S. Geol. Surv. Prof. Bull., 1299*, 67 pp., 1971.

Hall, W. E., and E. M. MacKevitt, Jr., Geology and ore deposits of the Darwin Quadrangle, Inyo County, California, *U.S. Geol. Surv. Prof. Pap., 368*, 87 pp., 1962.

International Association of Geodesy, Geodetic reference system 1967, *Internat. Assoc. Geodesy Spec. Pub., 3*, 116 pp., 1971.

Jackson, J. A., Active normal faulting and continental extension, Continental Extensional Tectonics, edited by M. P. Coward, J. F. Dewey, and P. L. Hancock, *Spec. Publ. Geol. Soc. Lond., 28*, 3-17, 1987.

La Compagnie Générale de Géophysique, Abaques de Sondage Électrique, *Geophys. Prospect., 3*, suppl. 3, 51 pp., 1955.

Larson, R. W., Chronology of Late Cenozoic basaltic volcanism: The tectonic implications along a segment of the Sierra Nevada and Basin and Range Province, Ph.D. thesis, 95 pp., Brigham Young Univ., Provo, Utah, 1979.

Longwell, C. R., Low-angle normal faults in the Basin-and-Range province, *Eos Trans. AGU, 26*, 107-118, 1945.

Mabey, D. R., Regional magnetic and gravity anomalies in the Darwin area, California, Geological Survey Research 1961, *U.S. Geol. Surv. Prof. Pap., 424-C*, C276-C279, 1961.

Maxson, J. H., Physiographic features of the Panamint Range, California, *Geol. Soc. Am. Bull., 61*, 99-114, 1950.

MIT Field Geophysics Course, A geophysical study of Mesquite Valley: Nevada-California border, *J. Geophys. Res., 90*, 8685-8689, 1985.

Morelli, C. (editor), The international gravity standardization net 1971, *Internat. Assoc. Geodesy Spec. Pub., 4*, 194 pp., 1974.

Motts, W. S., and D. Carpenter, Report of test drilling on Rogers, Coyote, Rosamond, and Panamint playas in 1966, Playa surface morphology: Miscellaneous investigations, edited by J. T. Neal, Air Force Cambridge Res. Lab. Environ. Res. Pap., *283*, p. 31-57, 1968.

Oliver, H. W., S. L. Robbins, R. H. Chapman, Appendix: Gravity measurements, reductions, and conversion formulas to IGSN 71 and GRS 67, Interpretation of the Gravity Map of California and Its Continental Margin, edited by H. W. Oliver, *Bull. Calif. Div. Mines and Geol., 205*, 47-52, 1980.

Plouff, D., Digital terrain corrections based on geographic coordinates (abstract), *Geophysics, 31*, 1208, 1966.

Plouff, D., Preliminary documentation for a Fortran program to compute gravity terrain corrections based on topography digitized on a geographic grid, *U.S. Geol. Surv. Open File Rep., 77-535*, 45 pp., 1977.

Press, F., Seismic velocities, Handbook of Physical Constants, edited by S. P. Clark, *Mem. Geol. Soc. Am. , 97*, 195-218, 1966.

Schweig, E. S., III, Neogene tectonics and paleogeography of the southwestern Great Basin, California, Ph.D. thesis, 207 pp., Stanford Univ., Stanford, Calif., 1985.

Smith, G. I., and W. P. Pratt, Core logs from Owens, China, Searles, and Panamint basins, California, *U.S. Geol. Surv. Prof. Bull., 1045-A*, 62 pp., 1957.

Smith, R. S. U., Late-Quaternary pluvial and tectonic history of Panamint Valley, Inyo and San Bernadino counties, California, Ph.D. thesis, 295 pp., Calif. Inst. of Technol., Pasadena, 1976.

Snyder, D. B., C. W. Roberts, R. W. Saltus, and R. F. Sikora, Description of magnetic tape containing the principal facts of about 64,000 gravity stations in the state of California, *NTIS-PB82-168-279*, 30 pp., Availible from U.S. Dep. of Commerce, Natl. Tech. Inf. Serv., Springfield, Va., 1981a.

Snyder, D. B., C. W. Roberts, R. W. Saltus, and R. F. Sikora, Magnetic tape containing the principal facts of about 64,000 gravity stations in the state of California, *NTIS-PB82-168-287*, 1 tape, Availible from U.S. Dep. of Commerce, Natl. Tech. Inf. Serv., Springfield, Va, 1981b.

Streitz, R., and M. C. Stinson, Geologic map of California: Death Valley sheet, Calif. Div. of Mines and Geol., Sacramento, 1974.

Telford, W. M., L. P. Geldart, R. E. Sheriff, and D. A. Keys, *Applied Geophysics*, 860 pp., Cambridge University Press, Cambridge, England, 1976.

U.S. Geologic Survey, Aeromagnetic map of the Panamint Dunes area, California, *U.S. Geol. Surv. Open File Rep., 82-1085*, 1 sheet, 1982.

Wernicke, B., Low-angle normal faults in the Basin and Range Province--Nappe tectonics in an extending orogen, *Nature*, *291*, 645-648, 1981.

Wright, L. A., and B. W. Troxel, Chaos structure and basin and range normal faults: Evidence for a genetic relationship (abstract), *Geol. Soc. Am. Abstr. Programs*, [*1*], (7), 242, 1969.

Wright, L. A., and B. W. Troxel, Shallow-fault interpretation of basin and range structure, in *Gravity and Tectonics*, edited by K. A. DeJong and R. Scholten, pp. 397-407, John Wiley, New York, 1973.

TABLE 1-A3. Principal Facts, Gravity Stations in Northern Panamint Valley

STA	LAT	LON	ELEC		IZ	OZ	NORTH	EAST	OBS G	THEO G	FAA	CBA
K52	1.65	44.90	3495		1.24	3.92	3987.06	432.58	1445.94	1820.70	-46.08	-162.52
P507	20.17	45.00	4653		0.00	2.14	4021.30	432.69	1397.37	1847.29	-12.37	-170.30
K63	1.15	44.81	4264		5.17	7.66	3986.13	432.70	1397.40	1819.98	-21.60	-160.68
K35	2.10	44.80	3555		0.34	3.11	3987.89	432.73	1443.02	1821.34	-44.00	-163.31
K43	4.26	44.71	3893		0.42	3.79	3991.88	432.90	1424.48	1824.44	-33.86	-164.09
K37	2.53	44.69	3615		0.39	3.28	3988.68	432.90	1439.10	1821.96	-42.90	-164.10
B174	6.10	44.72	4915		0.00	5.67	3995.28	432.91	1362.56	1827.08	-2.34	-165.71
3173	39.32	44.93	1531		0.17	9.66	4056.70	433.07	1601.58	1874.87	-129.29	-172.30
CB62	11.14	44.66	7323		0.00	7.52	4004.60	433.07	1217.55	1834.31	71.73	-172.02
THN8	35.34	44.77	4744		3.27	10.25	4049.34	433.25	1424.06	1869.13	1.02	-151.91
B208	14.21	44.57	6857		0.00	7.66	4010.27	433.25	1252.67	1838.72	58.65	-169.08
P797	18.00	44.60	4962		0.08	2.52	4017.28	433.26	1367.71	1844.16	-9.87	-177.99
P968	19.10	44.60	4771		0.02	2.19	4019.31	433.27	1384.41	1845.75	-12.70	-174.62
K64	1.38	44.43	3945		0.49	2.72	3986.55	433.28	1420.55	1820.31	-28.77	-161.85
P506	20.10	44.60	4680		0.00	2.10	4021.16	433.29	1396.08	1847.18	-11.03	-169.91
3177	38.15	44.71	2240		3.17	13.27	4054.53	433.38	1556.68	1873.19	-105.83	-166.63
3174	38.98	44.62	1702		0.17	10.04	4056.07	433.53	1591.71	1874.38	-122.59	-171.10
3175	38.65	44.60	1879		0.39	11.14	4055.46	433.55	1580.47	1873.91	-116.61	-169.94
K38	2.94	44.24	3800		0.69	3.49	3989.43	433.58	1429.09	1822.55	-36.10	-163.44
DVG51	36.89	44.56	5133		8.43	18.69	4052.20	433.59	1389.07	1871.37	0.36	-157.44
3176	38.36	44.47	2073		0.97	12.10	4054.92	433.74	1567.97	1873.49	-110.55	-168.97
K65	1.72	44.08	3965		0.55	2.84	3987.18	433.81	1421.97	1820.80	-25.96	-159.61
CB3	9.31	44.03	6834		0.00	6.61	4001.21	433.99	1251.90	1831.68	62.75	-165.24
P505	20.10	44.00	4713		0.00	2.06	4021.15	434.18	1397.50	1847.18	-6.50	-166.56
B205	13.31	43.94	7658		0.00	12.85	4008.60	434.18	1202.52	1837.43	85.06	-164.77
CB29	1.05	43.82	3881		0.00	3.83	3985.94	434.19	1425.79	1819.84	-29.08	-158.85
K44	4.70	43.70	4390		0.77	3.65	3992.68	434.42	1394.21	1825.07	-18.04	-165.44
CB4	6.93	43.58	5887		0.00	5.97	3996.80	434.63	1308.20	1828.27	33.47	-162.84
CB2	9.95	43.46	7362		0.00	10.77	4002.38	434.85	1217.55	1832.60	77.10	-164.73
P965	15.64	43.50	5606		1.34	4.50	4012.90	434.87	1334.80	1840.77	21.15	-167.02
P798	16.60	43.50	5199		0.47	3.26	4014.68	434.88	1354.12	1842.15	0.83	-174.66
P796	19.20	43.50	4760		0.08	2.16	4019.49	434.92	1390.58	1845.89	-7.71	-169.28
K40	2.82	43.00	4340		0.59	3.05	3989.20	435.44	1402.45	1822.37	-11.80	-158.09
2999	30.71	43.18	6531		0.55	4.85	4040.76	435.56	1322.02	1862.46	73.62	-145.25
CB63	10.72	42.98	7870		0.00	14.22	4003.80	435.58	1183.39	1833.71	89.57	-166.11
THN4	30.70	43.16	6531		0.63	5.48	4040.74	435.59	1319.75	1862.44	71.36	-147.42
TP131	12.17	42.80	8160		4.47	16.74	4006.48	435.87	1168.10	1835.79	99.44	-163.58
THN3	29.31	42.88	6197		0.44	4.45	4038.17	435.99	1338.86	1860.44	61.08	-147.33
CH232	19.88	42.78	4878		0.08	2.01	4020.73	436.01	1390.89	1846.87	2.75	-163.02
CSC070	19.89	42.78	4878	B	0.02	1.59	4020.75	436.01	1393.08	1846.88	4.89	-161.28
K41	4.24	42.58	4645		0.54	3.23	3991.82	436.09	1382.67	1824.41	-4.95	-161.51
CSC071	20.39	42.49	4846	B	0.02	1.66	4021.67	436.45	1402.05	1847.60	10.13	-154.87
THN5	32.00	42.59	6130		0.47	4.86	4043.14	436.46	1345.72	1864.32	57.77	-147.94
B254	20.40	42.47	4846		0.00	2.06	4021.69	436.48	1402.10	1847.62	10.17	-154.44
2872	20.39	42.47	4846		0.03	1.65	4021.67	436.48	1402.08	1847.60	10.16	-154.84
CB1	8.87	42.36	7562		0.00	18.83	4000.38	436.49	1202.45	1831.05	82.34	-158.24
CB16	3.23	42.26	4866		0.00	3.73	3989.95	436.56	1369.34	1822.96	3.95	-159.68
CB28	1.83	42.23	4755		0.00	4.23	3987.36	436.59	1378.18	1820.95	4.36	-154.97
C21	10.16	42.20	7525		2.14	10.26	4002.76	436.74	1212.73	1832.90	87.30	-160.60
B207	13.72	42.22	7499		0.00	18.48	4009.34	436.76	1213.63	1838.01	80.64	-158.15
DVG52	33.25	42.14	5972		0.13	5.01	4045.44	437.14	1358.46	1866.12	53.86	-146.31
CB5	7.31	41.90	6263		0.00	5.69	3997.49	437.16	1294.13	1828.81	54.19	-155.24
CB27	0.72	41.80	4408		0.00	5.04	3985.30	437.22	1398.90	1819.36	-5.95	-152.58
B194	14.64	41.86	5998		0.00	5.48	4011.04	437.31	1314.25	1839.34	38.88	-161.71
CB14	5.89	41.63	5403		0.00	4.22	3994.86	437.54	1345.19	1826.78	26.46	-155.05
CSC072	21.19	41.75	4866	M	0.08	1.98	4023.14	437.56	1405.12	1848.75	13.93	-151.37
2873	21.20	41.75	4866		0.26	1.99	4023.16	437.57	1405.21	1848.77	14.01	-151.10
THN6	31.41	41.70	6088		0.46	4.45	4042.04	437.78	1347.97	1863.47	56.92	-147.77
B206	12.41	41.50	7187		0.00	12.82	4006.91	437.82	1234.24	1836.13	73.81	-160.00
CSC073	21.75	41.49	4922	B	0.13	2.18	4024.17	437.96	1403.56	1849.56	16.83	-150.14
B256	21.75	41.48	4922		0.00	2.77	4024.18	437.98	1403.61	1849.56	16.88	-149.62
TP67	13.90	41.35	6075		1.13	4.87	4009.66	438.07	1307.87	1838.27	40.80	-163.03

TABLE 1-A3 (cont.). Principal Facts, Gravity Stations in Northern Panamint Valley

STA	LAT	LON	ELEC	IZ	OZ	NORTH	EAST	OBS G	THEO G	FAA	CBA
2886	19.39	41.38	5133	0.32	1.72	4019.81	438.09	1385.33	1846.16	21.82	-152.63
CSC069	19.39	41.38	5133 B	0.15	1.72	4019.81	438.09	1385.44	1846.16	21.93	-152.69
P964	15.64	41.34	5394	0.30	3.00	4012.88	438.10	1350.54	1840.77	16.96	-165.46
THN1	25.82	41.29	5557	0.63	3.66	4031.70	438.31	1370.56	1855.41	37.66	-149.68
CB64	10.61	41.03	7038	0.00	8.27	4003.58	438.50	1246.76	1833.55	74.92	-158.37
CB65	9.91	40.61	7116	0.00	11.48	4002.28	439.12	1238.95	1832.54	75.44	-157.29
CB35	1.08	40.54	4660	0.00	3.93	3985.96	439.12	1388.12	1819.88	6.44	-149.93
CB15	3.94	40.53	5688	0.00	6.49	3991.24	439.17	1329.13	1823.98	39.98	-149.00
DVS43	6.09	40.54	5777	0.42	3.55	3995.22	439.18	1328.88	1827.06	45.01	-149.95
DVS44	9.01	40.47	6412	0.46	4.48	4000.61	439.32	1288.73	1831.25	60.35	-155.37
TP71	9.03	40.46	6414	0.49	4.52	4000.65	439.34	1288.37	1831.28	60.15	-155.60
CSC074	23.02	40.51	5142 B	0.05	2.01	4026.51	439.44	1395.87	1851.38	27.99	-146.76
B257	23.02	40.50	5141	0.00	2.33	4026.51	439.46	1395.95	1851.38	27.98	-146.46
2875	23.00	40.48	5141	0.03	1.99	4026.48	439.49	1395.83	1851.36	27.88	-146.87
C20	8.67	40.30	6284	0.33	4.06	3999.98	439.57	1297.33	1830.76	57.41	-154.36
CB37	3.04	40.14	5416	0.00	3.93	3989.58	439.74	1346.36	1822.69	32.94	-149.31
CSC068	19.11	40.28	5250 C	0.01	1.71	4019.30	439.74	1379.11	1845.77	26.99	-151.79
CB6	7.39	40.15	6652	0.00	9.59	3997.62	439.78	1272.52	1828.93	69.02	-149.78
3187	39.50	40.40	1422	0.06	6.71	4056.98	439.82	1615.04	1875.13	-126.34	-168.65
B258	23.96	40.25	5126	0.00	2.52	4028.25	439.84	1399.24	1852.74	28.51	-145.23
CSC075	23.95	40.25	5126 M	0.01	2.21	4028.23	439.84	1399.24	1852.72	28.52	-145.52
C19	11.61	40.10	6180	0.48	4.36	4005.42	439.91	1305.53	1834.98	51.62	-156.31
TP66	11.63	40.07	6180	0.48	4.36	4005.45	439.96	1306.06	1835.01	52.12	-155.80
THN2	27.50	40.17	5507	0.03	2.71	4034.79	440.01	1378.33	1857.83	38.31	-148.27
B270	19.20	40.05	5238	0.00	2.04	4019.45	440.08	1380.66	1845.89	27.30	-150.75
CSB095	20.26	39.98	5255 C	0.22	1.72	4021.40	440.20	1381.89	1847.41	28.60	-150.13
B269	18.79	39.95	5287	0.00	2.08	4018.69	440.23	1375.20	1845.30	27.04	-152.65
2887	18.79	39.94	5286	0.32	1.77	4018.69	440.24	1375.19	1845.30	26.93	-152.71
B259	24.75	39.90	5129	0.00	2.49	4029.71	440.38	1401.24	1853.87	29.65	-144.22
2877	24.80	39.89	5129	0.14	2.20	4029.80	440.39	1401.02	1853.95	29.36	-144.66
CSC076	24.75	39.89	5130 B	0.02	2.19	4029.70	440.39	1401.20	1853.87	29.71	-144.48
CSC077	26.02	39.90	5247 M	0.06	2.34	4032.05	440.39	1394.17	1855.70	31.84	-146.16
2878	26.02	39.89	5247	0.23	2.34	4032.05	440.41	1394.01	1855.70	31.68	-146.15
B192	14.78	39.78	6147	0.00	8.02	4011.27	440.43	1311.59	1839.54	50.02	-153.11
P963	16.52	39.75	5610	0.19	2.72	4014.49	440.50	1348.24	1842.04	33.70	-156.39
B193	13.66	39.64	6065	0.00	6.93	4009.20	440.63	1316.21	1837.93	48.54	-152.88
4024	34.39	39.77	6572	0.00	18.90	4047.53	440.69	1303.29	1867.76	53.42	-153.34
3163	38.36	39.67	1761	0.07	7.36	4054.87	440.89	1596.77	1873.49	-111.08	-164.41
2996	30.76	39.56	5572	0.08	2.98	4040.81	440.96	1381.55	1862.53	42.94	-145.51
CB67	10.23	39.39	6292	0.00	6.17	4002.86	440.96	1296.29	1833.00	54.89	-155.05
THN7	30.71	39.55	5572	0.08	3.22	4040.72	440.98	1379.43	1862.46	40.90	-147.39
CB17	4.09	39.19	5834	0.00	5.48	3991.51	441.18	1327.49	1824.19	51.80	-143.16
CB13	5.17	39.13	6220	0.00	6.52	3993.50	441.28	1301.41	1825.74	60.50	-146.63
B190	13.07	39.11	6044	0.00	8.30	4008.11	441.41	1315.53	1837.08	46.74	-152.60
DVS42	3.57	38.99	5400	0.55	3.33	3990.54	441.47	1354.95	1823.45	39.26	-143.04
CB66	8.99	39.02	6361	0.00	7.44	4000.56	441.50	1292.06	1831.22	58.92	-152.10
C22	8.20	39.00	5987	0.08	3.18	3999.10	441.52	1317.63	1830.09	50.47	-152.04
CB36	2.61	38.80	5689	0.00	5.04	3988.77	441.75	1337.07	1822.07	49.92	-140.55
B189	11.93	38.70	6244	0.00	8.81	4005.99	442.01	1302.30	1835.44	53.94	-151.72
3154	37.19	38.87	2244	0.32	8.06	4052.69	442.07	1566.66	1871.80	-94.08	-163.09
CSB094	20.02	38.67	5150 C	0.10	1.79	4020.95	442.14	1389.99	1847.07	27.18	-148.01
CB7	7.22	38.55	6162	0.00	5.42	3997.29	442.18	1307.22	1828.68	57.92	-148.33
UCR067	29.23	38.65	5360 C	0.04	2.63	4037.97	442.30	1390.55	1860.32	34.22	-147.38
3162	36.67	38.66	2478	0.60	8.63	4051.73	442.38	1552.47	1871.05	-85.52	-161.73
CSB093	20.80	38.52	5050 C	0.08	1.81	4022.39	442.39	1396.69	1848.19	23.35	-148.41
B260	25.69	38.48	5168	0.00	2.37	4031.43	442.51	1405.39	1855.23	36.11	-139.21
2880	25.69	38.48	5168	0.07	2.07	4031.43	442.51	1405.36	1855.23	36.08	-139.48
CSC078	25.68	38.48	5169 B	0.07	2.07	4031.41	442.51	1405.30	1855.21	36.13	-139.46
B188	11.28	38.35	6259	0.00	8.73	4004.79	442.53	1302.13	1834.51	56.12	-150.13
CSC033	18.42	38.41	5445 B	0.10	2.13	4017.99	442.53	1370.18	1844.77	37.40	-147.54

TABLE 1-A3 (cont.). Principal Facts, Gravity Stations in Northern Panamint Valley

STA	LAT	LON	EL	EC	IZ	OZ	NORTH	EAST	OBS G	THEO G	FAA	CBA
B268	18.42	38.40	5445		0.00	2.47	4017.99	442.54	1369.86	1844.77	37.08	-147.62
B191	13.93	38.25	5567		0.00	4.87	4009.69	442.71	1349.79	1838.32	34.93	-151.54
B175	10.31	38.03	5899		0.00	5.96	4002.99	443.00	1323.45	1833.12	44.99	-151.73
CSC080	24.78	38.13	5110	M	0.08	1.98	4029.74	443.02	1409.93	1853.92	36.51	-137.14
3206	37.76	38.23	2043		0.08	7.03	4053.74	443.03	1580.32	1872.62	-100.15	-163.51
CB23	0.28	37.93	5180		0.00	3.54	3984.45	443.03	1369.77	1818.73	38.12	-136.44
2891	21.52	38.06	4627		3.75	2.72	4023.72	443.09	1431.04	1849.23	16.91	-135.80
CSC032	21.56	38.05	4948	M	0.06	1.81	4023.79	443.10	1414.26	1849.28	30.24	-138.05
CSC079	24.20	37.96	4995	C	0.07	1.88	4028.67	443.27	1416.47	1853.08	33.07	-136.75
C18	11.58	37.80	5426		0.55	3.31	4005.34	443.36	1357.03	1834.94	32.29	-150.91
CSC043	22.58	37.67	4825	C	0.00	1.81	4025.67	443.68	1420.20	1850.75	23.16	-140.99
3169	35.44	37.67	3092		0.13	7.66	4049.45	443.84	1518.46	1869.28	-60.02	-158.77
5012	24.38	37.48	5071		0.33	1.99	4029.00	443.99	1413.47	1853.34	36.96	-135.10
2855	17.72	37.40	5028		0.60	2.20	4016.69	444.03	1396.68	1843.76	25.71	-144.40
B271	17.71	37.36	5028		0.00	2.56	4016.67	444.09	1396.07	1843.75	25.11	-145.23
2882	28.34	37.44	5264		0.50	2.39	4036.32	444.10	1402.99	1859.04	38.92	-139.17
CSC082	28.34	37.44	5264	B	0.00	2.39	4036.31	444.10	1402.92	1859.04	38.85	-139.74
B262	28.34	37.43	5263		0.00	2.63	4036.32	444.11	1402.98	1859.04	38.82	-139.50
3207	38.46	37.48	1955		0.04	7.17	4055.03	444.16	1588.18	1873.63	-101.58	-161.80
2994	25.97	37.37	5306		0.24	2.25	4031.94	444.17	1401.68	1855.63	44.97	-134.96
TP130	1.50	37.15	5398		0.36	3.44	3986.70	444.21	1362.06	1820.48	49.15	-132.97
2881	26.68	37.33	5374		0.11	2.32	4033.25	444.24	1398.90	1856.65	47.56	-134.76
B261	26.66	37.33	5376		0.00	2.84	4033.21	444.24	1399.06	1856.62	47.97	-134.01
CSC081	26.66	37.33	5376	B	0.65	2.32	4033.21	444.24	1399.06	1856.62	47.94	-133.90
TP129	2.80	37.12	6876		8.91	17.66	3989.10	444.27	1258.72	1822.34	82.86	-135.51
3208	39.05	37.39	2026		0.27	6.67	4056.12	444.30	1587.93	1874.48	-96.00	-158.94
2856	18.97	37.19	5088		0.41	2.08	4018.99	444.36	1396.58	1845.56	29.45	-143.02
CSC042	15.59	37.09	4900	C	0.26	2.36	4012.74	444.47	1398.30	1840.70	18.35	-147.55
CB8	9.41	37.03	6170		0.00	7.64	4001.32	444.48	1304.12	1831.83	52.43	-151.88
C23	6.03	36.90	6262		2.14	6.24	3995.07	444.64	1300.53	1826.98	62.33	-146.51
CB12	5.36	36.85	6278		0.00	7.05	3993.83	444.71	1300.07	1826.02	64.34	-144.24
CSC034	17.28	36.91	4975	B	0.07	2.22	4015.86	444.76	1399.52	1843.13	24.20	-144.60
B272	17.29	36.90	4975		0.00	2.52	4015.89	444.77	1399.31	1843.14	23.98	-144.59
CSC035	18.17	36.91	5125	C	0.09	2.15	4017.51	444.77	1391.48	1844.41	28.98	-145.00
2854	17.30	36.89	4975		0.05	2.22	4015.90	444.79	1399.46	1843.16	24.11	-144.71
5006	20.33	36.86	5335		0.77	2.48	4021.51	444.87	1384.68	1847.52	38.81	-141.35
C17	14.19	36.80	4789		0.17	2.51	4010.15	444.89	1397.73	1838.69	9.37	-152.84
CSC040	18.93	36.83	5145	C	0.17	2.16	4018.91	444.90	1393.82	1845.50	32.11	-142.47
5011	24.41	36.85	5173		0.31	2.32	4029.05	444.93	1406.38	1853.39	39.42	-135.82
CSB103	22.29	36.78	4865	C	0.14	1.91	4025.12	445.01	1416.99	1850.33	24.12	-141.15
UCR064	29.80	36.73	5473	B	0.14	2.83	4039.01	445.17	1389.31	1861.14	42.78	-142.38
B263	29.80	36.72	5474		0.00	3.27	4039.01	445.19	1391.08	1861.15	44.65	-140.24
2883	29.80	36.71	5474		0.06	2.84	4039.01	445.20	1391.08	1861.15	44.64	-140.62
CSB102	13.92	36.42	4805	C	0.06	2.23	4009.65	445.44	1396.03	1838.30	9.56	-153.42
UCR065	29.03	36.54	5310	C	0.06	2.58	4037.58	445.45	1399.92	1860.04	39.18	-140.73
C16	12.21	36.40	4925		0.38	2.87	4006.49	445.46	1386.33	1835.85	13.60	-152.91
3209	38.98	36.59	2540		0.28	6.44	4055.98	445.49	1560.26	1874.38	-75.24	-156.08
MIT045	26.36	36.30	5243	C	0.13	2.40	4032.64	445.78	1405.74	1856.19	42.55	-135.18
CB9	8.47	36.13	5963		0.00	6.78	3999.57	445.82	1317.75	1830.48	47.95	-150.14
UCR061	34.02	36.33	3923	B	0.82	7.99	4046.80	445.82	1471.40	1867.23	-26.82	-153.10
3159	34.01	36.31	3923		0.84	8.01	4046.79	445.85	1471.80	1867.21	-26.40	-152.65
CB10	7.15	36.09	6055		0.00	7.18	3997.13	445.87	1315.49	1828.58	56.18	-144.63
CSC031	22.67	36.17	4865	M	0.07	2.08	4025.82	445.93	1422.80	1850.88	29.38	-135.79
B264	22.63	36.15	4865		0.00	2.49	4025.75	445.96	1422.84	1850.82	29.49	-135.35
2890	22.61	36.14	4865		0.15	2.10	4025.71	445.97	1422.97	1850.80	29.64	-135.43
CSC041	16.03	36.08	4740	C	0.02	2.16	4013.55	445.99	1409.07	1841.33	13.45	-147.41
TP72	4.70	35.94	5717		0.45	3.35	3992.60	446.07	1338.18	1825.07	50.67	-142.45
CSC036	19.38	36.05	5327	C	0.56	2.84	4019.74	446.07	1385.28	1846.15	40.03	-139.71
B273	15.65	36.00	4663		0.00	2.43	4012.85	446.10	1411.84	1840.79	9.53	-148.44
5003	15.64	35.98	4663		0.20	2.17	4012.83	446.13	1410.55	1840.77	8.25	-149.79
CB22	1.09	35.85	5694		0.00	6.29	3985.93	446.16	1342.13	1819.89	57.63	-131.76

TABLE 1-A3 (cont.). Principal Facts, Gravity Stations in Northern Panamint Valley

STA	LAT	LON	EL	EC	IZ	OZ	NORTH	EAST	OBS G	THEO G	FAA	CBA
TP74	3.85	35.70	5932		0.12	3.47	3991.03	446.42	1326.20	1823.85	60.11	-140.23
TP73	4.05	35.69	5925		0.18	3.49	3991.40	446.43	1325.88	1824.14	58.85	-141.23
B187	11.11	35.74	5604		0.00	6.57	4004.45	446.44	1339.10	1834.27	31.77	-154.26
2853	16.07	35.54	4745		0.06	2.18	4013.62	446.79	1411.72	1841.39	16.52	-144.46
B274	16.07	35.53	4746		0.00	2.68	4013.62	446.81	1411.67	1841.39	16.56	-144.01
CB18	3.05	35.20	6311		0.00	6.51	3989.55	447.16	1299.44	1822.70	70.12	-140.12
UCR066	28.49	35.38	5375	C	0.09	2.92	4036.57	447.17	1391.18	1859.26	37.33	-144.44
B252	14.85	35.27	4517		0.00	2.45	4011.36	447.18	1421.88	1839.64	7.00	-145.96
B186	10.36	35.13	5889		0.00	7.90	4003.06	447.34	1318.67	1833.19	39.20	-155.24
3153	38.32	35.23	3622		0.78	4.83	4054.75	447.51	1500.20	1873.43	-32.61	-151.73
CSC037	20.06	35.02	4895	C	0.16	2.91	4020.98	447.62	1421.02	1847.12	34.18	-131.10
CSB100	14.64	34.96	4445	C	0.11	2.23	4010.97	447.63	1423.47	1839.33	2.12	-148.48
CB11	5.69	34.90	5813		0.00	4.35	3994.42	447.64	1335.53	1826.49	55.62	-139.78
CSB005	18.49	34.98	4790	C	1.63	3.27	4018.08	447.66	1418.94	1844.87	24.49	-135.37
B176	8.73	34.90	5009		0.00	3.16	4000.04	447.67	1381.33	1830.85	21.49	-147.60
CSB002	15.46	34.94	4775	C	0.42	2.21	4012.48	447.67	1407.41	1840.51	15.91	-145.71
CSB101	13.93	34.92	4480	M	0.06	2.15	4009.65	447.68	1415.22	1838.32	-1.81	-153.75
5000	16.97	34.94	4417		7.12	3.47	4015.28	447.70	1439.76	1842.68	12.43	-128.96
THN10	30.15	35.01	5932		1.07	5.31	4039.64	447.74	1357.18	1861.65	53.29	-145.21
UCR063	30.15	35.01	5925	M	0.91	4.15	4039.64	447.74	1356.52	1861.65	51.97	-146.55
2889	21.73	34.94	4948		1.31	3.22	4024.08	447.75	1410.92	1849.53	26.66	-138.97
5007	22.60	34.94	4461		0.59	2.59	4025.68	447.76	1448.50	1850.78	17.21	-133.10
5008	23.48	34.94	4507		0.28	2.24	4027.31	447.77	1449.62	1852.05	21.38	-131.16
5005	20.00	34.92	4958		0.12	3.14	4020.88	447.77	1415.45	1847.04	34.62	-132.63
MIT020	21.75	34.92	4629	M	0.59	2.82	4024.11	447.77	1428.34	1849.56	14.07	-141.77
MIT021	22.62	34.92	4461	M	0.08	2.58	4025.72	447.78	1447.28	1850.81	15.96	-134.87
MIT037	24.36	34.92	4595	M	0.00	2.24	4028.93	447.80	1441.11	1853.31	19.88	-135.96
MIT036	23.49	34.92	4507	M	0.00	2.24	4027.33	447.81	1448.54	1852.06	20.29	-132.53
CSB011	16.82	34.85	4670	C	0.80	2.72	4014.99	447.84	1423.40	1842.47	20.07	-137.06
TP75	3.63	34.66	5922		0.13	3.56	3990.61	447.97	1326.34	1823.53	59.63	-140.28
3161	33.46	34.79	4405		1.61	6.38	4045.76	448.11	1447.97	1866.42	-4.22	-147.81
UCR060	33.46	34.79	4405	B	2.87	6.38	4045.76	448.11	1447.38	1866.42	-4.81	-147.14
C24	13.56	34.60	4463		0.11	2.36	4008.97	448.17	1413.63	1837.78	-4.47	-155.67
CSC038	19.73	34.50	4680	C	0.74	3.20	4020.37	448.39	1434.88	1846.65	28.31	-128.74
B251	14.33	34.36	4345		0.00	2.51	4010.39	448.54	1430.39	1838.89	0.09	-146.91
2884	30.55	34.44	6134		0.14	5.01	4040.38	448.60	1345.03	1862.23	59.55	-146.02
CSB003	15.73	34.21	5217	M	3.43	5.05	4012.97	448.77	1381.24	1840.90	30.90	-140.00
B185	10.04	34.04	5499		0.00	9.24	4002.46	448.97	1343.17	1832.73	27.51	-152.27
3152	39.32	34.19	3749		0.21	3.88	4056.59	449.07	1496.01	1874.87	-26.30	-151.30
UCR062	30.77	34.12	6085	C	0.34	5.01	4040.78	449.08	1347.41	1862.54	57.01	-146.69
CB20	2.73	33.91	6360		0.00	8.32	3988.94	449.09	1297.48	1822.24	73.23	-136.88
CSB099	14.11	33.96	4255	C	0.08	2.36	4009.98	449.12	1433.36	1838.57	-5.08	-149.08
DVR37	25.72	34.05	5109		2.73	6.54	4031.44	449.13	1407.54	1855.27	32.67	-136.46
MIT043	25.73	34.04	5109	M	2.83	4.11	4031.46	449.14	1407.07	1855.28	32.19	-136.55
B177	8.75	33.82	4725		0.00	3.21	4000.07	449.29	1396.80	1830.88	10.23	-149.09
B253	12.21	33.84	4439		0.00	2.68	4006.47	449.30	1417.21	1835.85	-1.21	-151.26
CSC039	19.23	33.89	4215	C	0.41	3.40	4019.44	449.30	1463.48	1845.93	13.92	-127.33
UCR059	32.21	33.96	5283	M	2.44	5.51	4043.44	449.32	1395.21	1864.62	27.35	-146.33
3160	32.19	33.96	5273		3.61	5.56	4043.40	449.33	1395.11	1864.59	26.34	-145.78
5009	23.48	33.89	4612		0.01	2.68	4027.30	449.34	1441.52	1852.05	23.16	-132.81
MIT022	22.62	33.87	4488	M	0.13	2.69	4025.71	449.36	1446.19	1850.81	17.41	-134.19
MIT026	23.48	33.88	4610	M	0.00	2.68	4027.30	449.36	1441.49	1852.05	22.94	-132.97
MIT038	24.36	33.88	4462	M	0.05	2.59	4028.92	449.37	1451.12	1853.31	17.39	-133.50
CSB004	17.68	33.76	4130	C	0.38	3.05	4016.57	449.48	1459.83	1843.70	4.50	-134.22
CB19	4.10	33.57	6715		0.00	11.34	3991.47	449.62	1270.67	1824.21	77.81	-141.39
MIT046	29.65	33.75	6158	M	2.79	7.20	4038.70	449.62	1339.75	1860.93	57.82	-143.73
CSB092	21.30	33.67	4436	M	1.93	3.13	4023.27	449.65	1442.75	1848.91	10.98	-136.59
5001	16.81	33.59	4045		0.42	3.08	4014.97	449.72	1461.50	1842.45	-0.56	-136.30
B250	13.87	33.56	4235		0.00	2.57	4009.53	449.73	1435.20	1838.23	-4.78	-147.96
B179	5.25	33.50	6158		0.00	5.86	3993.60	449.73	1310.13	1825.86	63.28	-142.39

TABLE 1-A3 (cont.). Principal Facts, Gravity Stations in Northern Panamint Valley

STA	LAT	LON	EL	EC	IZ	OZ	NORTH	EAST	OBS G	THEO G	FAA	CBA
CSB006	16.81	33.57	4050	C	0.36	3.05	4014.97	449.75	1460.87	1842.45	-0.72	-136.73
C15	10.16	33.50	4446		0.33	3.39	4002.67	449.78	1411.33	1832.90	-3.49	-153.07
MIT042	25.65	33.46	4804	M	2.33	3.92	4031.31	450.01	1428.02	1855.17	24.59	-134.40
CB21	0.66	33.23	6405		0.00	10.25	3985.11	450.09	1291.32	1819.28	74.26	-135.45
2885	31.16	33.41	6214		0.42	6.22	4041.50	450.14	1338.63	1863.11	59.79	-147.02
UCR057	31.16	33.34	6318	B	1.54	7.04	4041.49	450.25	1330.25	1863.11	61.18	-147.24
C4	1.47	33.00	7109		7.82	17.66	3986.61	450.44	1241.33	1820.44	89.27	-137.05
2852	16.75	32.98	3826		0.15	3.03	4014.85	450.63	1473.57	1842.37	-8.99	-137.54
MIT047	30.31	33.08	5727	M	3.20	5.56	4039.92	450.63	1369.26	1861.88	45.87	-142.19
C12	7.94	32.80	4816		0.22	3.81	3998.56	450.81	1385.53	1829.72	8.68	-153.16
C14	9.69	32.80	4562		0.14	3.39	4001.80	450.83	1402.13	1832.23	-1.11	-154.67
B178	5.82	32.76	5973		0.00	5.26	3994.64	450.85	1322.19	1826.68	57.13	-142.82
B182	12.20	32.76	4286		0.00	3.11	4006.44	450.92	1422.57	1835.83	-10.22	-154.60
CSB091	20.88	32.80	4132	M	1.25	3.48	4022.48	450.95	1471.21	1848.30	11.47	-126.02
B266	20.88	32.79	4130		0.00	4.42	4022.49	450.96	1473.35	1848.31	13.42	-124.30
MIT023	22.62	32.80	4594	M	0.00	4.48	4025.70	450.96	1435.84	1850.81	17.03	-136.54
MIT025	24.36	32.81	4450	M	0.13	3.61	4028.92	450.97	1452.15	1853.31	17.29	-132.08
2892	20.87	32.78	4132		0.33	3.50	4022.47	450.98	1473.78	1848.29	14.05	-124.33
MIT024	23.45	32.79	4833	M	0.70	5.54	4027.23	450.99	1416.56	1852.00	19.02	-140.97
MIT041	24.91	32.76	4340	C	0.79	3.51	4029.93	451.05	1457.70	1854.10	11.71	-133.33
CSB097	14.94	32.69	3959	C	0.09	3.10	4011.50	451.05	1455.16	1839.77	-12.20	-145.34
CSB098	14.15	32.57	4010	C	0.07	3.19	4010.04	451.22	1447.40	1838.63	-14.13	-148.91
TP128	2.54	32.34	7138		6.38	15.87	3988.58	451.45	1241.68	1821.97	90.81	-138.28
CSB096	15.97	32.38	3750	C	0.40	3.41	4013.40	451.52	1474.53	1841.25	-14.06	-139.37
CSB007	16.83	32.37	3590	C	0.18	3.50	4015.01	451.55	1489.20	1842.50	-15.68	-135.63
B180	3.19	32.23	6768		0.00	11.71	3989.78	451.62	1269.36	1822.90	82.74	-137.88
UCR058	32.19	32.31	6618	M	1.95	8.75	4043.39	451.80	1316.72	1864.59	74.36	-142.18
2851	17.78	32.15	3431		1.68	3.71	4016.75	451.89	1500.76	1843.85	-20.33	-133.15
CSB010	17.76	32.14	3431	B	1.98	3.71	4016.71	451.90	1500.84	1843.82	-20.22	-132.74
C11	6.65	32.00	5325		0.63	4.74	3996.17	452.00	1358.63	1827.87	31.48	-146.85
DVG 1	21.32	32.09	3609		1.95	5.10	4023.29	452.01	1497.97	1848.94	-11.58	-130.75
MIT048	30.28	32.10	4725	C	1.35	5.75	4039.85	452.09	1431.83	1861.84	14.30	-141.14
CSB008	18.90	31.83	3080	C	1.96	4.82	4018.81	452.38	1529.30	1845.46	-26.50	-125.84
B184	9.60	31.68	4780		0.00	4.39	4001.62	452.51	1392.18	1832.10	9.56	-150.46
3238	20.87	31.72	3343		1.25	3.71	4022.46	452.56	1514.95	1848.29	-18.95	-129.14
CSB090	20.88	31.72	3343	M	1.34	3.71	4022.47	452.56	1514.41	1848.30	-19.50	-129.61
MIT039	24.36	31.73	4060	M	0.22	5.03	4028.91	452.58	1470.89	1853.31	-0.62	-135.13
B181	14.18	31.60	4634		0.00	5.34	4010.09	452.67	1417.31	1838.68	14.39	-139.68
MIT008	21.39	31.64	3414	C	0.36	3.93	4023.41	452.69	1508.75	1849.04	-19.13	-132.47
MIT049	30.60	31.69	4907	M	3.64	6.09	4040.44	452.71	1420.89	1862.30	20.00	-139.03
DVR36	28.16	31.64	3942		3.41	7.47	4035.93	452.75	1478.24	1858.78	-9.84	-138.07
DVR89	35.75	31.59	6581		6.33	14.79	4049.97	452.91	1322.42	1869.72	71.45	-139.73
MIT050	29.93	31.50	4538	M	3.39	5.57	4039.20	452.98	1440.84	1861.33	6.24	-140.93
CSB009	18.29	31.40	3235	C	2.33	4.38	4017.68	453.01	1512.26	1844.58	-28.09	-132.82
MIT040	24.81	31.44	4195	C	2.74	6.30	4029.74	453.02	1455.00	1853.96	-4.47	-139.81
2850	17.92	31.37	3489		1.59	3.57	4017.00	453.06	1497.59	1844.05	-18.34	-133.34
C1	4.44	30.80	5723		0.43	4.90	3992.08	453.78	1333.73	1824.70	47.16	-144.62
2849	18.47	30.68	3419		1.21	4.47	4018.01	454.09	1500.97	1844.84	-22.24	-134.36
2848	19.52	30.68	2605		0.77	6.19	4019.95	454.10	1554.39	1846.35	-46.96	-129.80
UCR041	20.01	30.64	2409	M	1.35	6.50	4020.86	454.17	1566.06	1847.05	-54.42	-129.63
TP64	0.93	30.40	5677		0.06	3.82	3985.59	454.34	1341.34	1819.66	55.47	-135.80
C13	9.51	30.40	5637		4.41	9.86	4001.45	454.43	1340.23	1831.97	38.30	-145.57
C2	1.86	30.30	5687		0.08	3.99	3987.30	454.50	1336.83	1821.00	50.57	-140.88
MIT053	27.96	30.46	2920	C	0.21	6.01	4035.55	454.51	1539.46	1858.49	-44.42	-138.82
DVS56	13.72	30.31	6343		7.55	17.74	4009.23	454.60	1303.35	1838.01	61.73	-138.38
UCR029	26.15	30.39	2555	C	1.68	6.14	4032.20	454.60	1559.04	1855.89	-56.55	-136.81
UCR014	23.86	30.32	2190	C	1.70	7.69	4027.97	454.68	1578.82	1852.59	-67.80	-133.93
B183	11.66	30.18	6450		0.00	17.62	4005.42	454.78	1293.95	1835.06	65.34	-138.54
MIT009	21.44	30.18	2630	C	0.23	4.14	4023.50	454.87	1555.72	1849.11	-46.04	-132.33
2847	20.44	29.99	2277		2.04	5.61	4021.65	455.14	1573.96	1847.67	-59.55	-130.42
3143	38.00	30.07	4923		0.13	3.40	4054.11	455.19	1436.50	1872.97	26.45	-139.33

TABLE 1-A3 (cont.). Principal Facts, Gravity Stations in Northern Panamint Valley

STA	LAT	LON	EL	EC	IZ	OZ	NORTH	EAST	OBS G	THEO G	FAA	CBA
DVR88	14.50	29.90	6060		3.42	12.48	4010.67	455.22	1327.11	1839.14	57.77	-137.94
C6	1.80	29.70	5672		0.07	4.14	3987.19	455.40	1340.93	1820.91	53.35	-137.44
C5	0.90	29.60	5659		0.10	4.03	3985.52	455.54	1342.53	1819.62	55.01	-135.44
DVG63	17.79	29.69	5584		11.22	22.78	4016.75	455.57	1350.42	1843.86	31.61	-137.53
C7	2.73	29.50	5688		0.47	5.00	3988.91	455.71	1335.73	1822.24	48.32	-142.16
UCR015	23.84	29.63	1800	C	0.25	7.26	4027.93	455.72	1602.67	1852.56	-80.59	-135.18
MIT051	28.80	29.62	3314	M	0.72	5.47	4037.10	455.78	1516.67	1859.70	-31.37	-139.34
3144	39.65	29.66	4657		0.59	2.72	4057.16	455.82	1453.48	1875.35	16.05	-140.85
MIT052	27.23	29.55	2520	C	0.16	5.48	4034.20	455.87	1563.48	1857.44	-56.95	-138.19
UCR028	26.09	29.51	2230	C	0.28	5.73	4032.09	455.92	1576.58	1855.80	-69.49	-140.38
UCR013	23.20	29.32	1638	C	0.04	7.09	4026.74	456.17	1608.77	1851.64	-88.80	-138.20
MIT054	28.07	29.17	2840	C	0.19	5.22	4035.74	456.44	1546.52	1858.65	-45.03	-137.50
UCR016	23.68	29.12	1625	C	0.04	6.65	4027.63	456.48	1610.10	1852.33	-89.39	-138.77
MIT010	21.41	28.92	2798	M	5.48	4.93	4023.43	456.75	1536.03	1849.07	-49.89	-135.91
C10	5.06	28.80	8366		12.89	36.28	3993.21	456.78	1155.53	1825.59	116.44	-134.06
BIE387	23.46	28.81	1622	Z	0.00	6.83	4027.22	456.94	1610.99	1852.02	-88.46	-137.60
MIT011	22.27	28.73	1760	C	0.11	5.15	4025.02	457.05	1603.96	1850.30	-80.80	-136.27
CSC016	20.22	28.71	2040	C	1.26	5.89	4021.23	457.06	1590.06	1847.36	-65.42	-128.64
C8	2.76	28.50	6073		1.74	7.76	3988.95	457.21	1317.33	1822.29	66.06	-134.81
THN11	34.77	28.69	6580		0.57	8.10	4048.13	457.22	1328.41	1868.31	78.76	-139.08
UCR027	26.05	28.64	2040	C	0.30	5.26	4032.01	457.22	1587.50	1855.74	-76.38	-141.18
UCR017	23.57	28.58	1610	C	0.00	5.60	4027.42	457.28	1610.77	1852.17	-89.97	-139.93
UCR030	25.18	28.57	1800	C	0.07	5.53	4030.40	457.31	1600.05	1854.49	-85.15	-141.65
MIT055	27.23	28.55	2395	C	0.12	5.12	4034.19	457.36	1570.00	1857.44	-62.19	-139.53
3142	37.21	28.58	5048		0.78	3.69	4052.64	457.41	1433.48	1871.83	36.32	-132.80
D 5013	22.60	28.49	1683		0.07	5.01	4025.63	457.41	1608.23	1850.78	-84.26	-137.31
BIE386	23.46	28.38	1614	Z	0.00	5.92	4027.22	457.58	1611.15	1852.02	-89.06	-138.83
CSC015	20.29	28.35	2008	C	0.22	5.27	4021.36	457.60	1592.05	1847.46	-66.55	-130.32
2985	26.33	28.24	2014		0.20	5.29	4032.52	457.81	1592.33	1856.15	-74.30	-138.31
2893	26.03	28.19	1952		0.08	5.20	4031.97	457.89	1594.95	1855.72	-77.17	-139.22
2986	26.66	28.10	2111		0.15	5.19	4033.13	458.03	1586.22	1856.62	-71.86	-139.32
MIT012	22.12	28.06	1680	C	0.00	4.73	4024.74	458.05	1607.59	1850.09	-84.48	-137.72
A001	20.41	28.04	1920		0.00	4.30	4021.58	458.06	1595.91	1847.63	-71.15	-133.07
UCR018	23.54	28.05	1602	C	0.00	4.99	4027.36	458.07	1611.63	1852.13	-89.82	-140.11
2871	25.64	28.04	1864		0.04	5.07	4031.25	458.11	1598.78	1855.16	-81.06	-140.25
CSC014	20.39	27.99	1908	C	0.12	4.98	4021.54	458.14	1596.68	1847.60	-71.46	-132.18
2987	26.98	28.00	2205		0.11	5.23	4033.72	458.18	1581.28	1857.09	-68.42	-139.12
DVR21	32.61	28.02	7325		6.11	20.13	4044.13	458.20	1266.34	1865.20	89.81	-141.40
BIE385	23.46	27.95	1605	Z	0.00	4.95	4027.21	458.22	1611.72	1852.02	-89.34	-139.77
MIT030	28.44	27.98	2900	C	0.28	5.58	4036.42	458.22	1532.93	1859.19	-53.52	-147.60
THN12	36.43	27.95	5130		0.76	4.36	4051.19	458.34	1426.40	1870.70	38.07	-133.96
2988	27.20	27.89	2275		0.12	5.28	4034.13	458.35	1576.44	1857.40	-67.00	-140.04
DVS57	1.98	27.70	5719		1.69	7.22	3987.51	458.41	1340.75	1821.17	57.33	-131.99
UCR026	26.21	27.83	1940	C	0.07	5.21	4032.30	458.43	1597.16	1855.97	-76.35	-137.99
2870	25.28	27.79	1771		0.03	4.98	4030.58	458.48	1602.87	1854.64	-85.20	-141.29
C9	2.74	27.60	6155		2.67	10.13	3988.91	458.56	1311.93	1822.26	68.40	-132.90
CSC013	20.29	27.60	1870	C	0.08	4.74	4021.35	458.72	1598.69	1847.46	-72.89	-132.58
B164	10.74	27.47	4988		0.00	16.76	4003.70	458.83	1393.99	1833.74	29.29	-125.48
BIE384	23.46	27.52	1603	Z	0.00	4.57	4027.21	458.87	1614.07	1852.02	-87.17	-137.92
UCR019	23.51	27.43	1597	C	0.00	4.55	4027.30	459.00	1613.46	1852.09	-88.42	-138.98
BIE 19	20.03	27.40	1872	Z	0.00	5.11	4020.87	459.01	1595.98	1847.08	-75.03	-134.50
5014	22.65	27.41	1641		0.00	4.30	4025.72	459.02	1613.03	1850.85	-83.48	-135.79
2989	27.44	27.40	2372		0.23	5.28	4034.57	459.08	1568.92	1857.75	-65.74	-142.01
BIE337	21.84	27.36	1715	Z	0.00	4.06	4024.22	459.09	1610.00	1849.69	-78.29	-133.43
2869	25.19	27.35	1712		0.06	4.93	4030.41	459.13	1606.70	1854.51	-86.78	-140.86
BIE336	21.84	27.24	1708	Z	0.00	4.01	4024.21	459.27	1610.73	1849.69	-78.30	-133.22
MIT087	19.28	27.17	2325	M	1.94	4.49	4019.48	459.35	1565.35	1846.00	-61.98	-135.72
CSC012	20.21	27.18	1787	C	0.09	4.66	4021.20	459.35	1602.47	1847.34	-76.79	-133.70
MIT029	28.71	27.19	3040	C	0.26	6.16	4036.91	459.40	1525.94	1859.57	-47.74	-146.07
2846	20.23	27.08	1768		0.16	4.58	4021.24	459.50	1603.37	1847.37	-77.62	-133.91

TABLE 1-A3 (cont.). Principal Facts, Gravity Stations in Northern Panamint Valley

STA	LAT	LON	EL	EC	IZ	OZ	NORTH	EAST	OBS G	THEO G	FAA	CBA
BIE 20	20.22	27.08	1768	Z	0.00	4.76	4021.22	459.50	1603.60	1847.36	-77.37	-133.64
BIE383	23.46	27.08	1589	Z	0.00	4.40	4027.21	459.52	1615.85	1852.02	-86.71	-137.14
BIE335	21.84	26.97	1678	Z	0.00	3.96	4024.21	459.67	1611.83	1849.69	-80.03	-133.97
MIT028	27.33	27.00	2310	C	0.22	5.35	4034.36	459.68	1574.56	1857.59	-65.77	-139.85
UCR020	23.59	26.94	1582	C	0.00	4.41	4027.45	459.73	1616.43	1852.20	-86.98	-137.16
DVR70	12.32	26.87	3607		5.49	11.29	4006.62	459.74	1473.76	1836.00	-23.04	-135.95
CSB060	12.37	26.86	3630	C	2.94	8.45	4006.70	459.76	1473.29	1836.07	-21.41	-135.03
2990	27.59	26.93	2434		0.26	5.42	4034.84	459.78	1563.57	1857.96	-65.47	-143.71
MIT085	20.93	26.86	1723	C	0.02	4.00	4022.53	459.83	1607.53	1848.38	-78.79	-134.22
MIT084	21.79	26.80	1660	C	0.01	3.94	4024.12	459.93	1611.14	1849.61	-82.34	-135.67
CSC011	20.30	26.74	1715	C	0.02	4.36	4021.36	460.00	1607.24	1847.47	-78.92	-133.71
BIE334	21.84	26.71	1676	Z	0.00	3.85	4024.21	460.06	1613.86	1849.69	-78.19	-132.17
THN13	35.90	26.77	4944		1.19	4.87	4050.21	460.09	1437.15	1869.94	32.10	-133.05
MIT083	22.66	26.69	1618	C	0.00	4.03	4025.72	460.10	1614.04	1850.86	-84.64	-136.44
BIE382	23.46	26.65	1581	Z	0.00	4.31	4027.20	460.17	1617.89	1852.02	-85.42	-135.67
BIE 27	20.27	26.63	1700	Z	0.00	4.53	4021.31	460.17	1607.77	1847.43	-79.76	-133.88
UCR025	26.26	26.65	1790	C	0.02	5.65	4032.38	460.19	1608.08	1856.05	-79.61	-135.70
2991	27.77	26.63	2416		0.30	6.00	4035.18	460.23	1564.68	1858.22	-66.31	-143.31
CSB064	16.41	26.55	2785	C	0.71	6.45	4014.17	460.26	1536.22	1841.88	-43.73	-132.56
2867	24.77	26.54	1604		0.01	4.87	4029.63	460.34	1614.47	1853.90	-88.57	-139.03
BIE311	20.94	26.52	1663	Z	0.00	4.10	4022.55	460.34	1611.77	1848.39	-80.20	-133.48
BIE333	21.84	26.44	1658	Z	0.00	3.81	4024.21	460.47	1614.91	1849.69	-78.83	-132.23
MIT017	27.90	26.44	2450	C	0.18	6.38	4035.41	460.52	1562.13	1858.41	-65.85	-143.76
CSB067	14.21	26.35	3010	C	2.55	8.16	4010.10	460.54	1514.78	1838.72	-40.85	-133.86
MIT086	19.19	26.35	1735	C	0.05	5.16	4019.31	460.58	1602.34	1845.87	-80.34	-134.99
BIE324	20.04	26.33	1642	Z	0.00	4.75	4020.88	460.62	1611.41	1847.10	-81.24	-133.15
MIT027	26.88	26.35	1985	C	0.09	5.88	4033.53	460.64	1596.08	1856.94	-74.16	-136.66
MIT018	27.91	26.32	2404	M	0.18	6.74	4035.43	460.70	1565.41	1858.42	-66.91	-142.88
CSC010	20.33	26.27	1662	C	0.02	4.14	4021.41	460.71	1610.85	1847.51	-80.34	-133.53
2992	27.89	26.30	2405		0.17	6.68	4035.40	460.73	1565.24	1858.40	-66.96	-143.03
B163	10.02	26.19	4458		0.00	14.36	4002.36	460.74	1416.46	1832.70	2.92	-136.08
UCR021	23.56	26.27	1567	C	0.00	4.35	4027.39	460.74	1619.61	1852.16	-85.16	-134.89
DR105	6.50	26.15	5834		6.78	17.59	3995.85	460.77	1316.06	1827.65	36.96	-145.91
BIE381	23.46	26.22	1564	Z	0.00	4.35	4027.20	460.81	1619.62	1852.02	-85.29	-134.92
BIE310	20.94	26.19	1627	Z	0.00	4.06	4022.54	460.83	1614.28	1848.39	-81.08	-133.16
2928	20.30	26.18	1648		0.08	4.15	4021.36	460.84	1611.60	1847.47	-80.86	-133.50
BIE 28	20.29	26.18	1642	Z	0.00	4.27	4021.34	460.84	1611.66	1847.46	-81.35	-133.74
DVR35	30.69	26.19	6491		13.42	27.07	4040.57	460.91	1313.50	1862.43	61.37	-134.46
BIE332	21.84	26.13	1643	Z	0.00	3.77	4024.21	460.93	1616.22	1849.69	-78.93	-131.85
2845	24.55	26.14	1565		0.05	4.89	4029.22	460.94	1618.76	1853.59	-87.63	-136.69
2993	27.59	26.05	2231		0.14	6.73	4034.84	461.10	1576.28	1857.96	-71.85	-141.92
BIE309	20.94	25.99	1607	Z	0.00	4.03	4022.54	461.13	1615.28	1848.39	-81.96	-133.38
UCR022	23.54	25.92	1563	C	0.00	4.36	4027.35	461.26	1622.99	1852.13	-82.13	-131.71
BIE331	21.84	25.90	1628	Z	0.00	3.77	4024.21	461.27	1617.00	1849.69	-79.56	-131.97
CSC009	20.38	25.81	1608	C	0.02	4.02	4021.50	461.40	1614.75	1847.59	-81.59	-133.04
BIE323	20.04	25.79	1597	Z	0.00	4.24	4020.88	461.42	1614.81	1847.10	-82.08	-132.94
BIE380	23.46	25.79	1548	Z	0.00	4.47	4027.20	461.45	1622.18	1852.02	-84.24	-133.19
MIT080	21.23	25.78	1605	C	0.00	3.81	4023.08	461.45	1616.29	1848.81	-81.56	-133.13
MIT082	22.72	25.79	1584	C	0.00	4.00	4025.83	461.45	1618.21	1850.95	-83.75	-134.41
MIT081	22.09	25.78	1597	C	0.00	3.85	4024.67	461.46	1616.57	1850.05	-83.27	-134.52
BIE 25	20.33	25.72	1608	Z	0.00	4.01	4021.41	461.53	1615.45	1847.51	-80.82	-132.29
BIE308	20.94	25.72	1596	Z	0.00	3.89	4022.54	461.54	1616.79	1848.39	-81.49	-132.67
2837	24.34	25.73	1546		0.10	4.93	4028.83	461.55	1620.58	1853.28	-87.29	-135.61
CSB059	11.86	25.65	2960	C	1.63	7.23	4005.75	461.57	1509.75	1835.34	-47.21	-140.35
2838	24.68	25.70	1550		0.07	5.20	4029.46	461.60	1619.56	1853.77	-88.42	-136.64
MIT076	23.72	25.68	1553	C	0.00	4.52	4027.68	461.62	1622.66	1852.39	-83.66	-132.73
CSB013	19.75	25.64	1579	M	0.00	4.36	4020.34	461.65	1615.11	1846.68	-83.05	-133.18
2839	25.13	25.66	1564		0.05	5.60	4030.29	461.66	1617.70	1854.42	-89.61	-137.93
BIE330	21.84	25.63	1612	Z	0.00	3.77	4024.20	461.68	1617.11	1849.69	-80.96	-132.81
2929	19.70	25.61	1579		0.02	4.37	4020.25	461.69	1614.93	1846.61	-83.16	-133.26
CSB066	14.21	25.58	2725	C	1.64	6.42	4010.10	461.69	1535.39	1838.72	-47.04	-132.91

TABLE 1-A3 (cont.). Principal Facts, Gravity Stations in Northern Panamint Valley

STA	LAT	LON	EL	EC	IZ	OZ	NORTH	EAST	OBS G	THEO G	FAA	CBA
MIT019	26.90	25.64	1925	C	0.09	6.70	4033.56	461.70	1596.90	1856.97	-79.01	-138.63
UCR024	26.11	25.58	1700	C	0.05	6.34	4032.10	461.79	1611.78	1855.83	-84.15	-136.42
CSB063	16.06	25.46	2322	C	0.33	5.56	4013.52	461.88	1562.84	1841.37	-60.14	-134.32
2836	23.96	25.49	1545		0.08	4.77	4028.12	461.90	1622.29	1852.74	-85.13	-133.60
BIE341	21.84	25.48	1546	Z	0.00	4.07	4024.20	461.90	1615.43	1849.69	-88.84	-138.12
MIT075	23.72	25.47	1548	C	0.00	4.61	4027.68	461.93	1622.43	1852.39	-84.36	-133.17
BIE307	20.94	25.45	1581	Z	0.00	3.85	4022.54	461.94	1617.42	1848.39	-82.26	-132.97
BIE114	16.05	25.41	2320	Z	0.00	6.14	4013.50	461.96	1563.19	1841.36	-59.97	-133.83
CSB015	18.57	25.42	1739	C	0.11	4.66	4018.16	461.97	1605.48	1844.98	-75.84	-131.10
CH231	20.39	25.39	1576		0.00	3.96	4021.52	462.02	1616.49	1847.60	-82.92	-133.32
THN9	18.58	25.38	1736		0.33	4.59	4018.18	462.02	1604.58	1845.00	-77.14	-132.44
MIT001	20.39	25.39	1576	B	0.01	3.93	4021.52	462.02	1616.43	1847.60	-82.94	-133.38
UCR037	20.39	25.39	1576	B	0.00	3.93	4021.52	462.02	1616.48	1847.60	-82.88	-133.34
CSB001	20.39	25.39	1576	B	0.02	3.93	4021.52	462.02	1616.55	1847.60	-82.82	-133.25
CSC001	20.39	25.39	1576	B	0.01	3.93	4021.52	462.02	1616.61	1847.60	-82.76	-133.20
CSB016	17.71	25.37	1928	C	0.91	5.10	4016.57	462.03	1588.05	1843.75	-74.36	-134.86
BIE 70	20.36	25.38	1576	Z	0.00	3.96	4021.48	462.04	1616.49	1847.57	-82.85	-133.27
UCR023	23.68	25.40	1576	C	0.00	4.50	4027.60	462.04	1622.40	1852.33	-81.70	-131.59
2108	20.39	25.37	1576		0.02	3.92	4021.52	462.05	1616.49	1847.60	-82.87	-133.32
MIT005	23.87	25.39	1545	C	0.00	4.74	4027.95	462.05	1622.27	1852.61	-85.01	-133.59
MIT002	21.26	25.37	1579	C	0.01	3.80	4023.13	462.06	1617.06	1848.85	-83.27	-133.95
2835	23.53	25.37	1544		0.13	4.55	4027.33	462.08	1622.34	1852.12	-84.55	-133.15
B162	8.69	25.28	4343		0.00	12.20	3999.89	462.09	1426.98	1830.79	4.54	-132.69
BIE379	23.46	25.36	1547	Z	0.00	4.61	4027.20	462.09	1622.39	1852.02	-84.12	-132.90
BIE 80	20.36	25.34	1575	Z	0.00	3.95	4021.48	462.10	1617.16	1847.57	-82.27	-132.67
MIT003	22.16	25.35	1577	C	0.00	3.91	4024.79	462.10	1617.37	1850.15	-84.45	-134.96
MIT006	24.83	25.35	1549	C	0.00	5.58	4029.73	462.12	1619.45	1853.99	-88.84	-136.72
BIE 24	20.36	25.32	1576	Z	0.00	3.93	4021.48	462.13	1616.93	1847.57	-82.41	-132.86
MIT004	23.04	25.33	1554	C	0.00	4.28	4026.42	462.14	1621.22	1851.41	-84.03	-133.38
DVG 9	16.17	25.23	2276		0.65	4.91	4013.72	462.23	1564.04	1841.53	-63.44	-137.00
BIE322	20.04	25.25	1565	Z	0.00	4.05	4020.87	462.23	1616.01	1847.10	-83.89	-133.85
B158	1.19	25.14	5056		0.00	10.97	3986.03	462.24	1379.37	1820.04	34.76	-128.13
MIT074	23.72	25.26	1543	C	0.00	4.70	4027.68	462.25	1621.96	1852.39	-85.30	-133.85
BIE 81	20.23	25.23	1567	Z	0.00	3.97	4021.22	462.26	1616.90	1847.37	-83.08	-133.19
2827	20.69	25.22	1576		0.01	3.82	4022.08	462.28	1617.10	1848.03	-82.70	-133.25
BIE329	21.84	25.22	1603	Z	0.00	3.77	4024.20	462.29	1617.00	1849.69	-81.91	-133.46
BIE 53	23.22	25.21	1543	Z	0.00	4.52	4026.75	462.32	1622.80	1851.67	-83.74	-132.47
CSB062	16.75	25.17	2212	C	0.33	4.49	4014.79	462.32	1567.00	1842.37	-67.32	-138.78
BIE318	19.13	25.18	1585	Z	0.00	4.47	4019.19	462.33	1614.28	1845.79	-82.43	-132.65
BIE306	20.94	25.18	1572	Z	0.00	3.83	4022.54	462.34	1617.47	1848.39	-83.06	-133.48
2834	23.15	25.16	1542		0.13	4.42	4026.62	462.39	1622.59	1851.57	-83.94	-132.60
2840	25.19	25.15	1572		0.03	6.11	4030.40	462.42	1617.25	1854.51	-89.40	-137.51
BIE 82	20.08	25.12	1561	Z	0.00	4.03	4020.95	462.43	1616.53	1847.15	-83.80	-133.64
2828	21.14	25.09	1574		0.02	3.78	4022.91	462.48	1617.10	1848.68	-83.53	-134.05
MIT070	23.17	25.10	1543	C	0.00	4.44	4026.66	462.48	1621.14	1851.60	-85.33	-134.14
BIE328	21.84	25.09	1584	Z	0.00	3.84	4024.20	462.49	1616.85	1849.69	-83.85	-134.67
CSB065	15.15	25.05	2460	C	0.17	4.84	4011.83	462.49	1552.58	1840.07	-56.12	-135.93
BIE115	15.14	25.04	2460	Z	0.00	5.40	4011.81	462.51	1552.89	1840.05	-55.80	-135.21
BIE 54	22.92	25.08	1543	Z	0.00	4.44	4026.19	462.51	1621.92	1851.24	-84.19	-132.99
DVG 8	15.13	25.03	2459		0.67	4.84	4011.80	462.52	1552.62	1840.04	-56.16	-136.08
MIT073	23.72	25.06	1543	C	0.00	4.80	4027.67	462.54	1621.23	1852.39	-86.03	-134.47
BIE 83	19.96	25.01	1554	Z	0.00	4.04	4020.72	462.59	1616.58	1846.98	-84.24	-133.83
BIE 23	20.39	24.95	1562	Z	0.00	3.90	4021.52	462.68	1616.54	1847.60	-84.14	-134.15
BIE113	18.94	24.94	1575	Z	0.00	4.50	4018.84	462.69	1614.23	1845.51	-83.14	-132.99
MIT069	23.31	24.96	1543	C	0.00	4.58	4026.92	462.69	1621.29	1851.80	-85.38	-134.05
CSB014	18.95	24.93	1577	C	0.04	4.38	4018.86	462.70	1613.71	1845.53	-83.49	-133.49
CSC017	20.43	24.93	1560	C	0.00	3.84	4021.59	462.71	1616.49	1847.66	-84.44	-134.43
BIE 55	22.61	24.93	1552	Z	0.00	4.28	4025.62	462.73	1620.55	1850.79	-84.27	-133.55
2829	21.50	24.92	1567		0.03	3.83	4023.57	462.74	1616.49	1849.20	-85.32	-135.53
BIE 52	23.46	24.93	1542	Z	0.00	4.81	4027.19	462.74	1621.26	1852.02	-85.72	-134.13

TABLE 1-A3 (cont.). Principal Facts, Gravity Stations in Northern Panamint Valley

STA	LAT	LON	EL	EC	IZ	OZ	NORTH	EAST	OBS G	THEO G	FAA	CBA
BIE 84	19.82	24.90	1548	Z	0.00	4.12	4020.46	462.75	1616.43	1846.78	-84.75	-134.05
BIE305	20.94	24.91	1563	Z	0.00	3.84	4022.54	462.75	1616.90	1848.39	-84.48	-134.58
CSB061	11.07	24.84	2770	C	0.90	6.02	4004.29	462.77	1525.79	1834.21	-47.90	-136.45
2833	22.84	24.85	1544		0.12	4.36	4026.05	462.85	1620.78	1851.13	-85.12	-133.92
2043	11.60	24.79	2631		0.78	5.94	4005.27	462.85	1532.95	1834.97	-54.57	-138.54
2922	9.86	24.77	2684		2.45	8.53	4002.05	462.87	1528.76	1832.47	-51.28	-132.82
MIT068	23.44	24.84	1543	C	0.01	4.73	4027.16	462.87	1620.87	1851.99	-85.99	-134.50
MIT072	23.71	24.84	1543	C	0.00	4.93	4027.66	462.87	1621.02	1852.38	-86.22	-134.54
BIE327	21.84	24.82	1561	Z	0.00	3.96	4024.20	462.89	1616.64	1849.69	-86.22	-136.13
2930	19.55	24.80	1548		0.08	4.06	4019.97	462.90	1615.23	1846.39	-85.56	-134.84
CSB012	19.53	24.80	1548	B	0.00	4.07	4019.93	462.90	1615.17	1846.36	-85.59	-134.94
CSB058	11.61	24.76	2631	M	0.34	5.86	4005.29	462.90	1533.09	1834.98	-54.44	-138.94
BIE 85	19.68	24.79	1543	Z	0.00	4.12	4020.20	462.92	1616.11	1846.58	-85.34	-134.47
BIE317	19.13	24.78	1556	Z	0.00	4.31	4019.19	462.93	1614.81	1845.79	-84.62	-134.01
BIE 56	22.30	24.78	1553	Z	0.00	4.17	4025.05	462.95	1618.63	1850.35	-85.64	-135.07
MIT016	27.83	24.80	2350	C	1.17	10.20	4035.27	462.97	1576.29	1858.31	-61.00	-130.66
UCR056	23.92	24.77	1542	C	0.00	5.17	4028.04	462.98	1622.13	1852.68	-85.51	-133.55
BIE321	20.04	24.72	1548	Z	0.00	3.97	4020.87	463.02	1615.96	1847.10	-85.54	-134.99
UCR055	23.20	24.73	1542	C	0.06	4.63	4026.71	463.03	1621.14	1851.64	-85.47	-133.99
MIT067	23.57	24.73	1543	C	0.01	4.89	4027.39	463.04	1621.29	1852.17	-85.76	-134.10
UCR053	21.29	24.67	1552	C	0.00	3.86	4023.18	463.11	1615.96	1848.89	-86.96	-136.65
2841	25.27	24.68	1585		0.04	7.05	4030.54	463.12	1617.90	1854.62	-87.64	-135.25
2044	14.03	24.61	2346		0.22	5.04	4009.76	463.14	1557.92	1838.46	-59.89	-135.52
B160	5.48	24.56	4001		0.00	12.32	3993.96	463.15	1443.50	1826.19	-6.44	-131.84
BIE304	20.94	24.64	1562	Z	0.00	3.84	4022.53	463.15	1616.27	1848.39	-85.20	-135.26
UCR054	22.33	24.65	1550	C	0.00	4.17	4025.10	463.15	1618.30	1850.39	-86.31	-135.62
BIE 51	23.70	24.65	1543	Z	0.00	5.19	4027.64	463.16	1621.70	1852.36	-85.53	-133.59
BIE 57	22.00	24.63	1550	Z	0.00	4.11	4024.49	463.17	1617.26	1849.92	-86.87	-136.25
MIT000	25.26	24.64	1585	M	0.00	7.13	4030.52	463.18	1618.10	1854.61	-87.43	-134.99
UCR000	25.26	24.64	1585	M	0.00	7.13	4030.52	463.18	1618.08	1854.61	-87.45	-135.01
CSB000	25.26	24.64	1585	M	0.00	7.13	4030.52	463.18	1618.10	1854.61	-87.43	-134.99
CSC000	25.26	24.64	1585	M	0.00	7.13	4030.52	463.18	1618.19	1854.61	-87.34	-134.90
2832	22.42	24.62	1545		0.13	4.24	4025.27	463.19	1618.66	1850.52	-86.54	-135.48
MIT071	23.71	24.62	1543	C	0.03	5.09	4027.65	463.20	1621.69	1852.38	-85.56	-133.69
CSB033	14.04	24.57	2347	B	0.12	4.92	4009.78	463.20	1558.16	1838.47	-59.57	-135.46
2951	14.78	24.56	2542		0.58	4.02	4011.15	463.22	1546.17	1839.54	-54.29	-137.32
BIE 22	20.43	24.59	1546	Z	0.00	3.94	4021.59	463.22	1616.16	1847.66	-86.08	-135.49
BIE 86	19.41	24.56	1543	Z	0.00	4.13	4019.70	463.26	1615.12	1846.19	-85.94	-135.06
2831	21.98	24.56	1548		0.08	4.05	4024.46	463.28	1617.04	1849.89	-87.25	-136.54
DVR17	39.07	24.64	5645		10.29	17.32	4056.05	463.29	1392.72	1874.51	48.99	-127.70
BIE580	21.84	24.55	1548	Z	0.00	4.09	4024.20	463.29	1616.85	1849.69	-87.23	-136.56
BIE 58	21.84	24.55	1548	Z	0.00	4.09	4024.20	463.29	1616.82	1849.69	-87.26	-136.59
CSB032	14.14	24.49	2375	C	0.40	4.57	4009.96	463.32	1556.91	1838.62	-58.33	-135.25
2830	21.53	24.50	1549		0.07	3.92	4023.63	463.36	1615.99	1849.24	-87.55	-137.02
BIE 50	23.82	24.51	1542	Z	0.00	5.43	4027.85	463.37	1622.58	1852.53	-84.92	-132.70
BIE378	23.46	24.50	1536	Z	0.00	5.17	4027.19	463.38	1622.02	1852.02	-85.52	-133.36
UCR044	24.10	24.50	1695	M	0.46	5.07	4028.37	463.38	1614.29	1852.94	-79.22	-132.18
2948	13.28	24.44	2190		0.16	5.89	4008.37	463.39	1564.58	1837.38	-66.83	-136.30
CSC019	20.43	24.48	1547	C	0.00	3.82	4021.59	463.39	1615.52	1847.66	-86.63	-136.19
BIE 87	19.27	24.45	1542	Z	0.00	4.14	4019.44	463.42	1614.70	1845.99	-86.25	-135.32
CSC083	13.29	24.42	2190	C	0.06	5.81	4008.39	463.42	1565.29	1837.40	-66.13	-135.79
MIT066	23.85	24.47	1544	C	0.02	5.37	4027.91	463.43	1622.65	1852.58	-84.70	-132.60
BIE361	16.82	24.39	1967	Z	0.00	4.62	4014.91	463.49	1577.78	1842.47	-79.59	-142.85
UCR084	23.71	24.43	1545	C	0.15	5.25	4027.65	463.49	1622.86	1852.38	-84.20	-132.11
BIE 59	21.53	24.41	1544	Z	0.00	4.08	4023.62	463.50	1616.27	1849.24	-87.74	-136.94
CSB017	19.19	24.38	1548	C	0.01	4.02	4019.30	463.53	1613.88	1845.87	-86.39	-135.78
BIE303	20.94	24.37	1544	Z	0.00	3.98	4022.53	463.55	1615.59	1848.39	-87.57	-136.87
UCR045	23.95	24.38	1544	C	0.12	5.59	4028.10	463.56	1622.73	1852.72	-84.76	-132.34
2921	9.94	24.29	2495		0.55	7.25	4002.20	463.59	1541.48	1832.59	-56.44	-134.66
BIE 88	19.13	24.34	1543	Z	0.00	4.17	4019.19	463.59	1613.86	1845.79	-86.80	-135.88
BIE 49	23.91	24.36	1543	Z	0.00	5.76	4028.02	463.59	1622.58	1852.66	-84.96	-132.44

TABLE 1-A3 (cont.). Principal Facts, Gravity Stations in Northern Panamint Valley

STA	LAT	LON	ELEC	IZ	OZ	NORTH	EAST	OBS G	THEO G	FAA	CBA
2947	12.71	24.29	2239	0.12	5.52	4007.32	463.61	1559.13	1836.56	-66.85	-138.42
2842	25.57	24.35	1780	0.19	7.62	4031.09	463.62	1606.20	1855.06	-81.34	-134.97
CSC084	12.70	24.28	2235 C	0.05	5.52	4007.30	463.63	1560.49	1836.55	-65.85	-137.35
UCR048	23.37	24.32	1860 C	2.31	4.30	4027.02	463.65	1600.76	1851.89	-76.19	-133.74
UCR047	23.57	24.29	1744 C	1.53	4.62	4027.39	463.69	1609.46	1852.17	-78.59	-132.64
BIE338	21.84	24.28	1539 Z	0.00	4.23	4024.19	463.70	1616.95	1849.69	-87.98	-136.86
MIT065	24.06	24.28	1545 C	0.05	5.87	4028.30	463.71	1622.17	1852.88	-85.39	-132.79
BIE316	19.13	24.25	1548 Z	0.00	4.12	4019.18	463.72	1613.45	1845.79	-86.73	-136.03
2923	20.48	24.25	1541	0.09	3.83	4021.68	463.73	1614.62	1847.73	-88.17	-137.43
UCR083	23.73	24.27	1695 C	0.54	4.90	4027.69	463.73	1613.57	1852.40	-79.41	-132.45
BIE 60	21.23	24.25	1543 Z	0.00	4.00	4023.07	463.74	1615.83	1848.81	-87.85	-137.10
DVR19	34.87	24.31	4717	5.57	9.42	4048.29	463.75	1448.39	1868.45	23.49	-129.34
BIE 89	18.99	24.22	1543 Z	0.00	4.13	4018.93	463.76	1613.81	1845.59	-86.64	-135.76
BIE360	16.82	24.20	1953 Z	0.00	4.16	4014.91	463.78	1579.09	1842.47	-79.68	-142.89
UCR049	23.10	24.23	2030 B	4.70	4.27	4026.52	463.78	1589.09	1851.50	-71.48	-132.52
DVR18	36.34	24.29	4957	3.59	8.19	4051.00	463.79	1436.55	1870.57	32.09	-130.19
BIE 48	24.05	24.22	1547 Z	0.00	6.08	4028.28	463.80	1622.19	1852.87	-85.17	-132.48
UCR046	23.88	24.22	1779 C	1.95	4.91	4027.97	463.80	1608.47	1852.62	-76.73	-131.28
BIE320	20.04	24.18	1544 Z	0.00	3.92	4020.87	463.83	1614.44	1847.10	-87.43	-136.80
BIE 21	20.45	24.18	1541 Z	0.00	3.95	4021.62	463.83	1614.62	1847.69	-88.13	-137.36
UCR043	24.39	24.19	1570 M	0.10	6.49	4028.91	463.85	1620.47	1853.35	-85.22	-132.80
UCR082	23.69	24.19	1605 C	0.14	5.24	4027.61	463.85	1619.47	1852.35	-81.92	-131.92
CSB125	20.27	24.15	1541 C	0.00	3.82	4021.29	463.88	1614.15	1847.43	-88.34	-137.69
BIE 47	24.18	24.12	1553 Z	0.00	6.44	4028.52	463.95	1621.26	1853.05	-85.72	-132.88
CSB031	14.19	24.07	2350 C	0.27	3.93	4010.05	463.95	1558.22	1838.69	-59.45	-136.28
BIE 90	18.85	24.09	1544 Z	0.00	4.16	4018.68	463.96	1612.61	1845.40	-87.57	-136.69
BIE 61	20.94	24.10	1542 Z	0.00	4.02	4022.53	463.96	1615.12	1848.39	-88.24	-137.43
UCR050	22.79	24.10	1820 C	1.98	4.07	4025.95	463.97	1605.91	1851.05	-73.96	-130.70
CSC088	9.63	24.02	2345 C	1.18	7.73	4001.62	463.99	1552.87	1832.14	-58.72	-130.67
CSC020	20.46	24.05	1542 C	0.00	3.84	4021.64	464.03	1614.06	1847.70	-88.60	-137.97
UCR081	23.72	24.05	1670 C	0.30	5.21	4027.67	464.05	1613.98	1852.39	-81.33	-133.45
UCR051	21.94	24.03	1542 C	0.00	4.24	4024.38	464.07	1617.42	1849.83	-87.37	-136.34
BIE339	21.84	24.01	1542 Z	0.00	4.30	4024.19	464.10	1617.21	1849.69	-87.44	-136.35
MIT077	24.34	24.02	1605 C	0.11	6.57	4028.81	464.10	1617.91	1853.28	-84.41	-133.11
BIE 91	18.72	23.99	1546 Z	0.00	4.11	4018.42	464.11	1612.03	1845.20	-87.75	-137.00
MIT013	25.85	23.99	2070 C	1.20	8.41	4031.61	464.16	1589.38	1855.46	-71.38	-133.17
MIT015	27.13	24.00	2525 C	2.59	9.79	4033.97	464.16	1574.32	1857.30	-45.50	-120.17
BIE 62	20.63	23.95	1544 Z	0.00	3.97	4021.95	464.18	1614.30	1847.94	-88.42	-137.74
CSB018	18.66	23.94	1545 C	0.00	4.04	4018.31	464.18	1612.00	1845.11	-87.79	-137.07
UCR052	21.29	23.95	1542 C	0.00	4.01	4023.18	464.19	1615.44	1848.89	-88.42	-137.62
2843	25.87	23.96	2093	0.96	8.49	4031.65	464.20	1587.99	1855.49	-70.64	-133.38
BIE 46	24.04	23.95	1558 Z	0.00	6.43	4028.26	464.21	1620.82	1852.85	-85.49	-132.82
CSB124	20.00	23.93	1541 C	0.00	3.82	4020.79	464.21	1613.47	1847.04	-88.63	-137.99
A002	22.52	23.93	1548	0.00	3.00	4025.45	464.22	1620.94	1850.67	-84.15	-134.55
DVR71	11.80	23.88	2356	0.24	4.48	4005.63	464.22	1550.73	1835.26	-62.95	-139.69
UCR080	23.70	23.91	1555 C	0.21	5.82	4027.63	464.26	1620.97	1852.36	-85.13	-132.76
2920	9.79	23.83	2302	0.40	6.80	4001.92	464.28	1551.97	1832.37	-63.89	-136.07
BIE 92	18.58	23.87	1548 Z	0.00	4.15	4018.17	464.28	1611.56	1845.00	-87.83	-137.10
MIT078	24.47	23.90	1675 C	0.21	6.83	4029.05	464.28	1613.18	1853.47	-82.75	-133.50
CSB057	11.82	23.84	2355 B	0.23	4.58	4005.67	464.28	1550.48	1835.28	-63.31	-139.70
BIE 35	20.48	23.87	1562 Z	0.00	3.84	4021.68	464.30	1611.88	1847.73	-88.93	-138.99
BIE 14	20.48	23.87	1541 Z	0.00	3.99	4021.68	464.30	1613.97	1847.73	-88.82	-138.01
MIT014	26.47	23.87	2210 C	1.15	10.05	4032.75	464.34	1581.44	1856.35	-67.06	-132.07
CSB030	14.24	23.79	2307 C	0.19	3.69	4010.14	464.37	1560.11	1838.76	-61.67	-137.34
BIE193	18.45	23.76	1546 Z	0.00	4.12	4017.92	464.45	1610.94	1844.81	-88.46	-137.69
BIE 93	18.45	23.76	1550 Z	0.00	4.09	4017.92	464.45	1610.73	1844.81	-88.29	-137.69
MIT079	24.61	23.77	1779 C	0.31	7.09	4029.31	464.48	1607.29	1853.67	-78.96	-132.97
CSC085	11.06	23.70	2400 C	0.10	4.68	4004.26	464.48	1548.62	1834.19	-59.85	-137.82
BIE340	21.84	23.73	1531 Z	0.00	4.53	4024.19	464.52	1616.43	1849.69	-89.25	-137.56
BIE 15	20.19	23.72	1544 Z	0.00	3.92	4021.14	464.52	1613.47	1847.31	-88.62	-137.98

TABLE 1-A3 (cont.). Principal Facts, Gravity Stations in Northern Panamint Valley

STA	LAT	LON	EL	EC	IZ	OZ	NORTH	EAST	OBS G	THEO G	FAA	CBA
BIE315	19.13	23.71	1543	Z	0.00	3.98	4019.18	464.53	1611.88	1845.79	-88.77	-138.04
2950	14.63	23.68	2257		0.15	3.58	4010.87	464.54	1561.60	1839.32	-65.44	-139.54
UCR079	23.71	23.72	1550	C	0.04	6.18	4027.65	464.55	1619.39	1852.38	-87.20	-134.47
CSB123	19.71	23.70	1541	C	0.00	3.82	4020.25	464.55	1612.85	1846.62	-88.83	-138.19
BIE359	16.82	23.67	1818	Z	0.00	3.90	4014.91	464.57	1591.01	1842.47	-80.47	-139.29
BIE450	23.79	23.70	1555	Z	0.00	6.48	4027.80	464.58	1619.62	1852.49	-86.62	-133.80
BIE 45	23.79	23.70	1555	Z	0.00	6.48	4027.80	464.58	1619.62	1852.49	-86.62	-133.80
UCR001	23.86	23.67	1565	C	0.11	6.48	4027.92	464.62	1618.48	1852.59	-86.91	-134.32
BIE 99	18.31	23.64	1553	Z	0.00	4.10	4017.66	464.63	1610.73	1844.61	-87.80	-137.30
BIE 44	23.46	23.66	1557	Z	0.00	5.99	4027.18	464.63	1619.40	1852.02	-86.17	-133.91
BIE319	20.04	23.64	1544	Z	0.00	3.95	4020.86	464.64	1613.29	1847.10	-88.58	-137.92
BIE 29	20.50	23.62	1541	Z	0.00	4.00	4021.71	464.67	1613.36	1847.76	-89.46	-138.63
CSC021	20.50	23.62	1542	C	0.01	3.90	4021.71	464.67	1613.16	1847.76	-89.56	-138.86
BIE 43	23.13	23.62	1556	Z	0.00	5.54	4026.57	464.69	1618.74	1851.54	-86.45	-134.60
CSC096	22.98	23.60	1557	C	0.01	5.26	4026.30	464.72	1618.66	1851.33	-86.21	-134.67
CSB127	22.94	23.59	1555	C	0.01	5.23	4026.22	464.74	1618.30	1851.27	-86.71	-135.13
BIE 16	19.89	23.56	1544	Z	0.00	3.94	4020.59	464.76	1613.14	1846.88	-88.52	-137.86
BIE301	20.94	23.56	1547	Z	0.00	4.10	4022.53	464.77	1613.86	1848.39	-89.02	-138.31
BIE 42	22.81	23.57	1554	Z	0.00	5.21	4025.98	464.77	1618.19	1851.08	-86.73	-135.15
BIE100	18.18	23.52	1555	Z	0.00	4.06	4017.42	464.80	1609.94	1844.42	-88.23	-137.83
BIE 41	22.48	23.53	1555	Z	0.00	4.90	4025.37	464.82	1617.20	1850.61	-87.14	-135.91
CSC094	6.23	23.45	2540	C	1.88	7.76	3995.33	464.82	1538.52	1827.26	-49.85	-127.77
CSC086	10.08	23.46	2212	B	0.10	5.60	4002.45	464.83	1557.37	1832.79	-67.37	-137.96
CSB126	22.25	23.51	1556	C	0.00	4.67	4024.95	464.85	1615.98	1850.27	-87.94	-136.96
BIE 40	22.15	23.49	1559	Z	0.00	4.66	4024.76	464.88	1615.83	1850.13	-87.67	-136.81
CSB029	14.33	23.45	2200	C	0.62	3.56	4010.31	464.88	1565.11	1838.89	-66.86	-138.55
CSB122	19.42	23.47	1541	C	0.00	3.83	4019.71	464.89	1612.42	1846.20	-88.84	-138.19
MIT059	23.71	23.48	1570	C	0.06	6.52	4027.65	464.91	1617.65	1852.38	-87.06	-134.66
CSB120	18.83	23.44	1541	C	0.00	3.87	4018.62	464.93	1611.49	1845.36	-88.92	-138.23
2919	9.66	23.38	2143		0.13	6.20	4001.69	464.95	1560.80	1832.20	-69.84	-137.42
BIE 39	21.82	23.44	1562	Z	0.00	4.45	4024.15	464.95	1614.90	1849.66	-87.84	-137.29
CSB019	18.08	23.41	1558	C	0.01	3.97	4017.26	464.97	1609.34	1844.29	-88.41	-138.19
BIE101	18.05	23.40	1555	Z	0.00	4.08	4017.18	464.98	1609.52	1844.23	-88.45	-138.03
BIE388	23.79	23.43	1597	Z	0.00	6.69	4027.79	464.98	1616.27	1852.49	-86.01	-134.43
BIE 17	19.58	23.40	1544	Z	0.00	3.95	4020.03	464.99	1612.76	1846.45	-88.47	-137.80
BIE 38	21.49	23.40	1565	Z	0.00	4.29	4023.54	465.01	1613.75	1849.18	-88.23	-137.95
2942	2.66	23.30	2894		0.50	5.85	3988.74	465.02	1511.26	1822.14	-38.71	-132.09
2844	25.85	23.38	2518		3.32	9.53	4031.61	465.07	1560.80	1855.46	-57.84	-131.80
BIE 37	21.17	23.36	1570	Z	0.00	4.15	4022.95	465.07	1612.54	1848.72	-88.51	-138.54
UCR078	21.39	23.36	1568	C	0.02	4.21	4023.36	465.07	1613.25	1849.04	-88.31	-138.19
BIE 36	20.85	23.32	1571	Z	0.00	4.02	4022.36	465.12	1611.94	1848.26	-88.56	-138.75
2945	9.25	23.26	2026		0.17	7.09	4000.92	465.13	1568.36	1831.60	-72.68	-135.30
BIE102	17.92	23.28	1555	Z	0.00	4.06	4016.94	465.16	1608.58	1844.05	-89.21	-138.81
CSB121	19.18	23.28	1541	C	0.00	3.83	4019.27	465.17	1611.64	1845.86	-89.28	-138.63
2866	20.54	23.27	1566		0.03	3.94	4021.79	465.20	1611.29	1847.82	-89.23	-139.30
BIE 13	19.28	23.25	1541	Z	0.00	3.93	4019.45	465.22	1612.16	1846.00	-88.90	-138.15
BIE 30	20.53	23.25	1566	Z	0.00	3.97	4021.77	465.23	1611.44	1847.80	-89.07	-139.14
CSC008	20.51	23.25	1566	C	0.03	3.94	4021.73	465.23	1611.51	1847.77	-88.97	-139.04
CSC018	20.52	23.25	1566	B	0.03	3.94	4021.75	465.23	1611.54	1847.79	-88.95	-139.02
MIT060	23.70	23.25	1610	C	0.08	6.79	4027.63	465.25	1614.88	1852.36	-86.05	-134.73
BIE342	21.84	23.21	1578	Z	0.00	4.55	4024.19	465.30	1612.77	1849.69	-88.49	-138.39
BIE 12	19.13	23.17	1543	Z	0.00	3.95	4019.18	465.34	1611.83	1845.79	-88.83	-138.13
CSC087	8.79	23.11	1865	C	0.12	8.19	4000.06	465.35	1577.99	1830.94	-77.53	-133.56
BIE103	17.79	23.15	1556	Z	0.00	4.05	4016.70	465.36	1608.16	1843.86	-89.34	-138.99
BIE358	16.82	23.12	1714	Z	0.00	3.80	4014.91	465.39	1596.71	1842.47	-84.54	-139.88
BIE325	20.04	23.10	1559	Z	0.00	3.95	4020.86	465.45	1611.88	1847.10	-88.58	-138.43
BIE 11	18.96	23.09	1543	Z	0.00	3.95	4018.86	465.45	1611.44	1845.54	-88.98	-138.27
BIE302	20.94	23.09	1607	Z	0.00	4.02	4022.52	465.47	1609.94	1848.39	-87.30	-138.74
CSB119	19.01	23.07	1541	C	0.00	3.84	4018.95	465.48	1611.19	1845.62	-89.49	-138.82
B159	3.36	22.99	3053		0.00	7.09	3990.03	465.49	1502.32	1823.15	-33.71	-131.80
CSB117	18.89	23.06	1541	C	0.00	3.84	4018.73	465.50	1610.96	1845.44	-89.54	-138.88

TABLE 1-A3 (cont.). Principal Facts, Gravity Stations in Northern Panamint Valley

STA	LAT	LON	EL	EC	IZ	OZ	NORTH	EAST	OBS G	THEO G	FAA	CBA
BIE366	20.13	23.05	1562	Z	0.00	3.97	4021.03	465.52	1610.99	1847.23	-89.32	-139.25
CSB028	14.42	23.02	2080	C	0.67	3.43	4010.47	465.53	1571.76	1839.02	-71.63	-139.27
BIE104	17.66	23.03	1554	Z	0.00	4.06	4016.46	465.54	1608.27	1843.67	-89.24	-138.80
MIT061	23.69	23.04	1650	C	0.10	7.08	4027.61	465.56	1611.62	1852.35	-85.54	-135.29
BIE 10	18.66	22.93	1543	Z	0.00	3.95	4018.31	465.69	1611.00	1845.11	-88.98	-138.28
CSC093	6.30	22.87	2320	C	0.35	6.57	3995.46	465.69	1553.93	1827.36	-55.23	-128.31
CSB115	18.30	22.92	1541	B	0.00	3.86	4017.64	465.70	1609.77	1844.59	-89.88	-139.20
2931	18.28	22.91	1541		0.13	3.86	4017.61	465.72	1609.78	1844.57	-89.84	-139.03
BIE 98	17.52	22.90	1567	Z	0.00	3.97	4016.20	465.73	1607.33	1843.47	-88.76	-138.86
2040	8.48	22.84	1753		0.31	7.93	3999.49	465.75	1583.96	1830.49	-81.65	-133.89
BIE116	17.80	22.88	1544	Z	0.00	4.05	4016.72	465.76	1609.32	1843.88	-89.33	-138.56
2949	14.59	22.85	1984		0.06	3.47	4010.79	465.78	1576.08	1839.26	-76.58	-141.49
CSC089	8.48	22.82	1753	B	0.12	7.82	3999.49	465.78	1584.53	1830.49	-81.08	-133.62
CSB116	18.58	22.83	1541	C	0.00	3.85	4018.18	465.84	1610.25	1845.01	-89.82	-139.15
BIE326	20.04	22.83	1580	Z	0.00	3.94	4020.86	465.85	1610.47	1847.10	-88.02	-138.60
CSC022	20.56	22.83	1620	C	0.09	3.97	4021.82	465.85	1607.41	1847.85	-88.06	-139.90
MIT062	23.70	22.82	1695	C	0.19	7.47	4027.62	465.89	1608.22	1852.36	-84.72	-135.54
BIE 97	17.39	22.78	1582	Z	0.00	3.88	4015.96	465.91	1606.23	1843.29	-88.25	-138.96
BIE367	19.75	22.78	1557	Z	0.00	3.98	4020.32	465.92	1610.78	1846.68	-89.45	-139.20
BIE 9	18.34	22.77	1542	Z	0.00	3.97	4017.73	465.93	1610.18	1844.67	-89.45	-138.69
UCR002	23.84	22.78	1753	C	0.18	7.78	4027.88	465.95	1602.98	1852.56	-84.70	-137.22
DVR20	32.93	22.80	5887		15.92	26.97	4044.69	465.99	1360.47	1865.66	48.34	-126.96
BIE 31	20.56	22.73	1652	Z	0.00	3.98	4021.82	466.00	1606.01	1847.85	-86.46	-139.48
CSB020	17.33	22.71	1590	C	0.02	3.80	4015.86	466.01	1605.36	1843.21	-88.30	-139.35
UCR040	19.64	22.71	1558	C	0.00	3.93	4020.12	466.03	1610.56	1846.52	-89.42	-139.25
UCR031	22.24	22.70	1675	C	0.04	5.02	4024.93	466.06	1606.58	1850.26	-86.14	-138.87
CSB118	19.18	22.68	1541	C	0.00	3.91	4019.27	466.07	1611.04	1845.86	-89.88	-139.15
BIE 96	17.26	22.65	1590	Z	0.00	3.83	4015.72	466.10	1605.08	1843.10	-88.47	-139.51
CSB027	14.54	22.64	1958	C	0.06	3.39	4010.69	466.10	1577.41	1839.19	-77.62	-141.71
BIE312	19.13	22.63	1548	Z	0.00	4.00	4019.17	466.14	1611.04	1845.79	-89.15	-138.57
CSB114	18.33	22.62	1541	C	0.00	3.85	4017.71	466.15	1609.13	1844.65	-90.58	-139.91
BIE 8	18.06	22.60	1544	Z	0.00	3.98	4017.20	466.18	1608.76	1844.25	-90.27	-139.57
MIT063	23.70	22.61	1739	C	0.16	7.94	4027.62	466.21	1605.74	1852.36	-82.96	-134.90
BIE 95	17.13	22.53	1592	Z	0.00	3.82	4015.48	466.28	1604.50	1842.91	-88.67	-139.79
BIE368	19.36	22.46	1549	Z	0.00	4.09	4019.62	466.40	1610.73	1846.13	-89.70	-139.07
2941	2.72	22.37	2606		0.18	4.74	3988.84	466.42	1527.10	1822.23	-50.03	-134.95
BIE105	17.00	22.41	1595	Z	0.00	3.80	4015.24	466.46	1604.29	1842.73	-88.42	-139.65
CSC023	20.57	22.42	1720	C	0.10	3.94	4021.83	466.47	1601.52	1847.86	-84.56	-139.86
CSB113	18.05	22.38	1541	C	0.00	3.87	4017.18	466.51	1607.91	1844.23	-91.38	-140.69
MIT064	23.69	22.40	1790	C	0.20	8.44	4027.60	466.52	1602.49	1852.35	-81.50	-134.61
BIE177	17.80	22.35	1545	Z	0.00	3.97	4016.71	466.55	1607.90	1843.88	-90.66	-140.01
BIE 7	17.80	22.35	1547	Z	0.00	3.95	4016.71	466.55	1607.60	1843.88	-90.77	-140.20
UCR005	22.73	22.37	1705	C	0.05	6.11	4025.83	466.56	1604.68	1850.97	-85.92	-138.59
BIE106	16.86	22.29	1601	Z	0.00	3.77	4014.99	466.64	1601.94	1842.54	-90.02	-141.49
BIE369	18.98	22.28	1545	Z	0.00	4.07	4018.89	466.67	1610.10	1845.57	-90.15	-139.40
CSB026	14.63	22.26	1876	C	0.03	3.31	4010.85	466.67	1581.11	1839.32	-81.76	-143.14
UCR039	18.95	22.27	1552	C	0.00	3.96	4018.84	466.68	1609.88	1845.53	-89.67	-139.27
BIE 32	20.59	22.25	1761	Z	0.00	4.09	4021.87	466.72	1599.16	1847.89	-83.09	-139.76
BIE107	16.74	22.17	1606	Z	0.00	3.74	4014.75	466.82	1600.95	1842.35	-90.34	-142.02
CSB056	12.19	22.13	1944	C	0.05	3.52	4006.34	466.84	1573.09	1835.82	-79.79	-143.31
BIE 6	17.53	22.11	1553	Z	0.00	3.91	4016.21	466.91	1606.23	1843.49	-91.18	-140.86
2924	20.63	22.12	1780		0.09	4.02	4021.95	466.92	1597.77	1847.95	-82.66	-139.99
2918	7.70	22.06	1697		0.05	6.00	3998.04	466.92	1584.71	1829.37	-84.95	-137.49
BIE313	19.13	22.09	1571	Z	0.00	4.06	4019.17	466.95	1608.95	1845.79	-89.07	-139.22
CSB021	16.58	22.07	1608	C	0.02	3.69	4014.48	466.96	1599.69	1842.14	-91.21	-142.98
3137	13.07	22.04	1882		0.03	3.40	4007.97	466.98	1577.24	1837.08	-82.83	-144.32
BIE356	16.82	22.06	1597	Z	0.00	3.71	4014.90	466.98	1602.41	1842.47	-89.84	-141.24
BIE108	16.59	22.04	1608	Z	0.00	3.71	4014.49	467.01	1600.16	1842.15	-90.74	-142.52
BIE 94	16.55	22.03	1613	Z	0.00	3.70	4014.40	467.02	1599.85	1842.08	-90.51	-142.47
BIE370	18.58	22.03	1544	Z	0.00	4.11	4018.17	467.04	1608.95	1845.01	-90.83	-140.01

TABLE 1-A3 (cont.). Principal Facts, Gravity Stations in Northern Panamint Valley

STA	LAT	LON	EL	EC	IZ	OZ	NORTH	EAST	OBS G	THEO G	FAA	CBA
CSC092	6.49	21.94	1965	C	0.13	5.30	3995.80	467.09	1568.38	1827.63	-74.43	-136.79
CSC024	20.62	21.99	1825	C	0.22	4.01	4021.92	467.11	1595.23	1847.93	-81.05	-139.78
2013	2.75	21.89	2456		0.10	4.35	3988.89	467.14	1535.96	1822.27	-55.32	-135.55
UCR003	23.90	21.99	1960	C	1.56	10.79	4027.99	467.14	1588.54	1852.65	-79.76	-135.02
BIE 5	17.23	21.95	1561	Z	0.00	3.84	4015.66	467.15	1604.37	1843.06	-91.87	-141.89
BIE109	16.47	21.93	1611	Z	0.00	3.70	4014.25	467.17	1599.38	1841.96	-91.06	-142.95
BIE314	19.13	21.93	1584	Z	0.00	4.09	4019.17	467.19	1607.85	1845.79	-88.95	-139.52
DVR16	38.36	22.00	4394		7.24	13.33	4054.72	467.22	1472.58	1873.49	12.28	-125.58
CSC090	7.40	21.79	1730	C	0.08	5.42	3997.49	467.32	1581.44	1828.94	-84.79	-138.97
BIE110	16.33	21.81	1614	Z	0.00	3.67	4013.99	467.35	1598.49	1841.76	-91.46	-143.49
DVG 7	14.69	21.77	1781		0.03	3.27	4010.96	467.40	1585.24	1839.41	-86.66	-144.83
BIE 4	16.94	21.78	1574	Z	0.00	3.78	4015.12	467.40	1602.94	1842.64	-91.66	-142.19
BIE371	18.20	21.78	1557	Z	0.00	4.01	4017.45	467.41	1606.70	1844.45	-91.30	-141.02
CSB025	14.69	21.75	1780	B	0.06	3.29	4010.96	467.43	1585.12	1839.41	-86.78	-144.87
BIE 33	20.62	21.73	1890	Z	0.00	4.25	4021.92	467.50	1591.86	1847.93	-78.31	-139.26
UCR038	18.02	21.72	1570	C	0.01	3.90	4017.12	467.50	1606.00	1844.19	-90.52	-140.79
BIE111	16.20	21.70	1618	Z	0.00	3.65	4013.75	467.51	1597.34	1841.58	-92.05	-144.23
UCR032	22.31	21.71	1920	C	0.16	5.80	4025.05	467.54	1591.03	1850.36	-78.75	-139.02
BIE 3	16.64	21.61	1583	Z	0.00	3.74	4014.56	467.65	1601.13	1842.21	-92.18	-143.07
BIE112	16.06	21.58	1623	Z	0.00	3.62	4013.49	467.69	1596.87	1841.37	-91.85	-144.24
BIE372	17.81	21.55	1572	Z	0.00	3.92	4016.73	467.75	1604.77	1843.89	-91.26	-141.59
BIE350	16.82	21.54	1575	Z	0.00	3.78	4014.90	467.76	1601.78	1842.47	-92.55	-143.12
CSB038	16.80	21.54	1575	B	0.00	3.76	4014.86	467.76	1601.24	1842.44	-93.06	-143.65
2932	16.81	21.52	1575		0.02	3.72	4014.88	467.79	1601.36	1842.45	-92.95	-143.56
BIE 1	15.99	21.51	1630	Z	0.00	3.55	4013.36	467.80	1596.63	1841.27	-91.33	-144.02
BIE 2	16.33	21.50	1600	Z	0.00	3.67	4013.99	467.82	1599.27	1841.76	-92.00	-143.54
2039	7.01	21.44	1730		0.11	4.95	3996.77	467.84	1580.73	1828.38	-84.93	-139.56
UCR004	23.19	21.50	1920	C	0.89	9.65	4026.67	467.86	1589.66	1851.63	-81.38	-137.07
CSC025	20.65	21.49	1950	C	0.16	4.17	4021.98	467.86	1588.42	1847.97	-76.15	-139.08
CSC091	7.01	21.43	1730	B	0.08	4.93	3996.76	467.86	1581.32	1828.38	-84.34	-139.02
CSB022	15.93	21.46	1636	C	0.12	3.55	4013.25	467.87	1596.08	1841.19	-91.23	-144.01
CSB024	14.79	21.45	1738	C	0.06	3.29	4011.14	467.88	1588.50	1839.55	-87.49	-144.14
2940	2.93	21.26	2250		0.14	3.97	3989.22	468.08	1547.68	1822.53	-63.23	-136.71
BIE373	17.42	21.30	1579	Z	0.00	3.89	4016.01	468.12	1602.15	1843.33	-92.66	-143.26
2917	7.24	21.11	1623		0.11	4.71	3997.19	468.34	1586.32	1828.71	-89.74	-140.92
MIT034	19.51	21.16	1785	C	0.00	4.26	4019.87	468.35	1594.67	1846.34	-83.77	-141.10
2037	3.86	21.08	2072		0.13	4.09	3990.94	468.36	1557.42	1823.86	-71.56	-138.81
2944	6.14	21.08	1797		0.14	4.51	3995.16	468.38	1575.22	1827.13	-82.80	-140.18
DVR34	28.77	21.17	5712		3.79	12.21	4036.99	468.39	1383.51	1859.66	60.93	-123.16
CSB023	14.93	21.11	1700	M	0.15	3.33	4011.40	468.39	1591.77	1839.75	-88.08	-143.26
BIE 34	20.70	21.12	2081	Z	0.00	4.54	4022.07	468.41	1580.01	1848.05	-72.31	-139.55
2865	20.72	21.11	2081		0.25	4.30	4022.11	468.43	1580.02	1848.08	-72.33	-139.55
CSB055	12.23	21.06	1744	C	0.03	3.37	4006.41	468.45	1583.27	1835.87	-88.47	-145.28
BIE374	17.04	21.07	1583	Z	0.00	3.88	4015.30	468.46	1600.43	1842.78	-93.46	-144.21
CSC026	20.72	21.09	2105	C	0.28	4.28	4022.10	468.46	1580.06	1848.07	-70.03	-138.07
BIE351	16.82	21.00	1600	Z	0.00	3.79	4014.89	468.57	1599.64	1842.47	-92.33	-143.76
2943	4.76	20.87	1928		0.11	4.13	3992.60	468.68	1564.58	1825.15	-79.24	-141.50
CSB034	15.20	20.90	1670	C	0.01	3.41	4011.90	468.71	1595.01	1840.14	-88.06	-142.26
CSB035	15.55	20.86	1646	C	0.01	3.51	4012.55	468.77	1596.82	1840.64	-89.00	-142.28
2916	7.49	20.80	1538		0.09	4.52	3997.65	468.80	1590.91	1829.07	-93.49	-141.96
BIE375	16.68	20.78	1604	Z	0.00	3.84	4014.63	468.89	1598.70	1842.27	-92.70	-144.20
2939	3.10	20.72	2081		0.12	3.73	3989.53	468.90	1556.71	1822.77	-70.34	-138.26
CSC062	13.97	20.76	1735	C	0.03	3.18	4009.62	468.91	1589.84	1838.37	-85.34	-141.99
UCR033	22.47	20.76	2360	C	1.00	6.79	4025.34	468.96	1565.70	1850.59	-62.93	-136.51
2038	5.36	20.63	1843		0.08	4.03	3993.71	469.05	1570.38	1826.02	-82.29	-141.76
CSC027	20.76	20.59	2285	C	0.50	4.44	4022.18	469.21	1568.81	1848.13	-64.41	-138.26
MIT032	18.67	20.57	1855	C	1.29	4.14	4018.31	469.22	1594.09	1845.13	-76.56	-135.12
BIE362	15.92	20.55	1624	Z	0.00	4.02	4013.23	469.23	1600.16	1841.17	-88.26	-140.28
2933	15.89	20.51	1624		0.53	3.68	4013.18	469.29	1599.14	1841.13	-89.24	-141.07
2036	1.51	20.45	1947		0.08	3.89	3986.59	469.29	1564.53	1820.50	-72.84	-136.03
CSB036	15.88	20.51	1624	M	0.01	3.68	4013.16	469.29	1599.03	1841.12	-89.34	-141.68

TABLE 1-A3 (cont.). Principal Facts, Gravity Stations in Northern Panamint Valley

STA	LAT	LON	EL	EC	IZ	OZ	NORTH	EAST	OBS G	THEO G	FAA	CBA
UCR012	17.97	20.47	1779	C	0.09	4.02	4017.02	469.37	1589.24	1844.12	-87.46	-144.76
BIE352	16.82	20.46	1639	Z	0.00	3.94	4014.89	469.38	1597.34	1842.47	-90.96	-143.58
UCR034	22.69	20.48	2845	C	2.21	6.60	4025.74	469.38	1539.03	1850.91	-44.31	-133.55
CSC061	13.31	20.43	1720	C	0.02	3.17	4008.40	469.40	1592.07	1837.42	-83.58	-139.73
2915	7.76	20.39	1448		0.10	4.32	3998.15	469.42	1595.30	1829.46	-97.96	-143.52
BIE376	16.34	20.41	1625	Z	0.00	4.09	4014.02	469.45	1597.81	1841.79	-91.14	-143.12
2035	0.77	20.33	1855		0.24	4.14	3985.22	469.47	1568.62	1819.44	-76.34	-135.96
CSB037	16.15	20.20	1651	C	0.01	3.76	4013.65	469.76	1597.28	1841.50	-88.94	-142.13
2716	33.32	20.23	2558		3.24	8.12	4045.40	469.83	1582.06	1866.22	-43.58	-120.40
CSC028	20.91	20.16	2450	C	0.54	4.64	4022.45	469.85	1558.67	1848.35	-59.25	-138.54
CSC060	12.24	20.10	1600	C	0.01	3.42	4006.42	469.87	1593.88	1835.89	-91.51	-143.29
CSB054	12.20	20.08	1602	C	0.02	3.41	4006.35	469.90	1593.49	1835.83	-91.66	-143.51
2914	8.04	20.05	1380		0.04	4.21	3998.66	469.93	1598.78	1829.86	-101.28	-144.66
2925	20.95	20.08	2464		0.17	4.73	4022.53	469.97	1556.96	1848.41	-59.70	-139.75
BIE377	16.04	20.06	1640	Z	0.00	4.30	4013.45	469.97	1597.50	1841.35	-89.59	-141.88
UCR035	22.87	20.05	3120	C	1.16	6.82	4026.07	470.03	1525.37	1851.17	-32.38	-131.89
BIE363	15.63	20.00	1672	Z	0.00	4.30	4012.69	470.06	1597.44	1840.76	-86.06	-139.45
2934	15.62	19.99	1672		0.51	3.64	4012.67	470.07	1597.17	1840.74	-86.31	-139.85
CSC044	15.62	19.99	1672	B	0.02	3.64	4012.67	470.07	1597.48	1840.74	-86.00	-140.03
MIT033	19.69	20.00	2310	C	0.06	4.55	4020.19	470.08	1564.63	1846.59	-64.70	-139.74
DVR33	30.92	20.02	5160		6.91	14.90	4040.96	470.12	1418.50	1862.76	40.94	-121.58
CSC059	12.00	19.93	1585	C	0.01	3.41	4005.98	470.14	1594.76	1835.54	-91.70	-142.98
BIE353	16.82	19.92	1711	Z	0.00	4.06	4014.89	470.18	1592.79	1842.47	-88.75	-143.72
2012	3.26	19.78	1837		0.08	3.45	3989.82	470.31	1570.76	1823.00	-79.46	-139.31
DVR15	39.88	19.87	3015		7.11	12.37	4057.52	470.40	1560.43	1875.68	-31.71	-123.22
2913	8.29	19.73	1332		0.11	4.12	3999.12	470.41	1602.11	1830.22	-102.82	-144.57
CSC029	20.92	19.78	2620	C	0.32	4.70	4022.47	470.42	1547.53	1848.36	-54.42	-139.72
CSC095	8.28	19.67	1330	C	0.01	4.09	3999.10	470.50	1602.38	1830.20	-102.72	-144.53
CSB089	12.87	19.61	1595	C	0.02	3.45	4007.59	470.61	1600.06	1836.79	-86.71	-138.28
UCR011	18.09	19.58	2085	C	0.20	4.29	4017.25	470.70	1570.67	1844.31	-77.53	-144.95
CSC058	11.41	19.54	1515	M	0.02	3.52	4004.89	470.72	1596.93	1834.70	-95.27	-144.01
CSC030	20.88	19.57	2710	C	0.29	4.74	4022.39	470.73	1543.72	1848.30	-49.71	-138.09
2912	8.63	19.49	1294		0.34	4.10	3999.75	470.78	1605.04	1830.71	-103.95	-144.18
UCR036	23.07	19.48	3200	C	1.35	7.97	4026.44	470.88	1520.60	1851.46	-29.91	-130.83
BIE354	16.82	19.38	1815	Z	0.00	4.25	4014.89	470.99	1587.09	1842.47	-84.57	-142.97
2911	8.99	19.24	1282		0.17	4.02	4000.41	471.15	1606.65	1831.22	-103.99	-144.05
MIT058	27.17	19.28	6927	M	6.18	19.97	4034.02	471.21	1297.08	1857.36	90.99	-120.64
MIT057	26.28	19.26	7276	M	6.31	23.83	4032.37	471.23	1265.71	1856.08	93.70	-125.84
CSC045	15.46	19.17	1844	C	0.09	3.52	4012.37	471.30	1587.35	1840.51	-79.63	-139.67
2926	20.81	19.13	2952		0.30	4.80	4022.26	471.39	1527.20	1848.21	-43.37	-140.00
BIE 74	20.79	19.10	2952	Z	0.00	5.09	4022.22	471.42	1527.80	1848.18	-42.75	-139.39
CSC007	20.81	19.10	2952	B	0.36	4.82	4022.26	471.42	1528.20	1848.20	-42.37	-138.92
DVR31	25.21	19.07	7287		10.29	32.48	4030.40	471.51	1259.14	1854.54	89.70	-127.86
2910	9.37	19.00	1284		0.24	3.94	4001.12	471.52	1607.11	1831.77	-103.88	-144.03
MIT056	25.19	19.04	7282	B	7.20	27.14	4030.36	471.55	1259.08	1854.51	89.20	-126.34
UCR007	20.02	18.92	2905	C	0.51	4.90	4020.80	471.70	1526.31	1847.07	-47.55	-142.25
BIE355	16.82	18.83	1971	Z	0.00	4.65	4014.88	471.80	1578.77	1842.47	-78.31	-141.65
2938	3.50	18.77	1580		0.10	3.40	3990.26	471.83	1588.24	1823.35	-86.49	-137.52
2909	9.70	18.77	1291		0.08	3.90	4001.72	471.86	1607.66	1832.24	-103.15	-143.73
UCR010	18.70	18.79	2610	C	0.40	4.95	4018.36	471.89	1544.87	1845.17	-54.83	-139.45
CSC063	20.58	18.78	3080	C	0.38	4.94	4021.83	471.91	1512.20	1847.87	-46.01	-146.81
CSC057	10.85	18.61	1415	C	0.02	3.68	4003.85	472.09	1602.39	1833.89	-98.41	-143.55
2908	10.04	18.55	1315		0.04	3.84	4002.35	472.19	1606.55	1832.73	-102.49	-144.00
UCR009	19.16	18.57	2880	C	0.62	5.17	4019.21	472.22	1528.48	1845.83	-46.49	-139.95
2935	15.41	18.53	2002		0.21	3.60	4012.28	472.26	1576.03	1840.44	-76.02	-141.30
CSB088	13.22	18.52	1779	C	0.04	3.28	4008.23	472.26	1590.79	1837.29	-79.09	-137.18
CSC046	15.41	18.53	2002	B	0.09	3.60	4012.28	472.26	1576.64	1840.44	-75.41	-140.81
BIE364	15.40	18.52	2004	Z	0.00	3.80	4012.26	472.27	1576.68	1840.43	-75.26	-140.59
2715	35.84	18.50	1643		3.32	6.68	4050.05	472.42	1646.63	1869.85	-68.68	-115.38
2907	10.39	18.32	1341		0.02	3.83	4003.00	472.54	1605.69	1833.23	-101.41	-143.85

TABLE 1-A3 (cont.). Principal Facts, Gravity Stations in Northern Panamint Valley

STA	LAT	LON	EL	EC	IZ	OZ	NORTH	EAST	OBS G	THEO G	FAA	CBA
2906	10.64	18.17	1377		0.01	3.80	4003.46	472.77	1604.03	1833.59	-100.04	-143.76
UCR076	25.15	18.13	6625	M	4.12	16.33	4030.28	472.91	1311.53	1854.45	79.97	-127.06
2927	20.99	18.08	3518		0.22	5.34	4022.59	472.95	1492.69	1848.46	-24.93	-140.53
2009	9.95	18.02	1286		0.02	3.93	4002.18	472.99	1608.67	1832.60	-102.97	-143.41
CSC064	20.99	18.06	3540	C	0.37	5.35	4022.59	472.99	1486.43	1848.46	-29.12	-145.32
CSB085	9.95	17.99	1291	B	0.01	3.92	4002.18	473.03	1607.72	1832.60	-103.45	-144.08
CSC056	9.95	17.99	1286	B	0.01	3.93	4002.18	473.03	1608.86	1832.60	-102.78	-143.23
2011	3.70	17.95	1386		0.07	3.52	3990.63	473.06	1599.56	1823.64	-93.71	-137.95
UCR008	19.58	18.00	3530	C	1.69	5.61	4020.00	473.07	1488.16	1846.45	-26.31	-140.59
2905	10.94	17.92	1452		0.04	3.72	4004.01	473.14	1600.95	1834.02	-96.49	-142.85
CSB084	9.19	17.82	1215	C	0.01	4.02	4000.77	473.28	1612.00	1831.51	-105.23	-143.14
CSC055	10.84	17.77	1436	M	0.04	3.78	4003.82	473.37	1601.54	1833.88	-97.27	-143.01
CSC047	15.27	17.76	2140	C	0.10	3.86	4012.01	473.41	1568.84	1840.24	-70.12	-139.97
2714	37.37	17.83	1292		0.69	5.66	4052.87	473.43	1673.57	1872.06	-76.96	-115.21
2904	11.39	17.63	1564		0.04	3.67	4004.84	473.58	1597.02	1834.67	-90.54	-140.80
UCR075	24.73	17.65	6226	M	3.86	13.15	4029.50	473.63	1333.04	1853.84	64.58	-132.26
UCR006	20.69	17.58	3970	C	0.85	5.73	4022.03	473.69	1464.57	1848.03	-10.12	-140.21
CSB083	7.49	17.51	1130	C	0.00	4.10	3997.63	473.74	1615.97	1829.07	-106.81	-141.73
CSB087	13.53	17.52	2020	C	0.05	3.38	4008.80	473.76	1577.04	1837.74	-70.71	-136.96
DVR32	27.03	17.48	5681		6.63	15.11	4033.76	473.89	1380.92	1857.16	57.93	-122.19
UCR077	26.05	17.43	5869	M	2.40	9.90	4031.94	473.96	1367.65	1855.74	63.74	-125.62
CSC065	21.59	17.40	3858	B	4.76	5.97	4023.70	473.98	1475.72	1849.33	-10.80	-132.90
2864	21.58	17.39	3863		1.35	5.97	4023.68	474.00	1474.08	1849.31	-11.95	-137.63
BIE 75	21.57	17.38	3863	Z	0.00	7.32	4023.66	474.01	1474.70	1849.30	-11.31	-136.99
2903	11.66	17.33	1684		0.08	3.62	4005.34	474.03	1592.78	1835.06	-83.88	-138.29
DVG 6	6.67	17.22	1096		0.00	4.15	3996.12	474.17	1616.46	1827.89	-108.35	-142.03
CSB082	6.67	17.22	1096	M	0.00	4.17	3996.11	474.17	1617.43	1827.89	-107.37	-141.04
DVG64	18.48	17.22	3933		5.32	10.47	4017.95	474.23	1462.90	1844.86	-12.10	-137.02
2045	6.25	17.15	1095		0.33	4.16	3995.34	474.27	1616.19	1827.29	-108.11	-141.42
2937	3.77	17.08	1211		0.07	3.78	3990.75	474.36	1608.77	1823.74	-101.05	-139.01
CSB080	5.04	17.08	1120	C	0.01	4.04	3993.10	474.37	1613.71	1825.56	-106.50	-141.11
DVG 2	15.01	17.10	2326		0.29	4.15	4011.53	474.39	1557.41	1839.87	-63.70	-139.74
BIE365	15.01	17.08	2326	Z	0.00	4.00	4011.53	474.41	1557.60	1839.87	-63.50	-139.70
CSC048	15.02	17.08	2325	B	0.15	3.90	4011.55	474.41	1557.99	1839.88	-63.22	-139.34
DVG 3	11.93	17.06	1767		0.26	3.91	4005.84	474.44	1589.00	1835.44	-80.25	-137.30
2902	11.96	17.05	1787		0.09	3.64	4005.89	474.45	1588.24	1835.49	-79.17	-137.09
CSC054	11.92	17.05	1765	C	0.07	3.66	4005.82	474.45	1589.17	1835.43	-80.25	-137.41
CSB068	9.38	17.03	1204	C	0.01	4.26	4001.12	474.47	1613.13	1831.78	-105.40	-142.69
CSC066	22.50	17.08	4525	C	4.83	5.95	4025.38	474.47	1438.58	1850.64	13.45	-131.45
CSB079	3.84	16.85	1170	C	0.00	3.88	3990.88	474.69	1610.82	1823.83	-102.96	-139.48
BIE 76	23.02	16.91	4754	Z	0.00	6.61	4026.34	474.72	1426.27	1851.38	21.92	-134.99
CSC006	23.04	16.91	4754	B	0.58	6.02	4026.37	474.72	1427.69	1851.41	23.31	-133.62
2046	2.06	16.83	1303		0.10	3.50	3987.59	474.73	1603.58	1821.28	-95.14	-136.52
2863	23.05	16.90	4754		0.63	6.02	4026.40	474.74	1425.75	1851.43	21.35	-135.52
CSB081	5.79	16.83	1084	C	0.00	4.19	3994.48	474.75	1616.23	1826.63	-108.43	-141.67
CSB086	14.12	16.80	2250	C	0.28	3.65	4009.88	474.84	1562.42	1838.59	-64.55	-138.21
2713	38.69	16.79	848		1.09	5.54	4055.31	474.99	1702.18	1873.96	-91.92	-114.62
CSC067	24.06	16.71	4950	C	0.87	5.84	4028.26	475.03	1418.18	1852.88	30.76	-132.77
4022	30.29	16.55	2651		0.00	4.80	4039.78	475.30	1581.86	1861.85	-30.68	-117.25
2010	3.95	16.39	1102		0.39	4.11	3991.08	475.40	1615.99	1823.99	-104.34	-137.89
BIE 77	24.83	16.44	4724	Z	0.00	7.74	4029.68	475.44	1433.95	1853.99	24.18	-130.58
CSC053	12.58	16.27	1975	C	0.26	3.96	4007.03	475.62	1578.84	1836.38	-71.77	-135.68
2901	12.65	16.19	1991		0.08	4.02	4007.17	475.74	1576.84	1836.48	-72.28	-136.89
CSB069	8.91	16.09	1145	C	0.01	4.75	4000.25	475.86	1615.37	1831.11	-108.04	-142.81
CSC049	14.72	16.11	2460	C	0.17	4.25	4010.99	475.86	1548.20	1839.45	-59.88	-140.27
2900	13.01	15.85	2120		0.31	4.19	4007.83	476.26	1568.92	1836.99	-68.68	-137.29
2712	37.91	15.83	518		0.58	5.80	4053.86	476.41	1722.00	1872.84	-102.11	-113.63
CSC052	13.28	15.41	2235	C	0.09	4.58	4008.33	476.92	1562.06	1837.38	-65.11	-137.51
2899	13.33	15.40	2225		0.30	4.65	4008.42	476.93	1561.65	1837.45	-66.54	-138.32
2111	4.14	15.28	1043		0.89	4.71	3991.43	477.07	1618.31	1824.27	-107.85	-138.26
CSC050	14.36	15.23	2525	B	0.10	4.84	4010.32	477.19	1543.22	1838.93	-58.24	-140.34

TABLE 1-A3 (cont.). Principal Facts, Gravity Stations in Northern Panamint Valley

STA	LAT	LON	EL	EC	IZ	OZ	NORTH	EAST	OBS G	THEO G	FAA	CBA
2004	1.67	15.07	1097		0.32	4.44	3986.86	477.37	1615.56	1820.73	-101.98	-135.09
3119	13.76	15.10	2398		0.08	4.97	4009.21	477.38	1551.40	1838.07	-61.14	-138.77
2898	12.95	15.08	2150		0.13	5.14	4007.72	477.41	1565.03	1836.91	-69.66	-138.54
CSB070	8.90	15.02	1109	C	0.02	5.85	4000.23	477.48	1617.57	1831.09	-109.21	-141.63
BIE 78	26.05	15.04	4031	Z	0.00	6.11	4031.93	477.53	1482.44	1855.74	5.76	-126.88
CSC005	26.08	15.04	4029	B	0.45	5.66	4031.99	477.53	1483.67	1855.79	6.85	-125.75
2861	26.06	15.02	4031		0.35	5.71	4031.95	477.56	1482.20	1855.76	5.51	-127.18
2711	36.71	15.05	237		0.40	6.35	4051.64	477.57	1737.03	1871.11	-111.78	-113.23
CSC051	13.91	14.93	2492	B	0.17	5.13	4009.49	477.64	1544.86	1838.29	-59.05	-139.67
3121	14.24	14.75	2607		0.12	5.43	4010.10	477.91	1537.74	1838.76	-55.83	-140.15
2047	1.97	14.65	1043		0.75	4.98	3987.42	478.00	1618.76	1821.16	-104.29	-134.57
CSB071	8.91	14.66	1100	B	0.04	6.41	4000.24	478.02	1618.11	1831.11	-109.53	-141.06
2008	8.91	14.65	1099		0.41	6.43	4000.25	478.03	1617.86	1831.11	-109.87	-140.98
2115	11.48	14.51	1985		0.12	5.53	4005.00	478.26	1574.48	1834.80	-73.52	-136.37
3123	14.65	14.33	2819		0.29	6.12	4010.86	478.54	1524.30	1839.35	-49.93	-140.67
2860	27.67	14.21	3106		1.01	5.60	4034.93	478.78	1547.73	1858.08	-18.25	-119.65
CSC004	27.67	14.21	3109	B	0.30	5.15	4034.92	478.78	1548.39	1858.08	-17.30	-118.97
BIE 79	27.67	14.20	3109	Z	0.00	5.48	4034.92	478.79	1548.15	1858.08	-17.54	-119.18
4023	31.94	14.20	1390		0.00	3.60	4042.82	478.81	1665.63	1864.23	-67.87	-112.23
CSB072	8.69	14.01	1091	M	0.02	7.49	3999.83	478.99	1617.62	1830.79	-110.55	-140.71
2968	8.66	13.97	1091		0.39	7.55	3999.78	479.05	1617.50	1830.75	-110.63	-140.36
2117	14.90	13.97	3013		0.80	6.58	4011.32	479.08	1512.19	1839.71	-44.16	-140.60
2969	9.04	13.94	1175		0.03	7.49	4000.48	479.10	1615.43	1831.30	-105.34	-138.39
2970	9.44	13.85	1319		0.15	7.42	4001.22	479.24	1609.18	1831.87	-98.62	-136.58
2971	9.86	13.79	1503		0.19	7.32	4002.00	479.33	1598.98	1832.47	-92.12	-136.48
2859	29.07	13.80	2459		0.27	4.86	4037.51	479.40	1593.63	1860.10	-35.20	-115.11
CSC003	29.08	13.79	2459	B	0.19	4.86	4037.53	479.41	1593.65	1860.11	-35.19	-114.92
2972	10.27	13.64	1700		0.22	7.41	4002.76	479.55	1589.15	1833.06	-84.01	-135.04
CSB076	5.44	13.59	1090	C	0.02	6.85	3993.83	479.61	1619.39	1826.13	-104.21	-134.98
DVG 4	6.38	13.58	1082		0.17	7.79	3995.57	479.63	1621.44	1827.48	-104.27	-133.83
CSB075	6.38	13.57	1078	B	0.02	7.46	3995.56	479.64	1621.54	1827.48	-104.54	-134.28
2007	6.40	13.55	1080		0.45	7.51	3995.60	479.67	1621.09	1827.51	-104.83	-134.16
DVG65	23.02	13.55	7510		4.00	21.40	4026.33	479.74	1247.45	1851.38	102.12	-134.12
2005	2.81	13.48	1061		0.48	6.54	3988.97	479.76	1619.67	1822.36	-102.89	-132.50
CSC002	29.70	13.53	2190	C	0.14	4.90	4038.67	479.80	1611.85	1861.00	-43.18	-113.66
2974	10.90	13.40	1995		0.20	7.79	4003.92	479.92	1573.66	1833.96	-72.66	-133.48
2973	10.61	13.37	1903		0.27	7.92	4003.38	479.96	1578.35	1833.55	-76.11	-133.61
CSB078	4.07	13.33	1064	M	0.02	6.94	3991.29	479.99	1622.08	1824.16	-102.00	-131.78
2112	4.07	13.31	1064		0.52	7.00	3991.29	480.02	1622.10	1824.17	-101.98	-131.20
2121	30.47	13.37	1925		0.09	4.89	4040.10	480.05	1631.20	1862.11	-49.85	-111.28
2120	29.30	13.31	2377		0.43	5.04	4037.94	480.13	1599.83	1860.43	-37.04	-113.95
UCR068	29.31	13.31	2380	B	0.07	4.85	4037.95	480.13	1599.78	1860.44	-36.82	-113.96
CSB077	4.63	13.23	1082	B	0.00	7.32	3992.33	480.15	1619.75	1824.97	-103.44	-133.48
2006	4.63	13.22	1082		0.45	7.35	3992.33	480.16	1619.40	1824.97	-103.79	-133.35
CSB073	8.02	13.17	1050	C	0.01	9.99	3998.59	480.25	1616.31	1829.83	-114.75	-141.01
2961	4.89	13.15	1098		0.37	7.59	3992.81	480.27	1617.75	1825.34	-104.31	-134.26
2122	31.61	13.10	1539		0.08	5.04	4042.21	480.45	1660.56	1863.75	-58.44	-106.43
DVR87	19.34	13.03	6268		2.80	11.41	4019.52	480.51	1329.14	1846.09	72.39	-131.49
2284	36.67	13.01	107		0.04	4.80	4051.56	480.61	1739.05	1871.05	-121.84	-120.74
CSB074	7.40	12.86	1050	C	1.08	11.73	3997.45	480.71	1617.36	1828.94	-112.82	-136.26
UCR069	28.55	12.70	2720	C	1.00	5.08	4036.54	481.04	1577.84	1859.34	-25.69	-113.36
2113	4.67	12.62	1115		0.26	9.24	3992.40	481.06	1616.60	1825.03	-103.54	-132.54
2963	5.51	12.56	1298		0.11	9.29	3993.95	481.15	1606.25	1826.23	-97.89	-133.29
2123	32.57	12.62	1181		0.10	5.54	4043.98	481.17	1688.20	1865.14	-65.85	-100.98
CSB112	27.58	12.46	3110	C	1.09	5.53	4034.75	481.39	1550.27	1857.95	-15.19	-115.72
2694	40.04	12.35	76		0.02	3.74	4057.79	481.61	1729.82	1875.91	-138.94	-137.82
2964	5.84	12.26	1501		0.31	10.28	3994.56	481.61	1594.14	1826.70	-91.38	-132.59
2693	39.62	12.31	79		0.02	3.74	4057.01	481.66	1731.48	1875.31	-136.39	-135.37
2692	39.17	12.26	78		0.02	3.78	4056.18	481.74	1733.45	1874.66	-133.86	-132.77
2691	38.71	12.20	67		0.03	3.87	4055.33	481.82	1735.97	1873.99	-131.72	-130.14

TABLE 1-A3 (cont.). Principal Facts, Gravity Stations in Northern Panamint Valley

STA	LAT	LON	EL	EC	IZ	OZ	NORTH	EAST	OBS G	THEO G	FAA	CBA
2690	38.26	12.10	50		0.09	3.98	4054.50	481.97	1738.14	1873.34	-130.50	-128.16
2118	27.03	12.05	3370		2.34	7.03	4033.73	482.00	1531.93	1857.16	-8.30	-117.34
CSB104	27.05	12.02	3370	C	1.03	5.87	4033.77	482.05	1531.70	1857.18	-8.55	-117.73
2965	6.13	11.96	1724		0.80	11.45	3995.10	482.06	1581.58	1827.12	-83.39	-130.62
2689	37.84	11.99	36		0.11	4.11	4053.72	482.13	1739.41	1872.74	-129.93	-126.97
2688	37.46	11.95	35		0.08	4.24	4053.02	482.19	1740.41	1872.19	-128.48	-125.38
2119	26.64	11.89	3529		2.50	7.32	4033.01	482.24	1520.33	1856.60	-4.39	-118.60
2124	33.94	11.78	634		0.17	6.07	4046.51	482.43	1725.13	1867.11	-82.34	-98.01
2687	37.12	11.75	29		0.10	4.36	4052.39	482.49	1741.37	1871.70	-127.60	-124.15
UCR070	26.10	11.64	3759	C	1.92	6.46	4032.01	482.61	1504.11	1855.82	1.88	-119.20
2746	17.55	11.58	4583		1.03	5.26	4016.21	482.67	1431.43	1843.52	18.87	-133.53
2966	6.32	11.51	1966		1.86	13.33	3995.45	482.73	1565.49	1827.39	-76.99	-129.61
2748	15.93	11.50	4002		5.41	10.60	4013.21	482.78	1458.53	1841.19	-6.32	-133.47
CSB053	25.46	11.38	4060	C	1.20	6.32	4030.83	483.00	1481.84	1854.90	8.74	-123.49
CSB039	15.98	11.30	4130	C	1.42	6.29	4013.30	483.08	1456.20	1841.26	3.32	-131.12
2686	36.89	11.30	18		0.04	4.44	4051.96	483.16	1742.43	1871.37	-127.24	-123.39
2473	16.75	11.15	4460		0.38	4.79	4014.73	483.31	1439.13	1842.37	16.16	-132.50
CSB046	17.29	11.10	4650	M	0.09	4.48	4015.72	483.39	1428.04	1843.14	22.15	-133.24
2967	6.55	11.02	2269		2.58	14.98	3995.87	483.47	1546.07	1827.72	-68.25	-128.93
2745	18.86	10.94	5018		0.52	4.84	4018.63	483.63	1407.23	1845.40	33.68	-134.04
2283	36.73	10.88	6		0.02	4.54	4051.66	483.78	1743.85	1871.14	-126.62	-122.31
DVG 5	6.72	10.54	2595		11.00	23.10	3996.18	484.19	1519.97	1827.97	-63.94	-130.29
UCR074	24.61	10.49	4510	C	0.48	5.32	4029.25	484.33	1456.18	1853.67	26.60	-122.77
2741	24.61	10.42	4514		1.42	5.97	4029.26	484.43	1455.53	1853.67	26.33	-123.00
CSB045	15.69	10.36	4480	C	0.23	6.21	4012.76	484.49	1436.04	1840.84	16.47	-131.23
2125	35.05	10.36	194		0.07	6.50	4048.56	484.55	1752.12	1868.71	-98.34	-98.49
2744	19.62	10.01	5199		0.35	4.76	4020.03	485.03	1400.33	1846.49	42.70	-131.29
2472	18.10	9.99	4927		0.45	4.86	4017.22	485.05	1413.33	1844.31	32.32	-132.27
DVR86	28.40	9.74	4005		2.72	7.83	4036.26	485.46	1509.65	1859.13	27.14	-102.88
2285	36.23	9.74	-3		0.02	5.13	4050.74	485.48	1752.37	1870.42	-118.33	-113.08
CSB044	15.24	9.58	4820	C	0.29	6.90	4011.93	485.66	1416.90	1840.20	29.94	-128.66
CSB052	23.77	9.54	4787	C	0.94	4.81	4027.70	485.74	1437.66	1852.46	35.33	-123.57
CSB047	17.36	9.52	5235	C	0.57	5.32	4015.86	485.75	1395.19	1843.26	44.18	-129.92
2749	18.83	9.27	5387		0.38	5.19	4018.57	486.13	1388.13	1845.36	49.31	-130.69
2469	23.14	8.99	4863		0.52	4.84	4026.54	486.56	1434.13	1851.56	39.85	-122.56
UCR073	23.13	8.97	4865	C	0.17	4.60	4026.51	486.59	1434.14	1851.54	40.07	-122.49
CSB048	18.45	8.83	5220	C	0.37	5.27	4017.86	486.79	1397.48	1844.81	43.51	-130.32
CSB043	14.96	8.74	5135	C	0.52	7.81	4011.41	486.91	1393.86	1839.79	36.91	-131.32
2717	36.05	8.77	114		0.08	5.24	4050.40	486.93	1751.46	1870.16	-107.97	-106.60
2126	36.37	8.75	5		0.02	5.05	4050.99	486.96	1753.38	1870.62	-116.76	-111.87
2718	35.63	8.72	297		0.13	5.63	4049.62	487.00	1746.22	1869.55	-95.39	-99.90
2719	35.19	8.71	494		0.16	6.33	4048.81	487.01	1737.74	1868.92	-84.70	-95.28
2720	34.79	8.63	693		0.31	7.44	4048.07	487.13	1728.16	1868.34	-74.99	-91.18
2721	34.40	8.62	886		0.97	8.95	4047.35	487.15	1717.86	1867.78	-66.58	-87.25
TRC23	12.38	8.58	7117		14.70	30.07	4006.64	487.15	1262.32	1836.09	95.36	-118.82
UCR071	20.05	8.59	5310	C	0.13	4.88	4020.82	487.15	1397.13	1847.11	49.32	-128.23
2722	34.21	8.54	980		3.11	10.04	4047.00	487.26	1711.15	1867.50	-64.17	-84.86
CSB049	20.09	8.48	5314	B	0.18	4.90	4020.91	487.32	1396.94	1847.18	49.43	-128.18
2471	20.10	8.45	5318		0.39	5.11	4020.91	487.36	1397.03	1847.18	49.90	-127.82
CSB106	26.09	8.23	5680	C	0.12	8.01	4031.98	487.71	1398.28	1855.80	76.55	-110.52
4059	26.78	8.14	5834		4.87	14.29	4033.26	487.84	1388.73	1856.80	80.48	-105.69
UCR072	21.09	8.02	5035	C	0.02	4.65	4022.74	488.01	1418.62	1848.61	43.46	-125.02
2894	2.02	7.97	4518		3.39	13.66	3987.49	488.03	1416.82	1821.23	20.44	-117.95
2470	21.30	8.00	4998		0.12	4.62	4023.13	488.04	1421.43	1848.91	42.49	-124.76
CSB051	21.32	8.00	4998	B	0.09	4.59	4023.17	488.04	1420.84	1848.94	41.87	-125.32
4058	26.00	8.00	5724		0.42	8.54	4031.82	488.05	1395.93	1855.67	78.47	-109.70
CSB105	23.88	7.96	5040	C	0.03	4.73	4027.90	488.10	1431.24	1852.62	52.54	-116.02
TRC22	8.41	7.81	8726		21.80	54.84	3999.30	488.29	1138.57	1830.39	128.49	-115.68
DR103	5.10	7.70	7039		17.23	34.72	3993.18	488.45	1255.04	1825.64	91.20	-115.67
CSB042	14.92	7.56	5464	M	0.66	8.92	4011.33	488.68	1373.93	1839.74	47.96	-130.28
2747	14.90	7.55	5464		0.31	8.99	4011.30	488.69	1373.86	1839.71	47.92	-130.60

TABLE 1-A3 (cont.). Principal Facts, Gravity Stations in Northern Panamint Valley

STA	LAT	LON	EL	EC	IZ	OZ	NORTH	EAST	OBS G	THEO G	FAA	CBA
00H4	33.64	7.52	2516		0.00	14.00	4045.94	488.78	1616.02	1866.68	-14.04	-86.76
CSB108	21.64	7.42	4961	M	0.01	4.69	4023.75	488.91	1426.21	1849.40	43.30	-122.61
CSB050	19.94	7.27	5340	C	0.43	5.94	4020.61	489.13	1396.16	1846.95	51.33	-125.88
4060	24.19	7.15	5124		0.47	5.81	4028.47	489.31	1429.23	1853.07	57.98	-112.40
4027	39.21	6.95	-39		0.00	2.40	4056.24	489.65	1745.51	1874.71	-132.97	-129.19
CSB107	25.99	6.92	5610	C	0.45	8.47	4031.80	489.66	1405.92	1855.66	77.76	-106.14
4029	37.46	6.86	-49		0.00	3.00	4053.00	489.78	1751.48	1872.19	-125.40	-120.68
CSB041	15.20	6.77	5670	C	0.44	10.24	4011.85	489.86	1359.86	1840.14	52.85	-131.33
4028	38.21	6.80	-44		0.00	2.40	4054.39	489.87	1747.94	1873.27	-129.56	-125.61
2127	36.35	6.79	-3		0.05	5.33	4050.95	489.88	1764.07	1870.59	-106.80	-101.32
4026	39.73	6.67	-44		0.00	2.40	4057.20	490.06	1746.50	1875.47	-133.19	-129.24
CSB109	21.84	6.63	4965	C	0.15	5.22	4024.12	490.09	1428.33	1849.69	45.51	-119.87
2743	21.82	6.62	4969		0.64	5.61	4024.09	490.10	1428.43	1849.66	46.02	-119.26
4061	27.78	5.96	5249		0.83	10.14	4035.11	491.10	1440.83	1858.24	76.16	-94.17
2895	2.05	5.80	5881		1.10	10.80	3987.54	491.29	1339.79	1821.27	71.49	-118.68
4025	39.67	5.53	-49		0.00	2.40	4057.09	491.76	1753.03	1875.38	-127.04	-122.92
CSB040	15.08	5.14	6480	C	1.55	13.36	4011.63	492.30	1314.01	1839.97	83.30	-124.32
CSB110	21.93	4.89	5200	C	0.42	7.38	4024.29	492.69	1418.46	1849.82	57.60	-113.39
DVR91	16.53	4.68	9064		13.23	47.81	4014.31	492.99	1138.95	1842.05	148.96	-113.72
2133	39.56	4.67	-51		0.12	3.78	4056.88	493.04	1756.96	1875.22	-123.05	-117.40
2128	36.73	4.67	-65		0.17	4.47	4051.65	493.04	1764.93	1871.14	-112.32	-105.44
2132	38.67	4.45	-65		0.15	3.64	4055.24	493.37	1757.62	1873.94	-122.43	-116.40
2896	1.55	4.37	6340		1.54	10.55	3986.62	493.44	1319.21	1820.55	94.77	-110.89
DVG67	34.45	4.26	1370		5.19	10.25	4047.44	493.65	1689.87	1867.85	-49.13	-86.15
CSB111	21.14	3.96	5855	C	0.29	11.42	4022.83	494.08	1380.59	1848.68	82.44	-107.04
H6	29.34	3.76	5054		14.11	29.90	4037.99	494.39	1442.03	1860.48	56.78	-87.11
TRC24	23.71	3.70	3583		4.95	11.85	4027.58	494.47	1526.05	1852.38	10.62	-100.91
2131	38.14	3.61	-72		0.25	3.70	4054.26	494.62	1759.53	1873.17	-120.41	-113.98
DVG66	33.00	3.48	1385		3.56	9.69	4044.75	494.81	1688.86	1865.76	-46.63	-84.74
2742	21.42	3.10	6433		8.27	27.33	4023.35	495.36	1333.43	1849.08	89.19	-104.40
2129	37.73	3.04	-88		0.24	3.77	4053.50	495.47	1761.30	1872.58	-119.56	-112.51
2596	19.26	2.52	3382		5.21	15.38	4019.35	496.23	1522.13	1845.98	-5.79	-106.90
2138	37.37	2.47	-88		0.34	3.78	4052.83	496.32	1761.30	1872.06	-119.04	-111.89
2723	38.78	2.41	165		0.05	3.36	4055.44	496.41	1749.85	1874.09	-108.72	-111.02
2595	19.42	2.29	3239		5.65	15.73	4019.65	496.57	1530.83	1846.21	-10.77	-106.61
H7	27.20	2.15	2285		5.19	10.91	4034.03	496.79	1618.93	1857.40	-23.57	-91.44
2724	38.94	1.94	286		0.11	3.24	4055.73	497.11	1745.56	1874.33	-101.86	-108.40
2594	19.50	1.71	2968		5.22	15.14	4019.80	497.44	1548.63	1846.32	-18.57	-105.69
2130	39.19	1.64	398		0.09	3.16	4056.20	497.56	1741.63	1874.69	-95.61	-106.12
CH229	38.28	1.60	150		0.14	3.32	4054.51	497.62	1751.59	1873.37	-107.64	-109.52
DVG68	32.40	1.56	534		4.63	10.48	4043.64	497.67	1732.56	1864.89	-82.11	-90.07
2109	38.27	1.55	151		0.04	3.32	4054.50	497.69	1751.58	1873.36	-107.57	-109.44
TRC21	6.06	1.53	5925		6.97	19.40	3994.95	497.70	1340.97	1827.02	71.06	-113.12
2139	37.04	1.49	-65		0.13	3.66	4052.22	497.78	1759.48	1871.58	-118.21	-112.18
2725	39.48	1.20	544		0.08	3.05	4056.73	498.21	1735.47	1875.10	-88.46	-104.13
DVR72	11.17	1.19	3619		7.49	19.74	4004.40	498.22	1480.78	1834.35	-13.24	-118.11
2593	19.59	1.14	2708		5.49	15.14	4019.96	498.29	1563.73	1846.45	-28.04	-106.23
2726	39.86	1.04	672		0.08	3.01	4057.44	498.45	1729.47	1875.65	-82.97	-103.10
TRC20	3.41	0.87	5646		9.59	20.34	3990.05	498.69	1354.52	1823.22	62.18	-111.51
2592	19.57	0.54	2441		7.17	16.58	4019.93	499.19	1579.53	1846.42	-37.32	-104.89
2140	36.83	0.35	-24		0.03	3.49	4051.83	499.48	1758.83	1871.28	-114.71	-110.37
2591	19.26	0.04	2183		5.73	15.34	4019.35	499.94	1594.93	1845.98	-45.74	-105.67

Because of the many changes to the data from Snyder et al. [1981b] we list both our new data and the modified older data. Our stations all have six character identifications of three letters followed by three digits; all others are from a data tape based on Snyder et al. [1981b].

TABLE 1-A3 (cont.). Principal Facts, Gravity Stations in Northern Panamint Valley

KEY: STA - Station identification. LAT - Latitude in minutes north from 37°N. LON - Longitude in minutes west of 117°W. ELEV - Elevation above sea level in feet. EC - Elevation codes used to indicate the elevation control for that station if measured as part of the 1985 survey. The earlier survey by S. Biehler has a code of "Z" while this column is empty for the USGS data. The following codes are used. B - Benchmark M - Map elevation other than a benchmark. This includes section corners and summit elevations. C - Contour elevation. The elevation given is interpolated between contour lines. IZ - The inner zone terrain correction. For our surveys this is out to the F ring of Dobrin [1976]. OZ - The outer zone terrain correction. The total terrain correction is the sum of the IZ and OZ values. NORTH - The north-south Universal Transverse Mercator (UTM) coordinate in kilometers. EAST - The UTM east-west coordinate in kilometers. OBS G - The observed gravity, corrected for drift and earth tides, less 978000 mGal in mGals. THEO G - The theoretical gravity from the GRS 1967 formula (THEO G = $978031.846 \cdot (1 + 0.005278895 \cdot \sin^2(\text{LATITUDE}) + 0.000023462 \cdot \sin^4(\text{LATITUDE}))$, Internat. Assoc. Geodesy [1971]) less 978000 mGal in mGal. FAA - The free air anomaly in milligals. CBA - The complete Bouguer anomaly in milligals.

CHAPTER 2
SYSTEMATIC ERRORS AND UNCERTAINTIES OF LOCAL EARTHQUAKE PARAMETERS: AN EXAMPLE FROM NORTHERN UTAH AND SOUTHEASTERN IDAHO

Craig H. Jones
Department of Earth, Atmospheric, and Planetary Sciences,
Massachusetts Institute of Technology, Cambridge, MA 02139

INTRODUCTION

The results of microearthquake surveys and local earthquake studies, one of the few techniques available for discerning current tectonic activity in the crust, are subject to errors in most of the parameters typically under study: velocity structure, earthquake location, and focal mechanism. Most workers assume these errors to be independent of one another, except that errors in the velocity structure affect the source location. The data are usually analyzed by either assuming or inverting for the velocity structure, then locating the earthquakes, and finally determining any focal mechanisms. In each case the uncertainties quoted reflect the influence of noise in the source data on the final parameters; without a simultaneous inversion of the data for all parameters, the dependance of any one upon another is difficult to estimate. The additional problems introduced by the nonlinear relationships between the various parameters further hinders a fully analytical error analysis.

In this paper I explore some of the effects of errors in one parameter on another using body wave arrival times gathered with a seismic network in a portion of the Great Basin physiographic province in northern Utah. During the course of analysis of these data, I found that certain systematic changes in both focal mechanisms and earthquake locations occurred when the velocity structure was changed. Attempts to reduce the impact of these systematic differences revealed some surprisingly strong correlations between errors in the velocity structure and errors in earthquake locations and focal mechanisms. Because these correlations have not been described in the past, this paper presents the results of this investigation; the tectonic interpretation of these data and a more complete analysis of the uncertainties of the final results may be found in Chapter 3.

The network spanned several fault block ranges and valleys in northern Utah and southeastern Idaho; the central features of interest were Pocatello and Hansel valleys (Figure 2-1). The entire region is underlain by Paleozoic sedimentary rocks except for a small region

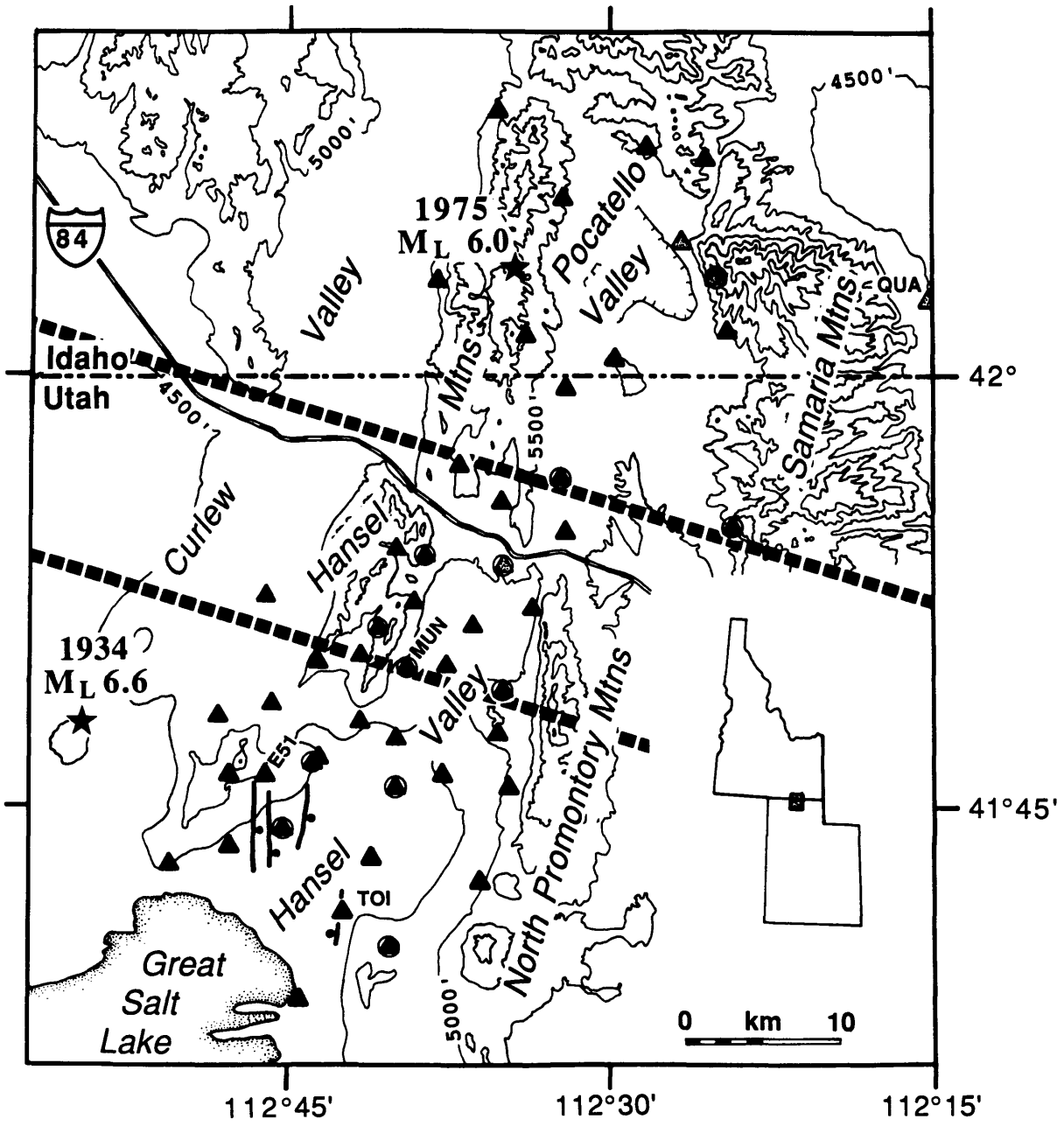

Fig. 2-1: Topography and station locations in the Hansel Valley--Pocatello Valley region. Digitally recorded seismometers are circled; sites abandoned before 15 September are shaded. Instrumental epicenters of the 1975 Pocatello Valley (M_L=6.0) earthquake [Arabasz et al., 1979] and 1934 Hansel Valley (M_L=6.6) earthquake [Dewey et al., 1972] are indicated by the stars. Contour interval is 500'; the Great Salt Lake is drawn with its approximate 1983 shoreline. The heavy dashes mark the boundaries of the low-velocity region (the

underlain by Tertiary volcanic and sedimentary rocks near the center of the network. Except for sedimentary fill in northern Hansel Valley and Pocatello Valley, bedrock is exposed or covered by a thin veneer of Pleistocene lake sediments. The seismicity in the region forms part of the Intermountain Seismic Belt [e.g., Smith and Sbar, 1974].

I first derived a one-dimensional velocity structure from the observed travel times to locate over 330 earthquakes and then used that structure to determine first-motion focal mechanisms for more than 110 of these events. The velocity structure was carefully derived to minimize both the variance of the travel-time residuals and the number of interfaces in the structure. I examined the uncertainties of earthquake locations caused by noise in the travel times and errors of the one-dimensional structure. The focal mechanisms obtained are strongly affected by the position of the earthquake in the velocity structure. In particular, events located in low velocity material above a strong refractor tend to appear to have oblique-slip mechanisms, while those just below the top of the high velocity medium tend to appear to have nearly pure dip-slip mechanisms. This tendency is in part due to the velocity structure; I determined the focal mechanisms for several events in velocity structures with a strong velocity contrast alternately above and below each mechanism. The orientations of the nodal planes deduced using these structures illustrate the dependance of these focal mechanisms on the details of the velocity structure near the source.

I then compared the locations derived using my best estimate of the one-dimensional velocity structure with those derived using my best estimate of the three-dimensional velocity structure. The differences I observed illustrate several important sources of systematic error when a one-dimensional velocity structure is assumed in a region with lateral velocity contrasts. These systematic errors are usually the same magnitude or greater than those of the uncertainties estimated from the one-dimensional structure. Additionally I find that some of these systematic errors strongly influence both absolute and relative earthquake locations, suggesting that analyses that depend on the accuracy of relative locations are susceptible to errors introduced by unrecognized velocity variations. Finally, the influence of errors introduced by lateral velocity contrasts on focal mechanisms are also investigated.

---

central block of the second layer) of the three-dimensional velocity structure M3D. Heavy lines in southern Hansel Valley are traces of scarps produced in the 1934 Hansel Valley Earthquake (as drawn by Richens [1979] from Shenon [1936]); bar-and-ball on downthrown side of scarp.

DATA COLLECTION

Forty-seven portable seismometers were deployed in the Hansel Valley region from 30 August to 4 October 1983 (Figure 2-1). The 32 Sprengnether MEQ-800, 1 Teledyne Geotech Portacorder, 10 digital seismographs from the University of Wisconsin, and 4 "big drum" seismographs from Cambridge University recorded events between 15 and 29 September, and most of these instruments were operating from 10 September through 3 October. All these instruments except the digital seismographs recorded the vertical-component of ground motion on smoked-paper; the instruments from the University of Wisconsin recorded all three components of ground motion digitally at 100 samples per second for between about 20 and 90s after an event was detected. A variety of different high-frequency (peak response near 1-5 Hz) seismometers were used. The internal clocks of each smoked paper recorder were set between 0.5 and 7.0 s after the WWV time signal; this time correction was measured when the record was changed, usually every 1, 2, or 4 days. The digital instruments recorded the Omega navigation signal, which was used to calibrate the internal clock when the record was processed [Schneider et al., 1981]. All stations were located on U.S. Geological Survey $7^1/2'$ topographic maps with an estimated precision of 50 m horizontally and 10 m vertically.

Virtually all P wave arrivals can be measured with uncertainties less than 0.2 s. Smoked-paper records were picked using a magnifying glass and a digitizing table with a precision of 0.001 inches (0.0254 mm); this results in a theoretical reproducibility of 0.013 s for recordings at 2 mm/s, collected in the southern half of the analog station network, and 0.025 s for the remaining recordings at 1 mm/s. Digital records were picked using an interactive computer program that permitted identification of an individual sample. Impulsive P arrivals, which accounted for just under half of all P arrivals, were found to be distinct over 1 to 5 samples (0.01 to 0.05 s) on the digital records; by repicking a small number of arrivals on the smoked-paper records I found that impulsive arrivals might be timed reproducibly to within about 0.05 s.

P arrivals on the smoked-paper records were assigned a quality of either 0 (for impulsive arrivals) or 1 (for other emergent or uncertain arrivals). Two stations (TOI and QUA on Figure 2-1) had unusually poor quality arrivals and so all arrivals (P and S) at these station were further downweighted by one. Arrivals at the digital stations were assigned qualities from 0 to 4, but almost all were assigned qualities of 0 or 1. The qualities of 0, 1, 2, and 3 are expected to be assigned to arrival times with standard deviations of 0.05, 0.1, 0.2, and 0.3 s, respectively.

The S-wave arrival typically is difficult to identify on vertical component records; hence S arrivals were all assigned a quality of 3 when picked from smoked-paper records. The

horizontal components recorded with the digital instruments greatly increased my confidence in the identification of the S arrival; these picks were assigned qualities from 0 to 4.

A list of events was constructed from arrivals picked from the analog stations; when winnowed for non-seismic events and distant earthquakes (S-P arrival times in excess of 10 s) 666 earthquakes were found to be in the vicinity of the network. Arrivals from the digital stations are only available for 73 events both that are within 5 km of the network and that triggered 5 or more of the digital stations.

ONE-DIMENSIONAL VELOCITY STRUCTURE

Many local earthquake studies have assumed that a one-dimensional structure adequately describes the variation of velocity in the earth. This assumption was often pragmatic: earthquakes could not be located within a laterally heterogeneous structure. In this section I analyze the arrival times assuming a one-dimensional structure and present a detailed examination of the uncertainties of locations derived from this analysis. The purpose is to establish these uncertainties using the assumption of lateral homogeneity, which can then be compared with the differences between these locations and those obtained using a three-dimensional velocity structure. In this manner I hope to demonstrate that even the most conservative error analysis that assumes a one-dimensional velocity structure can underestimate the error caused by this assumption.

Inversion for the Velocity Structure

Because the seismic velocity structure beneath northern Utah had not been studied in detail, the arrival time data from the earthquakes in the network were inverted for the velocity structure. Initial earthquake locations were determined assuming a velocity structure based on that of Smith et al. [1975] for Delta, Utah. The interfaces between the layers of this structure lie at depths of 2, 15, and 18 km; the P velocities of the layers were assumed to be 4.0, 5.9, 6.4, and 6.6 km/s, respectively, and the S velocity (v_S) was assumed equal to the P velocity (v_P) divided by 1.75. Several possible velocity structures perturbing the depths and velocities of this structure were then used to analyze the arrival times from the analog recordings. The result of these experiments is the velocity structure of "iteration 1" in Figure 2-2. I required that this structure have monotonically increasing velocities with depth despite some evidence for a region between about 2 and 4 km depth with a velocity v_P less than that above it.

To reduce the uncertainties both of first-motion focal mechanisms and of the locations of the earthquakes, additional velocity experiments were conducted with data from both digital

Ten Layer Structures

Iteration 1	2	3	4	5	6	7	8	9	10	Depth (km)
4.84 (2.78)	4.86 (2.78)	4.86 (2.78)	4.85 (2.66)	4.84 (2.66)	4.81 (2.68)	4.83 (2.69)	4.81 (2.69)	4.85 (2.69)	4.94 (2.70)	-2
4.84 (2.78)	4.86 (2.78)	5.25 (2.78)	5.10 (2.69)	5.01 (2.72)	5.11 (2.71)	5.04 (2.69)	5.08 (2.65)	5.05 (2.65)	5.08 (2.69)	0
4.84 (2.78)	4.84 (2.78)	5.00 (2.78)	5.00 (2.78)	4.95 (2.70)	4.63 (2.78)	4.61 (2.73)	4.47 (2.76)	4.53 (2.76)	4.59 (2.65)	1
4.84 (2.78)	4.84 (2.78)	5.00 (2.78)	5.00 (2.78)	4.95 (2.70)	4.67 (2.83)	4.65 (2.92)	4.52 (2.86)	4.58 (2.86)	4.59 (2.95)	2
4.84 (2.78)	4.84 (2.78)	5.00 (2.78)	5.00 (2.78)	4.95 (2.70)	4.84 (2.82)	4.90 (2.89)	4.95 (2.97)	5.14 (3.06)	5.27 (3.23)	3
5.72 (3.42)	5.99 (3.37)	5.81 (3.32)	5.78 (3.32)	5.75 (3.34)	5.69 (3.38)	6.08 (3.36)	5.83 (3.33)	6.00 (3.36)	6.07 (3.33)	4
5.72 (3.42)	6.19 (3.43)	6.22 (3.37)	6.20 (3.32)	6.24 (3.40)	6.26 (3.43)	6.26 (3.43)	6.26 (3.35)	6.26 (3.44)	6.30 (3.37)	5
5.72 (3.42)	6.19 (3.43)	6.25 (3.43)	6.37 (3.43)	6.24 (3.40)	6.26 (3.43)	6.26 (3.43)	6.40 (3.44)	6.40 (3.44)	6.30 (3.37)	6
5.72 (3.42)	6.19 (3.43)	6.25 (3.43)	6.37 (3.43)	6.24 (3.40)	6.26 (3.43)	6.26 (3.43)	6.40 (3.44)	6.40 (3.44)	6.30 (3.37)	7
6.23 (3.65)	6.81 (3.65)	6.81 (3.65)	6.81 (3.65)	6.81 (3.65)	6.81 (3.65)	6.81 (3.65)	6.81 (3.65)	6.81 (3.65)	6.81 (3.65)	8

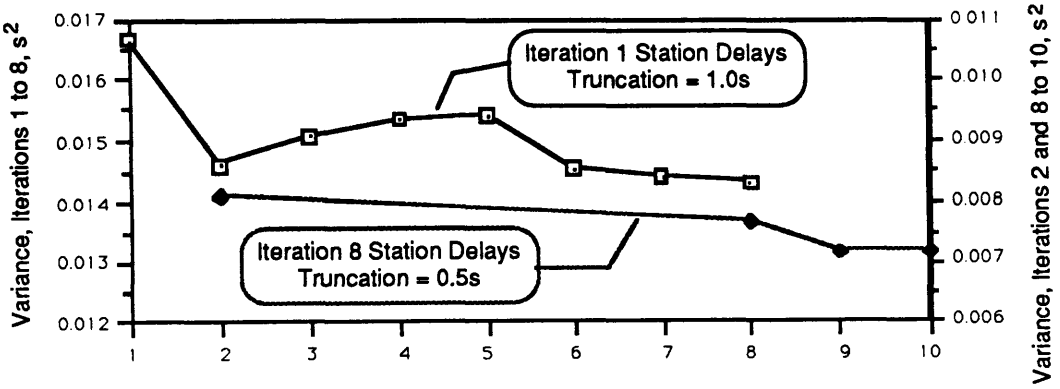

Fig. 2-2: Results from an iterative velocity--hypocenter inversion of observed traveltimes from 30 selected earthquakes located within the temporary network. Depth interfaces are relative to 1 km above mean sea level, which is nearly the lowest elevation within the network. P-wave velocities (S-wave velocities) are in km/s. Each velocity structure is inverted from the travel-time residuals of the locations determined from the previous iteration's velocity structure. Strong low-velocity layers were manually damped in iterations 1 to 5.

and analog recorders. These experiments were all conducted using the iterative velocity and hypocenter inversion routines HYPIT and REL3D written by S. Roecker (see Roecker [1981, 1982] for a more detailed description). Weights of 400, 100, 25, and 11.1 were assigned to arrivals with qualities of 0, 1, 2, and 3, respectively. These weights presume standard deviations of 0.05, 0.1, 0.2, and 0.3 s for the arrivals assigned each quality. These weights were multiplied by a truncation function,

$$T = \frac{50}{50 + \{50[e - 1]\}^{(r^2/t^2)}} \qquad (2\text{-}1)$$

where r is the travel-time residual and t is the truncation value, usually set to 1s. This function effectively prevents arrivals with residuals greater than the truncation value from affecting the inversion. Thirty earthquakes with locations well distributed within the network, well distributed in depth between about 2 and 8 km depth, and presumed relatively insensitive to changes in the velocity structure were selected for these experiments.

Initially the velocity structure was divided into 1-km-thick layers to estimate both the velocity and depth bounds of layers in the velocity structure. The least-squares inversion permitted the use of a large damping value that prevented unstable velocity perturbations from dominating the result of the inversion. Each iteration of the inversion consisted of two steps: relocation of the earthquakes using the velocity structure indicated for that iteration (Figure 2-2), and an inversion of the new arrival time residuals for a new velocity structure to be used in the following iteration. Low-velocity zones that were calculated from the structures used in iterations 1 through 4 were manually damped before the new velocities were used to relocate events in the next iteration. Because this manual damping caused the inversion to diverge, as illustrated by the increasing variance from iterations 2 to 5 in Figure 2-2, the later inversions (6 to 10) were freed from the prohibition against low-velocity zones. After locating the earthquakes in the velocity structure of iteration 1, the mean residual was calculated at each station, and unless the scatter about the mean was too great to permit an accurate estimate of the station delay, this mean was used as a station delay for iterations 1 to 8. Using these delays, the velocity structure of iteration 8, which includes a zone from 1 to 3 km depth thick with a P-wave velocity 10% less than that above 1 km, has a variance 1.8% smaller than the best structure lacking a low-velocity zone (that of iteration 2).

Because of the differences between the velocity structures obtained from iteration 1 and from iteration 8, the station delays were recalculated using the same thirty earthquakes and the iteration 8 velocity structure, and the new delays were used in iterations 9 and 10. Additionally, the truncation value was also reduced from 1.0 to 0.5 s for iterations 9 and 10 in

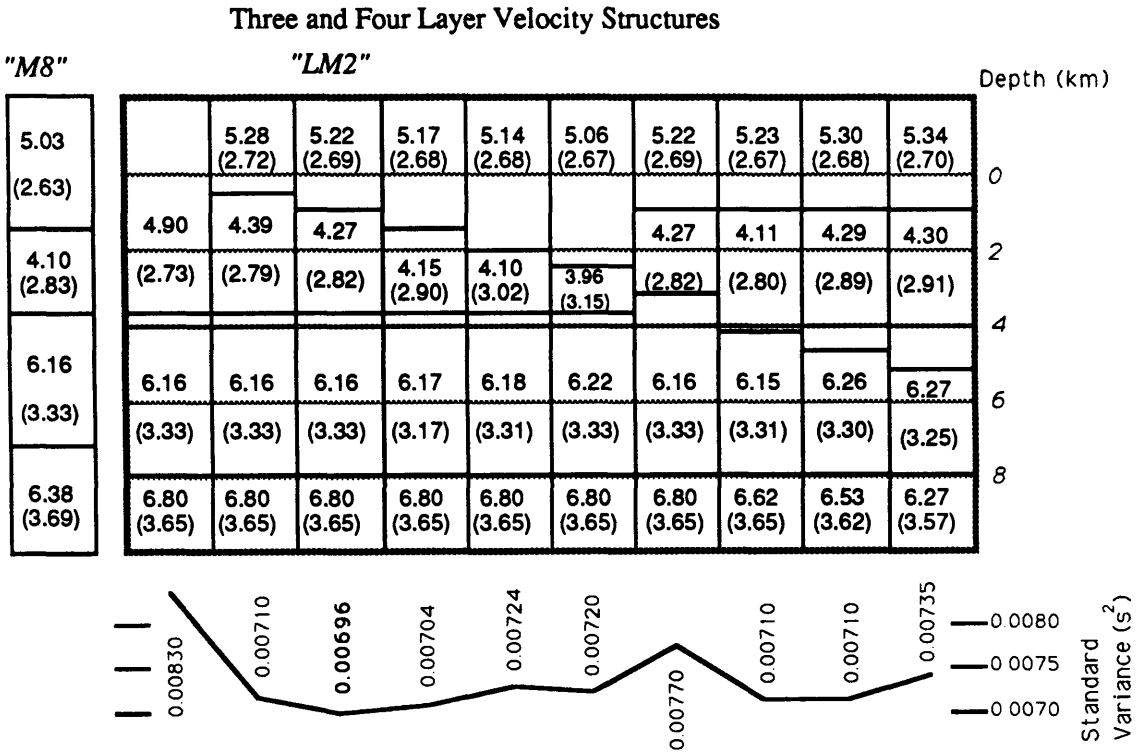

Fig. 2-3: Experiments comparing several four-layer and one three-layer velocity structure to constrain the depth to the upper two interfaces. In each experiment the layer depths were fixed and P (S) velocities and hypocenters were iteratively inverted using the same arrival time data as in Figure 2-2. Note that the bottom half-space was poorly sampled (and hence unresolved) due to the location of the 30 events selected. Structure M8 (the best-fitting one-dimensional structure) included for comparison.

the belief that any large residuals remaining were in error and did not reflect any velocity variations. The results from iterations 2 and 8 were recalculated to compare these iterations directly with iterations 9 and 10 (Figure 2-2). The best-fitting structure, that of iteration 9, has a variance about 12% less than that of iteration 2 and mainly differs from the structure of iteration 8 between 3 and 4 km depth.

Because the better-fitting ten-layer structures in Figure 2-2 appear to have large velocity gradients at only three depths (1.0, ~3.5, and 8.0 km), three- and four-layer structures were investigated (Figure 2-3). This reduction in the number of layers both improves the computational efficiency of the earthquake relocation routine and permits a more direct examination of the low-velocity zone between about 1 and 4 km depth. Several possible structures were investigated by fixing the depth of the layer interfaces and then iteratively inverting the arrival times for the velocity structure and the hypocentral locations. Initially, the P-wave velocities assigned to the layers of each structure were 5.22, 4.27, 6.16, and 6.80

km/s and S-wave velocities were 2.69, 2.82, 3.33, and 3.65 km/s, from top to bottom. The depths of both the upper and middle interfaces were varied to examine the effects of the depths of these steep gradients on the total variance. The depth of the bottom gradient was left untouched because of the poor sampling of the deepest part of the velocity structure. I also examined a three-layer structure (second from left in Figure 2-3) with its upper interface fixed at 3.7 km, very near the depth found from the earlier velocity inversions. Because the marked increase in velocity at this interface was the best resolved in the ten-layer inversion, it is unlikely that any improvement in the variance would be obtained by altering the depth of this boundary.

The differences in variance among structures with different upper layer boundaries indicate that that interface is poorly resolved; the differences among those with different depths of the middle velocity interface are greater and constrain it to be near 3.7 km depth (Figure 2-3). The standard variance is defined here as

$$\sigma^2 = \frac{n}{(n-n_f)\left(\sum_{i=1}^{n} w_i\right)}\left[\sum_{i=1}^{n} r_i^2 w_i - \frac{\left(\sum_{i=1}^{n} r_i w_i\right)^2}{\left(\sum_{i=1}^{n} w_i\right)}\right] \qquad (2\text{-}2)$$

where r_i is the residual of the i^{th} arrival, w_i is the weight, n is the total number of arrivals, and n_f is the number of degrees of freedom of the velocity structure and the earthquake locations. As the thickness of the low-velocity zone is reduced, the P-wave velocity within it decreases without large (> 4%) changes in the variance. The depth of the middle interface has a greater effect on the variance and appears to be between about 3.2 and 5.2 km deep; the depth of the second interface in the best fitting structure is near 3.7 km. The bounds on the P-wave velocity of the first and second layers are 5.06 to 5.30 km/s and 4.10 to 4.39 km/s, respectively. The P-wave velocity in the third layer is largely insensitive to the choice of the depths of its boundaries, with most values near 6.15 and all between 6.15 and 6.26 km/s. The underlying half-space is adequately sampled only for structures with a deep second interface; the results for these structures imply that P- and S-wave velocities lower than 6.8 and 3.65 km/s might be more appropriate.

The S-wave velocity structure is more poorly resolved than the P-wave structure. The S-wave velocity of the top and the third layers are relatively well-constrained, ranging from 2.67 to 2.70 km/s and from 3.17 to 3.33 km/s, respectively, with most structures containing a velocity closer to 3.33 km/s for the third layer. As the top interface is deepened, the S-wave

velocity of the second layer increases from 2.79 km/s to 3.02 km/s while the P-wave velocity decreases. This suggests that the S-wave velocity increases with depth within the depth range of the P-wave low-velocity zone. This is confirmed by the inversions for the ten-layer structure (Figure 2-2), which yielded an S-wave low-velocity zone only between depths of about 0 and 2 km. Hence the average P- and S-wave velocity structure between 0 and 4 km depth is probably fairly complex and appears to contain large variations in the ratio v_p/v_s with depth. Such large variations probably are due to changes in lithology with depth.

The apparent complexity of the shallow velocity structure might suggest that the inclusion of additional layers would improve the accuracy of the velocity structure, but the standard variance obtained for the best of these structures (LM2, Figure 2-3), 0.00696 s^2, is less than the lowest variance found for the ten-layer structures, implying that no substantial improvement in variance is likely to be obtained through the addition of velocity contrasts.

The halfspace is proportionally less sampled by the 30 well-recorded events used here than by all of the observed arrivals because the well-recorded events are concentrated toward the center of the network and paths with epicentral distances greater than about 30 km are rare. Additionally, those events located shallower than about 3 km depth were usually avoided in selecting the 30 events used in this inversion for the velocity structure because of the sensitivity of their locations to the velocity structure. Hence, the most poorly constrained parameters, the velocity and thickness of the upper layer and the velocity of the halfspace, were further examined using arrival times observed for all 341 earthquakes recorded in the network.

Because earlier experimentation had shown that the depth to the halfspace and the velocity of that halfspace were nearly totally coupled, I fixed the depth to the halfspace at 7.2 km, the depth to a 6.5 km/s layer found by Estill [1976] in Pocatello Valley. Holding the upper crustal velocities fixed as in structure LM2 (the best fitting structure of Figure 2-3), I inverted the arrival times for the velocity of the halfspace. The best-fitting velocities are 6.38 km/s for P waves, substantially smaller than the value from the inversions using 10 layers (Figure 2-2), and 3.69 km/s for S waves, but the total variance using these best-fitting velocities is only 2.3% smaller than that of the starting structure. Nevertheless, because rays sampling this layer both account for only about 10% of all arrivals and are usually assigned smaller qualities than the other, shorter rays, I consider this apparently minor decrease in the total variance to be significant.

The distribution of earthquakes with depth obtained using structure LM2 includes a disproportionately large number of earthquakes with depths less than 250 m below the reference surface fixed at 1km above mean sea level (Figure 2-4). Because most of the events used in constructing the best-fit structure were deeper than 3 km, the upper few

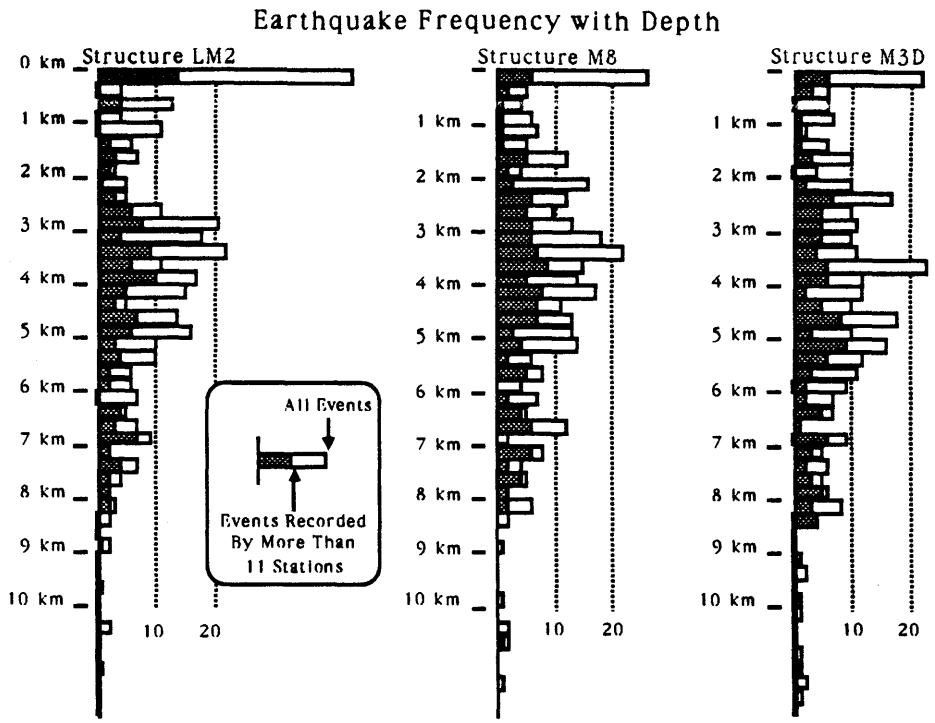

Fig. 2-4: Distribution of earthquakes with depth using the modified best-fit structure of Figure 2-3 ("LM2", left) , the final 1-D structure (M8, center) and the final 3-D structure (M3D, right). Note the number of events within the uppermost 250 m.

kilometers of structure LM2 are more poorly constrained than the remainder of the structure (Figure 2-3); this might account for the concentration of earthquakes located at the top of the velocity structure. Hence I again used data from all 341 earthquakes observed in the vicinity of the network to constrain the near-surface velocity structure. Because the velocities of the upper two layers and the depth of the interface between them were found to be strongly coupled, I considered structures with a depth of that interface at 1.0, 1.5, 2.0, and 3.0 km and allowed the velocities of these two layers to vary. The velocities for these layers were initially those of structure LM2 except that the halfspace P- and S-wave velocities were set to 6.38 and 3.69 km/s. The best of these structures, that with a boundary at 1.5 km, improved the variance 6.8% from 0.02321 s^2 to 0.02162 s^2, but this is only 0.7% smaller than the structure with a boundary at 1 km and 1.7% smaller than that with a boundary at 2 km. Thus the depth of the uppermost interface is not well resolved in this final one-dimensional velocity structure used to relocate events (M8, Figure 2-3).

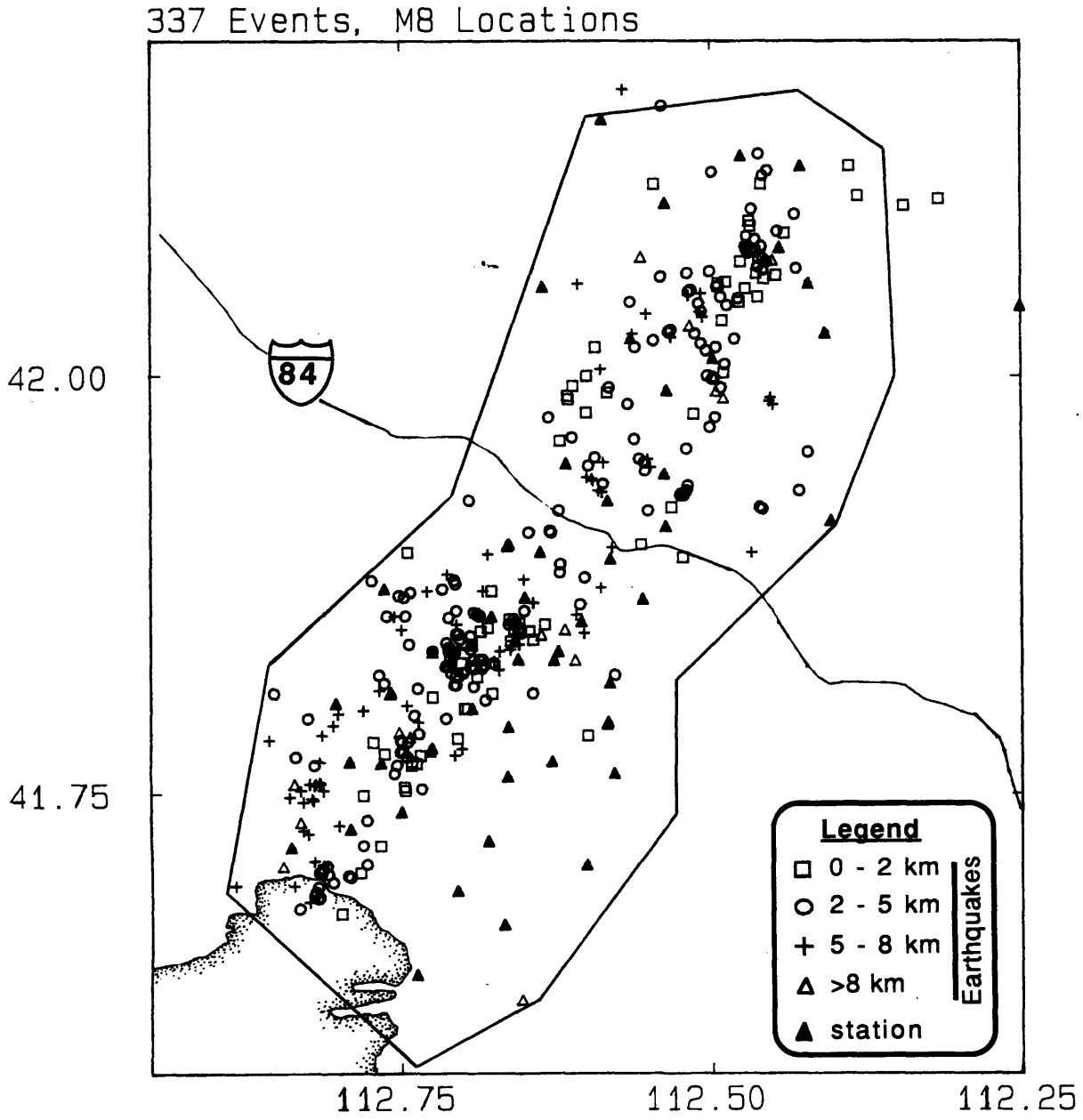

Fig. 2-5: Epicenters of microearthquakes located using structure M8. Only events earlier located within the large polygon were relocated to create this diagram. This polygon represents my estimate of the geographic limits of earthquakes I can reliably locate both horizontally and vertically. This map covers the same area as Figure 2-1.

TABLE 2-1
Standard Deviations of Computed Residuals
From Earthquakes Located Using Velocity Structure M8

Phase	Quality	Standard Deviation (s) of (and Number of Arrivals with) Residuals Less Than: 0.50 s		0.75 s		1.0 s	
		30 Earthquakes Used in Velocity Inversions					
P	0	0.063	(378)	0.071	(379)	0.095	(381)
P	1	0.156	(254)	0.175	(259)	0.191	(261)
S	0	0.070	(31)	0.070	(31)	0.070	(31)
S	1	0.145	(41)	0.202	(43)	0.202	(43)
S	2	0.220	(18)	0.263	(19)	0.263	(19)
S	3	0.222	(303)	0.283	(335)	0.317	(345)
		130 Earthquakes Recorded by 11 or more Stations					
P	0	0.091	(1514)	0.106	(1526)	0.123	(1534)
P	1	0.170	(997)	0.200	(1032)	0.236	(1056)
S	0	0.088	(69)	0.088	(69)	0.088	(69)
S	1	0.157	(133)	0.195	(138)	0.195	(138)
S	2	0.217	(58)	0.296	(66)	0.324	(68)
S	3	0.232	(1292)	0.298	(1456)	0.355	(1545)
		337 Earthquakes in Vicinity of Network					
P	0	0.091	(2425)	0.107	(2446)	0.127	(2461)
P	1	0.165	(1593)	0.194	(1645)	0.229	(1681)
S	0	0.089	(70)	0.089	(70)	0.089	(70)
S	1	0.159	(136)	0.196	(141)	0.196	(141)
S	2	0.215	(60)	0.292	(68)	0.320	(70)
S	3	0.227	(2179)	0.287	(2415)	0.338	(2535)

Standard deviations computed for residuals of earthquakes located using the M8 velocity structure. Note the correlation of the computed residuals with the postulated variances of 0.05, 0.1, 0.2, and 0.3 s for arrivals assigned qualities of 0, 1, 2, and 3.

Earthquake locations and uncertainties

I relocated all of the 341 events initially found to lie within the polygon of Figure 2-5 using the M8 velocity structure; four poorly located events were eliminated from further analysis. The weighted root-mean-square (rms) residuals for 237 of the 337 relocated events are below 0.10 s. The statistical standard errors (1σ) for these events typically are less than 100m in both depth and epicenter; before these errors can be considered representative of the actual uncertainty associated with each event, however, I must show both that the *a priori*

estimates of the variance of the arrival times are appropriate and that the uncertainties due to noise exceed those due to errors in the velocity structure.

The computed standard errors were calculated by assuming, as noted previously, that the standard deviation of travel-time residuals of arrivals provisionally assigned qualities of 0, 1, 2, and 3 was 0.05, 0.10, 0.20, and 0.30 s, respectively. The observed standard deviations (Table 2-1) have nearly the same 1:2:4:6 ratio for qualities of 0, 1, 2, and 3 as the assumed standard deviations. Because only the relative weights assigned to individual arrivals affect either the final hypocenter locations or the comparisons between velocity structures, the locations and velocity comparisons described above are not strongly affected by an error in the assigned weights. The absolute value of the weight does affect the statistical error; the standard errors are linearly dependant on the standard deviations, therefore doubling the standard deviations will double the standard errors. Because the actual standard deviations might be twice those assumed in assigning weights (Table 2-1), the computed standard errors should be doubled. Thus I estimate that the standard error (1σ) in location due to noise in the observed arrival times is less than about 200m for earthquakes with a weighted rms less than about 0.10 s.

The uncertainty in the hypocentral location due to possible errors in the velocity structure is not directly resolved by the inversion used here. I estimate the effect of an incorrect velocity structure by relocating all 337 earthquakes in a three-layer structure identical to that in Figure 2-3 except the top of the halfspace has been moved to 7.2 km and the P-wave velocity of the halfspace was set to 6.5 km/s following Estill [1976]. Travel-time residuals from events located in this structure have a variance about 20% greater than residuals from structure M8; hence this three-layer structure is plausibly not in the group of acceptable one-dimensional velocity structures, and differences between locations using it and using M8 probably exceed the differences in locations that would be found using M8 and any other acceptable layered structure. Roughly a third of the relocations (101 of 337) occupied the same position as the original location in the M8 structure; although most of these locations correspond to minima of the weighted variance of the residuals calculated using the three-layer structure, some might incorrectly have been left at their starting location because of numerical problems that prevented the relocation routine from finding the global minimum. Hence a conservative estimate of the dependance of earthquake locations on differing velocity structures can be derived by considering only the relocations that differ from their starting locations.

Of the 74 events recorded by more than 11 stations and for which the locations in the M8 structure differ from those in the three-layer structure, 73 pairs of epicenters are separated by less than 500m, and 70 (95%) are within 330m of one another (Figure 2-6). The depths of

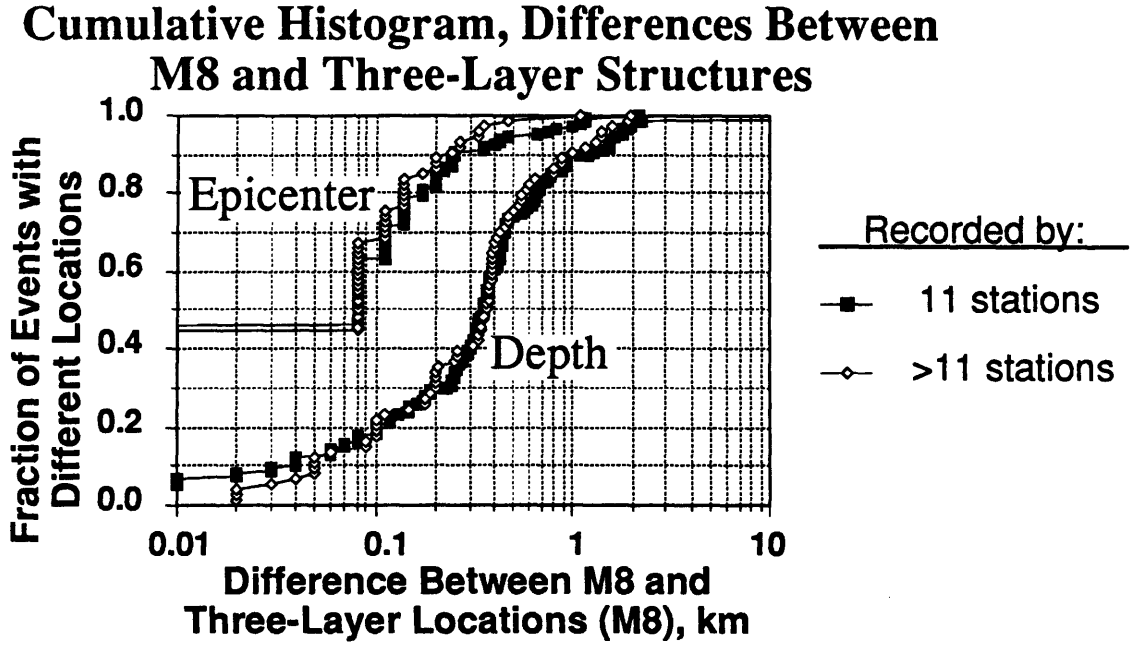

Fig. 2-6: Cumulative histogram of epicenter and depth differences for 337 events located in both M8 and the best-fit three-layer structure of Figure 2-3. Open symbols are for events recorded by more than 11 stations, solid squares are for events recorded by 11 or fewer stations.

only 56 (79%) of the 74 pairs of event locations are within 500m of one another; 70 (95%) are within 1.4 km of one another. The differences between the calculated locations are only slightly greater for the remaining 162 events recorded by less than 12 stations. Calculated epicenters of 154 (95%) of these 162 relocated events lie within 660m of the original epicenter in the M8 structure, and 95% of the depths differ by less than 1.8 km. Recalling that a third of the relocations may be identical to the original M8 location, I estimate that for events recorded by more than 11 stations, typical uncertainties in locations due to an erroneous velocity structure would be about 300m horizontally and 1km vertically. The equivalent uncertainties for the remaining events are about 500m horizontally and just over a kilometer vertically.

The standard errors of epicenters derived from the relocation of earthquakes are comparable to the errors estimated for an error in the velocity structure, but standard errors of depth are much less than those estimated for an error in the velocity structure. For most earthquakes the standard error computed using the M8 structure encompasses the epicenter determined using the three-layer structure. The difference in depth between the locations of an event computed in different velocity structures, however, does not correlate with the

standard error derived from the least-squares inversion routine that determines the location. This latter value reflects the projection of the estimated uncertainty in the measured arrival times through the linear approximation to the inversion procedure to an estimated uncertainty of the hypocentral location and therefore defines the precision of the depth, but not its accuracy. The term precision is used here as a measure of how well an earthquake's location can be determined under certain assumptions; it need not correspond to the accuracy of relative locations between earthquakes. Thus it appears that a precisely located event will have a more accurate epicenter than an imprecisely located event; the depths of precisely and imprecisely located events, however, are nearly equally accurate and equally likely to be incorrect if the assumed velocity structure is incorrect.

FOCAL MECHANISMS IN A 1-D STRUCTURE

Focal mechanisms for 113 earthquakes were determined using the polarities of the first motions of P-waves. Each event was examined thrice: first using the initial location and velocity structure (iteration 1 of Figure 2-2), second using the location from velocity structure LM2, and third using the location derived from velocity structure M8. The first set of mechanisms was obtained from the analog recordings. The second and third examinations were conducted with the focal mechanism previously obtained displayed with the new projection of the stations on the focal sphere. Both digital and analog data were used in these later examinations. The examination of the polarities of each event within several different velocity structures permitted a direct estimation of the effect of both different structures and different locations on the orientation and quality of the focal mechanism.

Grading of Focal Mechanisms

Uncertainties of focal mechanism parameters are difficult to bound quantitatively. One popular method searches through all possible focal mechanisms; the range of parameters bounding the mechanisms that are found to violate no more than a fixed number of observations are considered to delimit the uncertainty associated with the mechanism. While this procedure is useful in determining all mechanisms consistent with the observed polarities, uncertainties associated with mislocation of the earthquake or with an erroneous velocity structure can go undetected. As I show below, this is unusually important for studies of very shallow seismicity because relatively small differences from the assumed location of an earthquake relative to marked velocity gradients can require dramatically different focal mechanisms.

Each focal mechanism was examined by eye and assigned a grade from A to L. The quality of the fit to the first motions determined an initial grade. Grades A to C generally require both that at least 20 stations be used to locate the earthquake and both slip vectors be constrained within 10°: a change in the orientation of a slip vector by more than 10° increases the number of violations of observed polarities. Grades D to F require both slip vectors to be constrained within about 20°. Grades G to I require one slip vector to be constrained within 20° or both within about 30°. Grades J to L constitute the remainder for which a unique type of faulting, e.g. thrust or normal faulting, can be discerned but for which the orientations of the planes are more uncertain than 30°. Higher grades within these four groups require that the solution not be dependant on one or two first motions; if any two or more polarity observations were in error, the orientations of the planes would not be significantly altered.

The P-wave residual computed for a phase with a given polarity and the likelihood that the observed arrival has been assigned the correct takeoff angle were considered when evaluating critical polarities that constrain or violate a possible focal mechanism. Polarities of arrivals with magnitudes of residuals larger than 0.2 s were considered unreliable and were ignored. Those of arrivals between 0.1 and 0.2 s were considered suspect; they and emergent arrivals are considered to be roughly only half as important as impulsive arrivals within 0.10 s of the calculated arrival times. Hence the violation of two such suspect arrivals would constrain a focal mechanism as much as that of one good polarity. A polarity recorded at a station near the crossover point between refracted and direct first arrivals is considered to be violated only if that polarity would be violated for both possible take-off angles, thus mitigating somewhat any error in the location of an earthquake relative to a velocity contrast.

The grade assigned a focal mechanism was reduced if any of the following conditions occurred: substantial differences among focal mechanisms derived from the three velocity structures examined, high rms ($\geq$ 0.15 s) of the residuals of the earthquake under study, poor azimuthal distribution of stations recording the earthquake, or depth of the earthquake within about 1 km of an interface in the velocity structure. These considerations did not arise for most earthquakes and hence did not affect the grade assigned the mechanism of these earthquakes. In those instances where it seemed that a change in either the location of the earthquake or the velocity structure, within their respective uncertainties, would greatly change the focal mechanism, the grade was reduced. This reduction is in proportion to the estimated impact and likelihood of the perceived change in the mechanism. For example, if an earthquake's mechanism were initially assigned a grade of D and the earthquake was 200m from a strong velocity contrast, the final grade might be G; if the distribution of polarities indicated that the event would be unconstrained if located on the opposite side of the velocity contrast and if the rms of the event were high, the final grade might be J. The same polarities

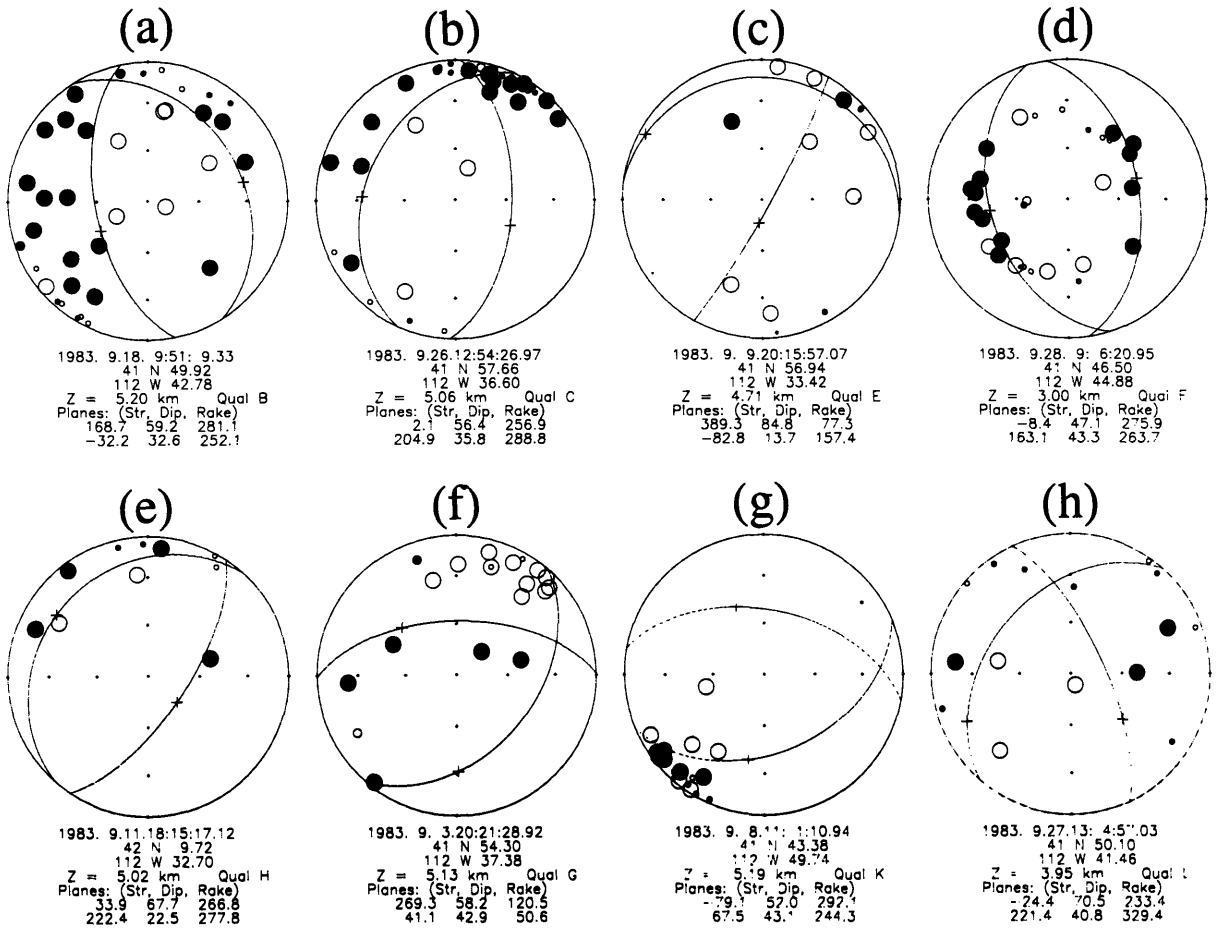

Fig. 2-7: Eight first-motion focal mechanisms illustrating the subjective classification scheme used in this report. Captions include the time, epicenter, and depth ("Z"), the quality of the focal mechanism, and the strike, dip, and rake of the two nodal planes. Projection is an equal area, lower hemisphere projection; filled circles are compressional first arrivals. Sizes of the symbols are roughly proportional to the quality of the polarities.

observed from an earthquake 0.7 km from the same velocity contrast might have a final grade of E or, if the earthquake seemed very accurately located, D. The intent of these modifications is to assign a grade to the focal mechanism that includes the range of uncertainty in the mechanism caused by errors within the estimated uncertainties of the velocity structure and the earthquake location.

Some sample mechanisms illustrate both typical (b, c, and e in Figure 2-7) and special (a, d, f, g, and h in Figure 2-7) applications of this grading scheme. Mechanisms b and c are both tightly constrained by the observed polarities; the small number of polarities caused us to assign c the lower grade of E. Mechanism e's gently-dipping plane is tightly constrained,

but the steep plane cannot be constrained better than about 30°; hence it was assigned a grade of H.

Least unusual of the special applications of the grading scheme, mechanism a would receive a grade of A if the polarity observed at the station near N120°E were dilatational; the violation of this station and the remote possibility that a relocation of the earthquake could produce a redistribution of the polarities in which the nodal planes could be oriented nearly north-south caused the assigned grade to be B.

Mechanism d illustrates a rare situation: a well-recorded, poorly-constrained earthquake and focal mechanism that suggest that either the earthquake is mislocated or the velocity structure near the earthquake is in error. If the velocity near the source were slightly greater, the polarities would plot nearer the margin of the focal hemisphere and few of the polarities would be violated. Such a mechanism would probably be assigned a grade of C or better, but the poor quality of the mechanism as shown in Figure 2-7 requires the grade to be no better than F.

Mechanisms were assigned a quality lower than F for a variety of reasons. Mechanism f, despite having many impulsive first motions, is only constrained by the compression observed at the most distant station recording the earthquake at an azimuth near N200°E. Hence this mechanism was graded G despite the fact that the mechanism as plotted might merit a higher grade. Mechanism g represents the extreme case of a mechanism with one tightly constrained and one unconstrained nodal plane. The quality of K assigned to this event reflects the lack of constraint on one nodal plane and the poor azimuthal distribution of stations; only the tight constraint on the other plane prevented us from assigning this mechanism a grade of L or eliminating it altogether. The final mechanism, h, could warrant a grade of H or even F based on the distribution of polarities; the large number of weak or emergent arrivals and the proximity of the earthquake to the velocity contrast at 3.7 km depth suggest that the focal mechanism might change drastically with a small change in location. For these reasons the mechanism was assigned the grade of L.

While not as objective as other techniques applied to similar data, the classification scheme used here is designed to evaluate not just the quality of fit of a given focal mechanism to polarities plotted on a focal sphere using a preferred velocity structure but also the possible errors due to mislocations, erroneous velocity structures, and errors of individual arrivals.

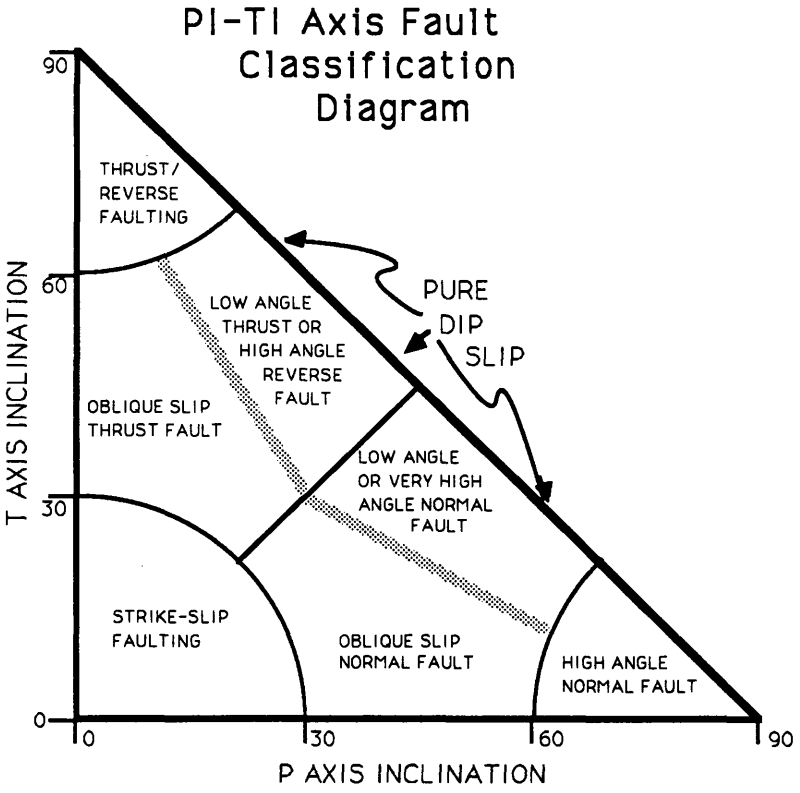

Fig. 2-8: Cartoon of the "PI-TI plot" illustrating the locations at which different types of focal mechanisms are plotted.

Classification of mechanisms

Because of the large number of focal mechanisms in a small geographic area, a plot of the inclination of the P-axis versus the inclination of the T-axis for each focal mechanism was constructed to help classify different types of faulting that occur in different areas (Figure 2-8). This "PI-TI plot" (Figure 2-9) shows, as expected for earthquakes within the Basin and Range Province, that the preponderance of focal mechanisms indicate normal faulting. The many events that fall well away from the high-angle normal faulting region of the plot cluster in two distinct groups: oblique-slip normal faulting and low-angle normal faulting. A smaller subset of events are clearly associated with thrust faulting. Note that all four groups of mechanisms include at least two mechanisms with a grade of C or better, and all groups except for that associated with thrust faulting include at least 10 mechanisms assigned a grade of F or better.

The distribution of these different types of mechanisms with depth suggests a systematic vertical variation in the style of deformation in this region (Figure 2-10). The most reliable

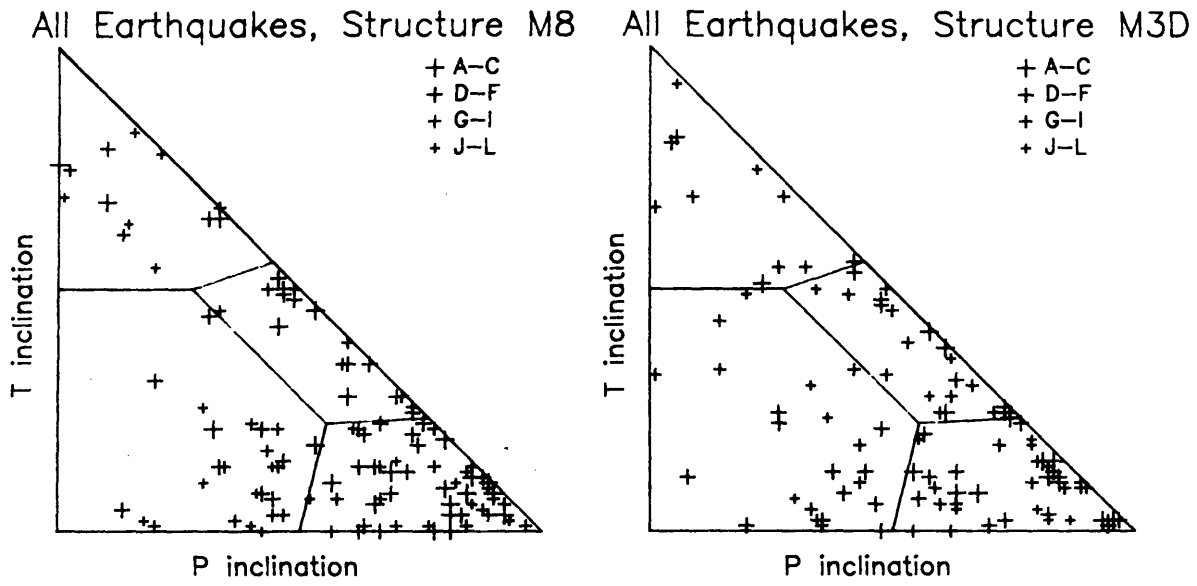

Fig. 2-9: "PI-TI" plot of all focal mechanisms determined in this study using both the one-dimensional M8 structure and the three-dimensional M3D structure; symbols are keyed to the quality of each mechanism. Compare with Figure 2-8. Note the distinct separation between the low-angle normal fault solutions (along the triangle's hypotenuse) and the oblique-slip solutions (bottom center of the triangle). The other two fields delimited here are termed "normal-slip solutions" (lower right corner) and "thrust-slip solutions" (top part of triangle).

(quality A-F) mechanisms indicating possible low-angle normal faulting are located below 4 km depth; most are between 4 and 6 km depth. A large concentration of events with oblique-normal slip appears to have occurred above 4 km; the presence of the velocity gradient at 3.7 km depth between the P-wave low-velocity zone and the higher velocity material below it suggests that this difference in the observed focal mechanisms might be an artifact of the velocity structure chosen to locate the earthquakes. For example, because of an error in the velocity structure used, events located just above this gradient might appear to represent oblique-normal slip despite having occurred as slip by some other mechanism.

Investigation of systematic errors of focal mechanisms

To test the possible effects that the velocity structure might have on the observed focal mechanism, I determined the takeoff angles and azimuths for each observed arrival using velocity structures differing from the original M8 structure only in the depth of the second velocity gradient. The earthquakes were not relocated in the new structures. Grades were then assigned to these new focal mechanisms to reflect only the quality of fit of the first motions to orthogonal nodal planes. This procedure tends to exaggerate the probable errors

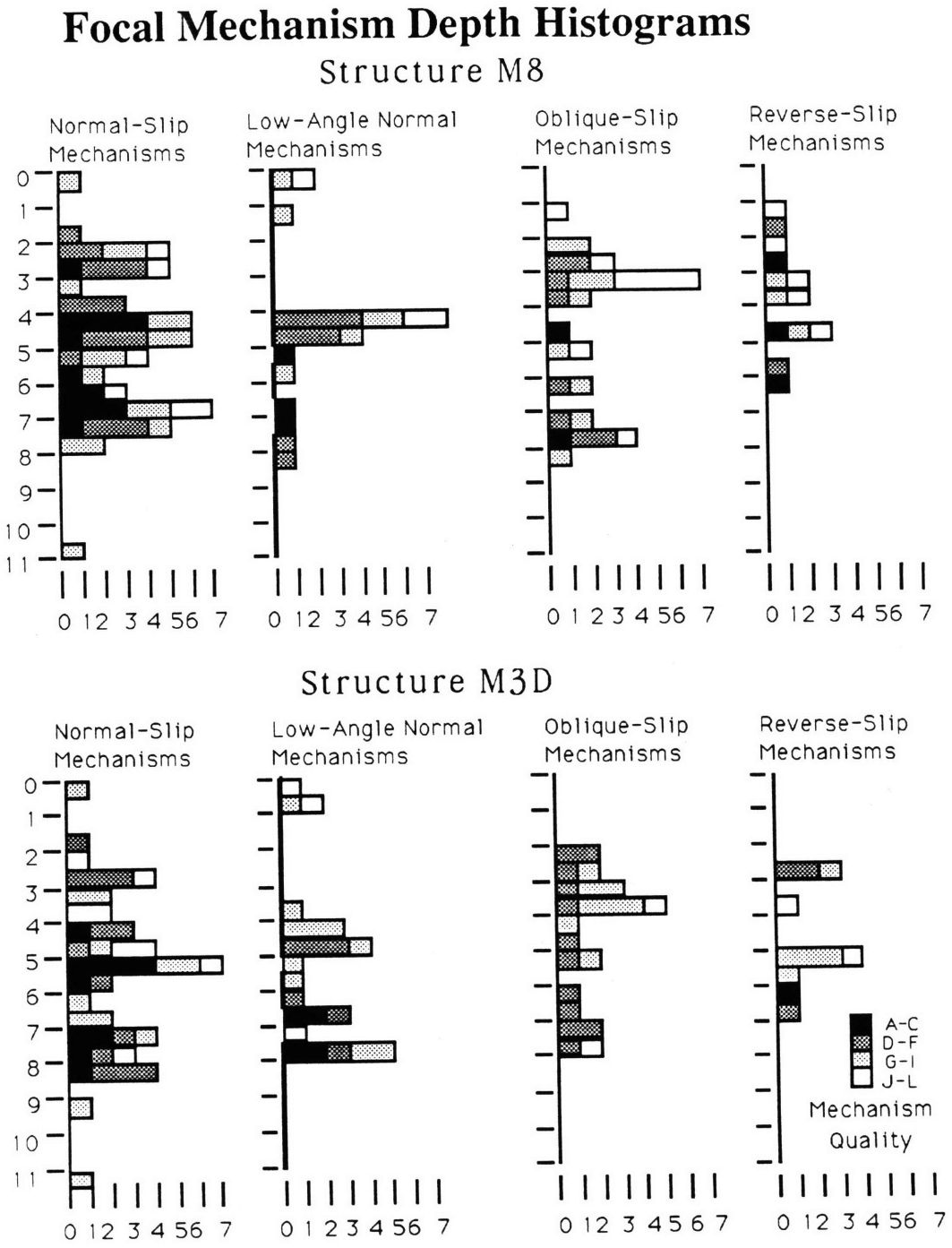

Fig. 2-10: Histogram of events with depth divided by fault type, as categorized in Figure 2-9, for events in structures M8 and M3D. Note, in particular, the differences in the "oblique-slip" and "low-angle normal slip" groups.

of the takeoff angles determined from the M8 velocity structure because if the events were relocated they would tend to return toward their original position relative to the steep velocity

gradient. Thus by placing an event both above and below the interface, the range of possible takeoff angles should be bracketed, and the effect of this range on the variability in the focal mechanisms can be constrained.

In these tests, the second velocity gradient, at 3.7 km depth in structure M8, was placed at three different depths: 6.0, 4.7, and 3.0 km depth for structures T6.0, T4.7, and T3.0, respectively. For each of these structures the earthquakes can be conveniently divided into three groups: events above the second gradient in both the new and original structure ("both above"), events below the gradient in one structure but above it in the other ("between"), and events below the gradient in both structures ("both below"). For all three test structures, mechanisms of events below the gradient in both the test and the M8 structure are usually the same as the M8 mechanisms (e.g., "both below" events, Figure 2-11). Mechanisms determined from the test structure for events within the two other groups are often significantly and systematically different from those determined from structure M8.

Mechanisms from the events that always lie above the second gradient ("both above") differ from structure to structure because of changes in some of the takeoff angles caused by the difference in depth of the prominent refractor beneath the earthquakes. Fewer phases will be refracted from a deeper interface than from one just below the hypocenter, and, thus, more first motions plot nearer the edges of the equal-area projection for a deeper interface. This makes nodal planes for oblique-slip solutions, determined using a structure with a shallower refractor, dip less steeply; and the solutions approach pure dip-slip faulting on planes dipping about 45° when a structure with a deeper refractor is used. On the PI-TI plot of Figure 2-12, mechanisms determined using a shallower refractor will plot nearer the center than the equivalent mechanisms using a deeper refractor. This effect, only slightly visible in Figure 2-12, is dominated by the lower quality of the mechanisms determined using any of the test structures. That is, when one of the test structures was used, most of the mechanisms examined simply became worse, because the number of violated polarities increased and the constraints on the nodal planes weakened. This change in quality is most noticeable when comparing mechanisms obtained using structures T3.0 and M8 (e.g., event 198, Figure 2-11; Figure 2-12).

The difference between the mechanisms obtained using two different velocity structures is much more dramatic for events lying above the velocity gradient in one structure and below it in the other (the "between" group, Figures 2-11 and 2-12). Two effects contribute to the differences in these mechanisms. First, many arrivals refracted along the velocity gradient for hypocenters above this velocity gradient will be reinterpreted as direct arrivals if the earthquake is relocated below the velocity gradient. These direct arrivals will be plotted both on the opposite hemisphere from and nearer to the horizontal than the equivalent

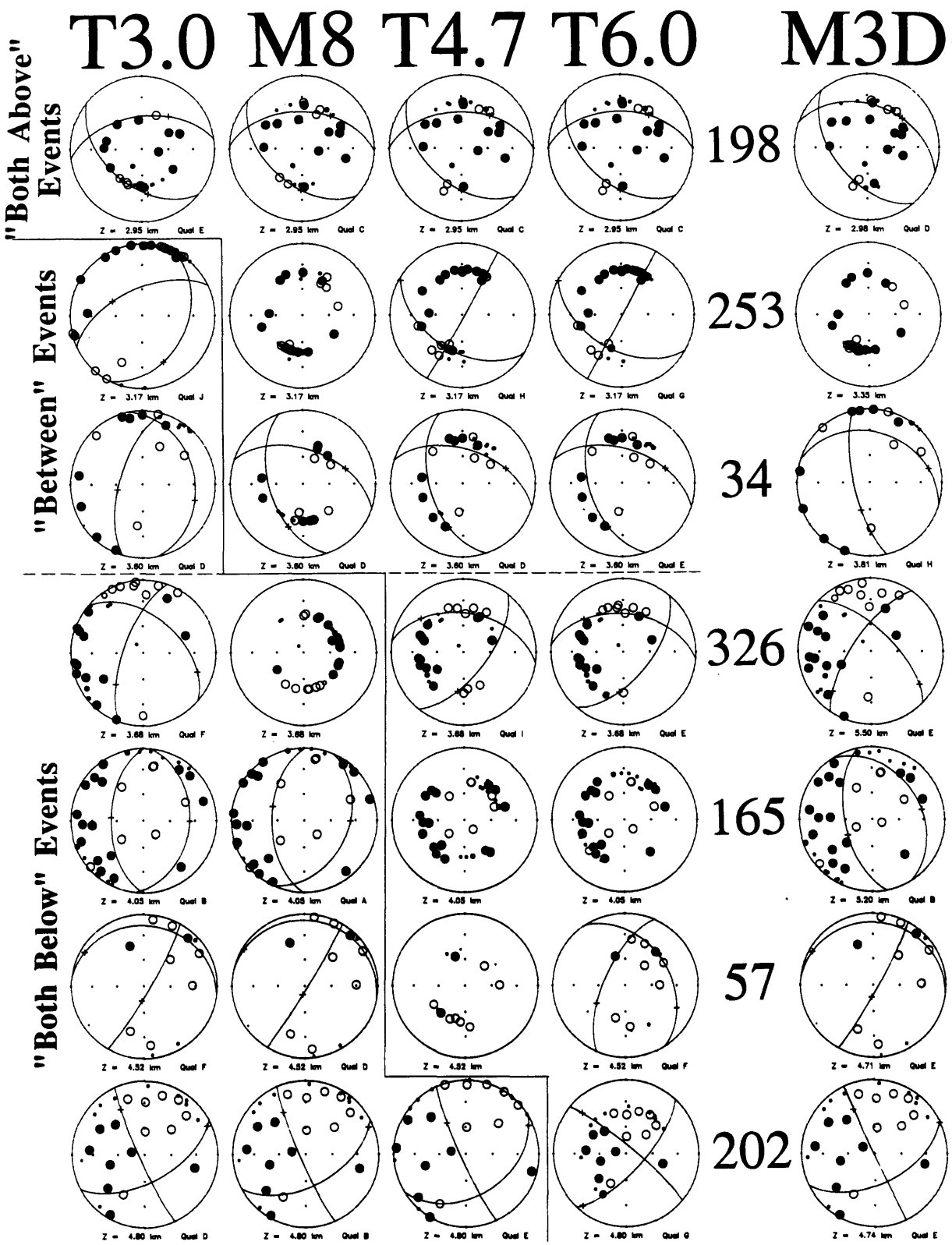

Fig. 2-11: Focal mechanisms of seven events located both in structures M8 and M3D and in the three trial structures T3.0, T4.7, and T6.0. The mechanisms are ordered with increasing

refracted arrivals. Second, those arrivals considered to be upgoing in both velocity structures will plot nearer the edges of the equal-area plot if the earthquake is located below the velocity gradient in the higher velocity material. Hence the takeoff angles of most arrivals will be shallower for hypocenters located beneath the velocity gradient than for those located above the gradient. This causes mechanisms determined using a deeper velocity gradient to lie nearer the hypotenuse in Figure 2-12 than the equivalent mechanisms determined with a shallower gradient.

These results strongly suggest that an apparent concentration of oblique-slip and low-angle-normal-slip mechanisms in a restricted depth range could be an artifact of their calculated depths relative to the assumed depth of a velocity gradient. Without some control on the depth of such a gradient, correlations of the style of faulting with the depths of these mechanisms are tenuous. Fortunately, some events are sufficiently well recorded that they can provide some control on the velocity structure; the polarities of first arrivals for these events are consistent with a double-couple source only when the events are located within a subset of the velocity structures considered. A well-recorded, well-located earthquake (event 165 in Figure 2-11) has tightly constrained normal-fault focal mechanisms when located beneath the second velocity gradient (structures T3.0 and M8, Figure 2-11). When placed above this gradient in structures T4.7 and T6.0, the observed distribution of polarities becomes inconsistent with a double-couple source, and no pair of orthogonal planes can separate up from down polarities without violating numerous (more than four) high-quality polarities. This is also true for event 233 (not shown). Hence these two events at 4 km depth and probably any other events reliably located beneath them very likely occurred below the second velocity gradient.

The shallow limit on the depth of this gradient is not well constrained. Events located between 3 and 3.7 km rarely produce tightly constrained focal mechanisms (e.g. events 253, 34, and 326 in Figure 2-11). Indeed, of the 21 events recorded by more than 30 stations, no

---

depths of the earthquakes. The solid line indicates the position of the refractor in each structure with respect to the focal depths determined using structure M8. The dashed line separates events located above and below 3.7 km depth. Mechanisms above both solid and dashed line are part of the "both above" group, those between these lines are in the "between" group, and those below both lines are in the "both below" group. Note the clustering of polarities in the center of the focal sphere for mechanisms of events above the refractor (toward the right side) relative to those of events below it (toward the left side). The event locations used to determine the M3D mechanisms are not the same as for the other mechanisms. Event numbers are keyed to Table 3-A1 (Chapter 3) and are chronological.

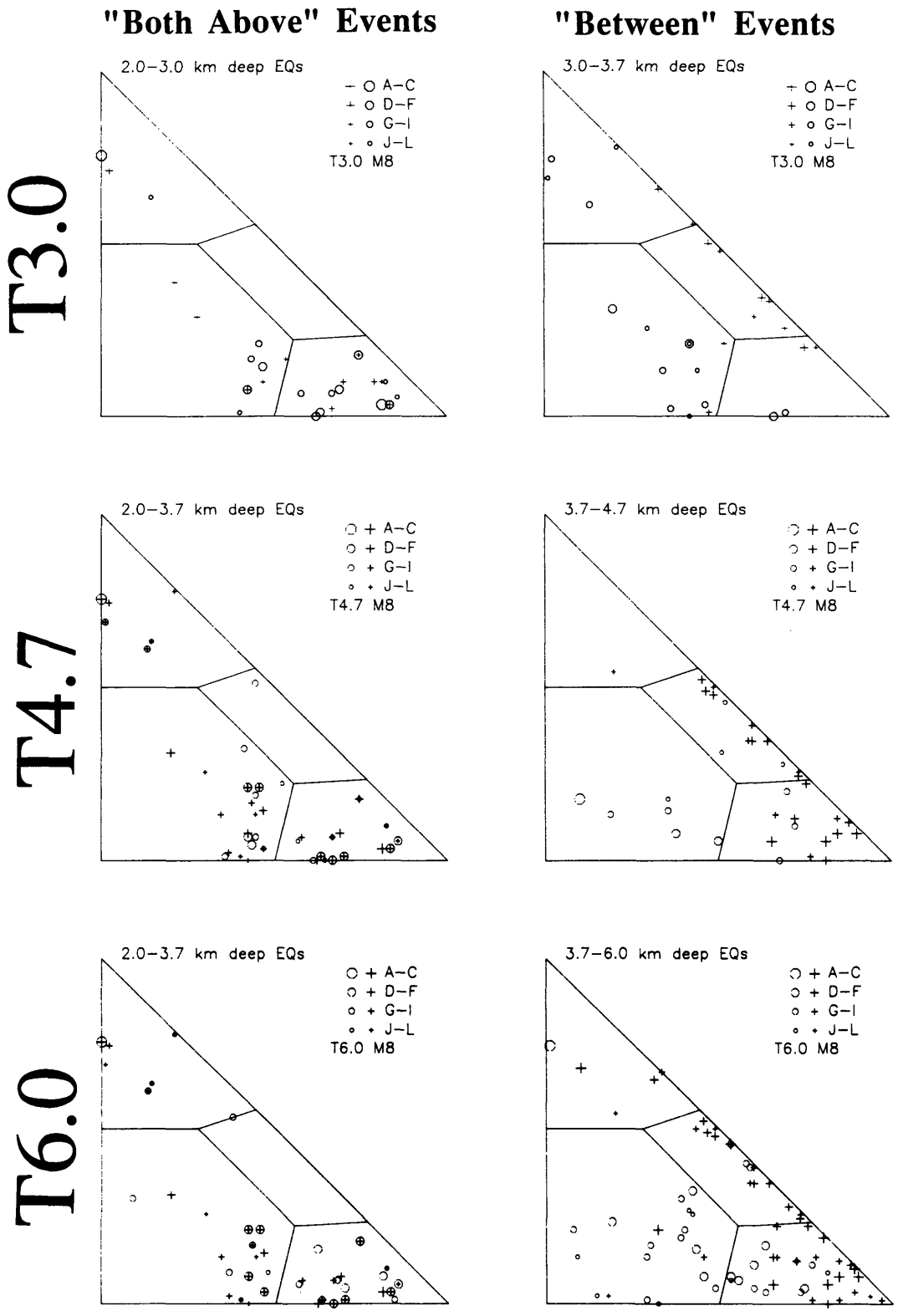

Fig. 2-12: PI-TI plots comparing focal mechanisms of velocity structure M8 with three test structures T3.0, T4.7, and T6.0. The left column of diagrams illustrates the difference in

reliable focal mechanism could be determined for 7 of them using structure M8; four of these seven lie between 3 and 4 km depth. Two of the other three occurred at the edge of the network, thus their focal mechanisms are poorly constrained; the other is located just below the 1.5 km velocity gradient. Hence a surprisingly high portion of the earthquakes recorded by more than 30 stations but lacking focal mechanisms lie between 3 and 4 km depth. Two of the four events located between 3 and 4 km depth without focal mechanisms using structure M8 were placed within the test structures T3.0, T4.7, and T6.0 (events 253 and 326, Figure 2-11). Focal mechanisms can be found for both events in any of the test structures. Unfortunately the quality of the fit of a double-couple to these events or the other shallow events (events 198 and 34) does not vary greatly from structure to structure. Although a disproportionately large number of events lacking focal mechanisms when the M8 structure is used are located between 3 and 4 km, none of the alternative structures consistently provides a superior fit to the observed polarity data. Hence the focal mechanisms interpreted from the observed polarities do not constrain the shallowest possible depth of the second velocity gradient, but they do indicate that the velocity structure between about 3 and 4 km is probably different from that of structure M8.

Although the observed distribution of focal mechanisms with depth could be an artifact of the velocity structure employed in locating the earthquakes, some bounds on the extent of any systematic error can be inferred from the focal mechanisms of events near the critical velocity gradient. Events located at 4 km depth yield well-constrained focal mechanisms using structures in which the second velocity gradient lies above them, but they do not produce focal mechanisms consistent with a double-couple source if this gradient is below them (Figure 2-11). This misfit appears to constrain the velocity gradient to lie above 4 km depth. Mechanisms of events between 3 and 4 km do not provide any constraint on the location of this gradient; indeed, the poor fits to many of the observed distributions of P-wave first motion polarities suggest that the M8 velocity structure inadequately approximates the true velocity structure in this depth range. This poor approximation of the M8 velocity structure

---

mechanisms of events located above the second refractor in both structures ("both above" events); the right column illustrates the difference in mechanisms for events located above the refractor in one structure and below it in the other ("between" events). The velocity structure of the test structures is identical to M8 except for the depth of the second velocity gradient (3.7 km in M8), which is at 6.0, 4.7, and 3.0 in structures T6.0, T4.7, and T3.0, respectively. Earthquake locations are identical in all structures. In the right column, crosses represent earthquakes located below the velocity gradient, circles represent earthquakes above that gradient.

could reflect either lateral velocity variations in the earth or greater complexity in the vertical structure than I can resolve using travel times. Events located above 3 km, while not tightly constraining the depth of the second velocity gradient, do indicate that a strong refractor is not likely to be as shallow as 3 km depth ("both above" group of structure T3.0, Figure 2-12). Hence focal mechanisms of events located above 3 km and below 4 km depth are tentatively considered to be free of the effects of any large systematic error associated with any incorrect approximations made to the true velocity structure near the second velocity gradient.

THREE-DIMENSIONAL STRUCTURE

The preceding discussion of the uncertainties of earthquake locations and focal mechanisms assumed that seismic velocities vary only with depth. The earth, especially at the shallow depths under study here, is laterally heterogeneous. Hence I inverted the arrival times for a three-dimensional velocity structure and evaluated the implications of such a structure for conclusions drawn from the one-dimensional structure.

Inversion for a 3-D structure

The three-dimensional structure was determined using the REL3D and HYPIT codes of S. Roecker (see Roecker [1981, 1982] for a detailed description of the inversion procedure). These codes permit us to locate earthquakes within a three-dimensional structure defined as a matrix of rectangular blocks, each with an internally uniform P- and S-wave velocity. Hence for a given block geometry the arrival time data can be alternately inverted for earthquake location and velocity structure until a stable solution for both is achieved. The codes do not determine the exact ray geometry for each arrival; instead, they use a ray geometry calculated from the average one-dimensional structure between the source and receiver [Thurber and Ellsworth, 1980]. The travel time is then calculated using this raypath and the full three-dimensional velocity structure. Near large lateral variations in the velocity structure this strategy can produce substantial errors; although I have not explicitly investigated these errors, I believe them to be less important than others that are addressed.

The three-dimensional structure was found through a series of experiments considering structures with different geometries and numbers of blocks. Starting with numerous blocks, I simplified each succeeding structure until the minimum variance found in a succeeding experiment increased. Because of the greater number of parameters being determined than for a one-dimensional structure, arrival times from all 130 events recorded by more than 11 stations were used in all the inversions for three-dimensional structure. As for the one-dimensional structures, each configuration of the velocity structure was inverted several times

for earthquake location and velocity structure until the variance of the residuals did not improve. These velocity inversions were conducted using station delays used for the 1-D structure M8. The first structure had six layers with interfaces at 1.5, 2.5, 3.7, 4.7, and 7.2 km depth; all layers except for that below 7.2 km were subdivided into 35 blocks. For two different trials the block x-axis was oriented at 11° and 50° clockwise from north; the final variances were 0.02102 and 0.02099 s^2, respectively. These represent a 5% improvement over the 0.02212 s^2 variance for these events using structure M8, but neither orientation is obviously better than the other. Although the mosaic of velocities in these structures is complex, a group of blocks with low velocities lying near the center of the network appeared to be the largest and most coherent feature.

After a succession of 15 further structures with progressively fewer blocks in the three layers above a halfspace, the best velocity structure had 12 blocks in its upper layer (-2 to 1.5 km), 3 blocks with interfaces oriented N107°E in its second layer (1.5 to 3.7 km), and the two deeper layers lacked any lateral variation. Its most prominent features are the relatively low seismic velocities (both P and S) inferred to underlie the center of the network to a depth of about 3.7 km. The variance associated with this structure is 0.02067 s^2; the improvement in variance over more complex structures reflects a similar fit to the arrival times with a reduction in the number of degrees of freedom. Although this indicates that a more complex source structure is not required, it does not preclude the existence of a more complex structure.

Because the station delays had been fixed throughout this experiment, I did not count station delays as degrees of freedom of the velocity structure, n_f in (2-2), in calculating the variances presented above. The delays were computed from the mean residual travel times, however, and hence are parameters of the velocity structure. By including all non-zero station delays in n_f, the variance increases from 0.02067 s^2 to 0.02101 s^2; including both zero and non-zero station delays increases the variance to 0.02118 s^2. Because the station delays probably represent lateral velocity contrasts, and to preclude the possibility that incorrect station delays were responsible for the lateral variations of velocity described above, I conducted a new experiment using a structure differing from the best-fit structure only in the top layer; this layer was divided into 117 blocks and all station delays were eliminated. The new structure (M3D, Figure 2-13) resulting from this inversion improved the variance to 0.02093 s^2 using only 80 of the 117 shallow blocks. Although the improvement of this structure over that with station delays is only 0.4% or 1.2%, depending on the number of station delays counted as degrees of freedom, I use it because I believe that most of the station delays that were measured reflect near-surface velocity variations rather than

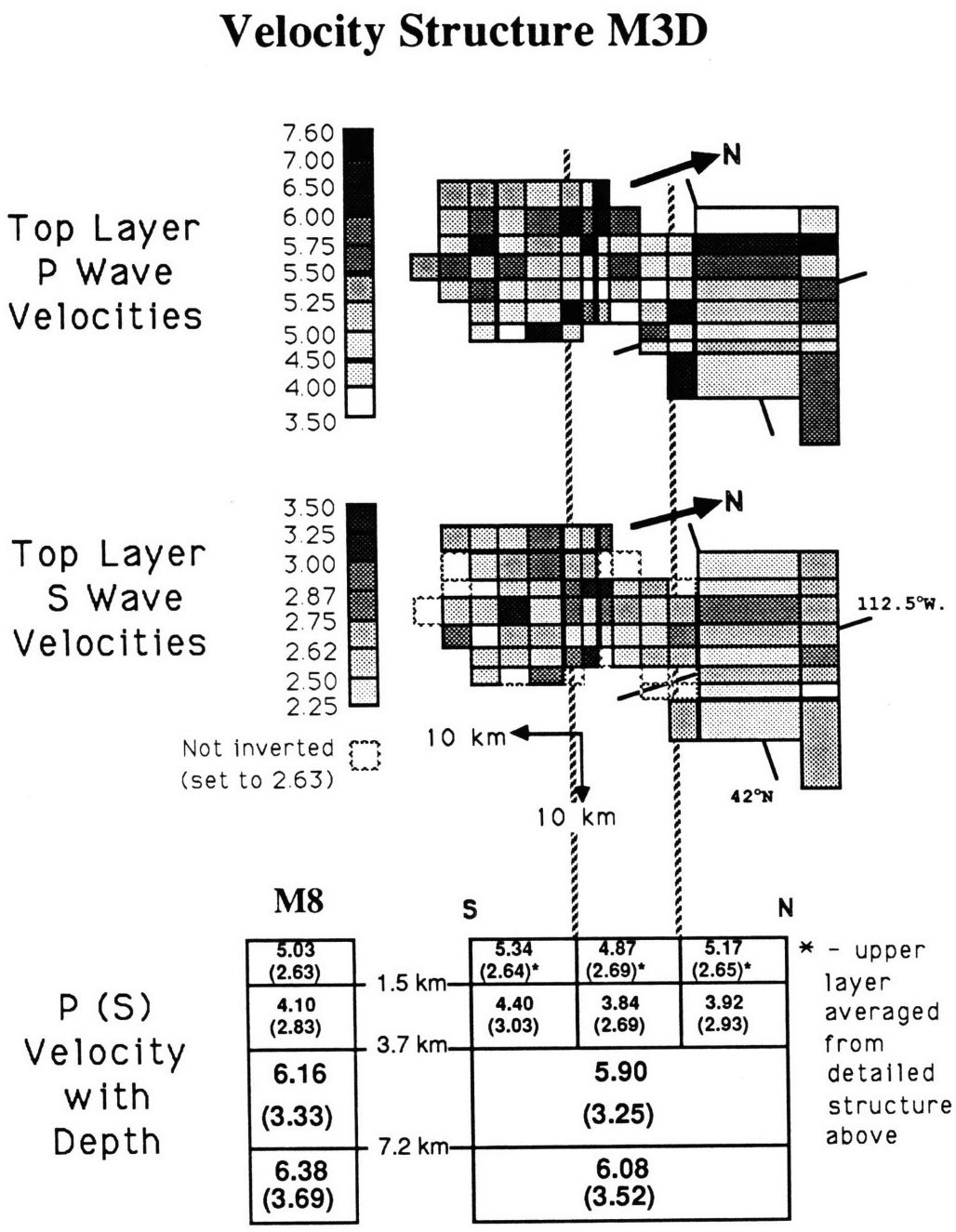

Fig. 2-13: Velocity structure M3D. Structure M8 is shown at bottom left for comparison with M3D. All velocities are in km/s. Uninverted blocks in the upper layer are set to the P or S velocity of structure M8.

mislocations of station, systematic errors in the time-corrections, or other effects. The velocities within this uppermost layer, however, should not be literally interpreted as actual velocities because these other effects, while minor, have been incorporated into these velocities.

The M3D structure reduces the variance of the travel-time residuals by about 7% from structure M8; the variance can be reduced by only 2.5% if the second layer lacks any lateral heterogeneity. The remaining 4.6% variance reduction can only be realized by including the three blocks in the second layer; this reduction is roughly equally due to the presence of the northern and southern contrasts. To increase the variance by 1%, the boundary between the southern and central blocks must be moved about 4 km north or south, or the more poorly defined boundary between the northern and central blocks can be moved about 8 km. The orientation of these boundaries can be changed up to about 20° before the variance increases 1%. Moreover, these uncertainties are probably conservative because the region affected by changing the parameters is sampled by a small subset of the total arrivals.

The final three-dimensional velocity structure M3D reduces the variance of the residuals of events recorded by more than 11 stations by about 7% while minimizing the number of parameters necessary to describe the velocity structure. This represents a significant improvement from the best-fit 1-D structure M8 and is almost as significant an improvement to that structure as was the addition of one layer to the best-fitting 3-layer velocity structure of Figure 2-3 to create M8. By minimizing the complexity of this 3-D structure, I suggest that this structure can be used to determine a conservative estimate of the errors in earthquake locations caused by using a one-dimensional structure in a laterally heterogeneous earth.

SYSTEMATIC ERRORS FROM A 3-D STRUCTURE

Reanalyzing the data from northern Utah in the M3D velocity structure produces many changes in the event locations and in focal mechanisms that suggest that results from the M3D structure are systematically different from those of the M8 structure. For clarity I shall consider the M3D structure to be an accurate description of the true velocity structure of northern Utah; hence these systematic differences are treated as errors resulting from the M8 structure. Differences between the locations and focal mechanisms of the two structures that do not appear to be systematic might include other, unrecognized systematic errors but are considered to be caused by random noise. Note that my assignment of the "error" to the M8 structure could instead be assigned to M3D if the one-dimensional M8 structure were more correct than the three-dimensional M3D structure, and thus the "errors" described below are a caution against both over-simplified and exaggerated velocity structures.

Location Errors

Four systematic differences in location were detected when the earthquakes previously located using the M8 velocity structure were relocated using the three-dimensional M3D

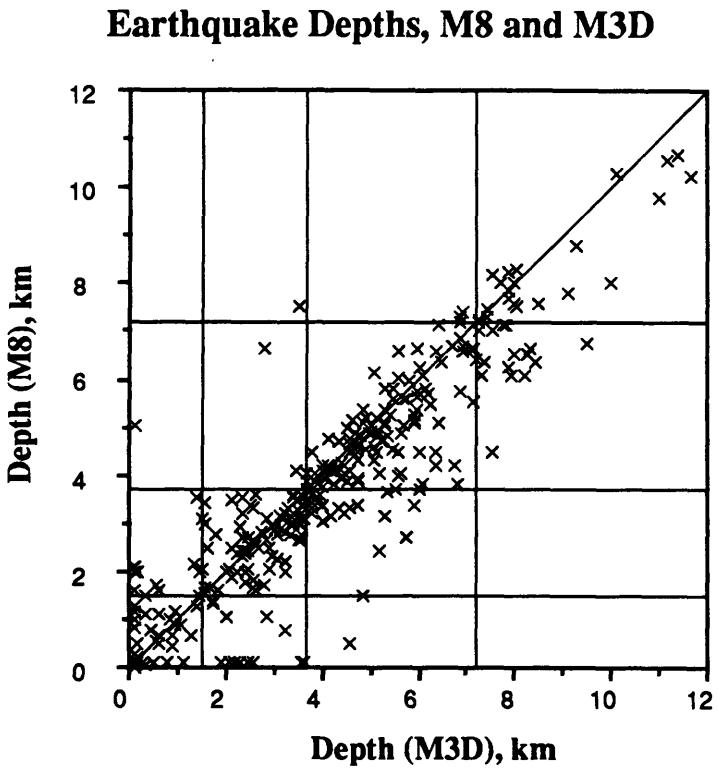

Fig. 2-14: Comparison of calculated focal depths using structures M8 and M3D. Horizontal and vertical lines mark velocity layer boundaries of the structures; events plotting within one of the blocks along the diagonal are within the same layer in both structures.

structure. The first systematic difference is common between velocity structures: earthquakes located at or near a velocity contrast in one structure tend to be freed in another and consequently are located farther from that contrast. The second is identical to changes observed when altering a one-dimensional structure: earthquakes tend to be relocated up or down if the mean velocity is increased or decreased, respectively. The third error is the horizontal analog to the second: in the presence of lateral velocity variations, earthquakes will tend to be located closer to the region with a lower velocity. All three of these systematic errors are easily anticipated. A fourth systematic error found in the northern Utah data is not so easily anticipated: the lateral changes in the velocity structure caused events recorded by large numbers of stations to be located at very different depths in the one- and three-dimensional structures, both in an absolute framework and relative to events recorded by a smaller number of stations. This error has the greatest potential for producing significant errors in any interpretation of the results of the inversion.

Events located erroneously near a velocity contrast are easily identified when an alternative structure is available because these events will be distributed over a greater depth range in the alternative structure than the structure under study. Hence when the depths of

events in the two structures are plotted versus one another, those events erroneously located near a velocity contrast in one structure will fall in a linear band near the depth of that contrast and parallel to the depth axis of the alternative structure. For structures M8 and M3D (Figure 2-14) we see that such a band does exist near the 3.7-km-depth velocity contrast in structure M8, suggesting that events were systematically incorrectly located near that depth in that structure. A more distinct but less populated band lies near the 1.5-km-depth boundary in structure M3D. The strongest bands for both structures are at a depth of 0.0 km.

Systematic location of earthquakes near a velocity boundary can be produced by the use of any iterative earthquake relocation program because the linearized approximations used in these programs fail near a velocity boundary; hence the computed change in the earthquake location can be incorrect and a new location on the opposite side of the interface will produce a greater misfit to the data and will be rejected, leaving the earthquake hypocenter near the velocity contrast. To avoid this particular problem I examined the best-fitting locations for each earthquake from four runs of the relocation routine, each with a different starting depth. For structures M8 and M3D these starting depths were 2, 5 and 8 km and the final location of the previous relocation, thus bracketing both of the deeper velocity contrasts. Thus for each earthquake, the hypocenter that best fits the observed arrival times within the structure used should be correctly determined.

Despite locating all events both above and below 3.7 km in structure M8, a cluster of locations was obtained at that depth (Figures 2-4 and 2-13). Because a more dispersed distribution probably cannot be found to fit the measured arrival times better, this cluster of events in structure M8 probably does not reflect a procedural error caused by the failure of the linearized approximations used in the earthquake-relocation program. Instead, if the cluster is an artifact of errors in the data or the location procedure, as discussed below, it, nevertheless, is located near a velocity contrast because such a contrast provides a global minimum in the variance of the travel-time residuals. This particular problem might be best described as a systematic grouping of earthquakes that are poorly located because of other errors in the velocity structure.

The shallower clusters in both structures are probably related to incorrect velocities near the surface and the prohibition on earthquakes being located above 0 km depth. Conceivably some of these events are mislocated because of unrealized errors that remain in these structures; for structure M8, these errors could include local velocity anomalies, and for structure M3D, these errors could include incorrect velocities in the shallowest layer that compensate for other errors at individual stations.

Systematic depth errors from a difference in the mean velocity near the earthquake are generally masked by other errors and uncertainties, but the tendency for events to be deeper

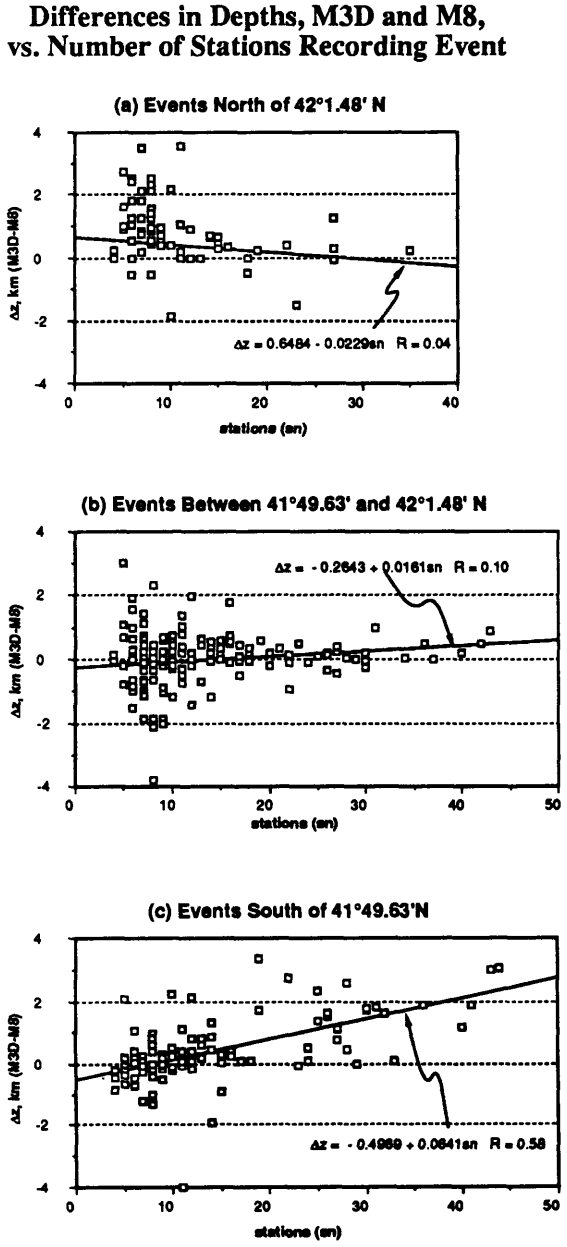

Fig. 2-15: Difference in depths of events located using structures M8 and M3D versus the number of stations recording the earthquake in the (a) northern, (b) center, and (c) southern portions of the network. Lines and equations describe a simple linear regression of depth difference onto the number of stations. The differences in depth are positive for events at a greater depth in M3D than in M8.

in M3D than M8 (Figure 2-14) might reflect such a systematic relationship. A clear example comes from the earthquakes north of about 42°N (Figure 2-15a), where the average one-dimensional P-wave velocity structure is about 5% lower in M3D than M8. In this region the events located using less than 11 stations have a median depth 0.9 km deeper in M3D than M8; this probably reflects the local decrease in velocity. Better-recorded events might be more tightly constrained (and hence less affected by changes in the velocity structure) or might be affected by other systematic errors that might tend to reduce the earthquake depth as discussed below.

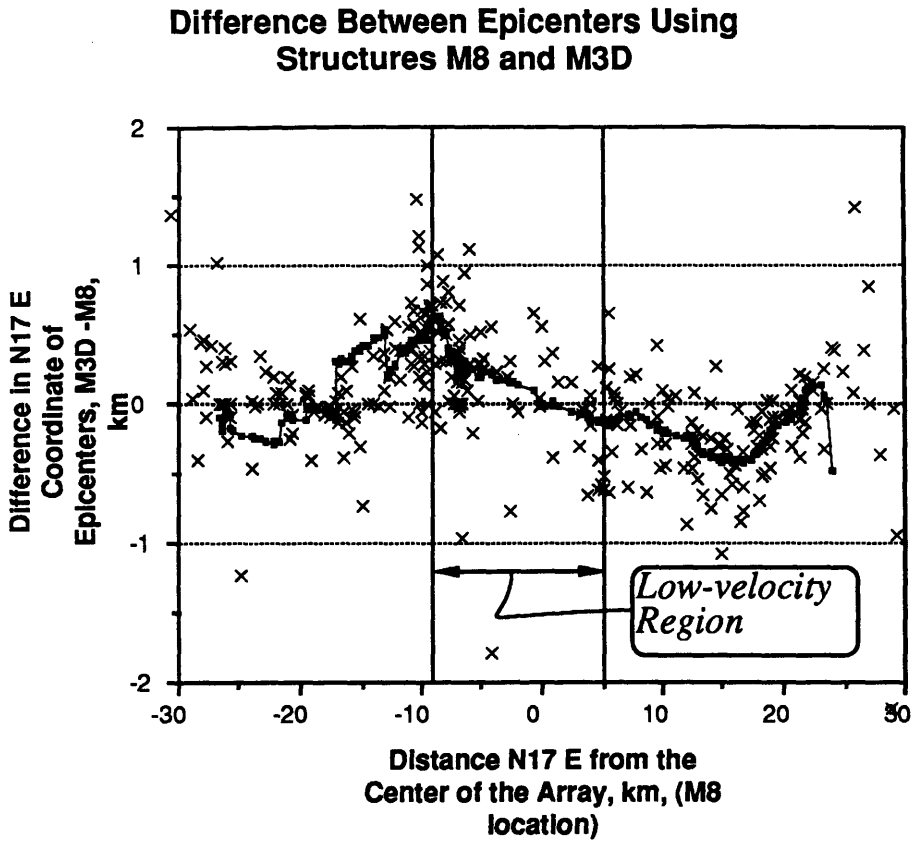

Fig. 2-16: Difference in distance along N17°E between M8 and M3D earthquake locations versus the distance of the M8 location N17°E from the center of the network at 41°55'N, 112°45'W. A more northerly latitude of the M3D location relative to the M8 location is positive. Curve is a 25-point running mean of the latitude difference.

The epicenters of events near horizontal velocity contrasts tend to lie nearer the region with lower velocities than when located with structure M8. In structure M3D, events located on the sides of the prominent low-velocity region in the center of the network are closer to that region by about 0.5 km than when located in structure M8 (Figure 2-16). This effect clearly dominates the differences in the epicenters determined using M8 and M3D; it is quite likely that some of the remaining scatter in the epicenter differences, roughly ≤0.5 km, is due to a variation of the intensity of this error with depth or the distribution of stations recording the earthquake rather than to the uncertainties of the epicenters due to noise in the arrival time data.

The final identified systematic error causes substantial changes in both absolute and relative depths of earthquakes if lateral variations of the velocity structure are ignored; these errors increase with the number of stations recording the earthquake. Generally one would expect that parameters of well recorded earthquakes would be the least sensitive to

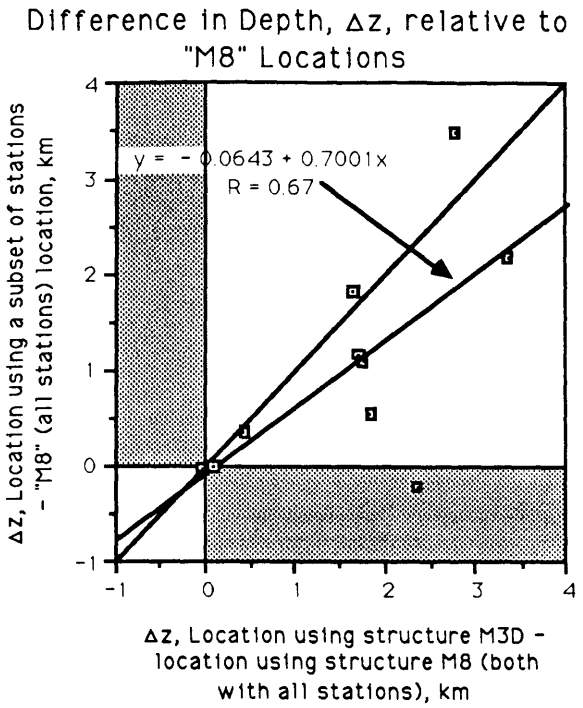

Fig. 2-17: Differences between depths of earthquakes located using M3D and those located using structure M8, horizontal axis, plotted versus the differences between the depths of earthquakes located using only local stations in structure M8 ("experimental" locations) and those using structure M8 and all available stations, vertical axis. In the absence of a systematic error, points would plot along the vertical axis. Positive values of both axes (in the unshaded quadrent at upper right) indicate an increased depth of either M3D or "experimental" location relative to M8 location.

perturbations of the velocity structure so that differences in location from one structure to another would tend to be smaller for better-recorded earthquakes than poorly recorded ones. This appears to be the case in the center portion of the network (Figure 2-15b). Calculated depths of events recorded by less than 15 stations differ by as much as 2 km between the M3D and M8 locations, while those recorded by more than 15 stations rarely differ by more than a few hundred meters. In contrast, in the southern portion of the network events recorded by larger numbers of stations are found to be systematically deeper with structure M3D than with structure M8 (Figure 2-15c). This systematic error requires close examination because of its effect on better-recorded earthquakes and the systematic change between events in the same area.

A simple test illustrates that the smaller and not the larger events are more accurately located within structure M8. Twelve of the events recorded at 18 or more stations were

selected as an experimental group; arrival times from the most distant stations were removed, leaving only the subset of stations that usually recorded the smaller earthquakes in the southern part of the network. These events were then relocated within the one-dimensional M8 structure. Ten of the twelve events yielded stable, acceptable locations. These "experimental" locations were then compared with the locations of the same events that had been calculated using all available data and structures M8 and M3D; the calculated depths of the "experimental" locations are closer to those of structure M3D than to those of structure M8, as indicated by the similar difference in depth from both the "experimental" and M3D locations to the M8 locations (Figure 2-17).

This test of removing data from some stations and examining the change in the computed location often is used to compare the relative uncertainties of well- and poorly-recorded earthquakes [Chatelain et al., 1980; Prevot et al., 1980; Grange et al., 1984]; certainly the inherently greater uncertainties accompanying the use of a smaller set of arrival times affect the results of Figure 2-17. In the absence of a systematic error, however, the differences between the "experimental" locations and the M8 locations should be random with respect to the difference between the M8 location and the M3D location. The greater uncertainty in the "experimental" locations, due to the smaller number of stations used, should cause the differences between these locations and those using the M3D structure to be larger than those between locations determined using the M8 and M3D structures, particularly for the large, well-recorded events used here. The opposite is observed: if the M3D locations are correct, then the "experimental" locations are far more accurate than the M8 locations that use all the available stations. This strongly suggests that the cause of the systematic change in depth is a lateral velocity anomaly sampled only by rays to distant stations; either removing arrival times for such rays, as for the "experimental" group of locations, or correcting for that velocity anomaly, as for the M3D locations, removes the bias caused by the anomaly and permits the earthquake to be correctly located.

In northern Utah I have found that a striking local low-velocity anomaly underlies the center portion of the network; this body is capable of producing anomalous residuals that will cause well-recorded earthquakes to be systematically mislocated (Figure 2-18). The 1-D inversion routine satisfies the arrival times at stations near the low-velocity material in two ways: first, the calculated origin time of the earthquake is late, satisfying the delay of the distant stations ("1" in Figure 2-18), and second, the depth of the earthquake is decreased to fit the arrival times at stations close to the earthquake ("2" in Figure 2-18). If more distant stations record the event, a third effect arises: inverting these arrival times, which now appear to be early at these more distant stations, for the 1-D velocity structure produces a

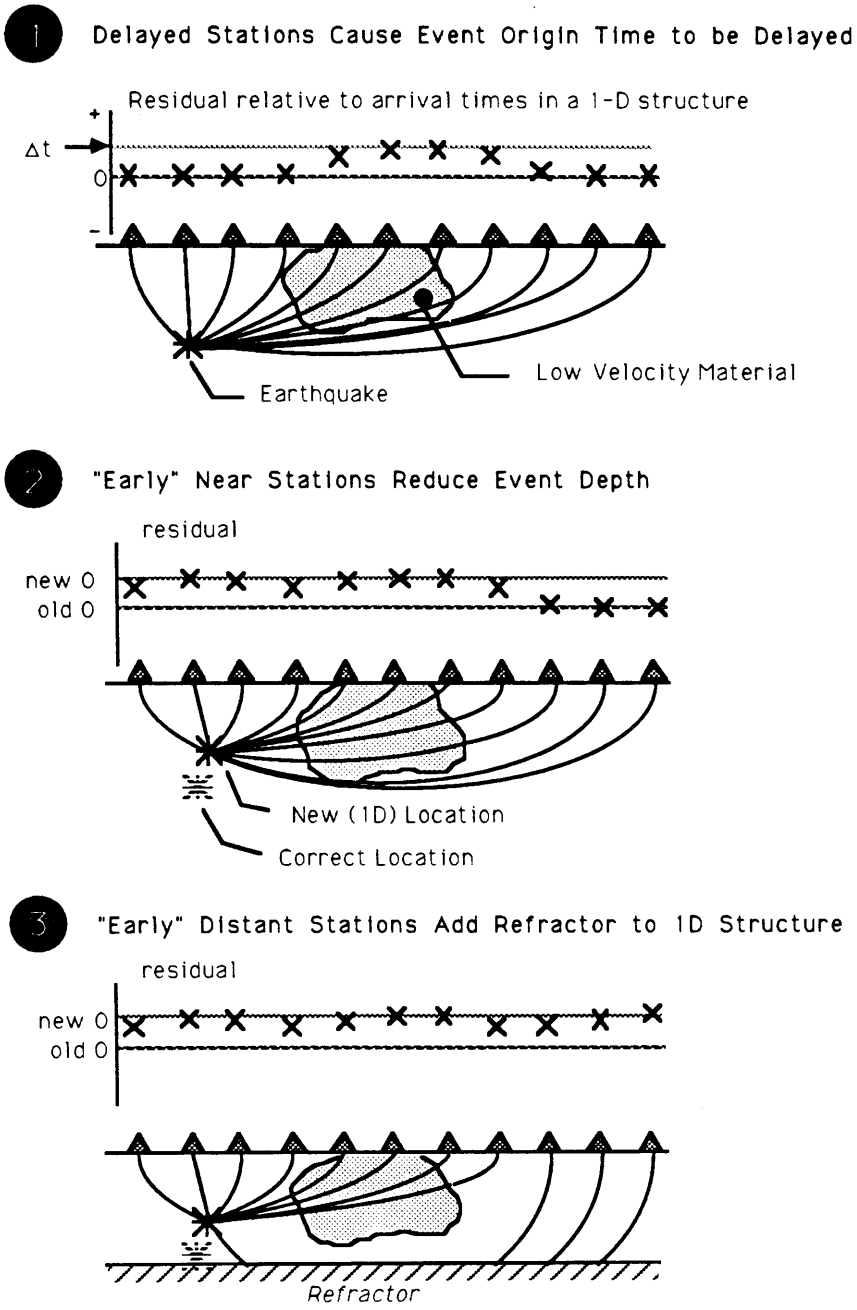

Fig. 2-18: Cartoon illustrating a possible explanation for the observed differences in M8 and M3D locations in the southern part of the network. The numerical ordering is solely for clarity.

high velocity refractor at the bottom of the layered structure. As noted above, arrival times from events only near the north or south end of the network constrained the velocity of this layer. Since these rays can pass under the low-velocity material, the phases are not delayed

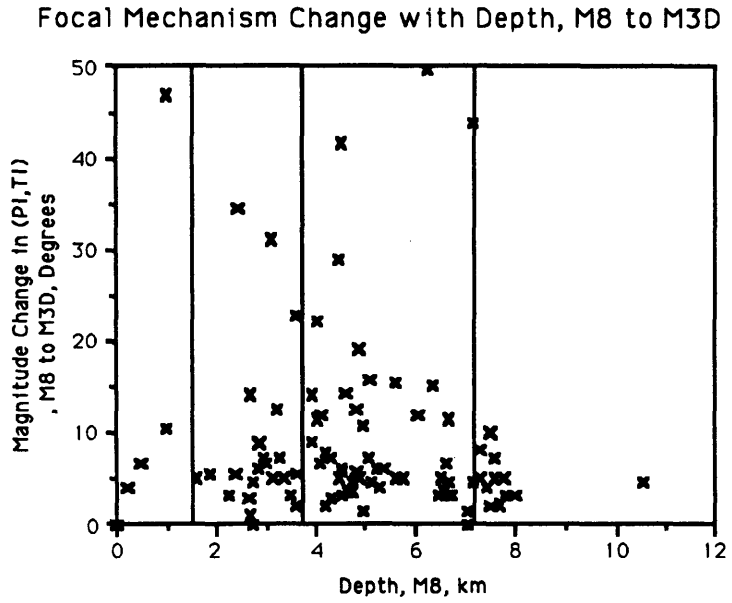

Fig. 2-19: Differences (in degrees) in event type, measured on a PI-TI plot (Figure 2-8), between focal mechanisms from M8 and M3D versus depth within structure M8.

and hence appear to be early when the earthquake has been relocated as just described. Thus, these early arrivals cause the velocity inversion routine to produce a higher velocity in the lowest layer ("3" in Figure 2-18; Figure 2-13).

Although the foregoing discussion applies to the southern part of the network, a similar systematic effect might exist in the northern part of the network (Figure 2-15a). In this case, the anomalously high velocities of the southern part of the network might cause the northern events to be located deeper than the local events; all the events might be shallower in the M3D structure because of the change to the local velocities as described above. The poorer correlation in the north of depth differences with the number of recording stations (Figure 2-15a), the sparser station density, and the accompanyingly greater uncertainties make any attribution of the exact cause of the observed depth variations tentative.

Errors in Focal Mechanisms

As discussed at length for a one-dimensional structure, any systematic error in the depth of an earthquake is capable of producing large changes in the nature of the focal mechanism obtained from that earthquake. Because of the strikingly large and systematic changes in the depths of earthquakes between structures M8 and M3D I could expect some systematic changes in the pattern of focal mechanisms described from the M8 structure. In particular,

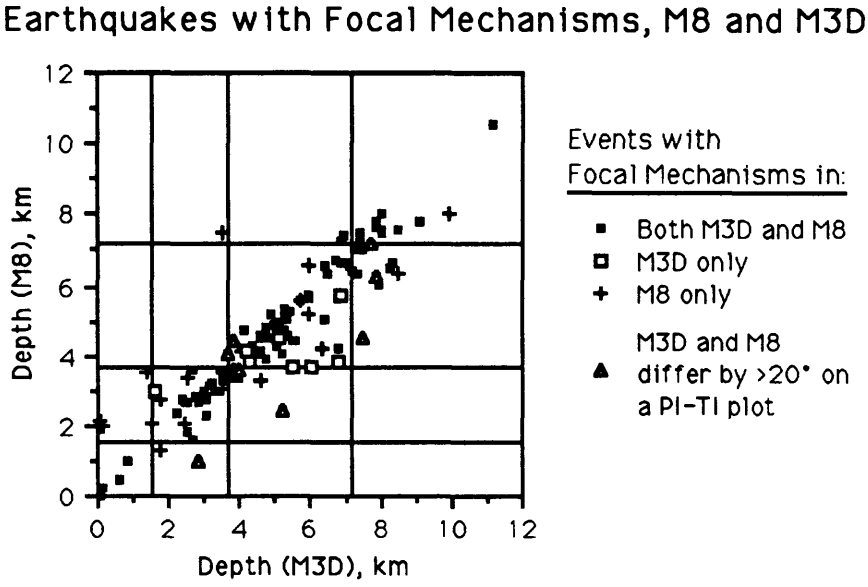

Fig. 2-20: Comparisons of depths using structures M8 and M3D of events with focal mechanisms obtained with either M3D or M8 or both; conventions as in Figure 2-14.

the large differences in calculated focal depths for earthquakes in the southern part of the network should result in substantial differences in the focal mechanisms of these events. I measure the difference between focal mechanisms obtained using structures M8 and M3D as the distance, in degrees, between the points for each mechanism on a PI-TI plot (e.g., Figure 2-8). Surprisingly, the PI-TI positions of most of the 90 events with mechanisms determined using both M8 and M3D have mechanisms that differ by no more than 20° (Figure 2-19). For these events most of the difference between mechanisms corresponds to a rotation of one mechanism of less than about 15° about the null axis; on a PI-TI plot, the two mechanisms would plot as a pair of points on a line parallel to the hypotenuse of the triangle (e.g., Figure 2-8).

Although the small number of events with a drastic difference between the mechanisms determined using M8 and M3D is reassuring, those few large differences urge caution in interpreting all mechanisms. Focal mechanisms were obtained in both structures only for a very few of the events that, from my earlier analysis, might be expected to have drastically different mechanisms: those events that were located using structure M8 on the opposite side of a velocity gradient from the locations found using structure M3D. In particular, focal mechanisms could be uniquely determined in both structures for only five of the many events that were located within the low-velocity zone in one structure and outside it in the other (Figures 2-14 and 2-20); all five pairs of mechanisms differ by more than 20° on a PI-TI plot

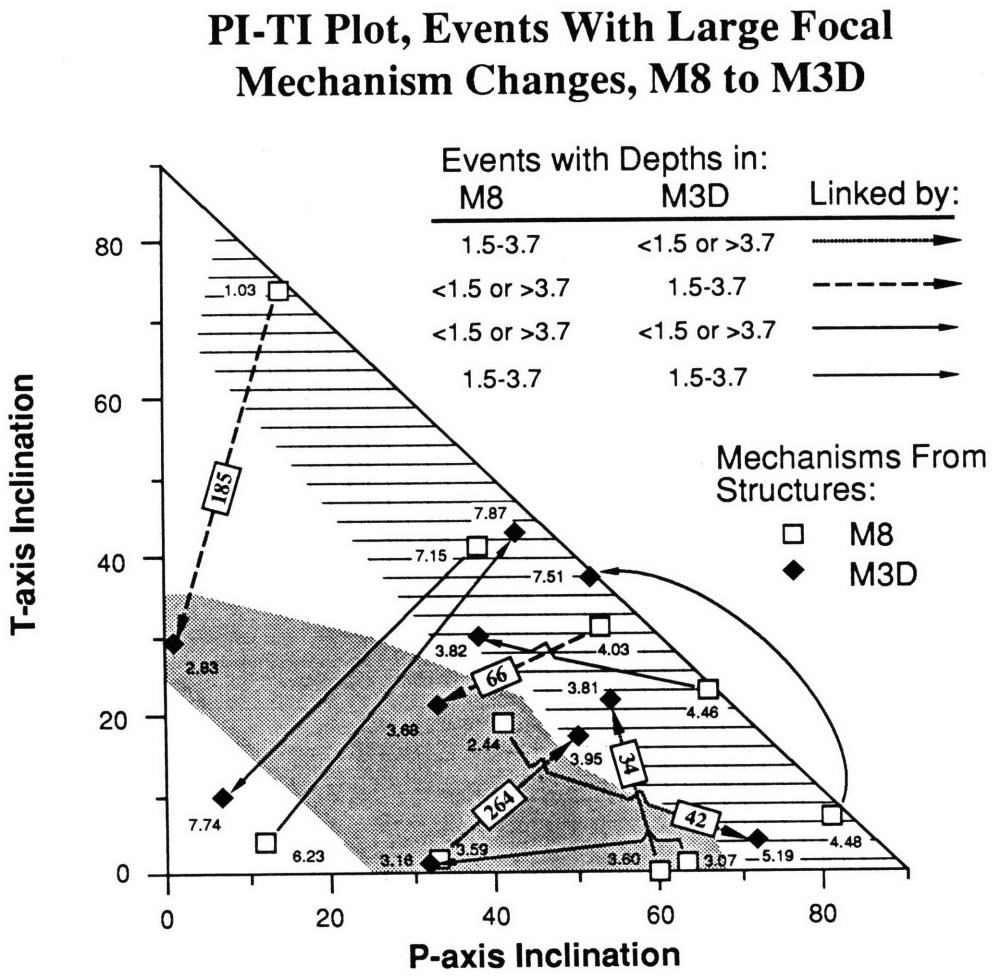

Fig. 2-21: "PI-TI plot" of the events with focal mechanisms using both M8 and M3D that differ by more than 20°. The shaded region includes those events located within the low-velocity zone between 1.5 and 3.7 km depth in only one of the two structures; the lined area includes the points representing the same events located in the other structure and outside the low-velocity zone. The two regions are analogous to the two groups of points in the "between" events plot of Figure 2-12. Small number near each point is the event's depth in that structure; numbers on lines connecting mechanisms of selected events are keyed to Table 3-A1 (Chapter 3).

(Figure 2-21) and display strong differences in the distributions of polarities over the focal sphere (Figure 2-22). The difference between the mechanisms is very similar to that anticipated from the experiments conducted with a one-dimensional structure: events located within the low-velocity zone tend to have mechanisms representing oblique-slip faulting (the shaded area on Figure 2-21), while those located outside tend to have mechanisms

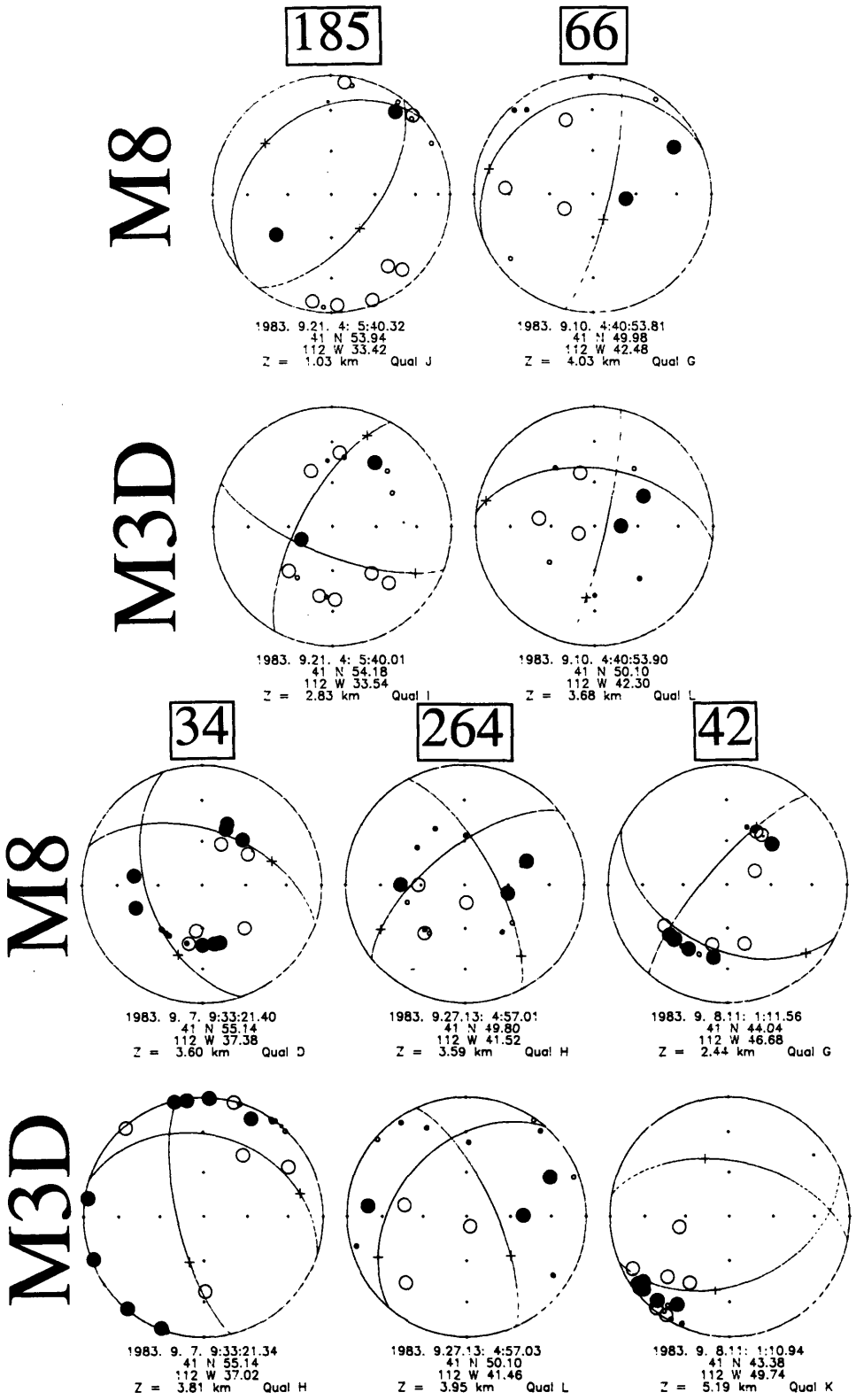

Fig. 2-22. Focal mechanisms of the only five events located within the low-velocity zone in either M8 or M3D but not both that yielded focal mechanisms in both M8 and M3D. Event

representing more nearly pure dip-slip faulting (the lined area on Figure 2-21; compare Figures 2-21 and 2-12). Hence the greatest errors in focal mechanisms determined using the one-dimensional structure appear to be caused by the differences in depth between locations within the one- and three-dimensional structures.

Focal mechanisms of 31 events could be determined using only one of the two structures. Twenty-one mechanisms found using M8 were not adequately constrained using M3D; these were low-quality (mean quality of I) mechanisms from poorly recorded earthquakes (mean of 12 stations recording each event) that usually could be fit by several different types of faulting when located in the M3D structure. Quite good (mean quality F to G) solutions were obtained using M3D (e.g., event 326, Figure 2-11) for ten events, most of whose mechanisms contain polarities that could not be fit without violating a large subset of the polarities when located with structure M8. Not surprisingly, 9 of these 10 events were located within 1 km of 3.7 depth when using structure M8 (Figure 2-19), confirming the preceding analysis that concluded that mechanisms of events between 3 and 4 km were not accurately determined in structure M8.

The combination of the changes in some individual mechanisms and the elimination and addition of several more mechanisms produces substantial changes in the distribution with depth of the different types of faulting (Figure 2-10). In particular, the "spike" of events with mechanisms possibly representing low-angle normal faulting located between 4 and 5 km in structure M8 does not exist when structure M3D is used; a similar "spike" of events with oblique-slip mechanisms at about 3 km depth is also somewhat smaller when M3D is used. This pair of spikes, which appeared to be very important when the M8 results were compiled, now appears to represent an artifact of the M8 structure.

The most dramatic difference in focal mechanisms occurs in the part of the network south of 41° 49.63'N, where well-recorded events were located at very different depths in structures M8 and M3D. In structure M8 I determined 45 focal mechanisms, 11 of which are consistent with slip on a low-angle normal fault and fall within the "low-angle normal-slip" field of Figure 2-9. Five of these events were assigned a quality of F or better, and the depths of the 11 events concentrate near 4 km. In M3D, 18 of the 42 focal mechanisms are consistent with

---

numbers are the same as in Figure 2-21. For the two events on top, the M3D location is within the low velocity zone between 1.5 and 3.7 km depth, and the M8 location is outside it. For the other three events, the M3D location is outside the low-velocity zone and the M8 location is inside it. Compare with the differences in mechanism of the same event in Figure 2-11.

slip on a low-angle normal fault; eight are of quality F or better, and the depths of the 18 events are distributed between about 4 and 8 km. The greater percentage and mean depth of events consistent with low-angle normal slip in structure M3D clearly suggests the possibility that these events form a more important part of the tectonic framework within the southern part of the network than might be inferred from the results from structure M8. Hence the use of even the best one-dimensional structure can produce results that do not accurately reflect the nature of faulting within the crust.

DISCUSSION

Despite my best efforts to produce an accurate one-dimensional structure and to define adequately the uncertainties associated with it, I have found that factors outside my initial assumptions tend to overwhelm the uncertainties constructed using those assumptions. Strong vertical velocity gradients are capable of producing focal mechanisms that tend toward a particular style of faulting; this tendency can be dictated as much by the position of the earthquake within the velocity structure as by the distribution of polarities from that event. This tendency can convert a systematic error of location, such as a systematically large depth for all events, into a systematic difference in the nature of faulting perceived, such as low-angle normal-slip instead of oblique-normal slip. I have also found that in some cases lateral velocity variations can produce errors in earthquake locations that are greater than the uncertainties estimated within a one-dimensional structure. Three of the four described types of systematic error produce systematic changes in the depths of earthquakes; these changes are an order of magnitude larger than the standard errors computed within a one-dimensional structure and can be a factor of two or three greater than the changes estimated from comparing the locations from a best-fit one-dimensional structure with those from another one-dimensional structure structure with unacceptably high travel-time residuals. Thus errors in depths resulting from an error in the velocity structure and the consequent errors in takeoff angles and hence focal mechanisms for earthquakes mistakenly located too near or too far from a strong velocity contrast can produce systematic mislocations and focal mechanisms that are nearly unrelated to the style of faulting that produced the earthquakes.

The errors described here indicate that in some situations relocating earthquakes relative to a "master event" might actually increase the errors rather than decrease them. So-called "master event" techniques can be employed to obtain locations of events relative to a larger earthquake that is considered to be accurately located, reducing the uncertainty and error of the location of a smaller event relative to a larger event. Any error in the location of the master event, however, will be transferred to the smaller events. I have shown that better-

recorded events can be systematically mislocated in depth if a lateral velocity contrast is present but not included in the velocity structure used to locate the earthquakes. Thus applying a relative relocation technique could systematically mislocate all earthquakes by several kilometers. This can become a serious problem if focal mechanisms are determined from the relocated events, because, as indicated earlier, systematic depth errors can change the apparent style of faulting to a large degree.

Close examination of travel times and their residuals can reveal the presence of lateral velocity contrasts. Systematically higher rms residuals for well-recorded events relative to more poorly recorded events can reflect velocity variations sampled by the larger events but absorbed as location errors by the smaller events. Relocating larger events using only a subset of the available stations can reveal systematic location errors caused by lateral velocity variations. Travel-time curves will reveal lateral velocity contrasts in some instances, but both the noise in and azimuthal dependance of systematic residuals often make these contrasts difficult to discern for individual earthquakes. Determining a one-dimensional structure for subregions within an network can allow the presence of lateral velocity variations to be detected, but the one-dimensional structures may not accurately represent the local one-dimensional structure at any point. Finally, the full inversion of travel-time data for a three-dimensional structure, such as that employed here, provides the best test for the presence or absence of lateral velocity contrasts.

Some constraints on the accuracy of focal mechanisms can come from the mechanisms themselves. If any well-recorded, well-located earthquakes with many well-distributed polarities cannot be made to be consistent with a double-couple seismic source, one should consider the possibility of systematic error in the focal mechanisms obtained with that velocity structure. If several such events are clustered in depth, it is likely that all events located in that depth range are in error to some degree; this is particularly true if a strong velocity contrast is present in that depth range. For northern Utah, I found that events located between 3 and 4 km depth using the one-dimensional structure were suspicious for this reason; when the data were reanalyzed using the M3D structure, most of the changes in the observed focal mechanisms came from events that had been located between 3 and 4 km in the one-dimensional structure (Figure 2-10). Note that strike-slip faulting is largely exempt from these problems because the polarities of arrivals from such events depend only on the azimuth from the earthquake to the recording station. Hence well-constrained, well-recorded strike-slip faulting mechanisms are not a good indicator of the absence of systematic error in focal mechanisms. The presence of either a strong velocity contrast or well-recorded earthquakes whose polarities cannot be fit by a pair of orthogonal planes indicates the

possibility of systematic errors in those other focal mechanisms for which the polarities appear to be consistent.

The procedure followed in this study adequately allows microearthquake arrival times to be used to locate earthquakes and define the velocity structure of a laterally heterogeneous medium:

1) Location of all events in a simple, one-dimensional structure,
2) Joint inversion of arrival times from well-recorded earthquakes for earthquake locations and a one-dimensional velocity structure with a large number of layers,
3) Experimentation using progressively less complex one-dimensional velocity structures to determine the minimum complexity necessary to adequately fit the arrival times,
4) Inversion for a complex three-dimensional velocity structure using arrival times from a sufficiently large subset of earthquakes to determine the structure,
5) Experimentation using progressively less complex three-dimensional structures to determine the minimum complexity necessary to fit the arrival times,
6) Testing of the final locations and velocity structure for uncertainties and unresolved systematic errors.

The progression of these steps increases the accuracy of both earthquake locations and the velocity structure without risking spurious results that can be generated by inverting noisy data for a structure with a large number of degrees of freedom. A somewhat unexpected aspect of this procedure is the reduction in the number of degrees of freedom following the initial overestimation of the complexity of the velocity structure in steps (2) and (4). This sequence permitted me to discard those velocity boundaries that are unimportant and to examine the locations of the marked gradients in velocity, which define the structure under study; estimating the positions of important velocity contrasts *a priori* is difficult and likely to produce results that falsely indicate that no velocity contrast is present.

This paper has documented that errors estimated from a one-dimensional velocity structure are inadequate to describe the uncertainties within a three-dimensional medium. Nevertheless some indications of the presence of lateral velocity contrasts or other errors in the assumed velocity structure can be gleaned from the results of an inversion that assumes a one-dimensional velocity structure:

1) Clustering of earthquakes near an assumed velocity contrast,
2) Somewhat higher residual variances of well-recorded events than of poorly-recorded events,
3) Systematic variations of travel time residuals with distance from earthquake epicenters, particularly for well-recorded earthquakes,

4) Distributions of first-motion polarities of well-recorded, well-located earthquakes that cannot be fit by orthogonal nodal planes without violating large numbers of polarities,

5) Systematic differences between locations derived using different subsets of stations.

The presence of any of these situations can indicate the presence of an unrecognized lateral velocity contrast that should be investigated as described previously; the absence of these situations, though perhaps supporting the absence of lateral velocity contrasts, cannot be considered proof of the absence of lateral velocity contrasts.

Using data gathered in northern Utah, I have illustrated some of the possible systematic errors caused by lateral variations in the velocity structure that might escape conventional error analysis. The error analysis discussed here is not exhaustive: for example, systematic problems might be caused by anisotropy, source-receiver geometry, synchronization errors between stations, mislocation of stations, or changes in the network geometry with time. These uninvestigated sources of error are, I suspect, less important than the lateral velocity contrasts for this data but indicate the range of problems usually excluded from an error analysis. I hope that this work illustrates that limitations of conventional error analysis and encourages a more exhaustive exploration of uncertainties when conditions warrant.

CONCLUSIONS

Using data gathered from a temporary network in northern Utah, I determined a one-dimensional structure for the region covered by the network. The final structure (M8) had four layers with interfaces at depths of 1.5, 3.7, and 7.2 km depth. By examining many other structures with different parameters, including a greater number of layers, I believe that this structure has the minimum number of layers necessary to fit the observed arrival times adequately and that no structure with a greater number of layers fits the data well enough to warrant the inclusion of additional layers. The depths of the top and bottom interfaces are poorly constrained; the top interface probably lies between 0.5 and 2.5 km depth, and the bottom interface was fixed at 7.2 km depth. The middle interface is constrained to be between 3.2 and 5.2 km depth. The uncertainties of all the velocities are about 0.10 km/s.

Using this structure (M8) I located 337 earthquakes; the standard errors (1σ) of both the epicenters and the depths of these events were about 200 m. Relocation of the events in another structure suggested that more realistic uncertainties in depth are about 600 m, but that the standard errors for the epicenters reliably describe the uncertainties insofar as a one-dimensional structure is appropriate.

Focal mechanisms were determined for 110 events; these mechanisms were graded to indicate the overall accuracy of each mechanism in the presence of uncertainties in both the location of the earthquake and the velocity structure. A very abrupt difference between oblique-normal slip mechanisms above 3.7 km and possible low-angle normal slip below 3.7 km was investigated. This pattern could be an artifact of the velocity structure; I showed that earthquakes located below the 3.7-km-deep velocity contrast and characterized by low-angle normal faulting can appear to have occurred on high-angle oblique-normal slip faults if their locations lie above the velocity contrast. For this reason I considered focal mechanisms of events located between 3 and 4 km to be of dubious accuracy.

Reexamination of these arrival times using a three-dimensional structure (M3D) indicated that several systematic errors in hypocenters, and hence focal mechanisms, had gone undetected in the earlier analysis. In many cases, the errors in hypocenters exceeded the uncertainties estimated from the one-dimensional structures. Four types of systematic error were recognized. First, poorly located events tended to be located near the velocity contrast at 3.7 km in structure M8. Second, events located in structure M8 tended to be deeper or shallower than when located using structure M3D in regions where the mean M3D velocity near the earthquake was higher or lower, respectively, than that of the M8 structure. Third, earthquake epicenters were located closer to regions with lower mean velocities in M3D than in M8. Fourth, depths of the better-recorded events in the southern part of the network were systematically too shallow in structure M8, because of the low-velocity material near the center of the network (Figure 2-18).

Although the differences in locations of many events was significant, the orientations of P- and T-axes for most of the focal mechanisms determined did not differ by more than 15° from those found using M8 . Most of those that did differ had been located between 3 and 4 km deep in M8; mechanisms in this depth range had been considered suspect because of the systematic errors associated with the velocity contrast at 3.7 km depth. Although the frequency of the different types of faulting was about the same in M8 and M3D, the distribution with depth and epicenter was markedly different (Figure 2-10). For example, in the southern part of the network, approximately equal numbers of solutions with low-angle normal slip mechanisms and oblique-normal slip mechanisms were found using M8, but three times as many low-angle normal fault mechanisms were found with M3D.

Both the locations and focal mechanisms of earthquakes located in structure M8 differ by more than their uncertainties from the locations and focal mechanisms of the same events located in structure M3D. The systematic differences between the results from the one- and three-dimensional structures indicates that large, systematic errors can escape notice in an error analysis assuming lateral homogeneity of structure. A detailed interpretation of local

earthquakes using a one-dimensional structure could be entirely in error because the uncertainties obtained from a 1-D structure could exclude the true values of virtually every parameter from consideration. For this reason a thorough consideration of errors caused by factors other than noise in arrival time data should accompany any detailed investigation into the locations and focal mechanisms of local earthquakes.

REFERENCES

Arabasz, W. J., W. D. Richins, and C. J. Langer, The Idaho-Utah (Pocatello Valley) earthquake sequence of March-April 1975, in W. J. Arabasz et al. (eds.), *Earthquake Studies in Utah 1850 to 1978*, University of Utah Seismograph Stations Special Publication, Salt Lake City, p. 339-373, 1979.

Chatelain, J. L., S. W. Roecker, D. Hatzfeld, and P. Molnar, Microearthquake seismicity and fault plane solutions in the Hindu Kush region and their tectonic implications, *J. Geophys. Res.*, *85*, 1365-1387, 1980.

Dewey, J. W., W. H. Dillinger, J. Taggart, and S. T. Algermissen, A technique for seismic zoning: Analysis of earthquake locations and mechanisms in northern Utah, Wyoming, Idaho, and Montana, in *Contributions to Seismic Zoning*, edited by S. L. Harding, *NOAA Tech. Rept. ERL 267-ESL 30*, U.S. Dept. of Commerce, 29-48, 1973.

Estill, R. E., Temporal variations of P-wave travel times and lateral velocity structure across the Wasatch Front, Utah, M. S. thesis, Univ. of Utah, Salt Lake City, 181 pp., 1976.

Grange, F., D. Hatzfeld, P. Cunningham, P. Molnar, S. W. Roecker, G. Suárez, A. Rodrígues, and L. Ocola, Tectonic implications of the microearthquake seismicity and fault plane solutions in southern Peru, *J. Geophys. Res.*, *89*, 6139-6152, 1984.

Prevot, R., D. Hatzfeld, S. W. Roecker, and P. Molnar, Shallow earthquakes and active tectonics in eastern Afghanistan, *J. Geophys. Res.*, *85*, 1347-1357, 1980.

Richens, W. D., The Hansel Valley, Utah, Earthquake sequence of November 1976, in W. J. Arabasz et al. (eds.), *Earthquake Studies in Utah 1850 to 1978*, University of Utah Seismograph Stations Special Publication, Salt Lake City, p. 409-421, 1979.

Roecker, S. W., Seismicity and tectonics of the Pamir-Hindu Kush region of central Asia, Ph. D. thesis, 298 pp., Mass. Inst. Technol., Cambridge, 1981.

Roecker, S. W., Velocity structure of the Pamir-Hindu Kush region: Possible evidence of subducted crust, *J. Geophys. Res.*, *87*, 945-959, 1982.

Schneider, J. F., R. P. Meyer, and L. A. Powell, Timing and positioning of seismographs from Omega navigation signals, Proc. 16th Ann. Mtg. Intl. Omega Assn., Montreal, Canada, August, 1981, p.11-1--11-8, 1981.

Shenon, P. J., The Utah earthquake of March 12, 1934, in F. Neumann, *United States Earthquakes, 1934*, U. S. Coast and Geodetic Survey serial 593, p. 43-48, 1936.

Smith, R. B., and M. L. Sbar, Contemporary tectonics and seismicity of the western United States with emphasis on the Intermountain seismic belt, *Bull. Geol. Soc. Am.*, *85*, p. 1205-1218, 1974.

Smith, R. B., L. Braile, and G. R. Keller, Crustal low velocity layers: Possible implications of high temperatures at the Basin Range-Colorado Plateau transition, *Earth Plan. Sci. Letters*, *28*, 1295-1317, 1975.

Thurber, C., and W. L. Ellsworth, Rapid solution of ray tracing problems in heterogeneous media, *Bull. Seismol. Soc. Am.*, *70*, 1137-1148, 1980.

CHAPTER 3
SEISMICITY ACCOMPANYING EXTENSION WITHIN THE BASIN AND RANGE PROVINCE IN NORTHERN UTAH AND SOUTHEASTERN IDAHO

By Craig H. Jones, Peter H. Molnar,
Department of Earth, Atmospheric, and Planetary Sciences
Massachusetts Institute of Technology, Cambridge, MA 02139

Steven W. Roecker,
Department of Geology
Rensselaer Polytechnic Institute, Troy, NY

Robert. B. Smith,
Department of Geology and Geophysics
University of Utah, Salt Lake City, UT 84112

and Denis Hatzfeld
Laboratoire de Géophysique Interne et Tectonophysique,
Université Scientifique, Technologique et Médicale de Grenoble,
Grenoble, France

INTRODUCTION

Over the past twenty years evidence has been gathered supporting the existence of normal faults dipping less than 30° and perhaps dipping less than 10° [e.g., Allmendinger et al., 1983; Anderson, 1971; Armstrong, 1972; Davis et al., 1980; Davis, 1983; LePichon and Barbier, 1987; Reynolds and Spencer, 1985; Wernicke et al., 1985]. Although many aspects of these structures remain enigmatic, one substantial mystery has been the dearth of observations of seismic slip on these faults; virtually all of the observed fault plane solutions of major earthquakes that show normal faulting are characterized by nodal planes dipping more steeply than 30° [Jackson, 1987]. Similarly, a detailed investigation of the seismicity in southern Utah failed to reveal any earthquakes that required normal-sense slip on a gently dipping fault plane despite the presence of low-angle normal faults inferred from seismic reflection profiles [Arabasz and Julander, 1986]. Indeed, the apparent lack of earthquakes requiring low-angle normal slip has reinforced a tendency to consider geologically-mapped low-angle normal faults to be inactive [e.g., Zoback et al., 1981; Eaton, 1982] and to ascribe

the gentle dips of these faults to a more recent deformation of the fault surfaces that formed with steep dips (>45°) [e.g. Proffett, 1977, Gans et al., 1985].

We are aware of only two instances where Quaternary range-bounding faults can be associated with deeper low-angle normal faults. Using MINI-SOSIE reflection data Crone and Harding [1984] traced a range-bounding fault down from a surface scarp to a high-angle fault, which, in turn, is truncated at greater depth by the Sevier Detachment, imaged by reflection profiles with a deeper penetration [McDonald, 1976; Allmendinger et al., 1983]. Thus an apparently active fault is truncated by a low-angle normal fault. Geological [Burchfiel et al., 1987] and geophysical arguments [MIT 1985 Field Geophysics Course and Biehler, 1987 (Chapter 1)] together suggest that northern Panamint Valley in the Basin and Range Province of east-central California has opened entirely by slip on a low-angle normal fault in the upper few kilometers of the crust.

These two observations suggest that low-angle slip on normal faults has occurred in Quaternary time and might continue to occur; this slip could be accommodated by a few large earthquakes, by many small earthquakes, or without any seismicity. Slip by great earthquakes would require that the historical record be too short and unrepresentative of the slip history of these faults, but that further observation would eventually reveal a large earthquake with slip on a low-angle fault. This hypothesis can only be tested by continued observation of the seismicity of areas with Quaternary normal faults. Aseismic slip could only be observed geodetically; no existing data capable of resolving such slip is known to us. Microearthquakes on a low-angle fault can be observed by a sufficiently dense network of short-period seismometers, but prior to our study, microearthquakes did not seem to have shown evidence for seismic slip on low angle normal faults.

To examine the possibility that low-angle normal slip is accompanied by microearthquakes and to evaluate the mechanism of seismic extension in a portion of the Basin and Range Province, we deployed an array of portable seismographs in northern Utah and southern Idaho. The region is notable for the relatively high seismicity detected by the permanent seismic array of the University of Utah [e.g., Richens, 1979a]. This relatively high level of seismicity and the inferred presence of listric normal faults in the Great Salt Lake Valley to the south [Smith and Bruhn, 1984] suggested that this area might provide an adequate test of the hypothesis that seismic slip does occur on low angle normal faults.

To interpret the data gathered in this experiment, we inverted the travel-times observed for both the velocity structure and earthquake hypocenters. Both one- and three-dimensional velocity structures were investigated; we tried to construct structures in both cases that minimized both the number of free parameters and the overall variance. Using focal mechanisms derived from the final earthquake locations, we attempted to determine

individual structures that caused the observed earthquakes. The overall patterns in the seismicity, the individual structures that we could resolve, and the regional geology were examined to deduce the larger structures that, over time, probably absorb most of the deformation in the region. Our particular goal was to determine the relative importance of horst-and-graben structures, found by faulting on steep (>45°) planes, or of low-angle normal faults in describing the seismicity present in the region.

GEOLOGY AND HISTORICAL SEISMICITY

The Hansel Valley--Pocatello Valley region includes the north-south set of ranges and basins east of the larger Curlew Valley and west of the valleys along the Wasatch Front (Figures 3-1 and 3-2). Pocatello Valley is a closed depression about 10 km long; physiographically, it appears to be an extension of the much longer Blue Creek Valley to the south. Hansel Valley is a 20 km long, north-northeast trending valley contiguous with Spring Bay of the Great Salt Lake. Both Pocatello and Hansel valleys are asymmetrical in east-west profile, bounded on the east by steep slopes and on the west by somewhat gentler slopes. Both valleys also exhibit internal complexities. Pocatello Valley has two separate gravity minima [Harr and Mabey, 1976], one at the east edge of the valley just north of the Utah border and the other about 6 km to the north-northwest in the north central part of the valley. Northern Hansel Valley also has a local minimum extending about 6 km south from the northern end of the valley. The most negative gravity anomalies in the southern part of Hansel Valley lie near its western edge near the mapped surface ruptures from the 1934 Hansel Valley earthquake (Figure 3-2; Peterson [1974]). Exposures of Paleozoic bedrock in the eastern half of the southern part of Hansel Valley (Figure 3-1) do not lie within the gravity lows, thus supporting the inference that these lows are caused by unconsolidated sediment filling tectonic basins.

The Hansel, North Hansel, and North Promontory mountains contain chiefly sandstones, sandy limestones, and limestones of the Permo-Pennsylvanian Oquirrh Formation, while older sedimentary rocks of the Paleozoic North American continental margin are exposed in the Samaria Mountains (Figure 3-2; Allmendinger and Platt [1983], Doelling [1980]). The entire region is part of the "hinterland" of the Mesozoic Sevier orogeny; the more than 140 km of roughly east-west shortening evident in the Sevier fold-and-thrust belt to the east suggests that the hinterland is underlain by the westward extension of these west-dipping Mesozoic thrust faults [e.g., Allmendinger and Jordan, 1981, Allmendinger et al., 1984].

Large scale crustal extension may have occurred since Oligocene time in the Raft River and Grouse Creek mountains and the Albion Range about 50 to 100 km to the west [Compton

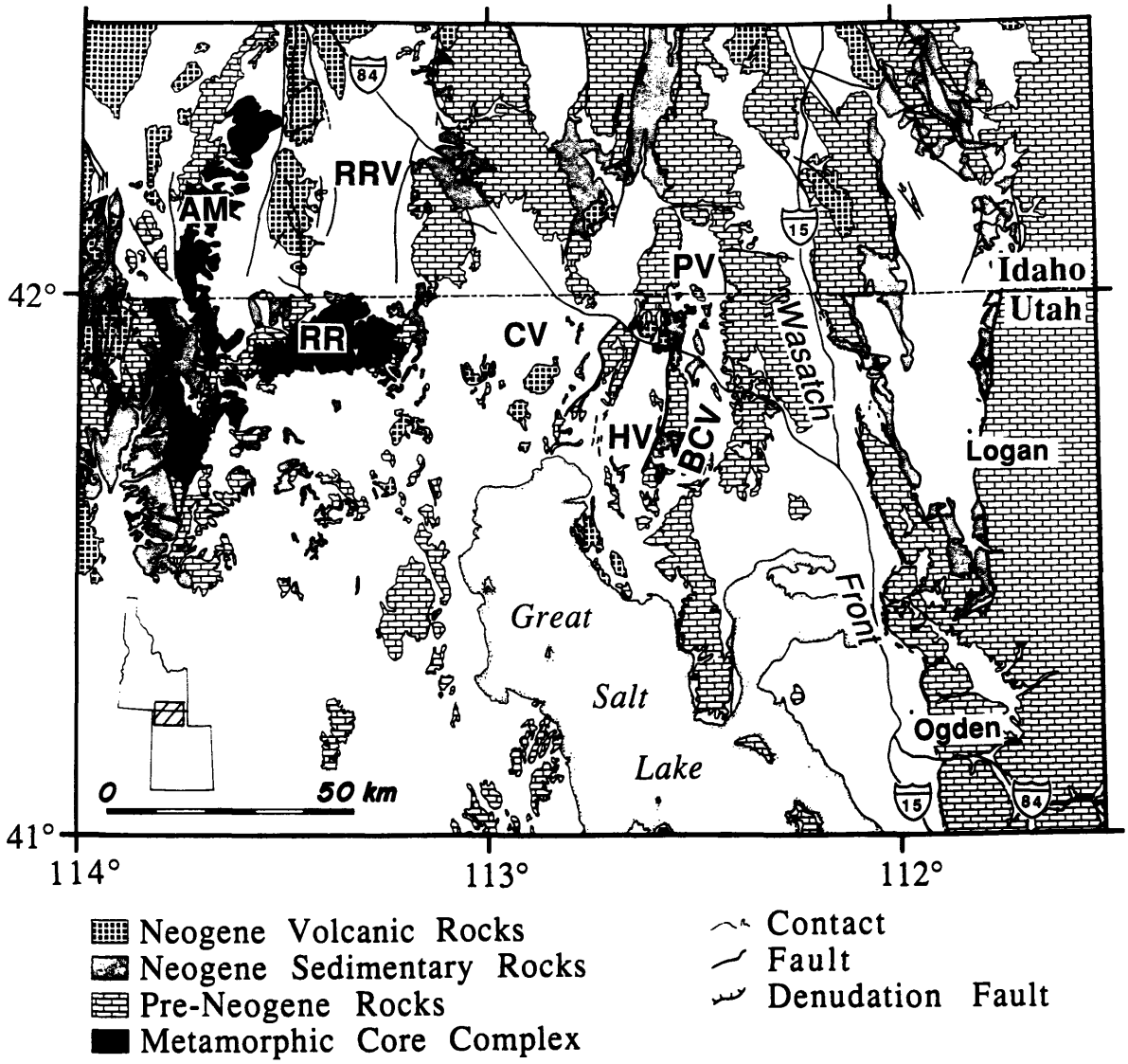

Fig. 3-1. Generalized geologic map of northern Utah and southeastern Idaho, modified from Hintze [1980] and Bond [1978]. Physiographic features include Albion Mountains (AM), Raft River Valley (RRV), Raft River Mountains (RR), Curlew Valley (CV), Pocatello Valley (PV), Hansel Valley (HV), and Blue Creek Valley (BCV).

et al., 1977; Malavieille [1987]; Miller, 1983; Todd, 1980]. Since about middle Miocene time east-dipping structures have either allowed denudation of these ranges through large rootless gravity slides [Compton et al., 1977; Todd, 1983] or accommodated crustal extension on low-angle normal faults [Covington, 1983; Malavieille, 1987]. Covington [1983]

Fig. 3-2. Topography and station locations in the Hansel Valley--Pocatello Valley region. Digitally recorded seismometers are circled; sites abandoned before 15 September are

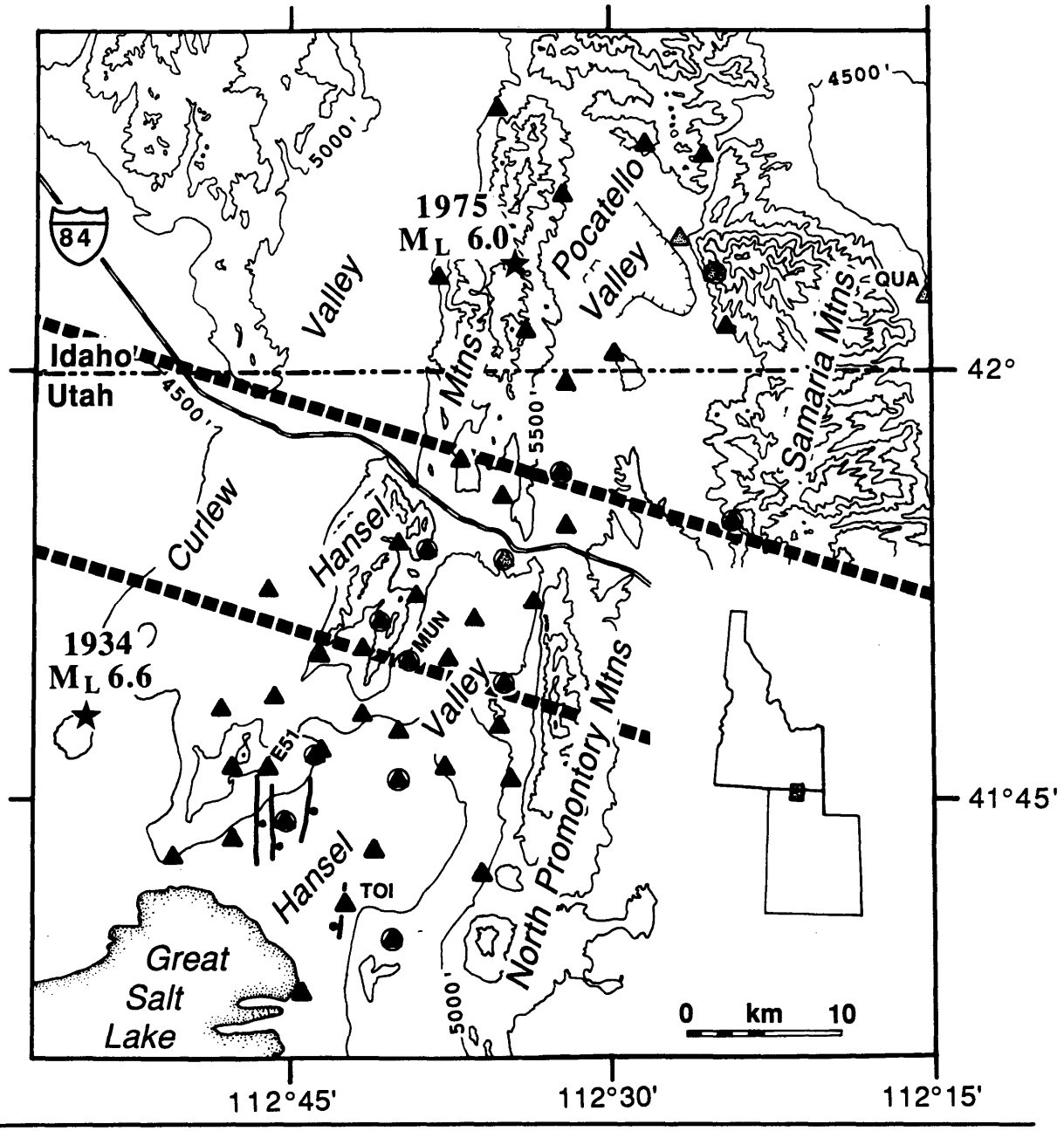

shaded. Instrumental epicenters of the 1975 Pocatello Valley (M_L=6.0) earthquake [Arabasz et al., 1978] and 1934 Hansel Valley (M_L=6.6) earthquake [Dewey et al., 1972] are indicated by the stars. Contour interval is 500'; the Great Salt Lake is drawn with its approximate 1983 shoreline. The heavy dashed marks the boundaries of the low-velocity region (the central block of the second layer) of the three-dimensional velocity structure M3D. Heavy lines in southern Hansel Valley are traces of scarps produced in the 1934 Hansel Valley Earthquake (as drawn by Richens [1979b] from Shenon [1936]); bar-and-ball on downthrown side of scarp.

interpreted seismic reflection and borehole data to infer that the Raft River Basin lacks the substrate appropriate for it to have been created by high-angle normal faults; instead he considers the basin to have opened above an east-dipping low-angle normal fault active in Pliocene and perhaps Quaternary time.

In contrast to the east-dipping structures found to the west of the Hansel Valley region, west-dipping listric normal growth faults are reported from the Great Salt Lake Valley to the south [Smith and Bruhn, 1984]. The geometric relationship of the older Tertiary strata to these faults suggests that they have been active since Miocene time [Smith and Bruhn, 1984]. Zoback [1983] inferred from gravity anomalies, seismicity, and surface fault exposures that the basins along the Wasatch Front to the east are bounded by high-angle normal faults, but these data seem to us to be equally compatible with a northward extension of the listric faults in the Great Salt Lake Valley that were described by Smith and Bruhn [1984].

Within the Hansel Valley--Pocatello Valley area there is little direct evidence for the nature and timing of Neogene deformation. Allmendinger and Platt [1983] suggested that some of the Mesozoic thrust faults were reactivated as normal faults in the Pocatello Valley region. From the observed eastward dip of the strata and structures in the ranges surrounding Pocatello Valley, they also inferred rotation on west-dipping listric normal faults. Similar eastward tilts exist around Hansel Valley and include Cenozoic sedimentary and volcanic rocks of the Salt Lake Formation at the north end of Hansel Valley, suggesting a similar set of west dipping listric normal faults around Hansel Valley [Jordan, 1985; Adams, 1962; McCalpin et al., in press].

The Hansel Valley--Pocatello Valley region has been one of the more active portions of the Intermountain Seismic Belt (e.g., Smith and Sbar [1974]); three earthquakes with local magnitudes $M_L \geq 6$ have occurred this century [Richens, 1979a]. The largest, the 1934 Hansel Valley earthquake ($M_L \approx 6.6$) produced scarps up to 50 cm high along several north-south trending faults in the alluvium of southern Hansel Valley (Figure 3-2, Shenon [1936]). Neither the 1909 Hansel Valley (?) earthquake nor the 1975 Pocatello Valley earthquake are reported to have ruptured the ground, but the latter did produce snowcracks [Cook and Nye, 1979]. The 1975 earthquake is the only event of the three with a well constrained focal mechanism; Arabasz et al. [1979] found a well-constrained N14°E striking, 58°E dipping nodal plane and a more poorly constrained N30°E striking, 34°NW dipping nodal plane. Although the focal mechanisms determined for the aftershocks of this earthquake indicate that the faulting in the area is complex, the foci of the aftershocks tend to deepen to the west, thus suggesting that slip occurred on the northwest dipping plane. This concurs with the inference of a west-dipping listric fault made by Allmendinger and Platt [1983] and McCalpin et al. [in press] from the surface geology.

The geology within the Pocatello Valley region suggests that west dipping listric faults similar to those observed to the south under the Great Salt Lake may accommodate Neogene extension in this area. This is also consistent with the geology in northern Hansel Valley, but the presence of scarps at the west side of the southern part of Hansel Valley might reflect slip on an east-dipping fault. All of these structures could be related to an eastward continuation of the east-dipping low-angle normal faults inferred to be present to the west.

DATA COLLECTION

We deployed 47 portable seismometers in the Hansel Valley region from 30 August to 4 October 1983 (Figure 3-2). The 32 Sprengnether MEQ-800, 1 Teledyne Geotech Portacorder, 10 digital seismographs from the University of Wisconsin, and 4 "big drum" seismographs from Cambridge University recorded events between 15 and 29 September, and most of these instruments were operating from 10 September through 3 October. All these instruments except the digital seismographs recorded the vertical-component of ground motion on smoked-paper; the instruments from the University of Wisconsin recorded all three components of ground motion digitally at 100 samples per second for between about 20 and 90s after an event was detected. A variety of different high-frequency (peak response near 1-5 Hz) seismometers were used. The internal clocks of each smoked paper recorder were set between 0.5 and 7.0 s after the WWV time signal; this time correction was measured when the record was changed, usually every 1, 2, or 4 days. The digital instruments recorded the Omega navigation signal, which was used to calibrate the internal clock when the record was processed [Schneider et al., 1981]. All stations were located on U.S. Geological Survey $7^1/2'$ topographic maps with an estimated precision of 50 m horizontally and 10 m vertically.

Most of our records permit identification of very small earthquakes (Figure 3-3). The greatest source of noise was produced by wind, particularly gusts associated with thunderstorms, which occasionally obliterated hours of record for substantial portions of the array. Farm machinery and vehicular traffic occasionally concealed portions of the record at certain stations. We suspect that the level at which earthquakes were detected is uniform throughout the array, even though the very smallest events probably can be located only within the denser southern part of the network.

As discussed elsewhere (Chapter 2), we consider the precision of our P-wave arrival times to be better than 0.2 s; impulsive P arrivals (assigned qualities of 0) are probably accurate to 0.05 s. Shear wave arrivals are difficult to pick on vertical component instruments and were considered to have uncertainties of about 0.3 s (corresponding to a quality of 3). These estimates are similar to the standard deviations of travel-time residuals

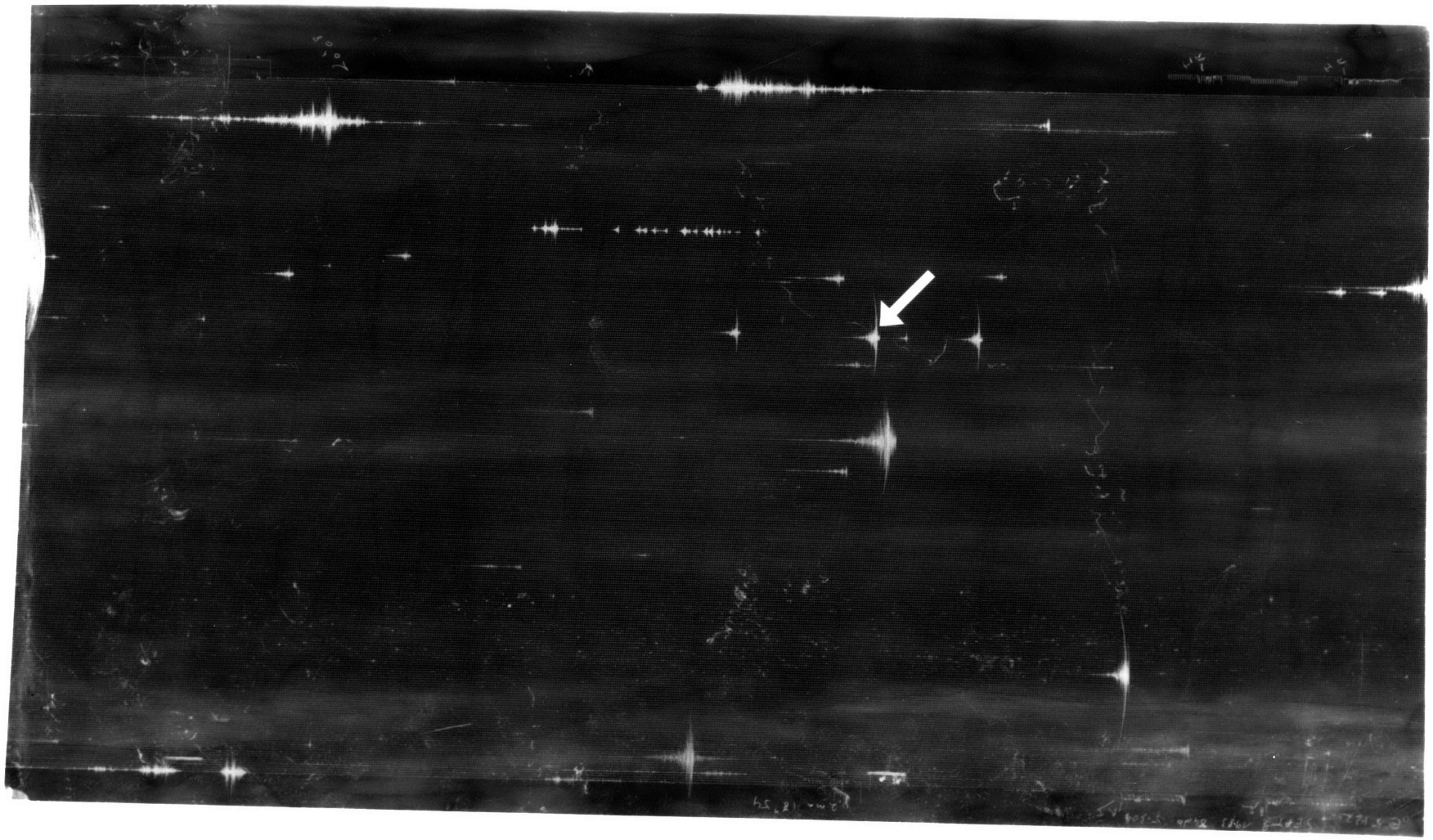

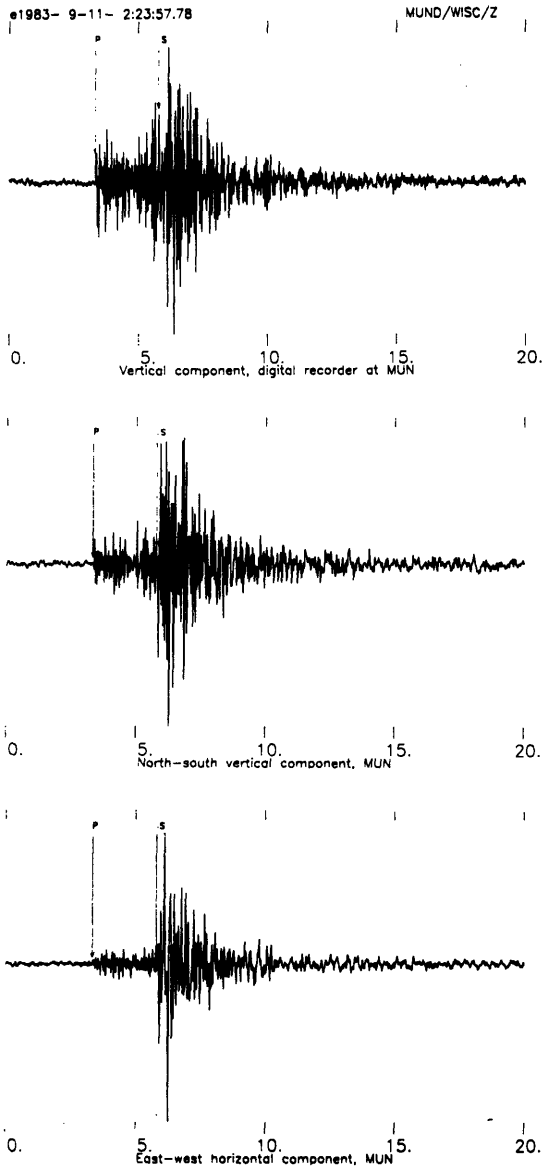

Fig. 3-3. (a, previous page) Smoked paper record from station E51 for 10-11 September; arrow points to event 76. (b,left) digital recording of event 76 at station MUN; vertical component (top), north-south component (center), and east-west component (bottom). Stations located on Figure 3-2.

from our final earthquake locations (Table 3-1), but the standard deviations of the residuals of impulsive P arrivals are twice those anticipated. Although we do not know if the distribution of the residuals that appear to exceed the estimated uncertainties in the original measurements is truly random, a random, unimodal distribution of residuals with the standard deviations of Table 3-1 will produce uncertainties of about 200m in the hypocenters of the earthquakes located with this data within a given, error-free velocity structure (see Chapter 2 for a more detailed discussion). Unfortunately, the uncertainties of the seismic velocities cause much larger uncertainties in the hypocenters of the earthquakes.

TABLE 3-1

Standard Deviations of Computed Residuals

From Earthquakes Located Using Velocity Structure M3D

Phase	Quality	Standard Deviation (s) of (and Number of Arrivals with) Residuals Less Than: 0.50 s		0.75 s		1.0 s	
		130 Earthquakes Recorded by 11 or more Stations					
P	0	0.097	(1524)	0.107	(1532)	0.116	(1536)
P	1	0.160	(1002)	0.196	(1042)	0.222	(1057)
S	0	0.070	(69)	0.070	(69)	0.070	(69)
S	1	0.164	(134)	0.202	(139)	0.202	(139)
S	2	0.241	(58)	0.302	(64)	0.348	(68)
S	3	0.225	(1310)	0.297	(1476)	0.338	(1535)
		334 Earthquakes in Vicinity of Array					
P	0	0.094	(2433)	0.103	(2444)	0.115	(2453)
P	1	0.157	(1590)	0.192	(1651)	0.220	(1678)
S	0	0.069	(70)	0.069	(70)	0.069	(70)
S	1	0.163	(137)	0.200	(142)	0.200	(142)
S	2	0.243	(60)	0.302	(66)	0.346	(70)
S	3	0.220	(2188)	0.287	(2435)	0.324	(2519)

Standard deviations computed for residuals of earthquakes located using the M3D velocity structure. Note the correlation of the computed residuals with the postulated standard deviations of 0.05, 0.1, 0.2, and 0.3 s for arrivals assigned qualities of 0, 1, 2, and 3.

VELOCITY STRUCTURE

Because the seismic velocity structure beneath northern Utah had not been studied in detail, we inverted the arrival times from the earthquakes in the array for the velocity structure (Chapter 2). The algorithm used, essentially that described by Roecker [1981, 1982], determines the velocity structure of a predetermined geometry of homogeneous blocks. The inversion consists of a series of iterations; in each iteration we first relocate the earthquakes in the structure produced by the previous iteration, and then we invert the new travel-time residuals for a velocity structure to be used in the next iteration. This procedure ends when the fit to the data does not improve in successive iterations. We measured the fit using the variance of the residuals of the travel times,

$$\sigma^2 = \frac{n}{(n-n_f)\left(\sum_{i=1}^{n} w_i\right)}\left[\sum_{i=1}^{n} r_i^2 w_i - \frac{\left(\sum_{i=1}^{n} r_i w_i\right)^2}{\left(\sum_{i=1}^{n} w_i\right)}\right] \qquad (3\text{-}1)$$

, where r_i is the travel-time residual of the i^{th} arrival, w_i is the weight assigned that arrival, n is the number of P and S arrival times, and n_f is the total number of free parameters in the inversion. We assigned weights to individual arrivals using the quality of the arrival and the computed residual through the relation

$$w_i = \frac{50}{\sigma_i^2\left(50 + \{50[e - 1]\}^{(r_i^2/t^2)}\right)} \qquad (3\text{-}2)$$

where σ_i^2 is the estimated variance for that type of arrival and t is the truncation value (usually 1 s). We used values of σ_i of 0.05, 0.1, 0.2, and 0.3 s for arrivals assigned qualities of 0, 1, 2, and 3. We determined first a one-dimensional structure and then a three-dimensional structure; in each case we started with a large number of degrees of freedom and gradually reduced the number of parameters until the fit to the observed arrival times deteriorated. The following description of our attempts to invert the arrival times for the seismic velocity structure beneath our array is summarized from Chapter 2.

For the one-dimensional structure we first found the structure with ten layers, the top nine 1 km thick, that best fit the observed arrival times of 30 selected events. We were able to reduce the number of layers to 4 without an increase in the variance; this structure ("M8", Figure 3-4) is notable for a pronounced P low-velocity zone between 1.5 and 3.7 km depth (0.5 to 2.7 km below mean sea level). The best three-layer structure without this low-velocity zone had a variance about 20% higher than that of structure M8.

We started investigating three-dimensional structures by finding the best fit to the arrival times using a structure with 35 blocks in each of five layers above a homogeneous halfspace. The five layer interfaces were at depths of 1.5, 2.5, 3.7, 4.7, and 7.2 km; the structure was oriented at both 11° and 50° clockwise from north. We then inverted for the velocities of a series of structures, each less complex than the last, until the use of any simpler structure increased the variance; all of these inversions were calculated using the same station delays used in the one-dimensional structure. Because these delays probably influence the velocity structure, we eliminated the station delays and replaced the uppermost layer with a layer composed of 117 blocks. Although we believe that the velocities of this uppermost layer

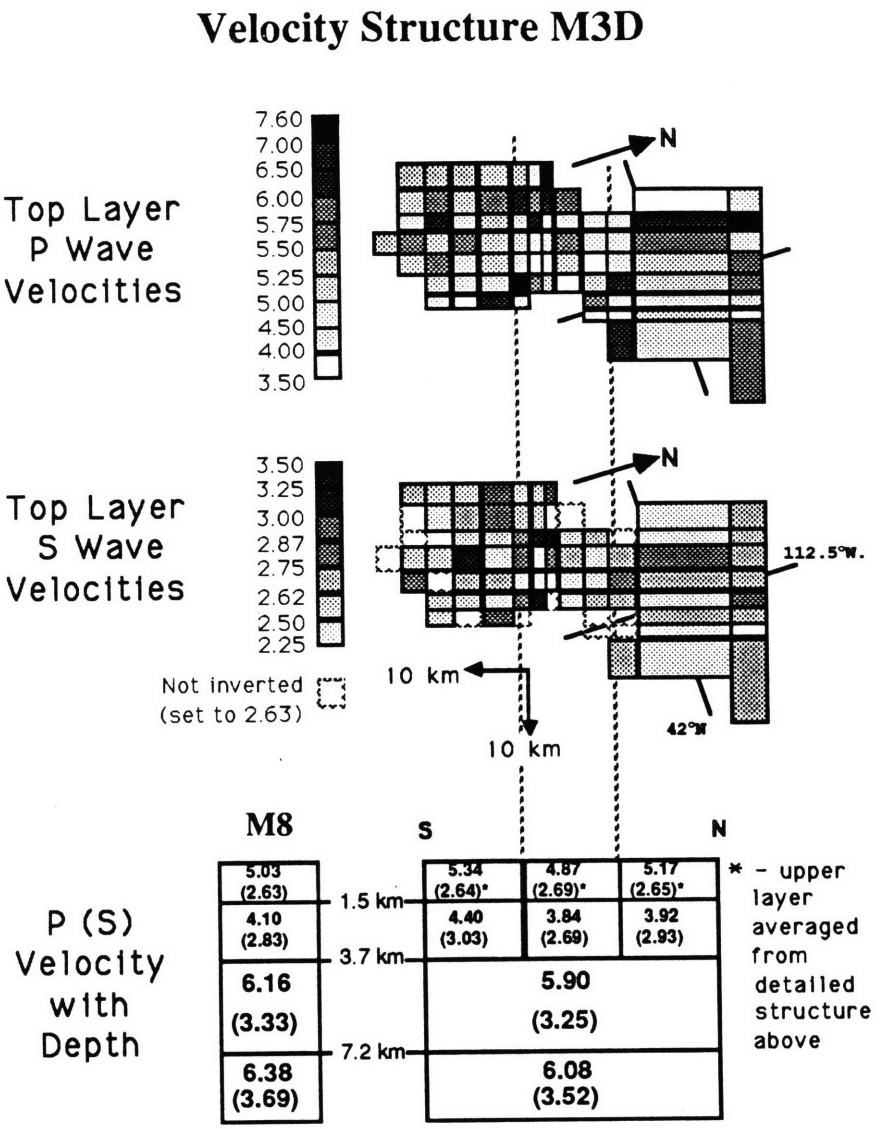

Fig. 3-4. Velocity structure M3D. All velocities are km/s; uninverted blocks in the top layer are set to the velocity of the top layer of the best-fitting one-dimensional velocity structure, M8 (lower left).

reflect the near-surface geology, they cannot be considered to be wholly accurate because other station-dependant effects unrelated to the true seismic velocities in the earth can cause the velocities to be in error. This final structure ("M3D", Figure 3-4) has a variance of 0.02093 s^2 for the 130 events recorded by more than 11 stations, about 7% smaller than that of M8.

Two low-velocity bodies, one the low-velocity zone between 1.5 and 3.7 km depth and the other a low-velocity region in the center of the array above 3.7 km depth, cannot be removed from our inferred velocity structure without an increase in the variance of the travel-

time residuals of at least 6%; hence we consider the existence of these two bodies to be well resolved. We tried to constrain the boundaries of the P-wave low-velocity zone by comparing the variances among a group of one-dimensional structures with different depths of the uppermost two interfaces and found that the top of the layer at 1.5 km depth can only be located within about 1 km (Chapter 2). The location of the bottom boundary has a stronger effect on the residuals; it lies between about 3.2 and 5.2 km depth, and the variance in minimized for a depth of 3.7 km. The resulting S-wave velocity structure consistently lacks a low-velocity zone. Because the starting velocity structure used for any particular inversion always lacked an S-wave low-velocity zone, we tried inverting the travel times for the velocities of a structure initially assigned an S-wave low-velocity zone, but the resulting structure also lacked an S-wave low-velocity zone. Similarly, for individual events the plotted values of the difference between S and P wave arrival times versus the P-wave travel time appear to lie on two or more nonparallel line segments (i.e., points on a "Wadati plot" do not lie along a single straight line), thus indicating that variations of the v_p/v_s ratio are present within the area.

The low-velocity region in the middle of the array has both P- and S-wave velocities less than the areas to the north and south (Figures 3-2 and 3-4). The southern edge of this region is the better constrained; shifting it north or south by 4 km increases the variance of the residuals by 1%. The northern bound is probably located within about 8 km. The orientation of the entire structure is only constrained within about 20°; the configuration of the array tends to make both the orientation and the east-west extent of the anomaly difficult to constrain. Although the standard errors of the velocities of the top two layers are minute ($\leq$0.02 km/s), fluctuations of these velocities observed through the many iterations of the velocity inversions indicate that the uncertainties of the absolute values of the velocities are probably closer to 10%, but the relative velocities within the second layer are less uncertain. In general, decreasing the velocities of the second layer increases the velocities of the first layer and vice-versa; the second layer, because it is a low-velocity zone, is the more poorly resolved and its average velocities fluctuate more. The lateral variations within the second layer are more stable and persist in the same sense as structure M3D in almost all structures with variances up to about 3% larger than that of structure M3D.

We cannot discriminate between source structures that represent the observed velocity anomalies either as the superposition of a separate low-velocity zone and low-velocity region or as lateral variations in the thickness or velocities of the low-velocity zone. The different behavior of S-waves in these two features, however, suggests that the cause of the low-velocity zone differs from that of the low-velocity region. The low-velocity region underlies the relatively thick sediments of northern Hansel Valley and the volcanic and sedimentary

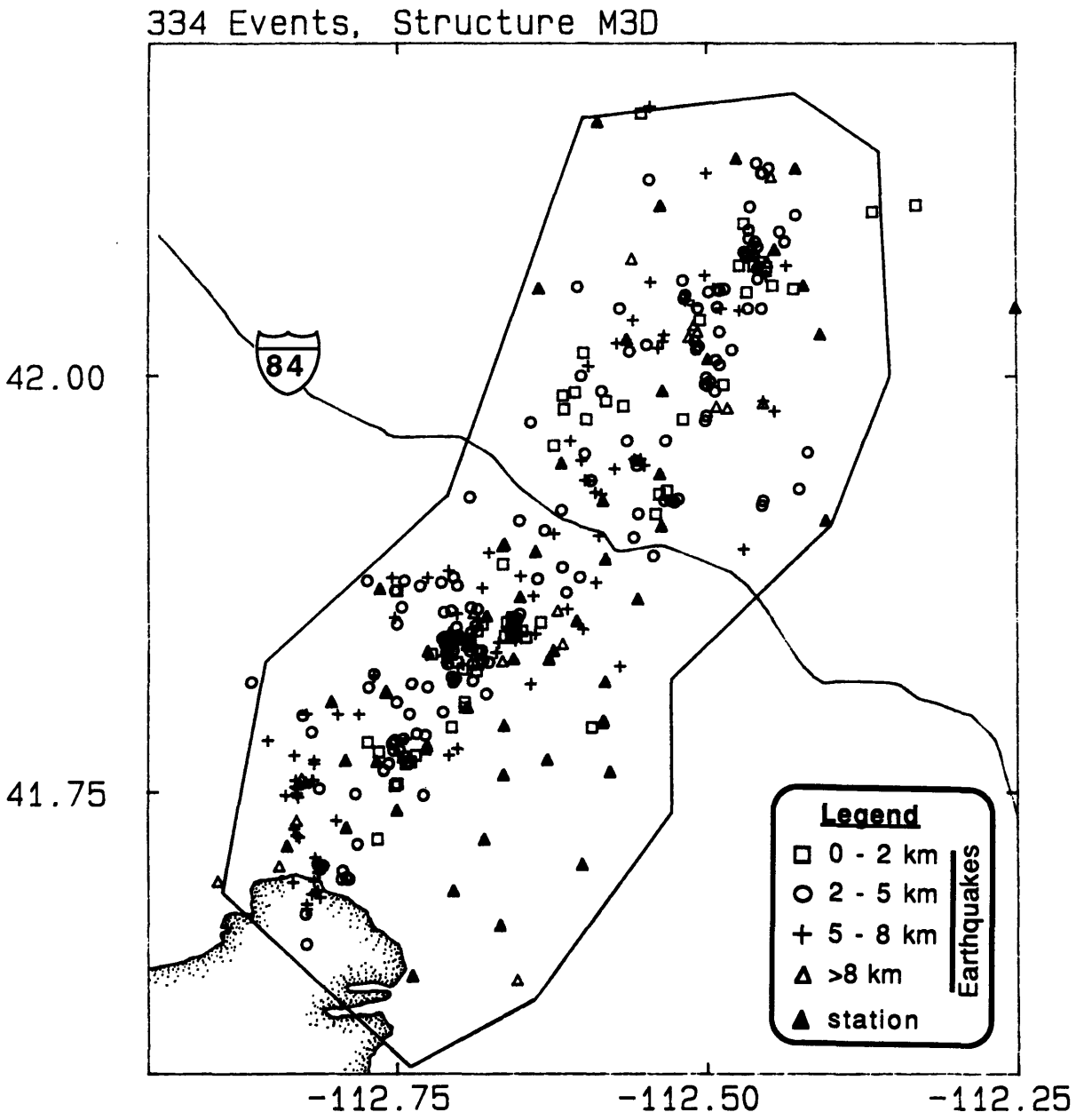

Fig. 3-5. Epicenters of microearthquakes observed in this study. Only events located initially within the large polygon were relocated to create this diagram. This polygon represents our estimate of the geographic limits of earthquakes that can be reliably located both horizontally and vertically.

rocks between Hansel and Pocatello valleys (compare Figures 3-1, 3-2, and 3-4); this correlation is somewhat stronger when the detailed structure of the upper layer is examined: the western blocks underlying the Paleozoic rock of the Hansel Mountains have higher P and S velocities than the other blocks within the low-velocity region (Figure 3-4). Hence we

suspect that the low-velocity region is directly related to the eruption of the volcanic rocks in this area and the creation of northern Hansel Valley; these events may have fractured or altered the rock in the upper 4 km or so of crust and thus reduced the seismic velocities in this region.

Because the rock of the low-velocity zone does not, to our knowledge, crop out at the surface, we can only speculate on the cause of this velocity inversion. The sizable differences in velocity and v_p/v_s ratio at the top of the low-velocity zone seem to indicate that this structure represents a juxtaposition of different lithologies. The presence of Mesozoic thrust faults throughout the region [e.g., Allmendinger et al., 1984] permits us to explain the low-velocity zone as the product of a Mesozoic thrust fault that placed rock with a higher velocity over rock with a lower velocity. We cannot eliminate a Cenozoic structure, thermal event, or intrusion as a possible cause of this velocity structure, but these possibilities seem to be more contrived and less consistent with the surface geology than our preferred explanation.

EARTHQUAKE LOCATIONS AND UNCERTAINTIES

We relocated 334 events initially found to lie within the polygon of Figure 3-5 using the M3D velocity structure. The bulk of the seismicity (Figure 3-5; Table 3-A1 in Appendix 3-A) occurred in a band about 10 km wide oriented about 30° east of north. The earthquakes are fairly uniformly distributed within this belt with two notable exceptions. A distinct cluster of earthquakes occurred near 41.85°N, 112.68°W; this cluster within a densely instrumented portion of the array occurred in the same location as a swarm described by Richens [1979b]. The region near the I-84 freeway has a noticeable paucity of earthquakes. The termination of Hansel Valley and the presence of a small volcanic field at this latitude suggest that this absence of seismicity may not be entirely due to cultural noise associated with the highway.

The standard estimates of the uncertainties in our locations are uniformly small: the weighted root-mean-square (rms) residual of 237 of the 334 relocated events is below 0.10 s, and 234 events have standard errors (1σ) less than 100 m both horizontally and vertically. Because the variances assumed in calculating these standard errors might be as little as a quarter of the actual variances, a better estimate of the standard error is twice that calculated and reported in Table 3-A1; hence the 234 events have standard errors less than 200m both horizontally and vertically. Unfortunately these estimates of the uncertainties do not include the effect of uncertainties in the velocity structure. We located all 334 events in velocity structure M8, the best-fitting one-dimensional velocity structure, and 130 events recorded by

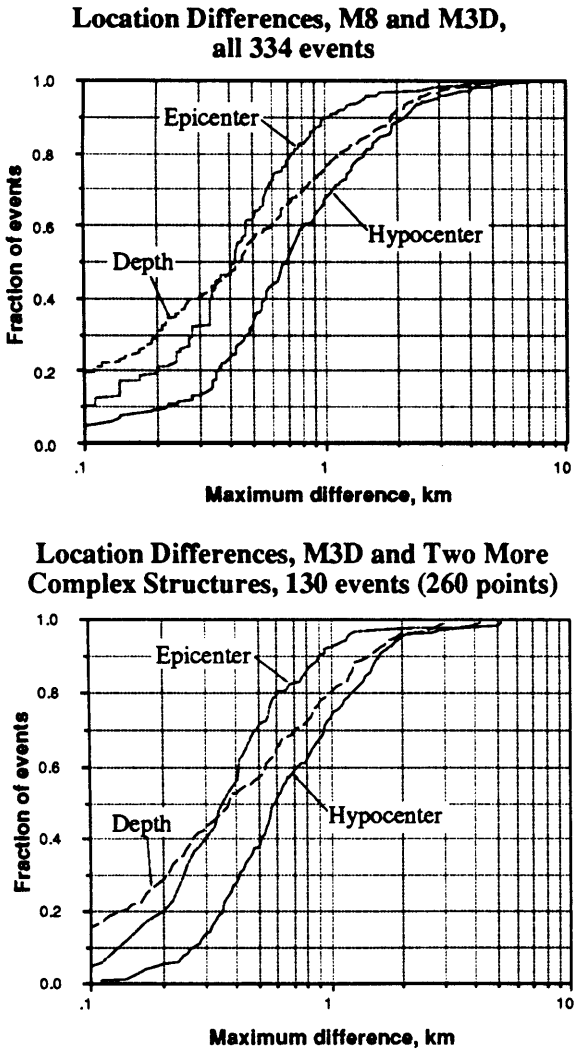

Fig. 3-6. Cumulative histogram of the difference in epicenter and depth locations derived using structure M3D and (a) those derived using structure M8, and (b) those derived using two structures with a large degree of lateral variation (see text for details).

11 or more stations in two different complex three-dimensional velocity structures; the differences between these locations and those calculated using structure M3D provides some estimate of the uncertainty in location caused by possible errors of the velocity structure.

Both because the M8 velocity structure produces residuals with a variance 7% greater than those from the M3D structure and because the M8 structure, being one-dimensional, is subject to the systematic errors described in Chapter 2, we believe that the differences in locations between structures M3D and M8 bound the mean uncertainties of locations caused by errors in the velocity structure M3D. The observed differences, as expected, are greater than the standard errors calculated for the locations using structure M3D, even if we double the originally calculated values in Table 3-A1; 67% of the epicenters are within about 550m and 67% of the depths are within about 700m of one another (Figure 3-6a). These differences do not correlate with the computed standard errors; hence these differences do not represent a systematic underestimation of the variance of the arrival times due to noise.

Instead these differences indicate that the independent uncertainty caused by possible errors in the velocity structure might exceed the uncertainty directly due to noise in the arrival times by a factor of about 3 to 7.

Sizable proportions of the differences between the M8 and M3D locations are probably due to systematic errors caused by the erroneous assumption of a one-dimensional velocity structure in a medium with lateral variations in velocity. A thorough investigation of the systematic errors apparently caused by assuming a one-dimensional velocity structure is presented in Chapter 2. Two of the systematic errors caused by unrecognized or incorrect lateral velocity variations are particularly important in this study: a systematic increase or decrease of the depth of well-recorded events relative to more poorly recorded events in the southern and possibly the northern portions of the array, and a systematic mislocation of epicenters near an unrecognized low-velocity region. The first source of error apparently caused many events recorded by more than 20 stations south of about 41°50' N to be located 1 to 3 km deeper in the M3D structure than in the M8 structure. The second source of error resulted in a difference between epicenters derived using structures M8 and M3D of about 0.5 ± 0.5 km for nearly all of the events within about 5 km of the edges of the low-velocity region of structure M3D. These two errors in the M8 structure indicate the type of errors that might be present in the locations derived using structure M3D, if there were lateral velocity contrasts that we failed to resolve and to define in structure M3D. Because any such unrecognized variations are more localized than those already incorporated into structure M3D, they probably affect the overall variance of the residuals to a smaller degree than those velocity variations included in structure M3D; these smaller variations would only cause small errors to a large number of events or perhaps similar errors to a small number of events.

The comparison between structures M8 and M3D shows the magnitude of the errors that might be present if the M3D structure were more complicated than the earth. We also compared M3D with two other structures, each of which has many more blocks than structure M3D, to evaluate the uncertainty that might have been introduced by underestimating the complexity of the velocity structure of the earth. Both structures consist of 5 layers with 35 blocks per layer overlying a uniform halfspace; the blocks in one structure were oriented 11° and in the other were oriented 50° clockwise from north. These two structures were among those examined in producing structure M3D from M8; for both of these complicated structures we jointly solved for both the earthquake locations and the velocities of the blocks as described previously. For both complex structures, the overall variance of residuals is about 2% worse than those from structure M3D, and the best-fitting locations of most of the 130 events differed from those obtained with M3D by more than the standard errors (Figure

TABLE 3-2.

Experiments removing stations from well-recorded events

Using all stations													
Origin Time		Location											
yrmodahrminsec		north	east	z	# stns	Δt	Δx	Δy	Δz	Δh	Δtd	rms1	rms2
					Southern Group								
830908 1101 10.94		-21.54	-13.42	5.19	6/22	-0.06	-0.66	0.75	0.70	1.00	1.22	0.11	0.04
830911 0223 13.68		-17.99	-13.51	8.34	7/30	0.19	0.33	0.66	-0.95	0.74	1.21	0.07	0.02
830911 0223 57.78		-17.88	-13.01	8.25	7/30	0.13	0.22	0.17	-0.89	0.28	0.93	0.06	0.02
830911 0234 57.47		-17.76	-12.51	7.07	8/16	-0.06	0.00	-0.08	0.13	0.08	0.15	0.04	0.02
830911 0608 10.55		-25.09	-12.16	6.05	5/25	0.13	-1.33	-0.58	-4.00	1.45	4.26	0.09	0.03
830911 0634 16.86		-21.64	-8.18	0.19	6/24	-1.38	-7.68	-8.06	7.76	11.13	13.57	0.12	0.70
~~830911 0737 21.61~~		~~-26.65~~	~~-12.99~~	~~4.87~~	~~7/19~~	~~-0.13~~	~~-0.45~~	~~-1.41~~	~~-0.89~~	~~1.48~~	~~1.73~~	~~0.13~~	~~0.03~~
830928 0906 20.95		-15.75	-6.70	3.00	5/33	1.00	1.33	-2.25	2.26	2.61	3.45	0.12	0.77
~~830929 0859 6.15~~		~~-18.66~~	~~-13.59~~	~~7.87~~	~~8/32~~	~~0.00~~	~~-0.11~~	~~-0.66~~	~~-0.33~~	~~0.67~~	~~0.75~~	~~0.06~~	~~0.02~~
~~830929 0904 51.06~~		~~-20.43~~	~~-13.59~~	~~8.00~~	~~9/29~~	~~-9.75~~	~~-24.54~~	~~-24.24~~	~~49.09~~	~~34.49~~	~~60.00~~	~~0.16~~	~~0.11~~
830930 0646 2.60		-15.09	-7.03	3.12	6/23	0.00	-0.33	-0.08	0.29	0.34	0.45	0.08	0.02
831003 0219 28.55		-10.76	-8.46	5.50	7/31	0.09	-0.22	0.00	-1.30	0.22	1.32	0.12	0.02
					Central Group								
830912 1944 44.85		6.42	12.21	1.05	9/26	0.00	0.11	0.00	-0.95	0.11	0.96	0.10	0.08
830918 0951 9.33		-9.41	-3.81	5.20	7/40	0.13	-0.22	0.50	-0.59	0.55	0.80	0.08	0.03
830923 1234 5.92		-7.29	1.00	2.37	10/26	0.00	-0.11	-0.58	0.13	0.59	0.61	0.07	0.04
830924 2027 58.59		2.28	5.68	6.69	8/29	0.00	0.00	-0.50	-0.25	0.50	0.56	0.07	0.06
830926 1254 26.97		4.94	4.68	5.06	8/42	0.00	-0.22	0.75	0.10	0.78	0.78	0.08	0.04
830926 1522 59.24		8.28	6.73	3.35	10/40	0.00	-0.22	0.25	-0.12	0.33	0.35	0.09	0.06
830926 2034 44.82		1.40	6.77	5.96	9/30	0.00	0.11	-0.75	0.81	0.75	1.11	0.08	0.03
830927 0723 42.72		-7.60	5.56	6.86	6/27	-0.25	1.22	0.41	1.96	1.29	2.35	0.07	0.04
830927 1836 42.25		4.60	3.60	1.59	10/34	-0.25	0.11	0.17	0.74	0.20	0.77	0.24	0.17
830928 1326 19.74		-5.39	2.23	7.52	7/36	-0.25	0.55	-0.33	0.26	0.65	0.70	0.11	0.03
					Northern Group								
830907 0412 7.42		14.98	13.90	3.68	7/35	0.06	0.11	0.33	-0.11	0.35	0.37	0.11	0.04
830914 2330 18.08		14.75	12.33	4.58	9/27	0.00	-0.45	-0.25	1.27	0.51	1.37	0.10	0.03
830922 0958 12.16		13.87	13.16	2.90	8/22	-0.25	-0.45	-0.49	3.00	0.67	3.07	0.10	0.03
830928 1403 43.43		18.35	19.01	2.12	7/27	-0.50	0.68	1.40	3.22	1.56	3.58	0.15	0.04
					Northern Group Using Alternative Structure								
830907 0412 7.42		14.98	13.90	3.68	7/35	0.04	0.22	-0.17	-0.05	0.28	0.28	0.11	0.02
830914 2330 18.08		14.75	12.33	4.58	9/27	-0.10	-0.33	0.41	1.25	0.53	1.36	0.10	0.02
830922 0958 12.16		13.87	13.16	2.90	8/22	0.02	0.11	0.33	0.10	0.35	0.36	0.10	0.02
830928 1403 43.43		18.35	19.01	2.12	7/27	-0.03	0.11	-0.08	0.37	0.14	0.40	0.15	0.04

Explanations: yrmoda (yymmdd) = year-1900 (yy), month (mm), and day (dd); hrmin (hhmm) = hours (hh) and minutes (mm); sec = seconds; north = distance north of 41° 55' N, km; east = distance east of 112° 40' W, km; z = depth, km; # stns (aa/bb) = number of stations that recorded the event (bb) and were used in the experimental relocation (aa); Δt ,

Table 3-2 (continued)

Δx, Δy, Δz = difference in origin time (s), east, north, and depth coordinates of hypocenter between M3D and experimental locations (these values, added to the M3D parameters, yield the experimental location); Δh and Δtd = difference in epicenter and hypocenter locations between M3D and experimental locations (km); rms1= weighted rms of residuals from M3D location; rms2 = weighted rms of residuals from experimental location.

Struckthrough lines (~~8309~~) indicate events with poorly constrained solutions when located using the experimental subset of stations.

3-6b), but the differences are less than those between locations from structure M3D and M8: 67% of the epicenters differ by 450m or less, and 67% of the depths differ by 600m or less.

A final estimate of the uncertainty in location independent of the noise in the arrival times was made by relocating a group of events using only 5 to 10 of the 16 or more stations recording each event. In addition to providing some estimate of the difference in the quality of locations derived using different numbers of stations, this technique is sensitive to possible systematic errors similar to those present in the one-dimensional structure; that is, unrecognized systematic errors will cause the locations obtained using arrival times from a subset of stations to differ systematically from those obtained using all available arrival times. Three groups of earthquakes were studied in this manner: twelve south of about 41°49.6'N, four north of about 42°1.5'N, and ten located between these two groups (Table 3-2).

Only nine of the twelve southern events relocated with a subset of the observed arrival times yielded a stable solution. Seven of these nine relocated epicenters and depths are within 1 km of the M3D epicenters and depths. Six of the nine new locations are shallower than the M3D locations. Most of these events are located in the southwestern corner of the array; thus, the possible presence of a systematic error in the locations derived using structure M3D for this portion of the array must be included in any interpretation of the events in this part of the array. The differences found between locations based on structure M3D using arrival times from all stations and a subset of stations are both less systematic and smaller than those found between locations based on structure M8 (Chapter 2); hence the systematic errors of locations using structure M3D are probably less than those found using structure M8, which were as large as 3 km for hypocenter depths. For these reasons we might expect systematic errors in depth up to about 1 km to be present in the M3D locations of events in the southwestern corner of the array.

All ten events in the central group of earthquakes yielded stable solutions when relocated using only a subset of stations; no systematic differences between these locations and the

original locations are evident. Seven of the ten epicenters lie within 650 m of the epicenters derived using all available arrival times; seven of the ten depths are within 750 m of the depths found using all available arrival times. The absence of any discernible systematic difference in these locations indicates that these numbers reflect the uncertainty of the more poorly recorded events relative to the better recorded events within the array and, to a lesser degree, the overall uncertainty of all locations in this part of the array. These uncertainties are probably also representative of those within the neighboring, interior portion of the southern and northern parts of the array.

Only four events north of about 42°1.5' N and west of 112°25' W were recorded by more than 20 stations; one of the four (83.09.28.14:03:43) is near the edge of the array, and its location is therefore likely to be more uncertain than those closer to the center of the array. The new epicenters of the other three events are within 700m of the original M3D epicenters; the depths, however, are up to 3 km different from and tend to be deeper than the M3D depths. Because of the sparser array and the smaller number of earthquakes in the northern than southern part of the array, we examined the possibility that the velocity structure in the northern part of the array was in error because of the large number of arrivals from the south and central portions. These arrivals might tend to couple the velocities in the northern part of the array with structures to the south without being sensitive to the local structure in the north. By using the arrival times from all events located within the northern part of the array and recorded by nine or more stations to invert for the velocities of those blocks north of the north edge of the low-velocity region (northern dashed line in Figure 3-2), we hoped to find a better estimate of the velocity structure beneath the northern part of the array; all other velocities were held fixed, and the inversion proceeded as described above. A structure with mean P and S velocities in the top layer about 3% and 0.5% higher than the M3D velocities, a P velocity in the second layer 0.5% lower than the M3D velocity, and an S velocity in the second layer 3% higher than the M3D velocity reduced the variance of the residuals of these events by 0.8%. None of these 34 events was relocated more than 500 m from its M3D hypocenter; 30 of the 34 events have epicenters within 250m of the M3D epicenters and depths within 130m of the M3D depths. Despite these apparently insignificant changes, using this new structure to repeat the experiment of relocating the four large events with only a subset of their stations yields locations much closer to the original M3D locations: all four epicenters are within 530m of their M3D equivalents, and three of the four depths are within 400m of the M3D depths (Table 3-2). Hence the M3D locations are probably adequately accurate and not strongly biased by a velocity error for events recorded by more than nine stations; more poorly recorded events, however, might be located as much as a few kilometers from their actual hypocenters.

Four sources of uncertainty contribute to the overall uncertainty of the locations found using structure M3D: noise in the arrival times, different groups of stations recording different events, errors in the gross velocity structure, and systematic errors from unrecognized velocity variations. The uncertainty due to noise in the arrival times was estimated by the linearized hypocenter location routine as a standard error; these errors are typically below 200m both horizontally and vertically. The greater uncertainty of events recorded by smaller numbers of stations was best isolated within the central part of the array; events recorded by less than 11 stations probably have uncertainties of about 0.65 km horizontally and 0.75 km vertically relative to those events in the same region recorded by more than about 20 stations. A comparison of the M3D locations with locations obtained using other structures reveals differences of about 500m horizontally and 700m vertically; these values include systematic errors caused by differences between the M3D and the other velocity structures. These systematic errors appear to be greatest in the southern and northern portions of the array, where the horizontal and vertical uncertainties might be near 1 km. Hence we suspect that well-recorded events in the center of the array have uncertainties from all causes of about 400m horizontally and 500m vertically; more poorly recorded events (less than about 11 stations recording the event) probably have uncertainties of about 800m horizontally and perhaps 1 km vertically. Events particularly susceptible to systematic errors, those located at the southwestern and northern ends of the array, might have both horizontal and vertical errors as large as about a kilometer. Systematic changes between the M8 and M3D locations suggest that these events probably have greater uncertainties in depth, perhaps 1.5 km, than in epicenter, perhaps 1 km (see Chapter 2 for details of the differences between M8 and M3D locations).

FOCAL MECHANISMS

Focal mechanisms for 102 earthquakes were determined using the polarities of the first motions of P-waves (Table 3-A1, Appendix 3-A). Each mechanism was assigned a grade from A to L reflecting the uncertainty of that mechanism. The details of this grading scheme are presented in Chapter 2. In essence, each grade is based on the uncertainty of the nodal planes assuming that the takeoff angles and azimuths computed from the M3D location are correct. These grades are then modified to reflect the probable errors that would be introduced by either a mislocation of the earthquake or an error in the velocity structure. Qualities of A to C indicate that both slip vectors are constrained within about 10°, D to F indicate constraints of 20°, G to I indicate constraints of 20° on one nodal plane or 30° on both, and J to L constitute the remaining focal mechanisms that are consistent with only one

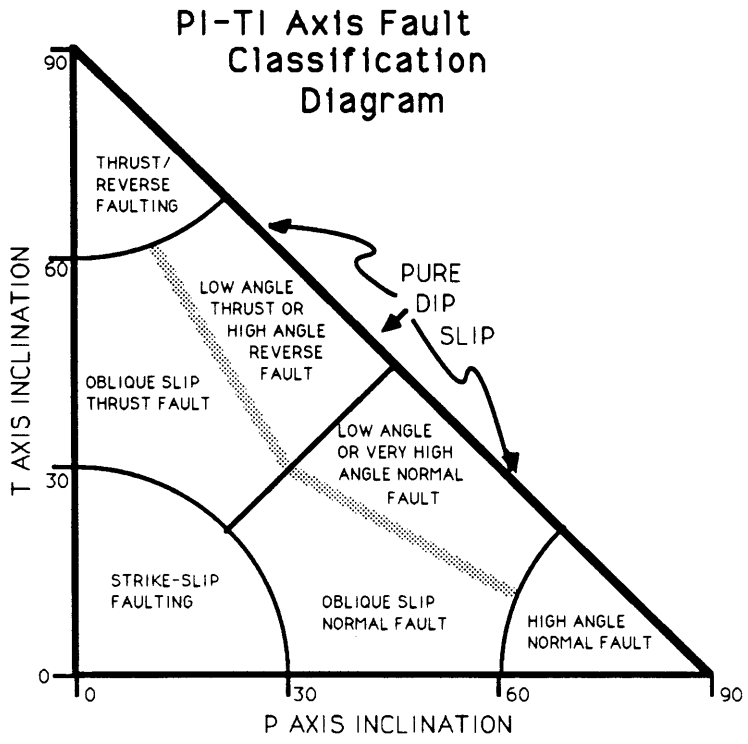

Fig. 3-7. Cartoon of the "PI-TI plot" illustrating the locations at which different types of focal mechanisms are plotted.

style of faulting (e.g., normal-slip, oblique-slip, and low-angle or very-high-angle dip-slip). These grades provide a straightforward means of comparison among large groups of events; specific events are best evaluated individually and can be examined in Figure 3-A1 (Appendix 3-A) and in numerous figures in this paper.

Because of the large number of focal mechanisms in a small geographic area, a plot of the inclination of the P-axis versus the inclination of the T-axis for each focal mechanism was constructed to help classify the different types of faulting occurring in different regions and differentiate between regions with different types of faulting (Figure 3-7). This "PI-TI plot" (Figure 3-8) shows, as expected for earthquakes within the Basin and Range Province, that the preponderance of focal mechanisms indicate that failure occurred by normal faulting. The many events not characterized by high-angle normal faulting region of the plot define two distinct groups: oblique-normal slip faulting and low-angle normal slip faulting. A smaller subset of events are clearly associated with thrust faulting. Note that all four groups of mechanisms include at least four mechanisms with a grade of F or better, and all groups except that associated with thrust faulting include at least 10 mechanisms assigned a grade of F or better.

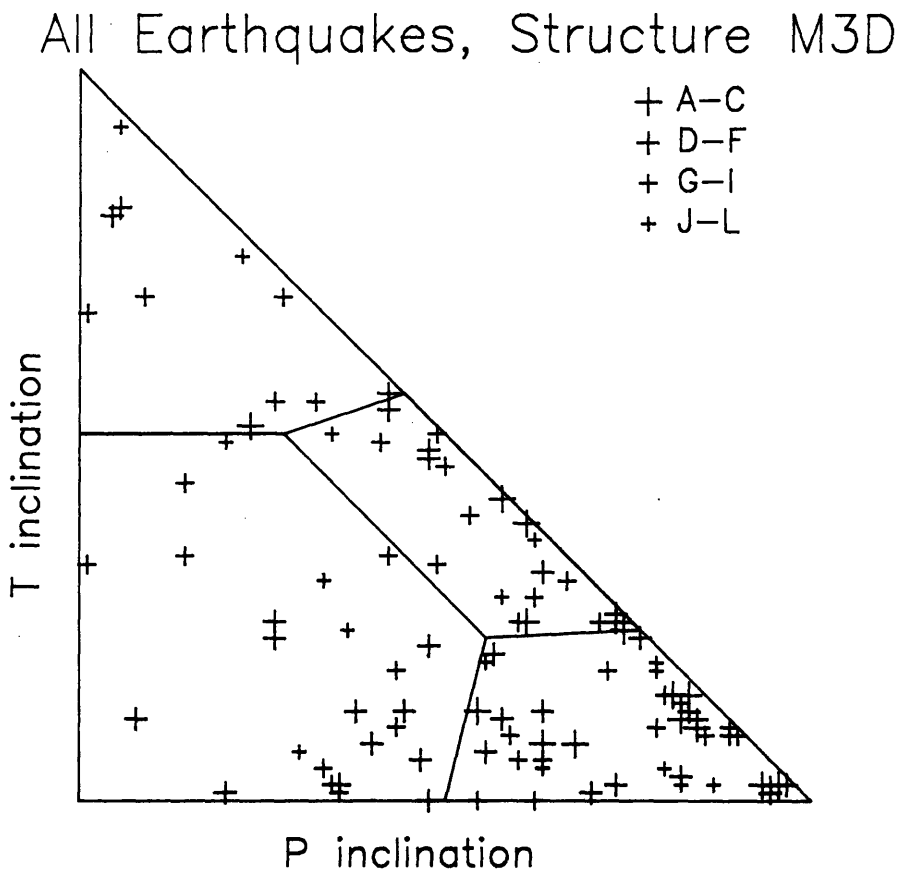

Fig. 3-8. "PI-TT" plot of all focal mechanisms determined in this study; symbols are keyed to the quality of each mechanism. Compare with Figure 3-7. Note the distinct separation between the low-angle normal fault solutions (along the triangle's hypotenuse) and the oblique slip solutions (bottom center of the triangle). The other two fields delimited here are termed "normal solutions" (lower right corner) and "thrust solutions" (top part of triangle).

An important problem that affects the focal mechanisms is that mislocations of events near a strong velocity contrast relative to that contrast, located at 3.7 km depth in this study, will produce sizable errors in the focal mechanisms obtained for these events. For example, the distribution of the different types of mechanisms with depth suggests a systematic vertical variation in the style of deformation in this region (Figure 3-11). The most reliable (quality A-F) mechanisms indicating possible low-angle normal faulting are for events located deeper than 4 km; most occurred between 6 and 8 km depth. There is a somewhat similar cluster of oblique-slip mechanisms for earthquakes located above 4 km depth. Because tests of the effect of velocity gradients on focal mechanisms indicated that this pattern of events with oblique-slip mechanisms overlying events with low-angle dip-slip mechanisms can be an artifact of their location relative to the velocity gradient (Chapter 2), mechanisms of those

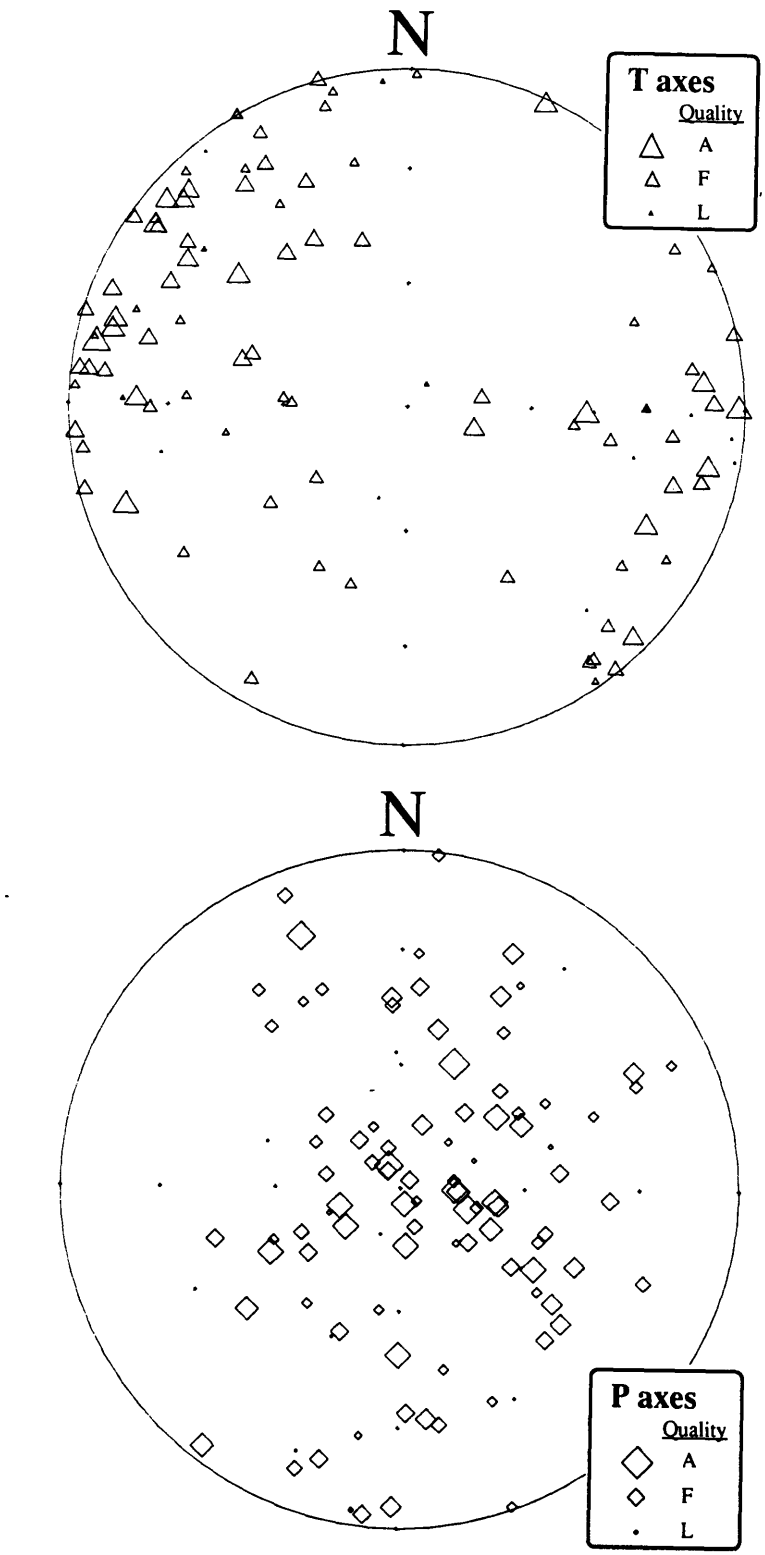

Fig. 3-9. Lower hemisphere projection of the P and T axes of focal mechanisms found in this study. Size of the symbol is proportional to the grade assigned the mechanism. Note the dominance of west-northwest--east-southeast extension.

events within about 1 km of the gradient were carefully graded. Those events that seemed particularly likely to have mechanisms strongly influenced by an error of the hypocenter relative to the velocity gradient were usually assigned grades from G to L; hence the cluster of events with oblique-slip mechanisms between 3 and 4 km depth may be an artifact of the velocity structure, as might the cluster of events with low-angle dip-slip mechanisms near 4 km depth. The absence of events with low-angle dip-slip mechanisms above 4 km depth does appear to be significant. Moreover, the apparent presence, discussed below, of an oblique-slip normal fault defined by events with oblique-slip focal mechanisms both above and below 3.7 km depth confirms our belief that most of our focal mechanisms are free of any systematic errors introduced by the presence of the strong velocity contrast at 3.7 km.

The errors that might be present in our focal mechanisms can be estimated using some generalized guidelines (Chapter 2), if we can bound the error of the hypocenters associated with the mechanisms. The mechanism of an event known to be located within a specified velocity layer will rarely differ by more than about 15° from the correct mechanism. If an event is incorrectly located in a layer different from that in which it occurred, the mechanism will often be substantially in error. If the event is located within material with a lower P-wave velocity than that at the correct location, the derived focal mechanism will tend to have a greater component of dip-slip than the actual mechanism. In contrast, if the mislocated event is in material with a greater P-wave velocity, the mechanism will tend to have a greater component of strike-slip than the correct mechanism.

STRUCTURAL INTERPRETATION

The earthquakes within our array lie in a north-northeast trending band about 10 km wide (Figure 3-5); closer examination of the locations indicates that the deeper events tend to lie to the west of the shallower events, particularly south of highway I-84. Most focal mechanisms in the area indicate nearly pure normal faulting (Figure 3-8), and the T-axes tend to cluster along a west-northwest orientation (Figure 3-9). These tendencies suggest that the earthquakes lie along a west-dipping normal fault; Richens [1979b] interpreted a cluster of earthquakes monitored in 1976 at about 41°49'N, 112°42'W with similar characteristics to lie on a west-dipping normal fault. Farther north, the 1975 Pocatello Valley earthquake appears to have occurred on a west-dipping normal fault [Arabasz et. al., 1979].

Two prominent features of the seismicity suggest that this simple interpretation understates the true complexity of seismicity in the region. South of about 41°52'N the epicenters lie almost exclusively in the Hansel Mountains, but to the north the epicenters lie mostly in Pocatello Valley. This is puzzling if seismicity in both areas lies on west-dipping

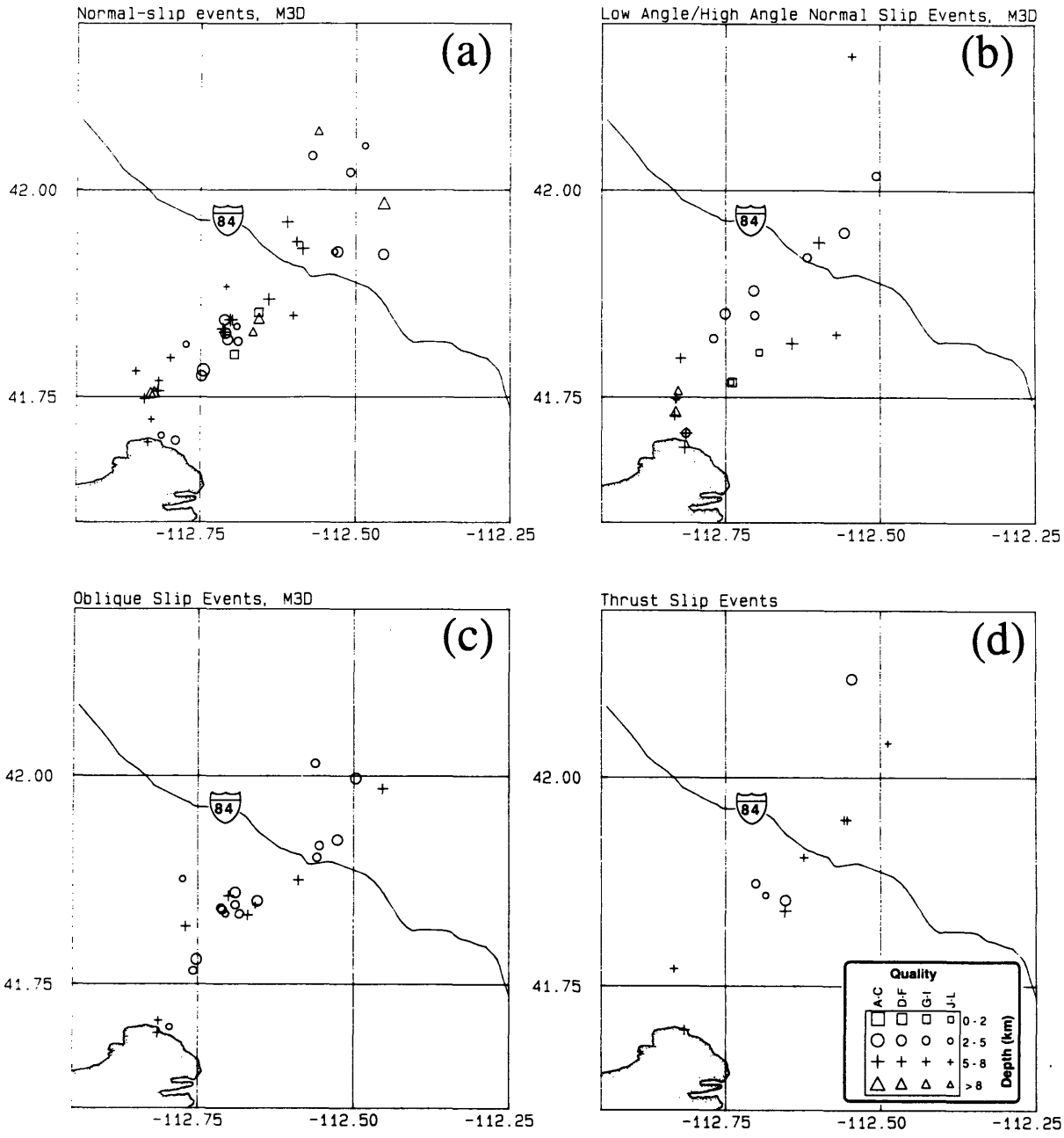

Fig. 3-10. Epicenters of events with (a) normal-slip mechanisms, (b) low-angle or very high-angle dip-slip mechanisms, (c) oblique-slip mechanisms, (d) thrust mechanisms. See Figure 3-8 for definitions of these categories; size of the symbol is proportional to the grade assigned the mechanism.

normal faults; in particular, the observed Quaternary fault scarps on the west side of Hansel Valley indicate that the valley has dropped down on east-dipping normal faults, though the scarps do tend to trend into the mountains [McCalpin et al., in press]. Second, the distribution in space of events with focal mechanisms of a certain type is very nonuniform

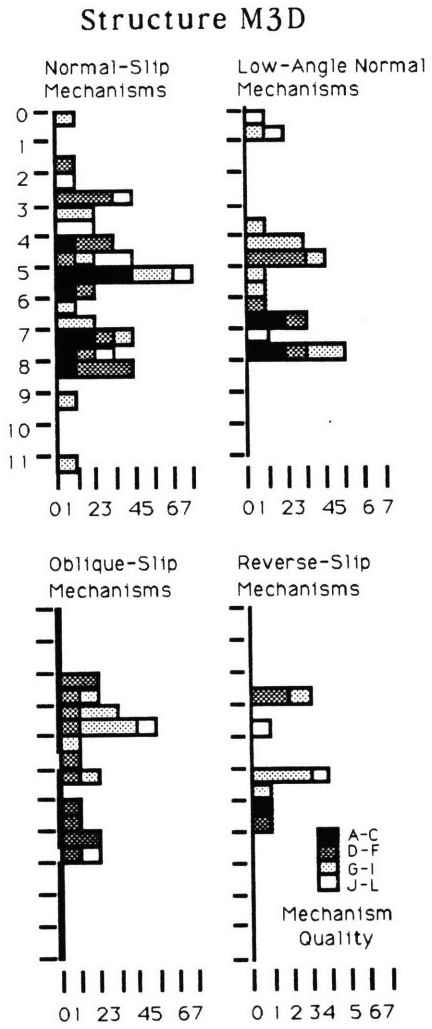

Fig. 3-11. Histograms of events with depth subdivided by the type of focal mechanism, as illustrated in Figure 3-8.

(Figure 3-10). Oblique-slip and thrust events are concentrated near 41.85°N, 112.7°W; events with mechanisms consistent with low-angle normal slip are nearly absent in this area but are numerous to the south. Events with mechanisms consistent with low-angle normal slip are also not uniformly distributed with depth; well-constrained mechanisms consistent with low-angle normal slip are present only for events below about 4 km depth (Figure 3-11) despite a relatively even distribution of events as a whole with depth (Figure 3-12).

These inconsistencies indicate that a closer examination of the earthquakes is required before considering a possible set of faults as the source of these earthquakes. Because of the lateral variations evident in the focal mechanisms, we consider the events south of about 41.81°N as one group, those between 41.81° and roughly highway I-84 as a second, "central" group, and the remainder to the north as a "northern" group. Our goal is to delineate individual structures both by the locations of earthquakes and by the nodal planes of any associated focal mechanisms; the coincidence of both a planar feature in the seismicity with

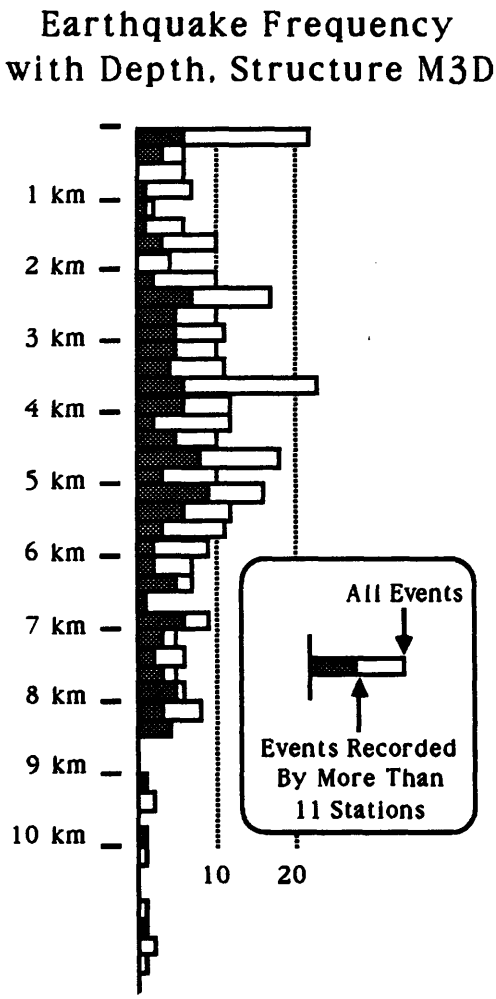

Fig. 3-12. Distribution of earthquakes with depth using structure M3D.

nodal planes of mechanisms of events within those planes is considered to be strong evidence that feature is a fault plane. Other planar alignments of seismicity, while possibly representing fault planes, can only be regarded as hypothetical alignments and are the seismological equivalent of geological lineaments.

Southern Group of Earthquakes

Earthquakes south of 41.81°N fall into three groups: those located above about 4 km, those located below about 5 km, and a few in between. The shallowest events trend about N30°E across the array; the eastern edge of the area in which these events occur is fairly sharp and closely follows the western side of Hansel Valley (Figures 3-13 and 3-2). The epicenters of the deepest events are aligned nearly north-south on the western edge of the array and roughly follow the western side of the southern Hansel Mountains. These events include the only 2 that were recorded within our array by the University of Utah Seismograph Stations [Richens et al., 1984], who assigned these events magnitudes of M_L = 1.6 (event 83)

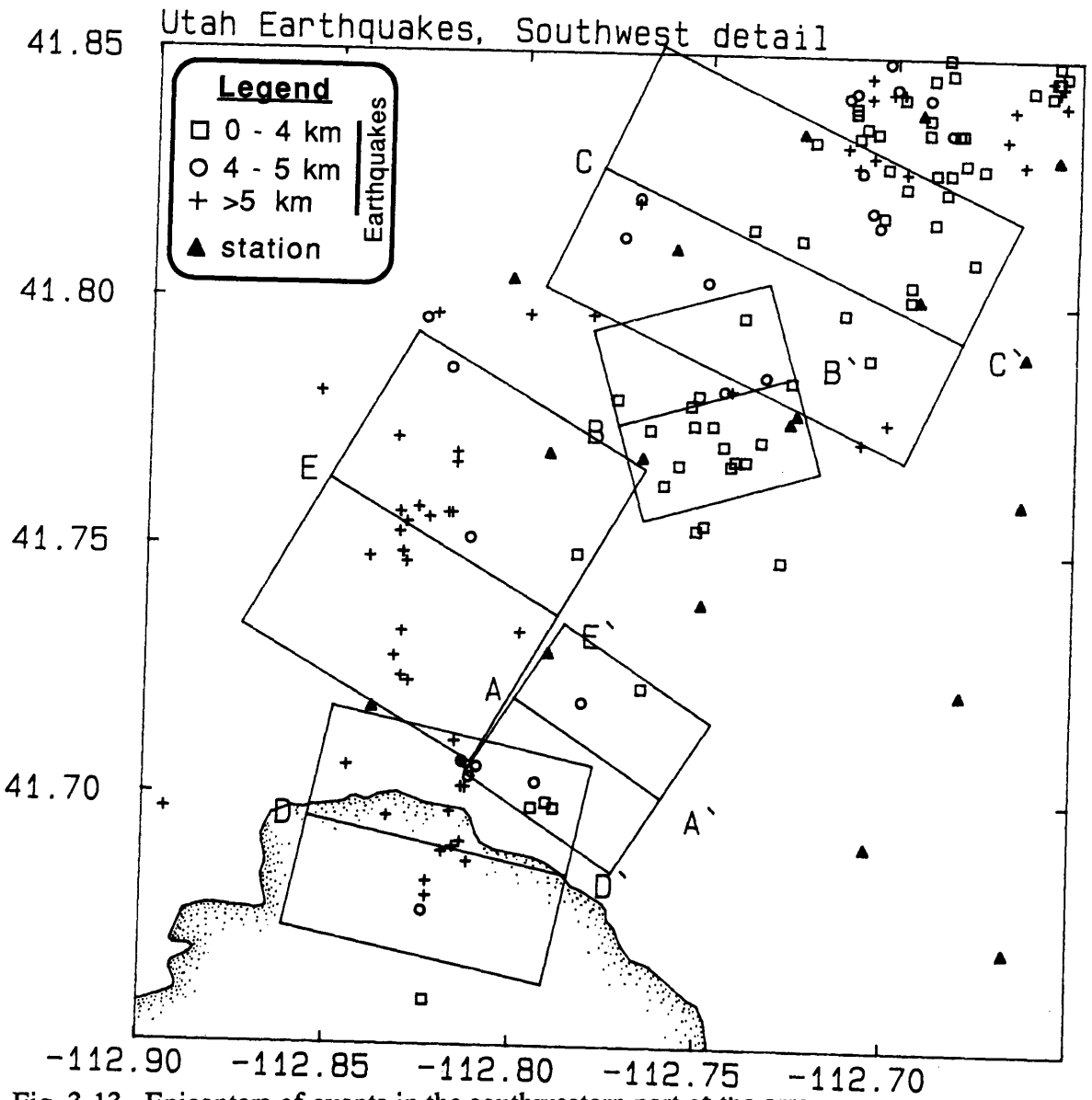

Fig. 3-13. Epicenters of events in the southwestern part of the array. Note the separation between epicenters of events with depths shallower than 4 km (squares) and deeper than 5 km (crosses). Cross-section lines of Figures 3-14, 3-16, 3-17, 3-18, and 3-19 (A-A', B-B', C-C', D-D', and E-E', respectively) indicated.

and 1.3 (event 142) (event numbers throughout this report refer to the chronological listing in Table 3-A1). The events between 4 and 5 km depth do not seem to provide a connection between the other two groups, as cross-sections described below show, and have epicenters more scattered than those in the other two depth groups. This pattern of seismicity suggests that two distinct sets of structures exist in the southern part of the array, one above and one below a depth of about 5 km; separated by as much as 5 km horizontally, the two groups are

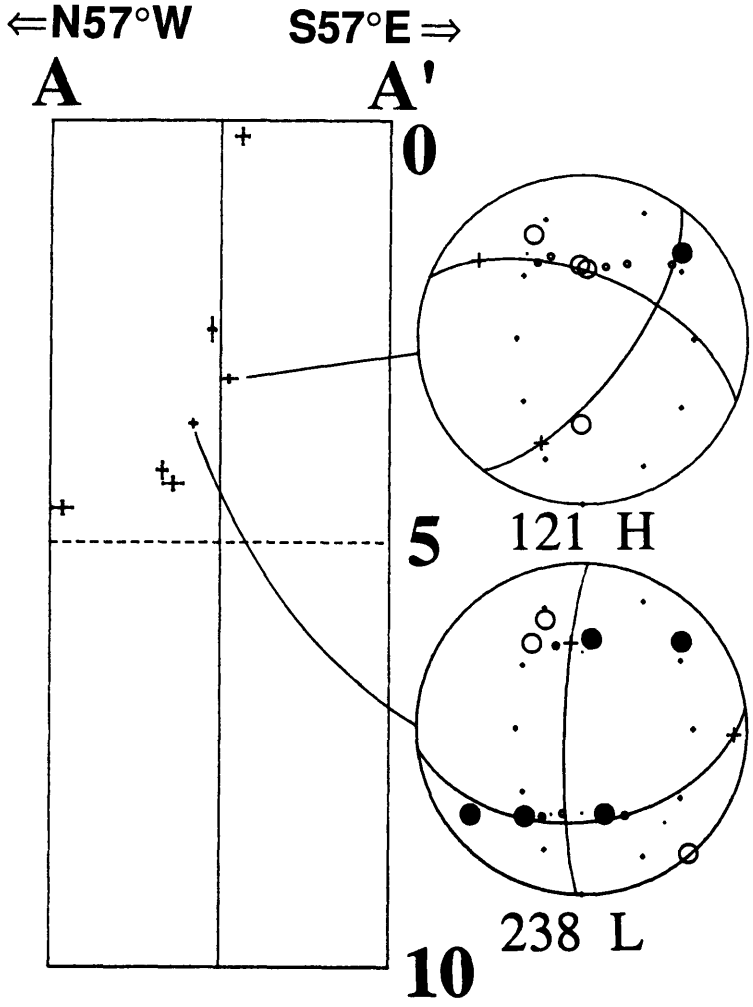

Fig. 3-14. Cross-section of shallow events in the southern end of the array. Focal mechanisms are projected into the plane of the cross-section using an equal-area, rear hemisphere projection. Event number are keyed to Table 3-A1 in Appendix 3-A. Solid first motions are compressional, open symbols dilatational. Small crosses are at 0°, ±30°, ±60°, and ±90° inclination within vertical north-south and east-west striking planes. Size of the polarity symbols is roughly proportional to their qualities. All cross-sections have no vertical exaggeration. Cross-section located on Figure 3-13.

only connected by a sparse horizontal band of seismicity. We therefore consider each group separately.

Shallow Seismicity. The shallow events in the southern part of the array tend to deepen from east-southeast to west-northwest; this pattern is simplest for the few shallow events south of 41.73°N. A cross-section oriented perpendicular to N33°E through these events (Figure 3-14) suggests that these events could lie on a fault whose dip might decrease with depth. The two available focal mechanisms lend some support to the inference of such a

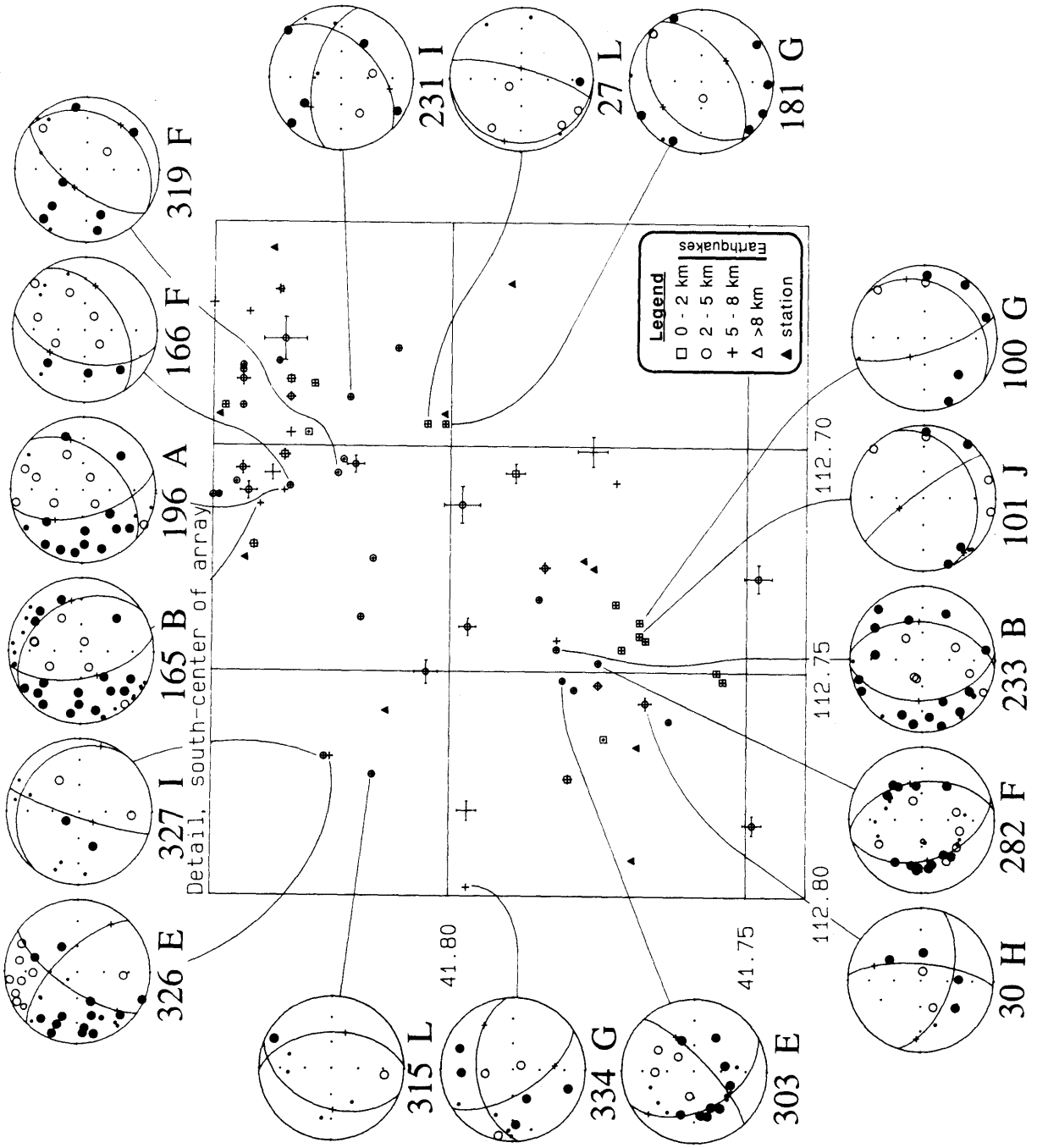

Fig. 3-15. Detail map of the southeastern part of the Hansel Mountains and southwestern Hansel Valley. Focal mechanisms show a lower hemisphere, equal area projection. Other conventions of the focal mechanisms as in Figure 3-14. Error bars on epicenters are twice the standard errors reported in Table 3-A1. Events keyed to Table 3-A1.

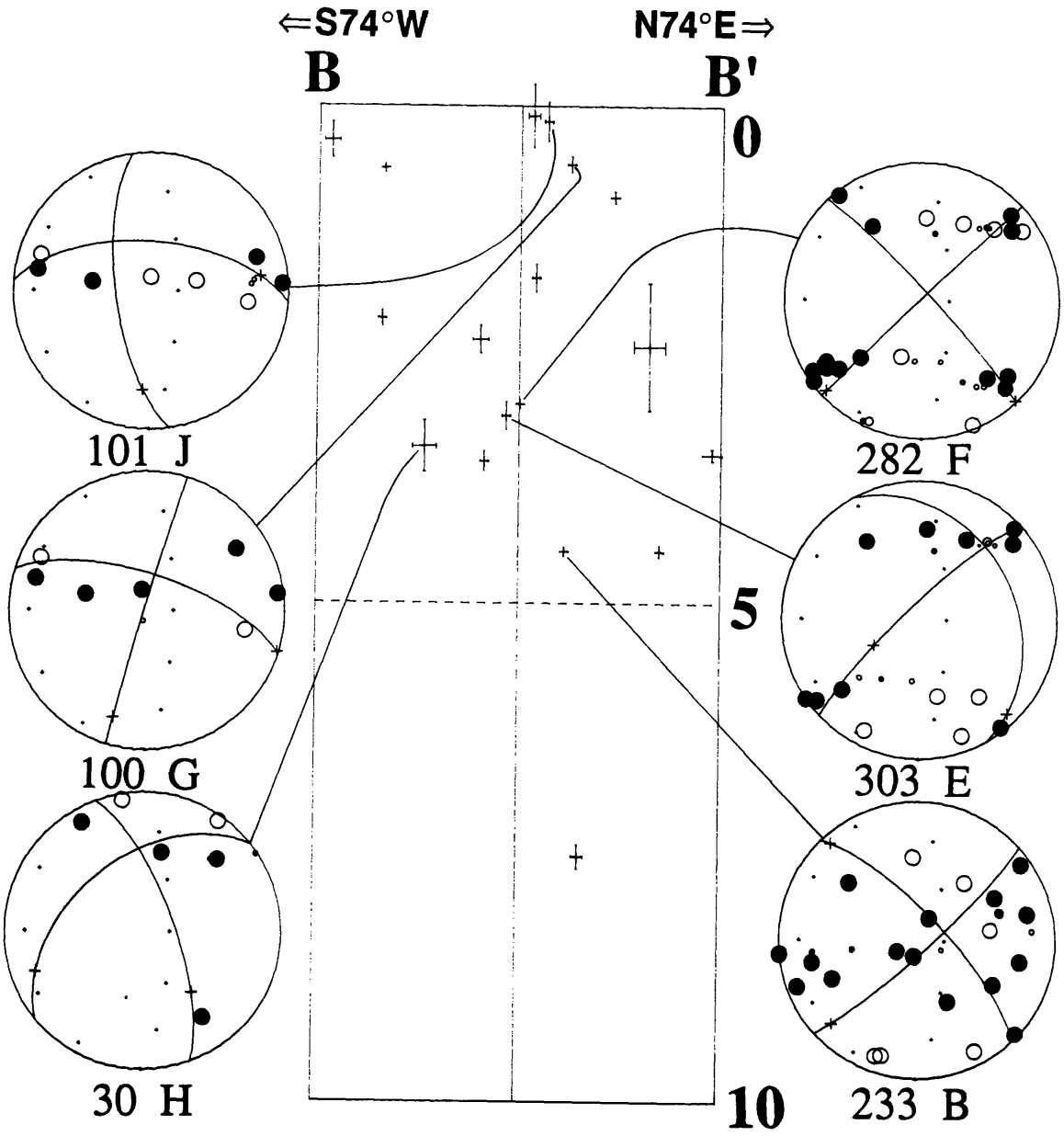

Fig. 3-16. Cross-section view toward N16°W; located on Figure 3-13. Conventions as on Figure 3-14.

northwest-dipping listric normal fault, but the small number of events and the location of this area at the margin of the seismic array make this inference very tentative. This hypothetical fault would project to the surface in the center of southern Hansel Valley.

The events between about 41.73° and 41.82°N do not lie as tightly on a single plane (Figures 3-15 to 3-17). Nodal planes of several of these events located south of 41.79°N strike north-northwest; these earthquakes are also aligned somewhat on this trend (Figure 3-15). A cross-section perpendicular to N16°W (Figure 3-16) shows that these events might

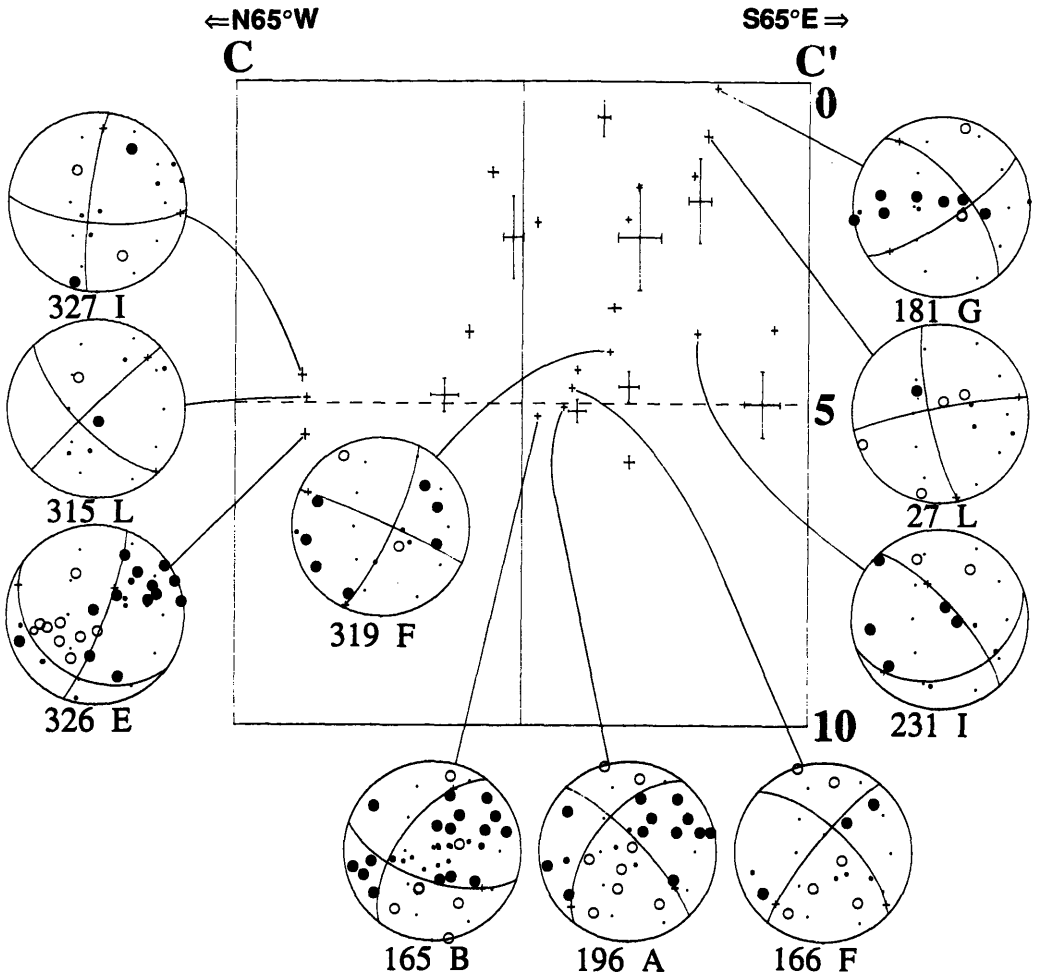

Fig. 3-17. Cross-section view toward N25°E; located on Figure 3-13. Conventions as on Figure 3-14.

deepen to the east-northeast; the southwestern boundary of this seismicity might be a east-northeast dipping normal fault consistent with the mechanisms of events 282, 233, and possibly 30. Other events, notably 100 and 101, might lie either on a parallel fault or a south-southwest-dipping normal fault. Both inferred faults project to the surface on the south side of the embayment in the Hansel Mountains, near the location of station E51 (Figure 3-2). The three earthquakes southeast of those included in Figure 3-16 (Figure 3-13) might lie on the range front fault, which here is very close to the easternmost event shallower than 2 km (Figure 3-2 and 3-15).

Viewed in cross-section, the shallow events above about 4 km depth and north to 41.82°N appear to lie mostly on one or two west dipping structures (Figure 3-17). These events occur near the eastern edge of the embayment in the Hansel Mountains (Figure 3-2) and near the southern projection of a west-dipping normal fault mapped immediately to the north within

the Hansel Mountains (Figure 3-1). On the ground, however, we observed an east-dipping normal fault scarp that offsets latest Quaternary lakeshores and trends nearly north-south almost through events 181 and 27 (Figure 3-15); this scarp is probably a strand of the *en echelon* faults bounding Hansel Valley on the west. Although slip on west-dipping faults probably accounts for the observed seismicity, either, or perhaps both, west and east dipping faults could be responsible for these events.

Viewed in cross-section, the events with depths near 5 km between about 41.82° and 41.84°N seem to lie very near a single west-dipping plane (events 319, 166, 196, and 165, Figure 3-17). The focal mechanisms indicate that if this were the fault plane, motion would be nearly purely dip-slip (Figure 3-17). Two curious features of these four events are visible from the map view (Figure 3-15): from south to north the events deepen, and the nodal planes of the focal mechanisms trend more to the northwest. If the fault is curving, either nodal plane might represent the fault plane. This structure apparently underlies or merges with an east-west trending, north-dipping fault that lies to the north and is described below. If the two faults merge, then the north-dipping nodal plane of event 165--the event nearest this other fault--should define the southern fault, and the actual fault plane that slipped to produce these earthquakes would parallel the gently eastward dipping nodal plane. Farther south from the east-west striking fault, this fault might be expected to be subparallel to the east-dipping nodal plane of event 319. Because these events occurred at depths between those of the shallow and deep groups of earthquakes farther south, the implications of this inference might apply over much of the southern part of the array: the gap between these two groups might be occupied by a quiescent or aseismic east-dipping low-angle normal fault.

Deeper Seismicity. The deeper earthquakes in the southern part of the array are aligned slightly east of north along two segments offset from one another near 41.72°N (Figure 3-13). Because these events lie on the margin of the array, their locations are more uncertain than most of the other events located within the array. Additionally, these events are strongly influenced by the lateral velocity contrasts in the center of the array (Chapter 2). To understand better the uncertainties in the locations of these events and to reduce the influence of unrecognized lateral variations of seismic velocities, we relocated two subsets of these events using arrival times from two groups of stations. One group included 9 and the other 18 stations; each event within a subset was recorded at all of the stations used for that subset. This eliminates most of the bias in the relative locations of these events caused by the different groups of stations recording each event.

When located using all of the available arrival times and structure M3D ("M3D locations"), events south of 41.72°N appear to lie near a subvertical plane between about 4.5 and 8 km depth (Figure 3-18). Although this plane parallels a nodal plane of many of the

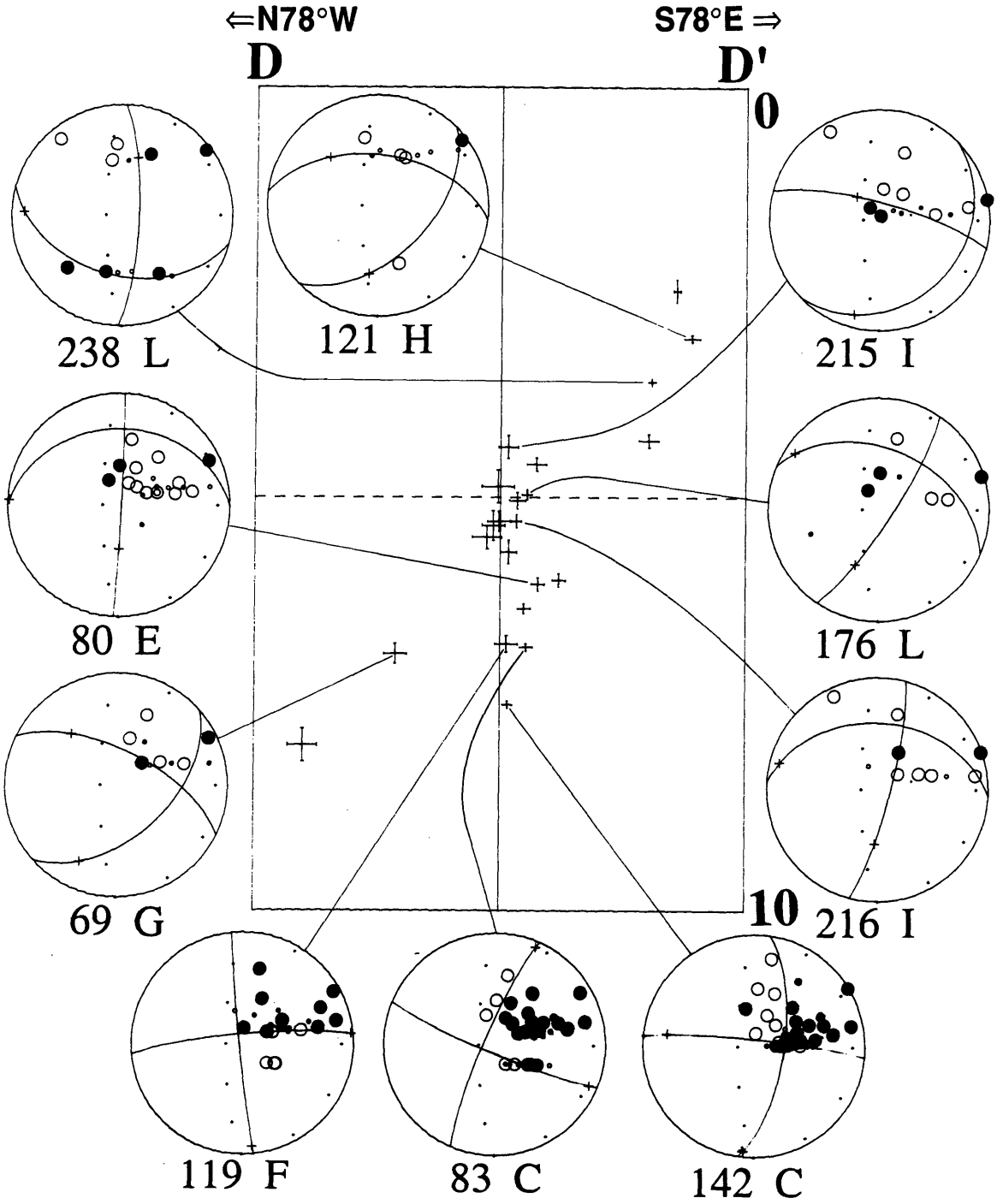

Fig. 3-18. Cross-section view toward N12°E of deep events south of the array; located on Figure 3-13. Conventions as on Figure 3-14.

focal mechanisms obtained from these events, the actual fault plane, should only one exist, cannot be resolved. Standard errors in the locations of these earthquakes tend to be only a few hundred meters, but relocating these events using different subsets of the arrival times

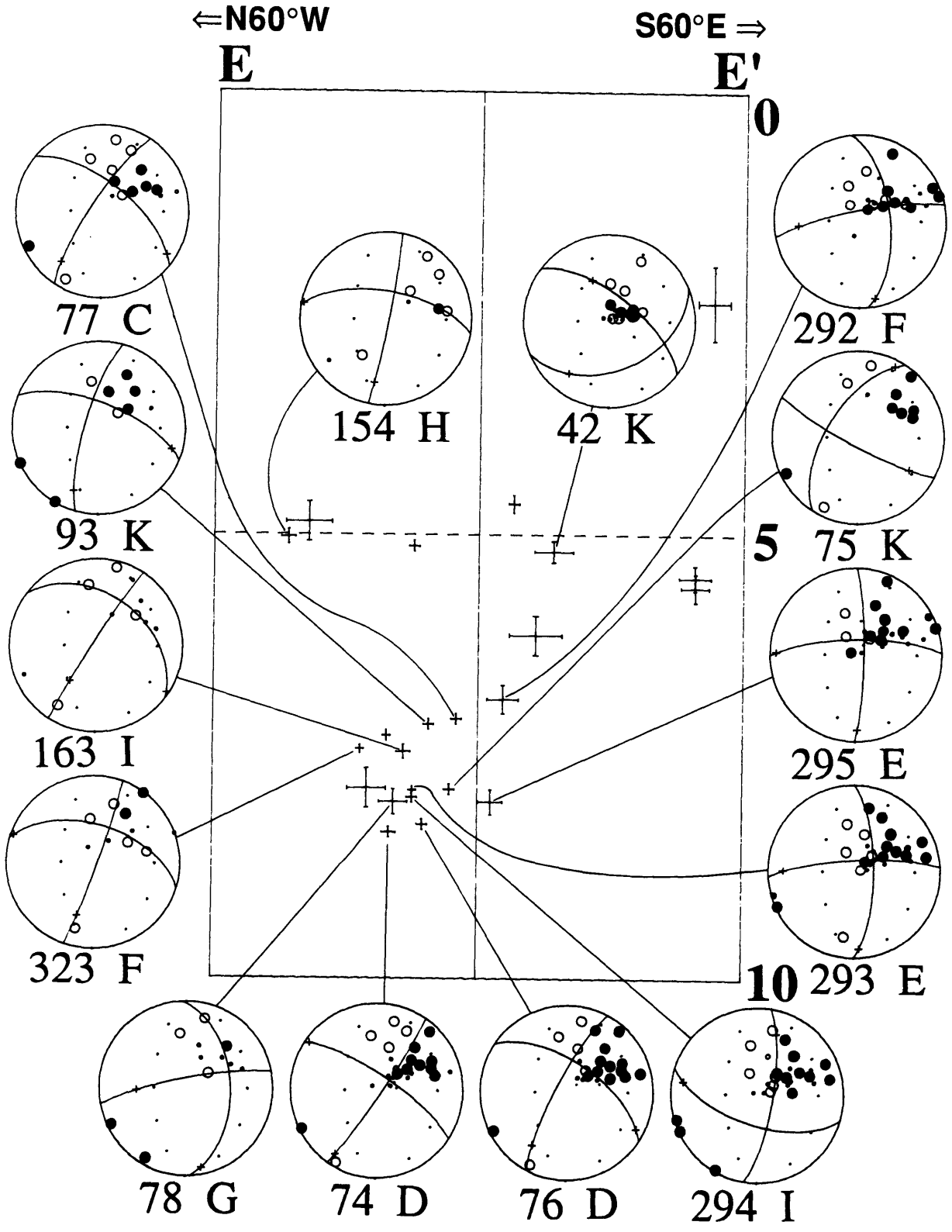

Fig. 3-19. Cross-section view toward N30°E of deep events in the southwestern corner of the array; located on Figure 3-13. Conventions as on Figure 3-14.

produces startlingly different results. Using only the arrival times at nine of the closest stations we find that the earthquake locations cluster tightly on a gently east-dipping plane that also parallels many of the nodal planes of focal mechanisms of these events. But when using 18 stations, we find all the events cluster more tightly than the M3D locations on a steep, west-dipping plane. Clearly the uncertainties in the locations of these mechanisms is at least 1-2 km vertically and about 1 km horizontally. All but one of the earthquakes are consistently located below the 3.7 km velocity contrast; for this reason, we believe that the focal mechanisms of these events are not too strongly affected by the large uncertainties of the locations of these events. We can only conclude that the deep events in the southernmost part of the array are probably all below 4 km depth and that the focal mechanisms of these events are consistent with slip on either a near-vertical, north-south fault that drops the west side down or a very low-angle fault that moves the upper plate to the east-southeast.

The locations of the events deeper than about 4 km and north of 41.72°N are better constrained but do not unambiguously resolve the fault(s) on which these earthquakes occur. Relocating these events using either subset of the stations described above produces locations that differ from the M3D locations less than the differences between locations of the events farther south. Relocations of the events initially located near 8 km depth (Figure 3-19) differ little from the M3D locations; the depths of these relocations are within 600m of the M3D locations and the epicenters are within 800m. Only two of the events much shallower than 8 km were recorded by enough stations to be relocated using either subset of stations described above; the three locations of one (event 292) differed from one another by several kilometers. Hence it appears that the most accurately located, well-recorded events cluster at a depth of about 8 km; this cluster appears to be aligned more with the gently east-dipping nodal plane than the steep, west-dipping plane prevalent in the focal mechanisms obtained from these earthquakes (Figure 3-19). Because the uncertainties in depth of these events are perhaps twice those in any single horizontal direction, it is more likely that these events occurred on a single, gently dipping plane between 7 and 8 km depth than on a single steep west-dipping plane. Although we prefer this gently-dipping plane, we cannot ignore the possibility that these events lie on a steep, west-dipping fault.

Central Group of Earthquakes

North of 41.81°N and south of about 41.90°N events deeper and shallower than 5 km occur within the same area; this area has the highest density of earthquakes observed within the array (Figure 3-5). Because these events occurred within a fairly dense array of stations (Figure 3-2), the locations of these events are among the most tightly constrained of any that

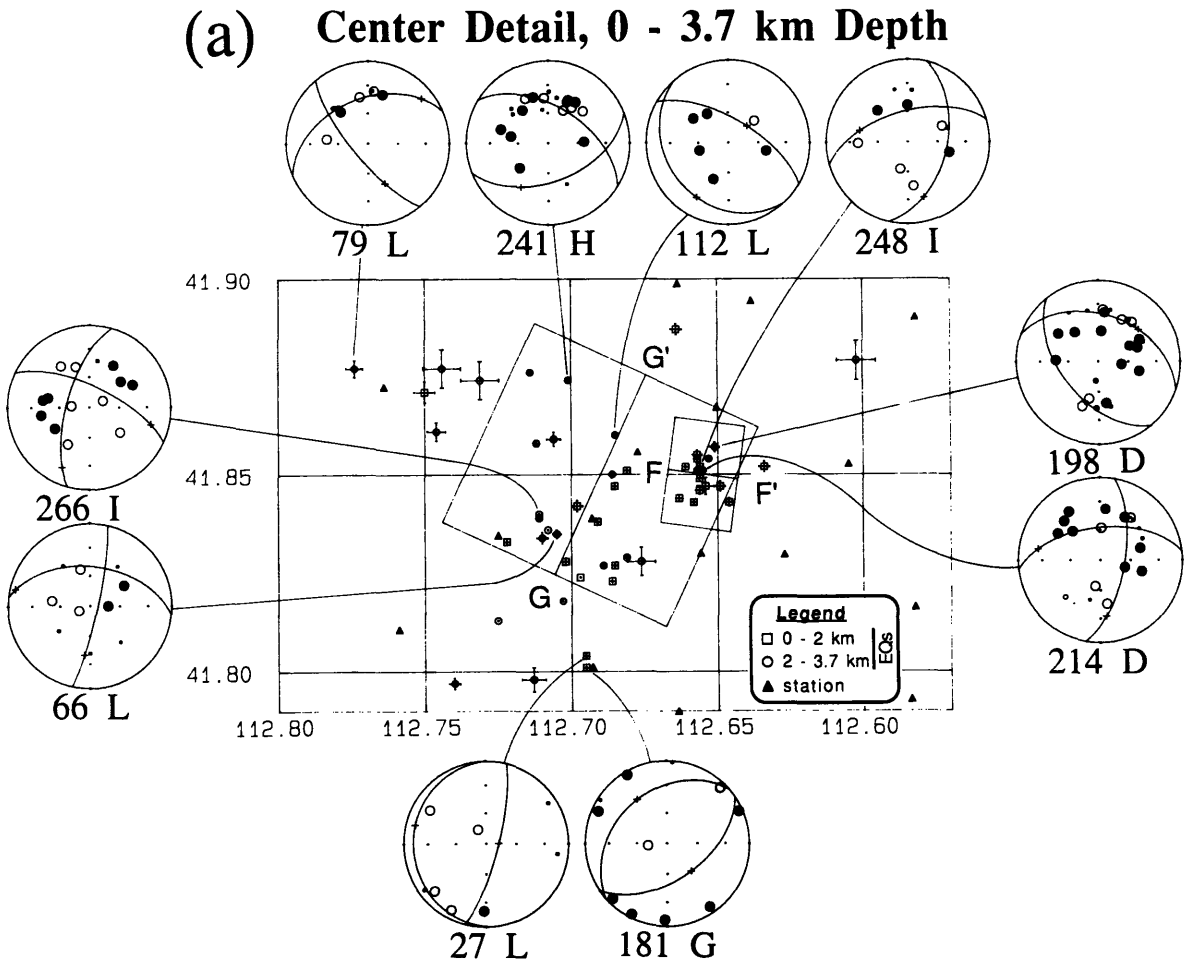

Fig. 3-20a. Map of events in the central part of the array with depths between 0.0 and 3.7 km. Conventions as in Figure 3-15.

we determined, and the large number of focal mechanisms found for these events permit us to define several faults on which slip apparently occurred during these earthquakes.

The two structures best defined from maps, crosssections, and focal mechanisms are a pair of oblique-slip normal faults, one trending about N65°W, the other about N8°E (Figures 3-20 to 3-22). Both faults have a right-slip component of strike-slip motion and thus are not conjugate faults. The smaller of the two faults, which trends N8°E and dips about 75°E, parallels the east edge of the Hansel Mountains about 1 to 4 km north of station MUN (Figures 3-2, 3-20a, and 3-21). Two focal mechanisms (events 248 and 214) were found from the earthquakes along this fault; both indicate that the fault's hanging wall moved nearly equally down and to the south-southeast relative to the footwall. An event with a mechanism indicating north-south thrust faulting (event 198) might represent the truncation near 3 km depth of this fault by an east-west trending thrust fault. This north-south trending oblique-

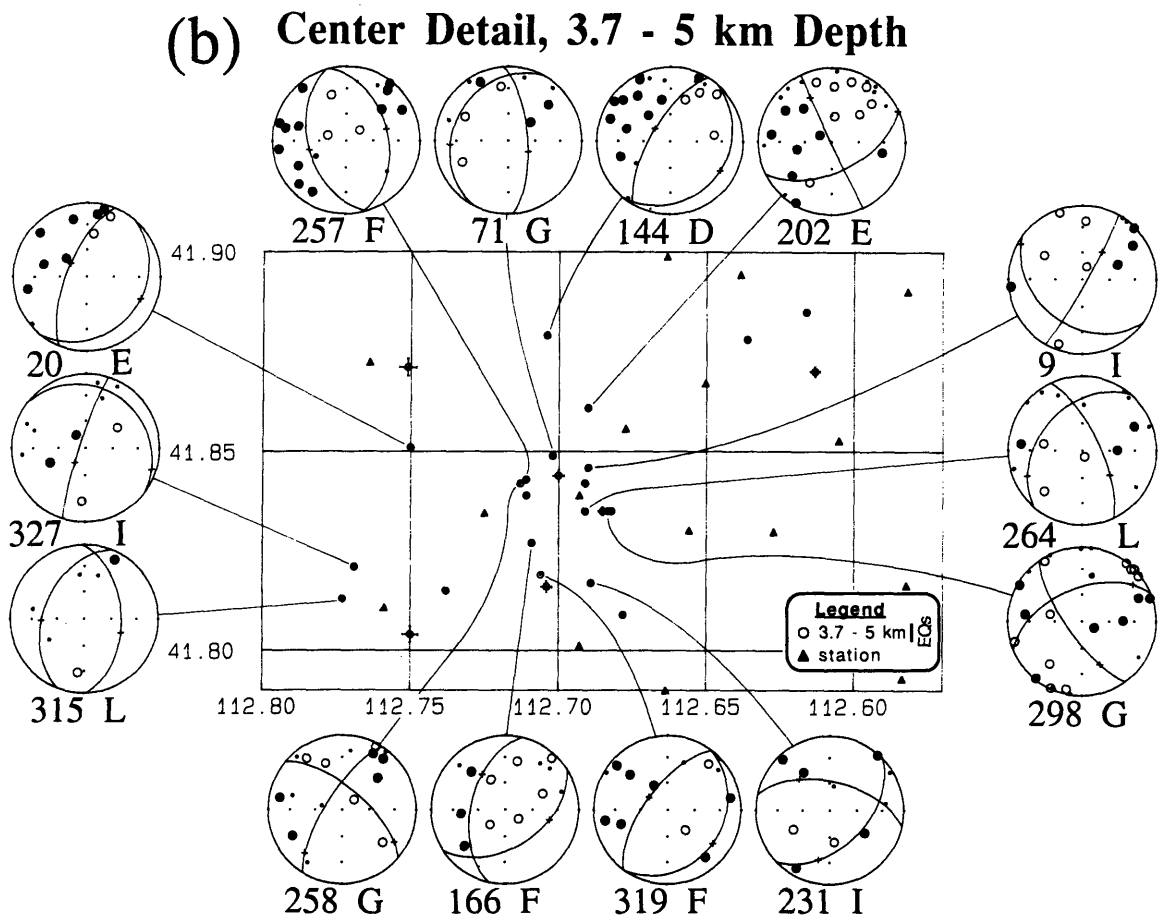

Fig. 3-20b. Map of events in the central part of the array with depths between 3.7 and 5.0 km. Conventions as in Figure 3-15.

normal fault appears to be part of the range-front fault system along the east side of the Hansel Mountains.

The other well-defined fault appears to stretch from the surface to a depth of about 5 km and is seen as a north-northwest dipping plane in cross-section (Figure 3-22). Five of the six focal mechanisms found from events within this alignment (events 266, 264, 258, 257, and 298) indicate a right-slip component of motion along any east-northeast striking fault; all six support a normal sense of dip-slip on this north-dipping fault. It is instructive to note that this fault appears to cross both the seismic discontinuity at 3.7 km depth and the southern boundary of the low-velocity region under the center of the array, and the focal mechanisms do not seem to be unaffected by these variations in structure. This fault projects to the surface along a line about 2-3 km south of and nearly parallel to the southern dashed line in Figure 3-2. Although it seems to parallel the southern edge of a higher part of the Hansel Mountains, the sense of slip is opposite that expected from the topography.

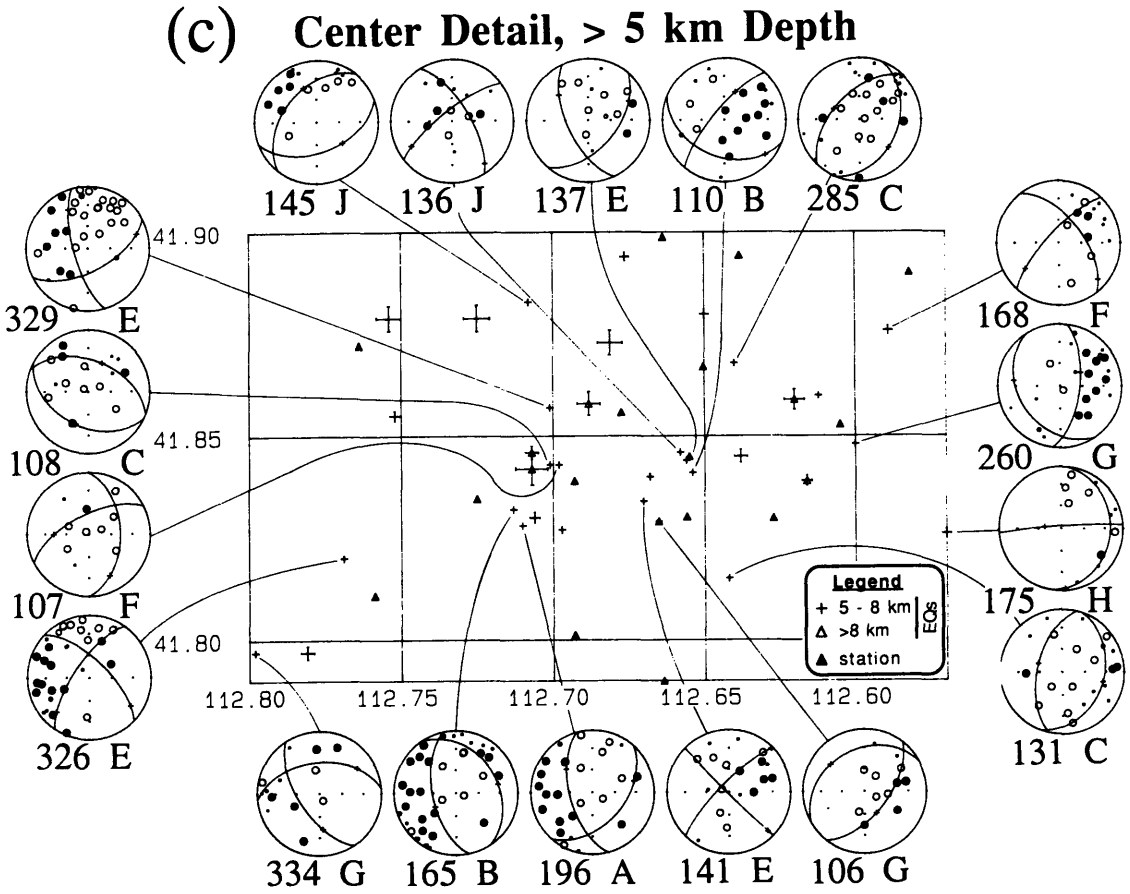

Fig. 3-20c. Map of events in the central part of the array with depths greater than 5.0 km. Conventions as in Figure 3-15.

Three other features can be distinguished from the earthquakes above 5 km depth: north-south striking normal faulting, east-west striking thrust faulting, and east-dipping low-angle normal faulting (Figures 3-20 and 3-21). The north-south normal fault was described with the southern group of earthquakes (Figures 3-15 and 3-17); it appears to extend near the east-west oblique-slip fault but cannot be continued north across it. Two events that might lie north of the oblique-slip fault, event 257 and event 71, may indicate normal slip on a north-south striking plane, but such a fault, if present, cannot be verified from our earthquake locations.

A diffuse, south-dipping band of seismicity lies to the north of the east-west oblique slip fault; four focal mechanism obtained from events in this band (events 79, 241, 112, and 198) indicate that it might represent south-over-north thrust faulting (Figures 3-20 and 3-22). As noted above, this feature seems to underlie the inferred range-front fault at the east side of the Hansel Mountains, but it does not clearly extend under Hansel Valley. Although this band of seismicity might extend south to the east-west oblique-slip fault, the thrust mechanisms are

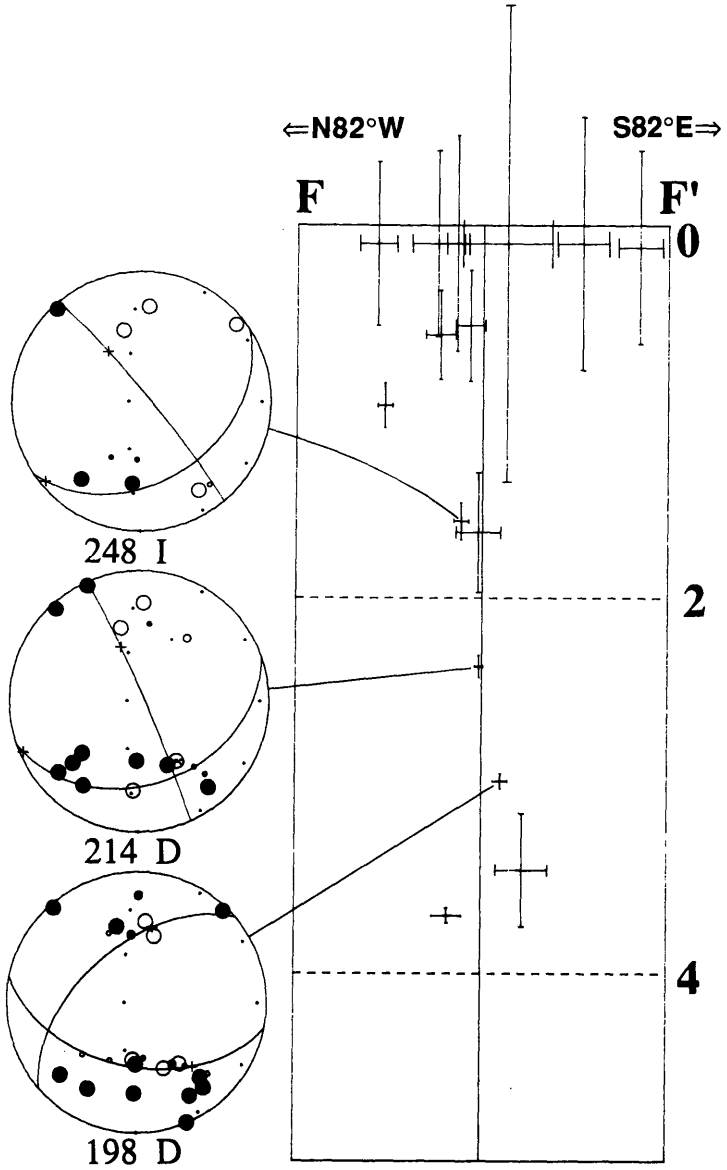

Fig. 3-21. Cross-section toward N8°E of very shallow cluster of events at east side of center of array. Conventions as in Figure 3-14.

only observed for events located north of 41.85°N and shallower than 3.7 km. This band of seismicity projects to the surface near the northern edge of the high part of the central Hansel Mountains just south of I-84 (Figure 3-2).

Three focal mechanisms between 4.5 and 5 km depth might represent slip on an east-dipping low-angle normal fault: events 327, 20, and 144 (Figure 3-20b). Six other events might be consistent with such faulting: events 315, 166, 319, 131, 165, and 175 (Figures 3-20b,c). All but one of these events lies south of the east-west oblique-slip fault described previously. Although the mechanisms comprising this group are poorly defined, and any associated band of seismicity is poorly defined, the possibility of a low-angle normal fault at this depth is intriguing. As we found farther south, the other structures found at shallower depths and described above do not extend below 5 km (Figure 3-22); this is particularly

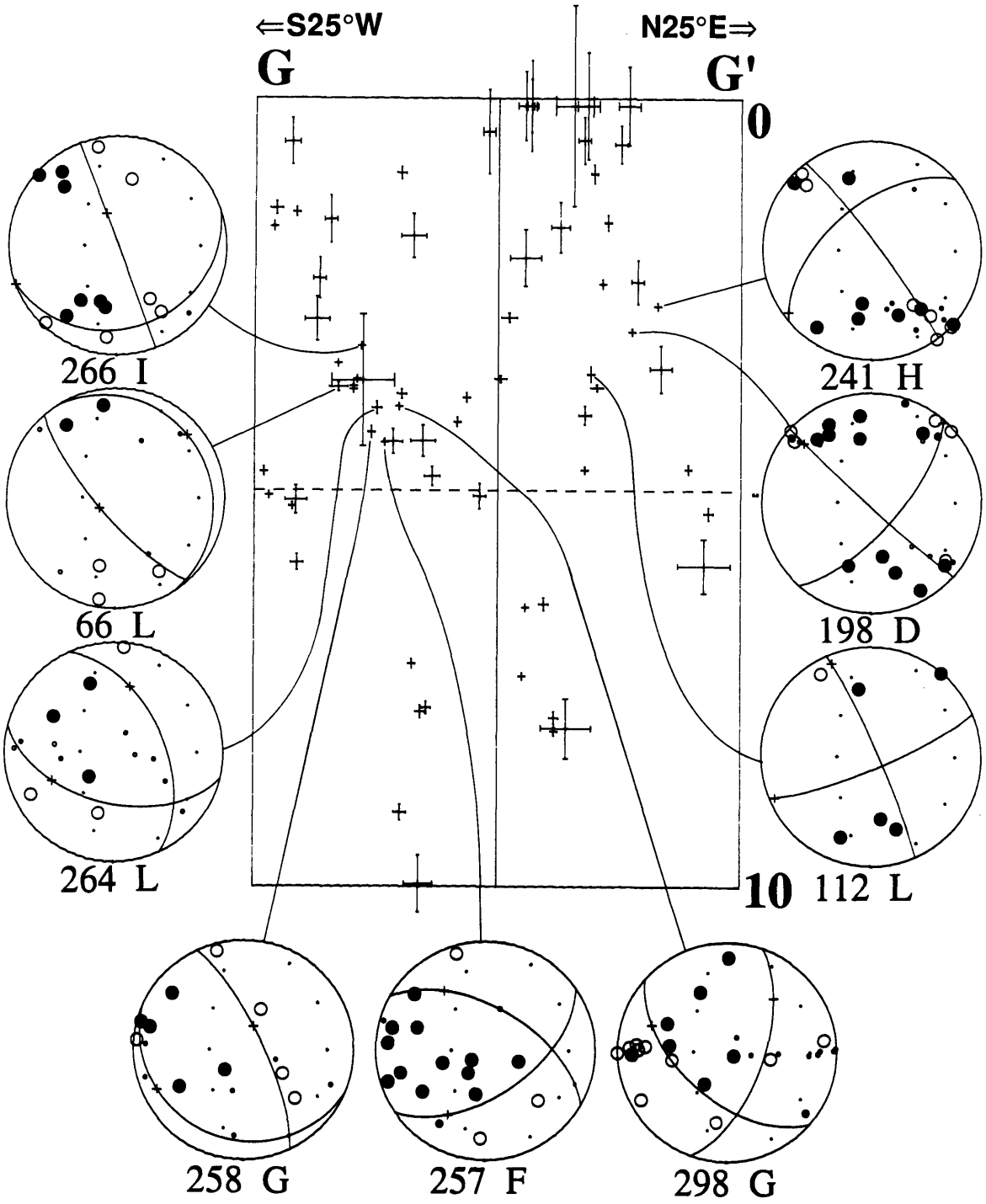

Fig. 3-22. Cross-section toward N65°W of events in center of array with selected focal mechanisms. Note the well-defined north-dipping plane at left and the south-dipping plane containing events with thrust mechanisms at right. Most events above these two planes are shown in Figure 3-21. Conventions as in Figure 3-14.

striking for the east-west oblique slip fault. Events with mechanisms consistent with slip on a low-angle normal fault are present beyond the region with epicenters of almost all other events, suggesting that these events lie on a fairly flat structure. Although the evidence is not compelling, we suspect that a gently east-dipping normal fault lies near a depth of 5 km in this area and is the lower boundary for the shallower structures.

The large number of earthquakes deeper than 5 km, many with well-constrained focal mechanisms, fail to define even a single structure (Figure 3-20c). These deeper events, however, are only present north of a plane extending down from the base of the east-west striking oblique-slip fault (Figure 3-22). Most events fall into two groups: those with a varying degree of oblique-slip consistent with right-lateral motion on a north-northwest striking plane (e.g., events 329 and 141, Figure 3-20c), and those with very nearly pure dip-slip, normal-slip mechanisms and northeast striking nodal planes (e.g., events 285 and 145). In general, the oblique-slip mechanisms seem to be dominant for events near the southern edge of the deeper seismicity, near 41.82°N, and the dip-slip mechanisms are more prevalent among the earthquakes farther north. This tendency becomes clearer when events north of I-84 are considered (Figure 3-23). One group of events with oblique slip mechanisms (events 136, 137, and 110, Figure 3-20c) seems to be aligned to the northwest, suggesting that the right-lateral component of motion, similar to that recognized above 5 km, might be prevalent below 5 km. The decreasing oblique-slip component in focal mechanisms determined farther north, and the total absence of oblique-slip mechanisms to the south, suggests that a roughly east-west "zone" of oblique-slip faulting crosses through this area between about 41.82°N and 41.86°N. Both the right-lateral component of slip on the east-west plane above 5 km and the more nearly east-west strike of the nodal planes with a right-lateral sense of strike-slip below 5 km depth suggest that this zone probably accommodates right-slip along its length.

Northern Earthquakes

The lower density of stations north of highway I-84 results in greater uncertainties for both hypocenters and focal mechanisms determined for events within the northern group of earthquakes (Figure 3-2). For this reason we offer only a cursory summary of the possible structures within this region. Earlier workers analyzing the aftershocks of the 1975 Pocatello Valley earthquake found a diverse group of focal mechanisms in this area [Arabasz et al., 1979], and the focal mechanisms presented here underscore this diversity.

Most focal mechanisms found in this area are associated with earthquakes located south of 42°N (Figure 3-23). Most of the events yielding focal mechanisms fall into one of two northwest-trending groups. In cross-section, both groups appear to dip steeply away from the

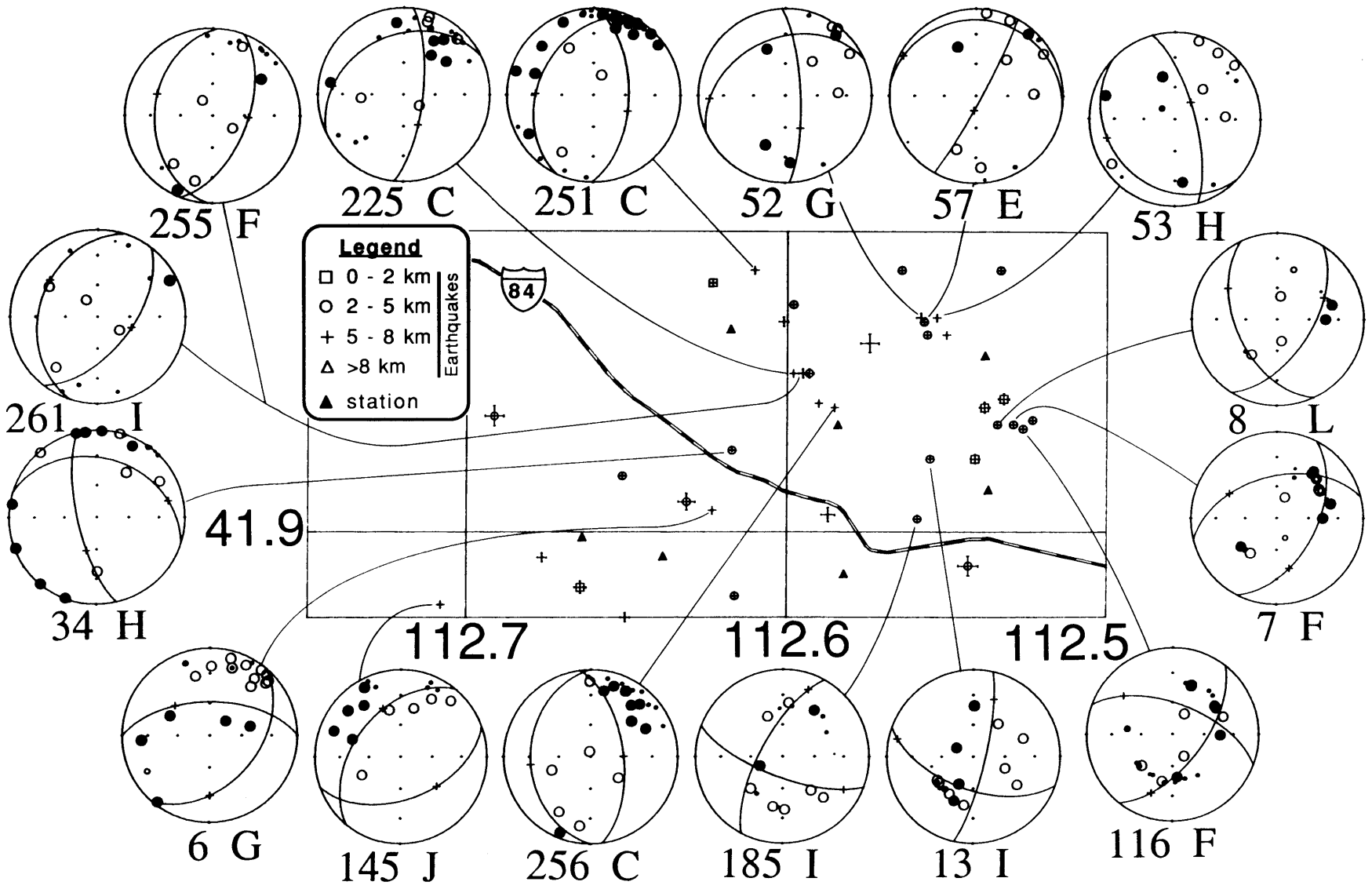
255 F
225 C
251 C
52 G
57 E
53 H
261 I
8 L
34 H
7 F
6 G
145 J
256 C
185 I
13 I
116 F
Legend
0 - 2 km
2 - 5 km
5 - 8 km
>8 km
station
Earthquakes
84
41.9
112.7
112.6
112.5

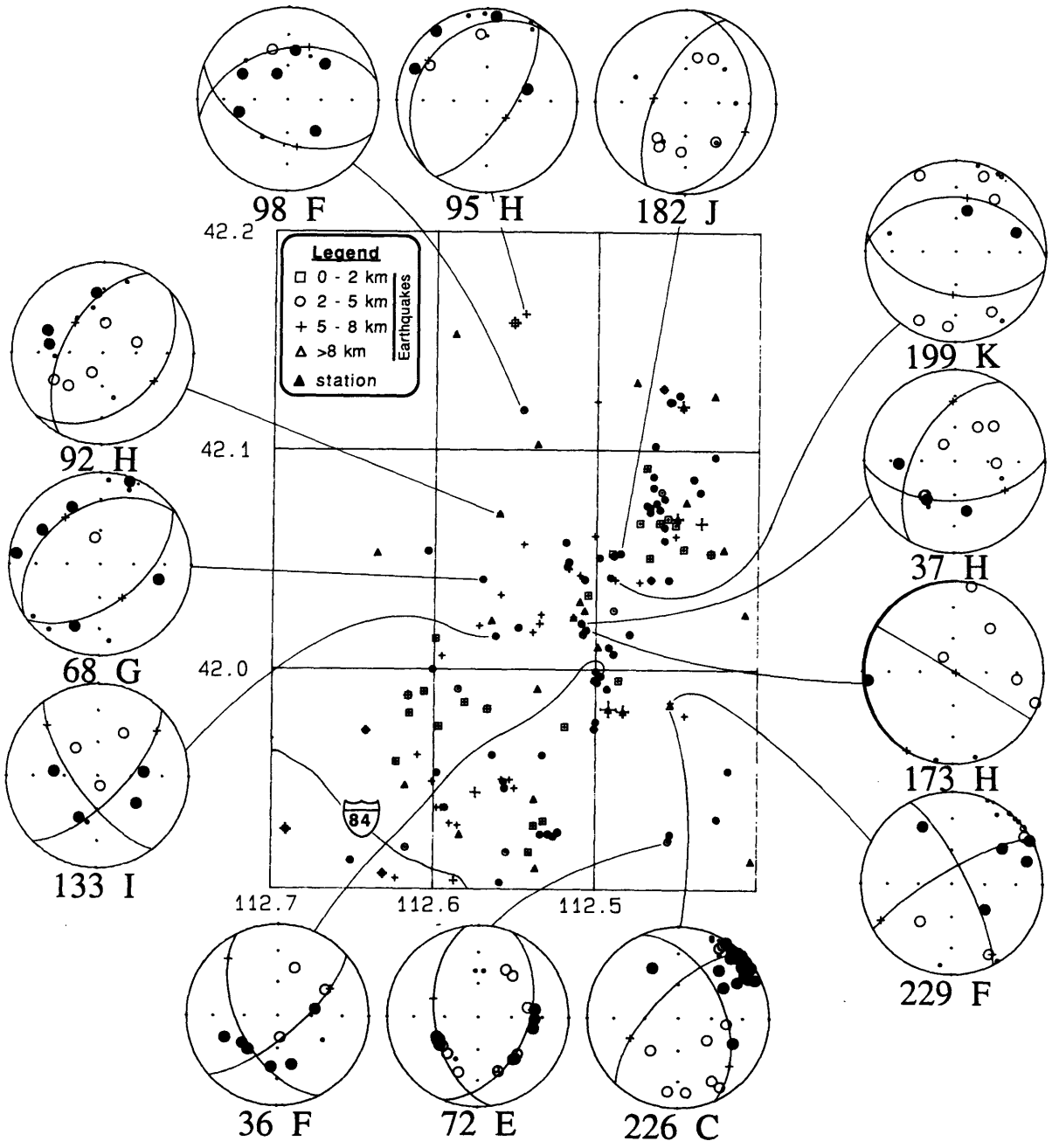

Fig. 3-24. Map view of events in the northern part of the array; the mechanisms of several events in the lower-left hand corner are shown in Figure 3-23. Conventions as in Figure 3-15.

Fig. 3-23 (opposite). Map view of events just north of the center of the array along highway I-84. Conventions as in Figure 3-15.

other, but neither nodal plane of many of the mechanisms of these events parallels this trend. These structures extend only between about 4.5 and 6 km depth; few earthquakes shallower than 3.7 km depth were located between 41.86°N and 41.96°N. The limited depth extent of these bands of seismicity prevents us from eliminating the more gently dipping nodal plane from consideration as the fault plane, but the opposite sense of slip indicated by the mechanisms on these two structures (compare events 52 or 53 with 251 or 256) seems more consistent with a pair of north-northwest-striking high-angle dip-slip faults.

Seismicity farther north is increasingly poorly located, but much of it defines two nearly north-south trending bands (Figure 3-24). The southern band, along 112.5°W between about 41.98°N and 42.05°N, apparently dips steeply to the east and lies along a small ridge that projects into Pocatello Valley (Figure 3-2). This band's northern termination is roughly the same latitude of the southern end of the band of seismicity along the eastern side of Pocatello Valley. Although the focal mechanisms that we found from these two bands are not very enlightening, the locations of these epicenters suggests that these events are associated with the normal faults bounding Pocatello Valley on its eastern side. Unlike the southern part of the array, there does not appear to be a sharp lateral offset of seismicity at any depth in the northern part of the array.

The structures inferred from the seismicity suggest a simple categorization of the tectonics of the Hansel Valley--Pocatello Valley region. South of about 41.82°N, the seismicity above and below 4 to 5 km depth is separated by several kilometers; most of the focal mechanisms are dominantly dip-slip. The shallower seismicity might be associated with several faults within the Hansel Mountains; the deeper seismicity could lie along either high- or low-angle normal faults. From about 41.82°N to 41.9°N, no horizontal offset of seismicity with depth was observed. The dominant feature is a west-northwest trending, north-dipping fault apparently accommodating right-lateral normal slip. This oblique-slip fault seems to mark the northern edge of the offset seismicity seen to the south and falls near the southern edge of the low-velocity region of structure M3D (Figures 3-20 and 3-4). North of 41.9°N we find neither vertical offsets of bands of seismicity nor well-defined oblique-slip structures; although the seismicity in this region exhibits complexities beyond the resolution of our data, most of the seismicity appears to be related to range-bounding normal faults that could be inferred from the surface topography.

DISCUSSION

Perhaps the greatest obstacle to interpreting the results of a microearthquake survey is the limited amount of time that the instruments are deployed; any interpretation can be

discounted as merely reflecting a moment in time and not necessarily being representative of the long-term seismicity of a region. There certainly are risks in using seismicity recorded for only a short time, but the presence of features in the seismicity are not artifacts; they represent faults, however small, that have slipped enough to generate seismic energy. The interpretation of such structures should not merely amplify them to fit the strain release anticipated for a region over time, for it is likely that only some of the structures that produce small earthquakes will produce the large earthquakes that absorb most of the strain that is expressed seismically.

The task of a student of microearthquakes is exactly analogous to that of a field geologist inferring large, unseen structures from the smaller structures he or she observes. Any individual structure could be highly misleading, but the overall strain evident in the numerous small structures can lead to a correct inference of the presence of a larger structure. The analogy is particularly relevant for the case of small "accessory" faults; the offsets observed across such faults were produced by earthquakes such as those described here. We contend that the results of this study can produce a meaningful picture of the active structures in our region; we desire an explanation that accounts for these structures and that does not ignore them. With these goals in mind, we present an interpretation of our results that, although probably not unique, does provide an explanation for much of what we have described.

The greatest problem in forcing a simple horst-and-graben structure to fit our observations is the persistent lack of earthquakes in Hansel Valley, which should overlie all faults responsible for its creation. Perhaps the second greatest problem is the variety of types of faulting within the Hansel Mountains; the east-west trend of the oblique-slip fault zone and the possible thrust fault are not obviously consistent with the Hansel Mountains being a simple north-south trending horst. A third difficulty in applying a horst-and-graben structure to these events is that bands of epicenters of the shallow and deep seismicity south of about 41.8°N are offset from one another. None of these features seem particularly easy to explain if the structures in this area represent slip on high-angle normal faults, particularly if such faults must extend throughout the seismic part of the crust [e.g., Jackson, 1987].

The most obvious explanation for the vertically offset seismicity south of 41.8°N is that active faults in the area are offset at depth; the offset must be on a structure with a gentle dip, or strain must be accumulating across the gap between the bands of earthquakes. Although a low-angle normal fault is not sharply defined by our results, there are some palpable indications of its presence. Several events in the central part of the array (Figures 3-20b,c) with depths near 5 km yielded focal mechanisms consistent with a low-angle normal fault that displaces its hanging wall to the east or southeast. A series of earthquakes just south of the east-west trending oblique-slip fault in the central part of the array were located near 5 km

depth (Figures 3-15 and 3-17); the differences between the mechanism of the event farthest north and those to the south suggests that the fault plane responsible for these events curves as it nears the east-west trending oblique-slip fault. If the two faults merge, then the nodal plane representing the fault plane appears to be an east-dipping low-angle normal fault in the vicinity of the southernmost earthquakes of this group. Both the apparent termination of this fault against the east-west striking oblique slip fault and the presence at this latitude of the northern boundary of the vertically discontinuous events indicates that the oblique-slip fault provides some insight into the possibility of low-angle normal-slip in this area.

The west-northwest trending right-lateral oblique normal-slip fault in the central part of the array might be the best determined structure in the area. This fault marks the northern edge of a region where earthquakes deeper and shallower than about 5 km occur in regions kilometers apart; to its north, epicenters of both deeper and shallower events are in the same area. Near this fault, some structural continuity across a depth of 5 km is indicated by the focal mechanisms indicating right-lateral oblique-normal slip on northwest trending planes for events beneath the well-defined oblique-slip fault. The sharp change from almost no earthquakes below 5 km south of this fault to a large number below 5 km north of the fault suggests that the fault overlies the boundary between a seismically inactive block to the south and a seismically active block to the north. If we accept the presence previously suggested of a low-angle normal fault at about 5 km depth south of this fault, then a reasonable hypothesis is that this low-angle normal fault is offset across this fault and lies at a greater depth, perhaps below any observed earthquakes, to the north of the fault.

A review of the regional geology supports this hypothesis. Covington [1983] presented evidence strongly supporting the existence of a low-angle normal fault under the Raft River Valley (Figure 3-1). This valley is abruptly truncated at its south end by the Raft River Mountains, which are the lower plate of a low-angle normal fault that dips east from the eastern edge of the mountains (Figure 3-1; Malavieille [1987], Allmendinger et al. [1985]). If the faults under the Raft River Valley and at the east margin of the Raft River Mountains form part of a single fault system that separates a lower plate including the Albion and Raft River mountains from an upper plate that includes rocks east of and in both Raft River and Curlew valleys, then the boundary between the Raft River Valley and the Raft River Mountains will be a right-lateral oblique normal-slip fault (Figure 3-25). This structure lies west-northwest from the west-northwest trending oblique slip fault within the Hansel Range, nearly along the strike of both structures.

Because it only juxtaposes upper plate rocks, the east-west trending oblique-slip fault in the Hansel Mountains above 5 km depth is not strictly analogous to that on the north flank of the Raft River Mountains; this shallow oblique-slip fault and the thrust fault(s) to its north

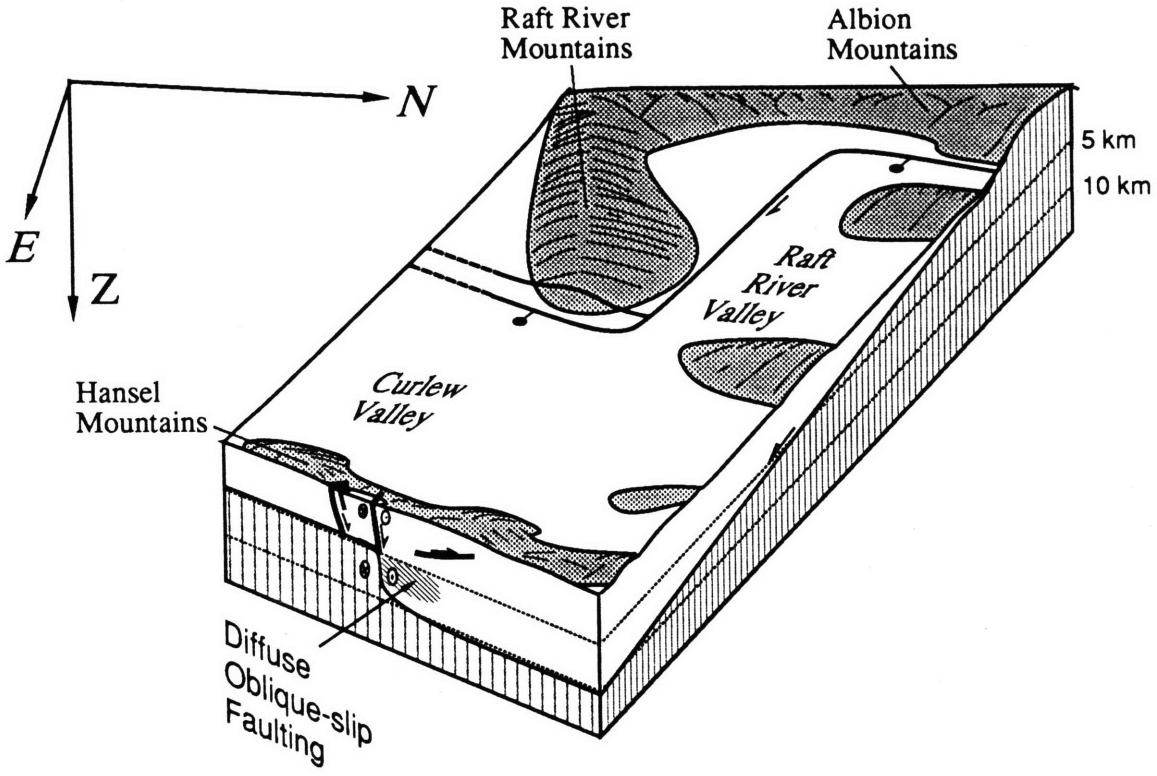

Fig. 3-25. Simplified block diagram illustrating the possible relationship between the fault between the Raft River Mountains and the Raft River Valley and the faults observed within our array. The lower plate of the low-angle normal fault is ruled; heavy faults under Hansel Mountains are those inferred to have produced earthquakes observed in our experiment. Structure under the Raft River Valley simplified from Covington [1983].

probably represent an adjustment between the motions of the thicker upper plate to the north and the thinner upper plate to the south. Such an adjustment could reflect either slightly different extension rates within the upper plate or slightly different dips of the fault at the base of the upper plate to the north and south of the fault. The deeper portion of this oblique-slip fault zone, that below 5 km, is inferred to juxtapose upper and lower plate rock and could be considered the eastern extension of the northern boundary of the Raft River Mountains (Figure 3-25); if so, it then forms a step in a low-angle normal fault beneath the region.

The presence of an east-west trending step in a low-angle normal fault beneath the Hansel Mountains provides an explanation for other geologic and seismologic features. The small volcanic field and Tertiary sedimentary rocks at the northern end of Hansel Valley might be

due to this step, which could have provided a zone of weakness for intruding magma. The small basin of northern Hansel Valley might be bounded by faults that owe their origin to the deeper step in the low-angle normal fault in the same way that the east-west trending fault in the Hansel Mountains might.

The low-velocity region in the center of the array, earlier considered to be related to the volcanic rock and sediments exposed within it, could also be caused both by intense shearing of the rock near the oblique slip fault and by the greater thickness of low-velocity lower plate rock north of this fault. The somewhat lower velocities of the northern and central portions of the array relative to the portion south of the southern dashed line of Figure 3-2 might reflect the increased thickness of low-velocity upper plate rock north of this oblique-slip fault zone.

Because of the uncertainties in the depth of our second velocity contrast, the bottom of the low-velocity zone might coincide with the inferred low-angle normal fault beneath the southern portion of our array. We considered the depth of this boundary to lie between 3.2 and 5.2 km depth; a somewhat larger uncertainty might be appropriate if considering only a portion of the array. A large displacement on a low-angle normal fault should juxtapose low velocity upper crustal rock with higher velocity, mid-crustal rock; hence the location of this velocity contrast in the southern portion of the array is consistent with a large low-angle normal fault at that depth. Although structure M3D extends this contrast well to the north (Figure 3-4), the velocity structure, as indicated previously, is not as tightly constrained in the northern portion of the array. Estill [1976] found a velocity structure within Pocatello Valley using travel-times from aftershocks of the 1975 Pocatello Valley earthquake that were recorded by a temporary array of 10 stations; this structure has velocity contrasts at 1.5 and 7.2 km depth. Hence it is possible that the strong velocity contrast is strongest in the southern part of the array and is related to the presence of a low-angle normal fault. Arabasz and Julander [1986] found offsets of seismicity across velocity gradients in southern Utah; they also ascribed this phenomenon to the presence of a subhorizontal (but apparently aseismic) fault.

A possible objection to interpreting the seismicity as the product of low-angle normal faulting is the observation that the seismicity falls within a fairly narrow band trending north-northeast across the area. Without assuming that the observed seismicity is nonrepresentative of the long term seismicity of the area, the earthquakes located deeper than about 5 km in the southern part of the array provide one possible explanation within the framework of low-angle normal faulting. We noted earlier that we cannot establish whether the steep, west-dipping nodal plane or the shallow, east-dipping nodal plane is the fault plane ruptured by these earthquakes. If, as we prefer, the east-dipping plane is correct, then we suggest that the

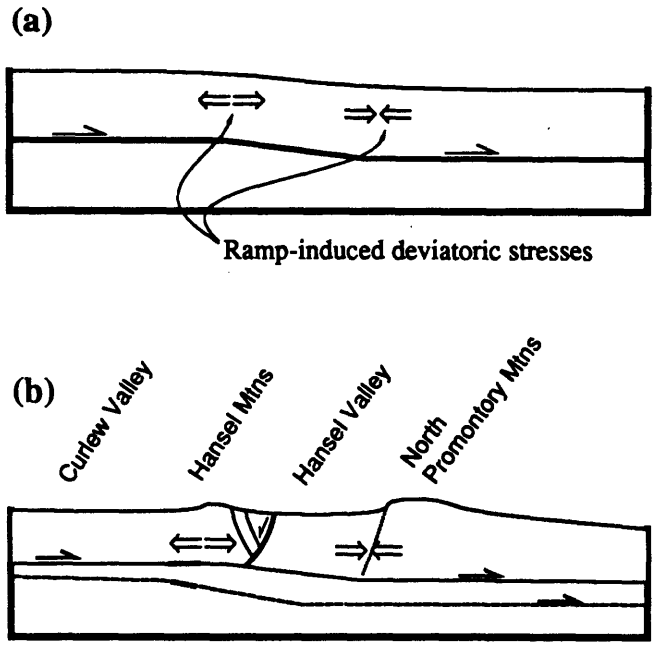

Fig. 3-26. (a) Cartoon illustrating the effect of a gentle ramp on a low-angle normal fault on the deviatoric stress within the upper plate. Because the upper plate has a horizontal least-principal stress, failure will occur within the region of deviatoric extension (left) and will be suppressed within the region of deviatoric compression (right). (b) Hypothetical relationship between a ramp either in the low-angle normal fault inferred to lie near 5 km depth (solid line) or in a deeper low-angle normal fault (dashed) and the structures in southern Hansel Valley. Heavy line segments are those portions of faults that might have produced earthquakes recorded in this experiment; dotted line marks the fault at the east side of Hansel Valley that might now be inactive because of stresses induced by the ramp.

east-dipping fault plane is somewhat steeper than the overall low-angle normal fault; in other words, this seismically active segment of the low-angle normal fault could be a gentle ramp of a branch of the low-angle normal fault system below that inferred to be near 5 km depth. The motion of the upper plate over a ramp in the low-angle normal fault will produce deviatoric extensional stresses above the upper inflection point and compressive deviatoric stresses above the lower inflection point of the ramp (Figure 3-26; e.g., McClay and Ellis, [1987]). In an overall extensional regime, we would expect seismicity where the additional deviatoric stress is extensional, above the upper inflection point of the ramp. The interaction of this deviatoric stress with the preexisting fractures could produce the linear pattern of the epicenters found in the Hansel Valley region.

The presence of a ramp, while speculative, also suggests solutions both for the presence of seismicity beneath the Hansel Mountains and for the contradiction between the

geomorphic asymmetry of Hansel Valley and the location of the most recently active faults (Figure 3-26b). In both cases, the motion of the upper plate over the ramp will eventually move any given fault within the upper plate from the favorable position for rupturing above the upper infection point on the ramp to the unfavorable position above the lower inflection point; at this position the earthquake activity on the fault should drop dramatically. This might explain the relatively small amount of evidence for seismic slip of the fault at the east side of Hansel Valley despite several favorable localities for the preservation of scarps [McCalpin et al., in press]; physiographically, this fault is far more impressive than that on the west side of the valley. Perhaps most of the relief across this fault was created when the fault was closer to the suspected ramp currently under the west side of the Hansel Mountains; when it moved away from the ramp, the fault on the east side of the valley became relatively quiescent as those on the west side of Hansel Valley became more active. This process may be recurring now. As the faults on the west side of Hansel Valley move farther from the ramp under the west side of the Hansel Mountains, faults within the Hansel Mountains start to become more active than in the past. The point of this highly speculative history is that virtually all of the well defined features observed in the seismicity and Quaternary geology in the Hansel Valley region are consistent with the presence of an active low-angle normal fault beneath the region, but they are not simply interpreted in terms of a horst and graben structure.

CONCLUSIONS

Using arrival times of 334 earthquakes gathered from 47 seismometers deployed in part of northern Utah and southeastern Idaho, we determined a three-dimensional velocity structure, 334 hypocenter locations, and 102 focal mechanisms. We inverted for the velocity structure in a manner designed to minimize the complexity of the structure, and thus minimize the number of poorly constrained velocities, without ignoring possible lateral variations. At least two low-velocity bodies must be present (Figure 3-4): one is a P-wave low-velocity zone throughout this region at depths between about 1.5 and 3.7 km (0.5 and 2.7 km below mean sea level), and the other is a lateral P- and S- wave low velocity region above about 3.7 km depth with velocities 10-15% lower those to the north or south. We suspect that the low-velocity zone represents a lithologic contrast perhaps caused by motion of a Mesozoic thrust fault; the low-velocity region appears to be related to volcanic rock and sediments near the surface and may be related to an inferred oblique normal-slip fault at depth.

Our examination of the microearthquakes that occurred in the Hansel Valley and Pocatello Valley regions has revealed several features of the microseismicity not easily reconciled with a simple horst-and-graben structure for the area. The epicenters of 334 earthquakes located within the array fall in a north-northeast trending band mostly within the Hansel Mountains in the south and mostly within Pocatello Valley to the north. The presence of seismicity within both ranges and basins implies a diversity of structures not generally implied by a simple horst-and-graben structure. Furthermore, the seismicity south of about 41.82°N occurs in two disjoint locations: an eastern group that includes events almost exclusively located at depths less than 5 km and a western group that includes events almost exclusively below 5 km depth. We also found that events with focal mechanisms representing certain classes of faulting were not evenly distributed; in particular, mechanisms consistent with low-angle normal faulting are common for events in the southern part of the array, but oblique normal-slip and thrust-slip solutions are prevalent among earthquakes located between about 41.82°N and 41.95°N.

Because of the unusually high accuracy of many of our earthquake locations, for which the uncertainties of epicenters and depths are less than 500m, individual faults can occasionally be defined from the earthquake locations and focal mechanisms. The best defined structure is a west-northwest trending right-lateral, oblique-normal-slip fault that dips north and strikes across the southern edge of the high part of the Hansel Mountains near 41.83°N. This fault has no known surface expression; those faults clearly active into Quaternary time, however, are relatively quiet: only two possible segments of the range-front fault at the west side of Hansel Valley appeared to be seismically active during the field experiment.

Although a search of the seismicity failed to clearly resolve any low-angle normal faults, we infer that one might be present at about 5 km depth in the southern part of the array. Three features support the presence of a low-angle normal fault in the southern part of the array: the different locations of the bands of epicenters of events located above and below this depth, several focal mechanisms of events near this depth that are consistent with slip on a gentle, east-dipping low-angle normal fault, and faulting indicating that this low-angle fault might dip north to parallel or merge with the west-northwest striking oblique-slip fault at the northern edge of this area. The numerous oblique-slip faults in the center portion of the array are consistent with a right-lateral shear on a west-northwest striking plane. Oblique-slip mechanisms of events deeper than about 5 km increase southward from just south of highway I-84 to the southern limit of these deeper events near 41.84°N. Hence we suspect that the volume of rock below 5 km depth and north of about 41.84°N is bounded on its south side by an oblique-slip fault or fault zone. Because this fault trends roughly west-northwest, has a

right-lateral component of strike-slip, drops the north side down, and apparently separates the lower plate of a low-angle normal fault to the south from the upper plate of one to the north, we suspect that this structure is the lateral extension of the fault zone that presumably bounds the south side of the Raft River Valley to the west-northwest. This interpretation implies that any low-angle normal fault north of about 41.84°N must lie deeper than about 7 or 8 km.

This interpretation permits explanations of several features in the area. The lateral differences of focal mechanisms mentioned previously could represent the presence of a shallow, east-dipping, low-angle normal fault in the south, a complex oblique-slip zone in the center, and a more poorly defined normal-faulting region to the north. The low-velocity region appears to represent a highly disrupted body of rock within the oblique-slip zone, invaded by igneous rocks that erupted within this zone, that probably has a greater thickness of low-velocity upper plate material than the area to the south.

The results of our investigation of the microearthquakes that occurred in the Hansel Valley region failed to produce a low-angle normal fault defined by both numerous earthquake locations and well-constrained focal mechanisms. The observations, nevertheless, are consistent with the existence of such a fault; the absence of a large number of earthquakes on this fault might indicate that the fault is locked or that it creeps aseismically. We infer the fault to be both active and within the seismically active portion of the crust; several events were located below the low-angle normal fault that we suggest is present in the area at a depth of about 4 to 5 km. The occurrence of some events that might be directly linked to a low-angle normal fault indicates that this fault is capable of generating small earthquakes. If our interpretations are correct, then low-angle normal faults might be present elsewhere within the seismogenic portion of the crust but be difficult to detect.

REFERENCES

Adams, O. C., Geology of the Summer Ranch and North Promontory Mountains, Utah, M.S. thesis, Utah State Univ., Logan, Utah, 57 pp., 1962.

Allmendinger, R. W., and T. E. Jordan, Mesozoic evolution, hinterland of the Sevier orogenic belt, *Geology, 9*, 308-313, 1981.

Allmendinger, R. W., and L. B. Platt, Stratigraphic variation and low-angle faulting in the North Hansel Mountains and Samaria Mountain, southern Idaho, *Geol. Soc. Am. Mem., 157*, 149-163, 1983.

Allmendinger, R. W., J. W. Sharp, D. Von Tish, L. Serpa, L. Brown, S. Kaufman, J. Oliver, and R. B. Smith, Cenozoic and Mesozoic structure of the eastern Basin and Range province, Utah, from COCORP seismic-reflection data, *Geology, 11*, 532-536, 1983.

Allmendinger, R. W., D. M. Miller, and T. E. Jordan, Known and inferred Mesozoic deformation in the hinterland of the Sevier belt, northwestern Utah, in *Geology of northwest Utah, southern Idaho, and northeast Nevada*, edited by G. J. Kerns and R. L. Kerns, Jr., *Utah Geol. Assoc. Publ., 13*, 21-34, 1984.

Anderson, R. E., Thin skin distension in Tertiary rocks of southeastern Nevada, *Geol. Soc. Am. Bull., 82*, 43-58, 1971.

Arabasz, W. J., and D. R. Julander, Geometry of seismically active faults and crustal deformation within the Basin and Range-Colorado Plateau transition in Utah, *Spec. Pap. Geol Soc. Am., 208*, 43-74, 1986.

Arabasz, W. J., W. D. Richins, and C. J. Langer, The Idaho-Utah (Pocatello Valley) earthquake sequence of March-April 1975, in W. J. Arabasz et al. (eds.), *Earthquake Studies in Utah 1850 to 1978*, University of Utah Seismograph Stations Special Publication, Salt Lake City, 339-373, 1979.

Armstrong, R. L., Low-angle (denudation) faults, hinterland of the Sevier orogenic belt, eastern Nevada and western Utah, *Geol. Soc. Am. Bull., 83*, 1729-1754, 1972.

Bond, J. G., Geologic map of Idaho, Idaho Bur. Mines Geol., Moscow, Idaho, 1:500000, 1978.

Burchfiel, B. C., K. V. Hodges, and L. H. Royden, Geology of Panamint Valley--Saline Valley pull-apart system, California: Palinspastic evidence for low-angle geometry of a Neogene range-bounding fault, *J. Geophys. Res., 92*, 10422-10426, 1987.

Compton, R. R., V. R. Todd, R. E. Zartman, and C. W. Naeser, Oligocene and Miocene metamorphism, folding, and low-angle faulting in northwestern Utah, *Geol. Soc. Am. Bull., 88*, 1237-1250, 1977.

Cook, K. L., and Nye, R. K., Effects of the Pocatello Valley (Idaho-Utah border) earthquake of March 28,1975 (UTC), in W. J. Arabasz et al. (eds.), *Earthquake Studies in Utah 1850 to 1978*, University of Utah Seismograph Stations Special Publication, Salt Lake City, 445-457, 1979.

Covington, H. R., Structural evolution of the Raft River Basin, Idaho, *Geol. Soc. Am. Memoir, 157*, 229-237, 1983.

Crone, A. J., and S. T. Harding, Relationship of late Quaternary fault scarps to subjacent faults, eastern Great Basin, Utah, *Geology, 12*, 292-295, 1984.

Davis, G. A., J. L. Anderson, E. G. Frost, and T. J. Shackelford, Mylonitization and detachment faulting in the Whipple-Buckskin-Rawhide Mountains terrane, southeastern California and western Arizona, *Mem. Geol. Soc. Am. , 153*, 79-130, 1980.

Davis, G. H., Shear-zone model for the origin of metamorphic core complexes, *Geology, 11*, 342-347, 1983.

Doelling, H. H., Geology and mineral deposits of Box Elder County, Utah, *Utah Geol. and Mineralogical Surv. Bull., 115*, 251 pp., 1980.

Eaton, G. P., The Basin and Range Province: Origin and tectonic significance, *Annu. Rev. Earth Planet. Sci., 10*, 409-440, 1982.

Gans, P. B., E. L. Miller, J. McCarthy, and M. L. Ouldcott, Tertiary extensional faulting and evolving brittle-ductile transition zones in the northern Snake Range and vicinity: New insights from seismic data, *Geology, 13*, 189-193, 1985.

Harr, C. J., and D. R. Mabey, Gravity survey of Pocatello Valley, Idaho and Utah, *U. S. Geol. Surv. Open File Rept., 76-766*, 12 pp., 1976.

Hintze, L. F., compiler, Geologic map of Utah, Utah Geol. Minerol. Surv., 1:500000, Salt Lake City, 1980.

Jackson, J. A., Active normal faulting and continental extension, Continental Extensional Tectonics, edited by J. F. Dewey, M. P. Coward, and P. L. Hancock, *Spec. Publ. Geol. Soc. Lond., 28*, 3-17, 1987.

Jordan, T. E., Geologic map of the Bull's Pass quadrangle, Box Elder County, Utah, *U. S. Geol. Surv. Misc. Field Studies Map, MF-1491*, 1:24000, 1985.

Le Pichon, X., and F. Barbier, Passive margin formation by low-angle faulting within the upper crust: The northern Bay of Biscay margin, *Tectonics, 6*, 133-150, 1987.

Malavieille, J., Extensional shearing deformation and kilometer-scale "a"-type folds in a cordilleran metamorphic core complex (Raft River Mountains, northwestern Utah), *Tectonics, 6*, 423-448, 1987.

McCalpin, J., R. M. Robinson, and J. D. Garr, Neotectonics of the Hansel Valley-Pocatello Valley Corridor, Northern Utah and Southern Idaho, *U. S. Geol. Surv. Prof. Paper*, in press.

McClay, K. R., and P. G. Ellis, Geometries of extensional fault systems developed in model experiments, *Geology, 15*, 341-344, 1987.

McDonald, R. E., Tertiary tectonics and sedimentary rocks along the transition, Basin and Range province to Plateau and thrust belt province, Utah, in Symposium on Geology of the Cordilleran hingeline, edited by J. G. Hill, Denver, Rocky Mountain Assn. of Geologists, 281-317, 1976.

Miller, D. M., Structural geology of the northern Albion Mountains, south-central Idaho, *Geol. Soc. Am. Mem., 153*, 399-423, 1983.

MIT 1985 Field Geophysics Course, and S. Biehler, A geophysical investigation of the northern Panamint Valley, Inyo County, California: Evidence for possible low-angle normal faulting at shallow depth in the crust, *J. Geophys. Res., 92*, 10427-10441, 1987.

Peterson, D. L., Bouguer gravity map of part of the northern Lake Bonneville Basin Utah and Idaho, *U. S. Geol. Surv. Misc. Field Studies Map, MF-627*, 1:250000, 1974.

Proffett, John M., Jr., Cenozoic geology of the Yerington district, Nevada, and implications for the nature and origin of Basin and Range faulting, *Geol. Soc. Am. Bull., 88*, 247-266, 1977.

Reynolds, S. J., and J. E. Spencer, Evidence for large-scale transport on the Bullard detachment fault, west-central Arizona, *Geology, 13*, 353-356, 1985.

Richens, W. D. (compiler), Earthquake data for the Utah Region, 1850 to 1978 in W. J. Arabasz et al. (eds.), *Earthquake Studies in Utah 1850 to 1978*, University of Utah Seismograph Stations Special Publication, Salt Lake City, 57-251, 1979a.

Richens, W. D., The Hansel Valley, Utah, Earthquake sequence of November 1976, in W. J. Arabasz et al. (eds.), *Earthquake Studies in Utah 1850 to 1978*, University of Utah Seismograph Stations Special Publication, Salt Lake City, 409-421, 1979b.

Richens, W. D., W. J. Arabasz, G. M. Hathaway, E. McPherson, P. J. Oehmich, and L. L. Sells, *Earthquake data for the Utah region, January 1, 1981 to December 31, 1983*, University of Utah Seismograph Stations Special Publication, Salt Lake City, 111 pp., 1984.

Roecker, S. W., Seismicity and tectonics of the Pamir-Hindu Kush region of central Asia, Ph. D. thesis, 298 pp., Mass. Inst. Technol., Cambridge, 1981.

Roecker, S. W., Velocity structure of the Pamir-Hindu Kush region: Possible evidence of subducted crust, *J. Geophys. Res., 87*, 945-959, 1982.

Schneider, J. F., R. P. Meyer, and L. A. Powell, Timing and positioning of seismographs from Omega navigation signals, Proc. 16th Ann. Mtg. Intl. Omega Assn., Montreal, Canada, August, 1981, 11-1--11-8, 1981.

Shenon, P. J., The Utah earthquake of March 12, 1934, in F. Neumann, *United States Earthquakes, 1934*, U. S. Coast and Geodetic Survey serial 593, 43-48, 1936.

Smith, R. B., and M. L. Sbar, Contemporary tectonics and seismicity of the western United States with emphasis on the Intermountain seismic belt, *Bull. Geol. Soc. Am., 85*, 1205-1218, 1974.

Smith, R. B., and R. L. Bruhn, Intraplate extensional tectonics of the eastern Basin-Range: Inferences on structural style from seismic reflection data, regional tectonics, and thermal-mechanical models of brittle-ductile deformation, *J. Geophys. Res., 89*, 5733-5762, 1984.

Todd, V. R., Structure and petrology of a Tertiary gneiss complex in northwestern Utah, *Geol. Soc. Am. Mem., 153*, 349-383, 1980.

Todd, V. R., Late Miocene displacement of pre-Tertiary and Tertiary rocks in the Matlin Mountains, northwestern Utah, *Geol. Soc. Am. Mem.*, *157*, 239-270, 1983.

Wernicke, B., J. D. Walker, and M. S. Beaufait, Structural discordance between Neogene detachments and frontal Sevier thrusts, central Mormon Mountains, southern Nevada, *Tectonics*, *4*, 213-246, 1985.

Zoback, M. L., R. E. Anderson, and G. A. Thompson, Cainozoic evolution of the state of stress and style of tectonism of the Basin and Range province of the western United States, *Phil. Trans. R. Soc. Lond.*, *A300*, 407-434, 1981.

Zoback, M. L., Structure and Cenozoic tectonism along the Wasatch fault zone, Utah, *Geol. Soc. Am. Mem.*, *157*, 3-27, 1983.

Appendix 3-A

Fig. 3-A1 (next 5 pages). Focal mechanisms determined using structure M3D, ordered by grade (A-C, then D-F, then G-I, finally J-L) and time. All plots are lower hemisphere, equal area projections. Filled circles are compressional first arrivals, open symbols are dilatational. Symbol sizes are in proportion to the quality of the first arrival and inversely proportional to the travel time residual of that arrival. Small crosses are positioned at inclinations of 0°, 30°, 60°, and 90° at azimuths of 0°, 90°, 180°, and 270° clockwise from north . Captions include event origin date and time (UTC), latitude and longitude (degrees and decimal minutes north and west), depth in kilometers from a datum plane 1 km above mean sea level ("Z"), the grade assigned the focal mechanism, the strike (clockwise from north with the nodal plane dipping to a direction 90° clockwise from the strike; i.e. dipping to the right) and dip of each nodal plane, and the rake of the slip vector within the plane (positive up from the strike of the plane; the vector points in the direction of motion of the hanging wall of the fault).

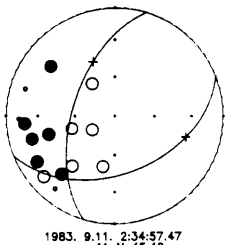

1983. 9.11. 2:34:57.47
41 N 45.42
112 W 49.08
Z = 7.07 km Qual C
Planes: (Str, Dip, Rake)
198.8 57.9 236.4
88.1 45.2 311.4

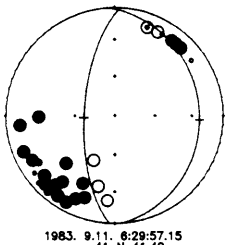

1983. 9.11. 6:29:57.15
41 N 41.40
112 W 48.96
Z = 6.82 km Qual C
Planes: (Str, Dip, Rake)
183.1 67.0 272.8
-4.0 23.2 263.5

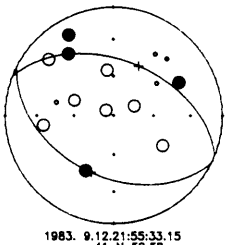

1983. 9.12.21:55:33.15
41 N 50.58
112 W 42.06
Z = 7.18 km Qual C
Planes: (Str, Dip, Rake)
-68.4 47.8 266.5
116.7 42.5 273.8

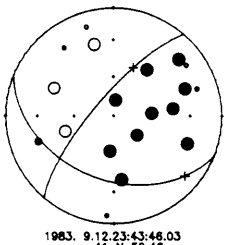

1983. 9.12.23:43:46.03
41 N 50.48
112 W 39.24
Z = 6.47 km Qual B
Planes: (Str, Dip, Rake)
220.4 75.3 52.2
112.3 40.2 156.8

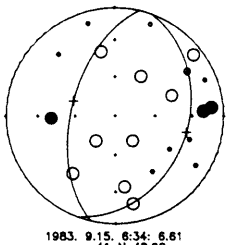

1983. 9.15. 6:34: 6.61
41 N 48.80
112 W 38.52
Z = 5.24 km Qual C
Planes: (Str, Dip, Rake)
193.4 56.9 266.3
20.1 33.3 275.6

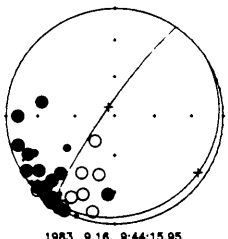

1983. 9.16. 9:44:15.95
41 N 42.42
112 W 48.84
Z = 7.51 km Qual C
Planes: (Str, Dip, Rake)
214.4 82.5 267.0
56.1 8.1 291.5

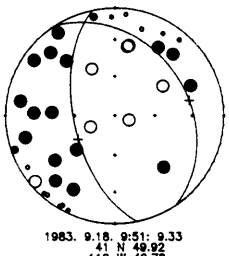

1983. 9.18. 9:51: 9.33
41 N 49.92
112 W 42.78
Z = 5.20 km Qual B
Planes: (Str, Dip, Rake)
168.3 59.7 281.5
-33.4 32.8 251.6

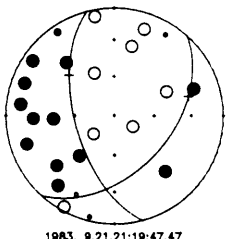

1983. 9.21.21:19:47.47
41 N 49.68
112 W 42.80
Z = 5.08 km Qual A
Planes: (Str, Dip, Rake)
165.3 59.7 232.2
42.2 48.9 316.4

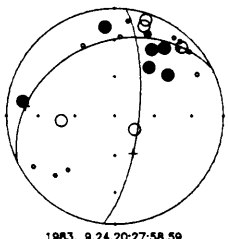

1983. 9.24.20:27:58.59
41 N 56.22
112 W 35.88
Z = 6.89 km Qual C
Planes: (Str, Dip, Rake)
6.2 71.8 243.4
244.2 31.8 323.7

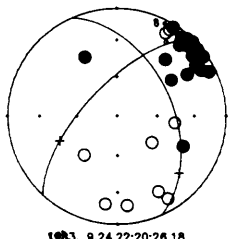

1983. 9.24.22:20:26.18
41 N 59.04
112 W 27.24
Z = 8.48 km Qual C
Planes: (Str, Dip, Rake)
223.2 66.6 312.9
-23.7 47.7 212.4

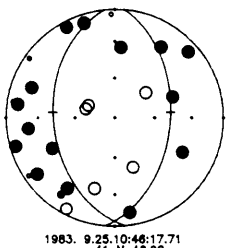

1983. 9.25.10:46:17.71
41 N 46.92
112 W 44.70
Z = 4.48 km Qual B
Planes: (Str, Dip, Rake)
5.1 47.6 277.2
174.4 42.9 262.1

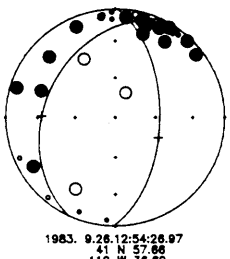

1983. 9.26.12:54:26.97
41 N 57.66
112 W 36.80
Z = 5.06 km Qual C
Planes: (Str, Dip, Rake)
1.2 56.5 256.2
205.2 35.9 289.8

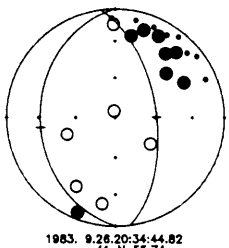

1983. 9.26.20:34:44.82
41 N 55.74
112 W 35.10
Z = 5.96 km Qual C
Planes: (Str, Dip, Rake)
-7.5 58.9 266.5
179.3 31.3 275.8

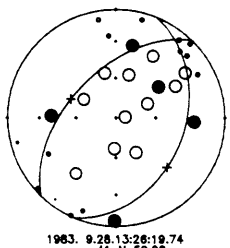

1983. 9.28.13:26:19.74
41 N 52.08
112 W 38.40
Z = 7.52 km Qual C
Planes: (Str, Dip, Rake)
224.0 55.0 282.7
22.8 37.0 252.6

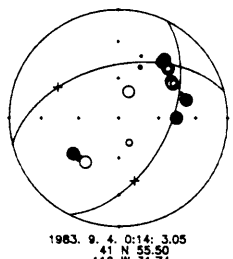

1983. 9. 4. 0:14: 3.05
41 N 55.50
112 W 31.74
Z = 2.72 km Qual F
Planes: (Str, Dip, Rake)
27.1 52.0 234.9
255.9 49.8 308.4

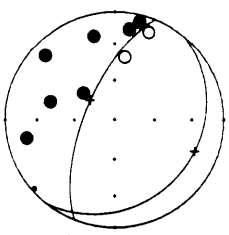

1983. 9. 6. 9:39:36.19
41 N 51.06
112 W 45.00
Z = 4.56 km Qual E
Planes: (Str, Dip, Rake)
201.8 87.8 263.2
38.5 23.2 286.3

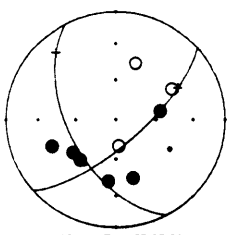

1983. 9. 7.19:53:23.29
41 N 59.82
112 W 29.82
Z = 2.85 km Qual F
Planes: (Str, Dip, Rake)
48.5 71.3 321.1
152.7 54.0 203.3

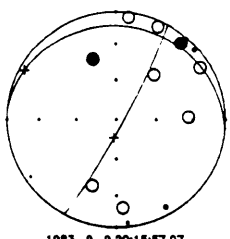

1983. 9. 9.20:15:57.07
41 N 56.94
112 W 33.42
Z = 4.71 km Qual E
Planes: (Str, Dip, Rake)
168.5 64.8 77.1
-82.7 13.9 158.2

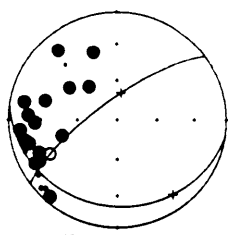

1983. 9.10. 3: 1:58.19
41 N 47.82
112 W 49.36
Z = 8.43 km Qual F
Planes: (Str, Dip, Rake)
233.8 75.0 248.8
98.5 20.7 313.0

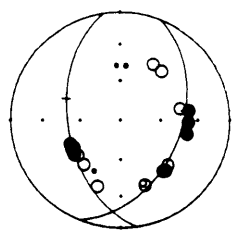

1983. 9.10.18:59:45.85
41 N 55.12
112 W 27.30
Z = 2.58 km Qual E
Planes: (Str, Dip, Rake)
171.8 50.3 249.8
22.0 43.9 292.8

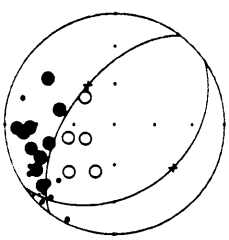

1983. 9.11. 2:23:13.68
41 N 45.30
112 W 49.80
Z = 8.34 km Qual D
Planes: (Str, Dip, Rake)
218.3 55.9 259.1
55.2 35.8 285.6

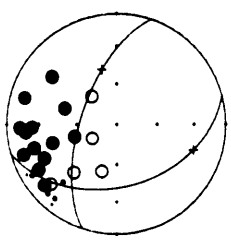

1983. 9.11. 2:23:57.78
41 N 45.36
112 W 49.44
Z = 8.25 km Qual D
Planes: (Str, Dip, Rake)
198.3 63.7 235.7
74.8 42.8 318.0

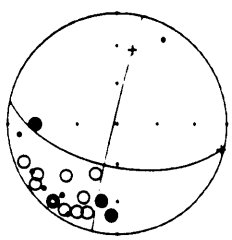

1983. 9.11. 6: 8:10.55
41 N 41.48
112 W 48.84
Z = 6.05 km Qual E
Planes: (Str, Dip, Rake)
193.7 87.4 212.2
102.0 57.9 356.9

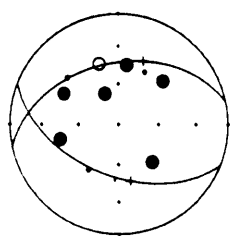

1983. 9.12. 1: 6:59.14
42 N 7.08
112 W 32.78
Z = 2.64 km Qual F
Planes: (Str, Dip, Rake)
111.8 51.5 112.8
258.0 43.7 64.2

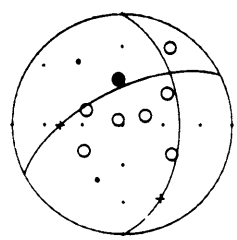

1983. 9.12.21:18: 0.57
41 N 50.58
112 W 41.88
Z = 7.79 km Qual F
Planes: (Str, Dip, Rake)
243.1 84.7 311.0
-0.3 47.2 216.3

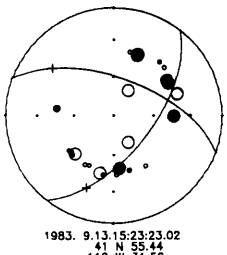

1983. 9.13.15:23:23.02
41 N 55.44
112 W 31.56
Z = 2.45 km Qual F
Planes: (Str, Dip, Rake)
37.8 61.2 213.4
-69.8 61.2 326.6

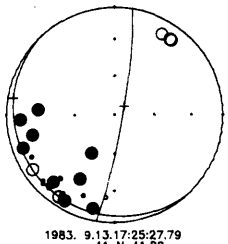

1983. 9.13.17:25:27.79
41 N 41.82
112 W 49.02
Z = 6.78 km Qual F
Planes: (Str, Dip, Rake)
369.7 83.9 97.6
138.1 9.7 38.8

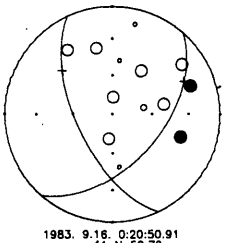

1983. 9.16. 0:20:50.91
41 N 50.70
112 W 39.30
Z = 8.04 km Qual E
Planes: (Str, Dip, Rake)
155.3 82.1 224.1
40.9 52.1 323.6

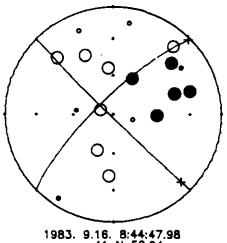

1983. 9.16. 8:44:47.98
41 N 50.04
112 W 40.20
Z = 7.74 km Qual E
Planes: (Str, Dip, Rake)
134.8 87.9 167.9
225.2 77.9 2.1

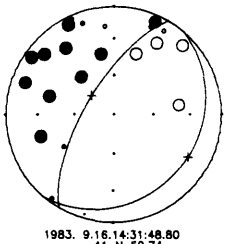

1983. 9.16.14:31:48.80
41 N 52.74
112 W 42.24
Z = 4.73 km Qual D
Planes: (Str, Dip, Rake)
210.2 88.4 286.4
40.0 21.8 279.1

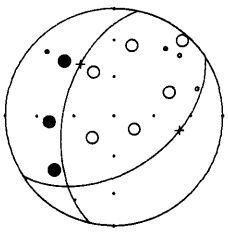

1983. 9.18. 9:53:43.27
41 N 49.62
112 W 42.54
Z = 4.76 km Qual F
Planes: (Str, Dip, Rake)
192.8 51.8 239.1
56.9 47.6 303.2

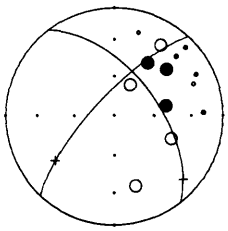

1983. 9.18.12: 5: 1.74
41 N 52.56
112 W 35.34
Z = 6.93 km Qual F
Planes: (Str, Dip, Rake)
222.8 75.0 326.6
-37.5 57.9 197.9

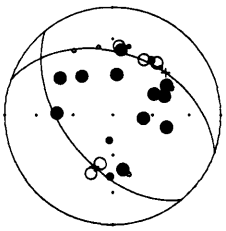

1983. 9.21.23:11:13.35
41 N 51.24
112 W 39.18
Z = 2.98 km Qual D
Planes: (Str, Dip, Rake)
141.2 52.3 110.4
-70.1 42.1 65.7

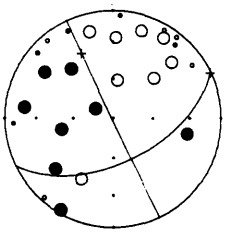

1983. 9.22. 9: 0:46.48
41 N 51.66
112 W 41.40
Z = 4.74 km Qual E
Planes: (Str, Dip, Rake)
154.8 88.7 213.7
64.0 56.3 358.4

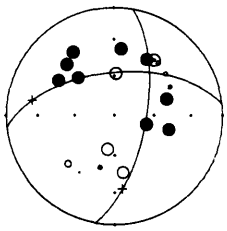

1983. 9.23.12:34: 5.92
41 N 51.08
112 W 39.30
Z = 2.37 km Qual D
Planes: (Str, Dip, Rake)
10.5 65.9 216.2
263.8 57.3 331.0

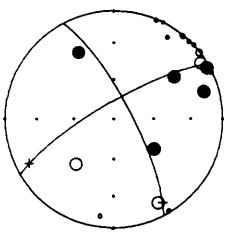

1983. 9.25. 0:40:35.68
41 N 59.10
112 W 27.24
Z = 7.28 km Qual F
Planes: (Str, Dip, Rake)
239.6 78.1 346.4
-27.6 76.7 192.3

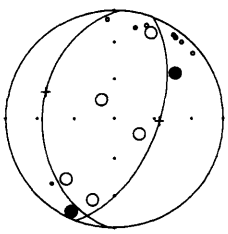

1983. 9.26.20:32:38.34
41 N 56.22
112 W 35.70
Z = 5.95 km Qual F
Planes: (Str, Dip, Rake)
21.1 57.2 280.0
183.1 34.1 254.9

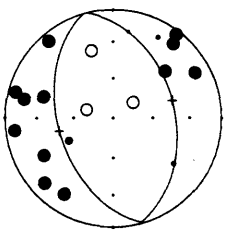

1983. 9.27. 4:34:56.21
41 N 50.58
112 W 42.66
Z = 4.39 km Qual F
Planes: (Str, Dip, Rake)
163.8 47.4 268.3
-13.7 42.6 271.8

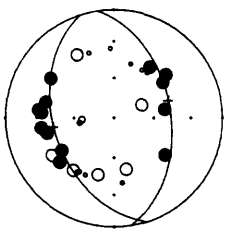

1983. 9.28. 9: 6:20.95
41 N 46.50
112 W 44.88
Z = 3.00 km Qual F
Planes: (Str, Dip, Rake)
-8.6 46.7 276.3
162.3 43.7 263.4

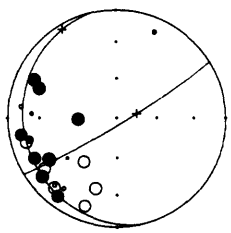

1983. 9.29. 8:58:39.64
41 N 43.68
112 W 49.98
Z = 6.85 km Qual F
Planes: (Str, Dip, Rake)
418.8 84.6 104.4
168.1 15.3 19.9

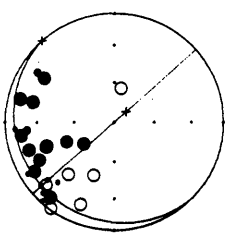

1983. 9.29. 8:59: 6.15
41 N 44.84
112 W 49.86
Z = 7.87 km Qual E
Planes: (Str, Dip, Rake)
228.5 90.0 257.9
138.5 12.1 180.0

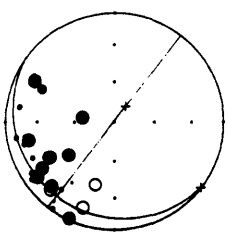

1983. 9.29. 9: 4:51.06
41 N 43.98
112 W 49.88
Z = 8.00 km Qual E
Planes: (Str, Dip, Rake)
217.8 89.3 255.7
125.8 14.3 357.9

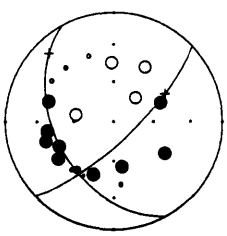

1983. 9.30. 6:46: 2.60
41 N 46.86
112 W 45.12
Z = 3.12 km Qual E
Planes: (Str, Dip, Rake)
46.3 75.4 312.5
151.7 44.5 201.1

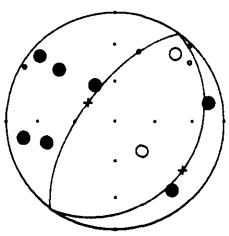

1983.10. 2. 0:14:33.10
41 N 49.14
112 W 42.36
Z = 4.19 km Qual F
Planes: (Str, Dip, Rake)
216.8 65.5 270.7
34.8 24.5 268.4

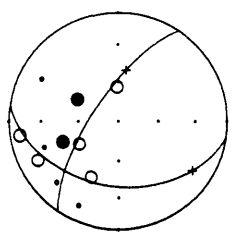

1983.10. 2.11:32:52.32
41 N 44.88
112 W 50.40
Z = 7.41 km Qual F
Planes: (Str, Dip, Rake)
213.9 70.5 234.9
98.8 39.4 328.8

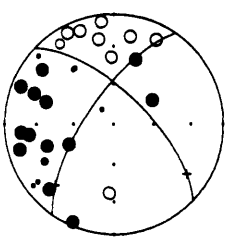

1983.10. 3. 2:19:28.55
41 N 49.20
112 W 48.14
Z = 5.50 km Qual E
Planes: (Str, Dip, Rake)
214.3 69.6 334.8
-46.2 66.3 202.3

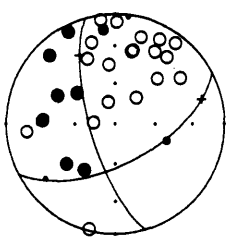

1983.10. 3. 7:54:11.07
41 N 51.42
112 W 42.06
Z = 7.34 km Qual E
Planes: (Str, Dip, Rake)
164.2 70.8 212.3
62.5 59.7 337.7

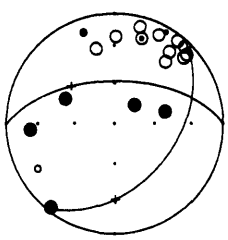

1983. 9. 3.20:21:28.92
41 N 54.30
112 W 37.38
Z = 5.13 km Qual G
Planes: (Str, Dip, Rake)
269.7 58.5 121.4
40.2 43.3 49.6

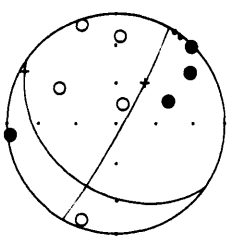

1983. 9. 4. 2: 5:28.54
41 N 50.76
112 W 41.40
Z = 3.82 km Qual I
Planes: (Str, Dip, Rake)
29.4 85.3 307.2
125.5 37.4 187.7

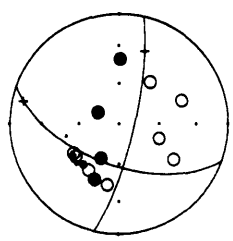

1983. 9. 4.21:58:15.38
41 N 55.02
112 W 33.30
Z = 3.41 km Qual I
Planes: (Str, Dip, Rake)
373.1 76.8 148.4
109.9 59.1 13.1

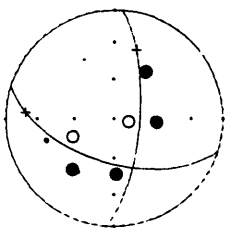

1983. 9. 7. 8:15:14.48
41 N 48.02
112 W 45.42
Z = 3.43 km Qual H
Planes: (Str, Dip, Rake)
4.1 70.5 323.7
107.8 56.1 203.7

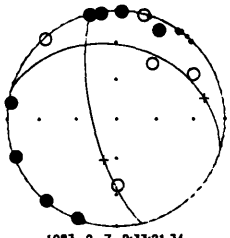

1983. 9. 7. 9:33:21.34
41 N 55.14
112 W 57.02
Z = 3.81 km Qual H
Planes: (Str, Dip, Rake)
166.8 72.2 298.0
−73.2 32.8 214.4

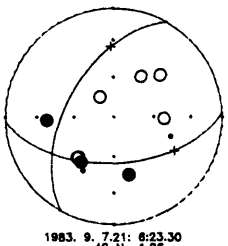

1983. 9. 7. 21: 6:23.30
42 N 1.26
112 W 30.54
Z = 3.09 km Qual H
Planes: (Str, Dip, Rake)
87.7 54.5 313.4
209.3 53.7 226.1

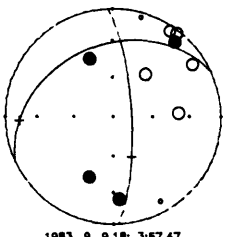

1983. 9. 9.18: 3:57.47
41 N 57.00
112 W 33.48
Z = 5.13 km Qual G
Planes: (Str, Dip, Rake)
357.8 75.9 58.8
245.7 34.0 154.1

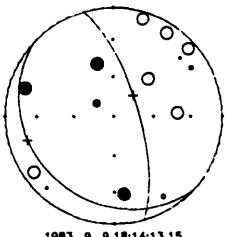

1983. 9. 9.18:14:13.15
41 N 57.00
112 W 33.18
Z = 5.70 km Qual H
Planes: (Str, Dip, Rake)
344.5 71.1 101.0
133.6 21.7 80.9

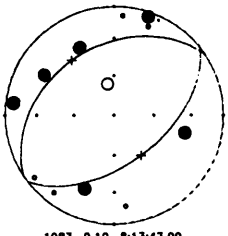

1983. 9.10. 8:13:43.99
42 N 2.48
112 W 34.20
Z = 4.92 km Qual G
Planes: (Str, Dip, Rake)
52.4 53.4 267.7
236.2 36.6 273.1

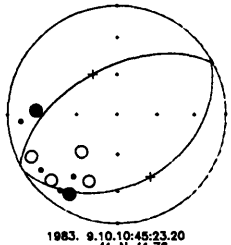

1983. 9.10.10:45:23.20
41 N 41.76
112 W 50.04
Z = 6.90 km Qual G
Planes: (Str, Dip, Rake)
242.2 54.5 271.7
59.3 35.6 267.6

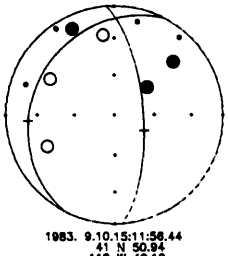

1983. 9.10.15:11:56.44
41 N 50.94
112 W 42.12
Z = 4.13 km Qual G
Planes: (Str, Dip, Rake)
−3.8 88.4 257.0
208.3 25.1 299.6

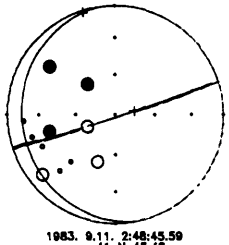

1983. 9.11. 2:48:45.59
41 N 45.48
112 W 49.62
Z = 8.00 km Qual G
Planes: (Str, Dip, Rake)
72.5 87.9 284.5
170.4 14.7 188.2

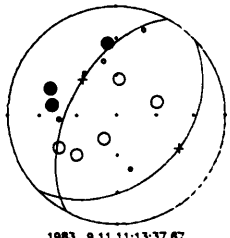

1983. 9.11.11:13:37.67
42 N 4.26
112 W 33.60
Z = 11.17 km Qual H
Planes: (Str, Dip, Rake)
208.3 54.3 259.0
48.7 37.1 284.9

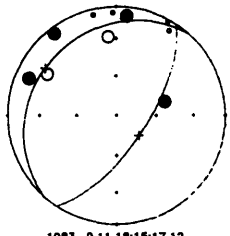

1983. 9.11.18:15:17.12
42 N 9.72
112 W 32.70
Z = 5.02 km Qual H
Planes: (Str, Dip, Rake)
33.8 87.5 268.9
221.7 22.7 277.5

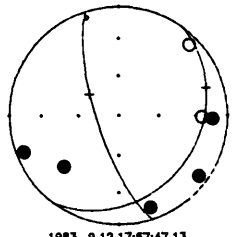

1983. 9.12.17:57:47.13
41 N 46.08
112 W 44.34
Z = 0.59 km Qual G
Planes: (Str, Dip, Rake)
182.5 73.4 248.4
36.8 26.9 321.0

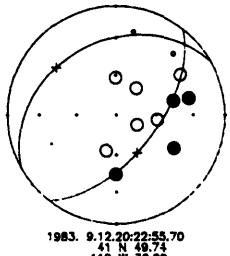

1983. 9.12.20:22:55.70
41 N 49.74
112 W 39.90
Z = 9.07 km Qual G
Planes: (Str, Dip, Rake)
38.3 59.8 257.9
241.3 32.6 289.7

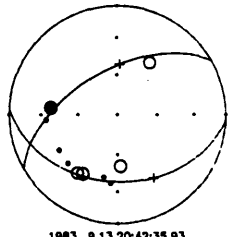

1983. 9.13.20:42:35.93
41 N 41.88
112 W 47.34
Z = 3.07 km Qual H
Planes: (Str, Dip, Rake)
240.2 56.3 250.4
92.9 38.3 296.7

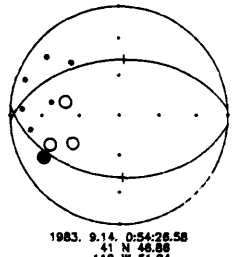

1983. 9.14. 0:54:26.58
41 N 46.88
112 W 51.24
Z = 8.39 km Qual I
Planes: (Str, Dip, Rake)
267.3 47.7 284.7
95.2 42.6 275.8

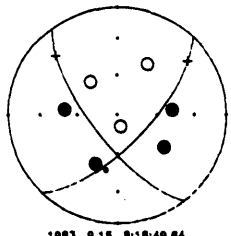

1983. 9.15. 8:18:49.84
42 N 0.90
112 W 33.72
Z = 3.51 km Qual I
Planes: (Str, Dip, Rake)
142.8 70.7 264.4
44.0 67.2 338.3

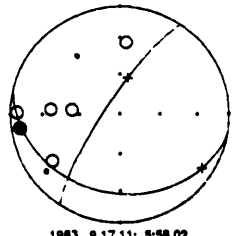

1983. 9.17.11: 5:58.02
41 N 48.32
112 W 48.98
Z = 5.03 km Qual H
Planes: (Str, Dip, Rake)
213.8 79.1 84.3
102.2 27.8 154.1

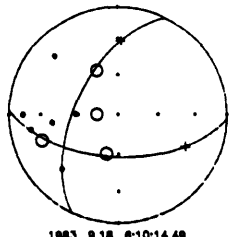

1983. 9.18. 6:10:14.49
41 N 48.14
112 W 49.02
Z = 7.44 km Qual I
Planes: (Str, Dip, Rake)
92.1 57.7 320.9
209.7 57.7 219.1

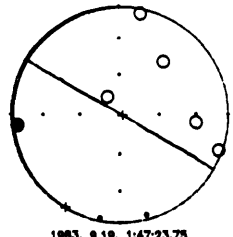

1983. 9.19. 1:47:23.75
42 N 1.08
112 W 30.36
Z = 4.03 km Qual H
Planes: (Str, Dip, Rake)
300.4 84.6 87.5
198.4 2.8 168.8

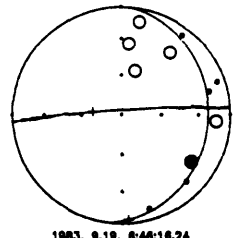

1983. 9.19. 8:48:16.24
41 N 49.56
112 W 34.20
Z = 5.88 km Qual H
Planes: (Str, Dip, Rake)
264.5 64.3 111.5
5.9 21.8 10.1

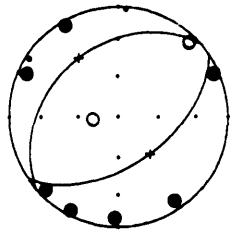

1983. 9.20.19:37:21.67
41 N 48.06
112 W 41.70
Z = 0.10 km Qual G
Planes: (Str, Dip, Rake)
55.8 53.8 274.2
228.9 36.4 284.3

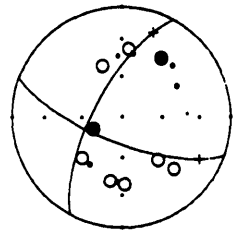

1983. 9.21. 4: 8:40.01
41 N 54.18
112 W 33.54
Z = 2.83 km Qual I
Planes: (Str, Dip, Rake)
110.7 70.8 157.8
208.4 68.1 20.8

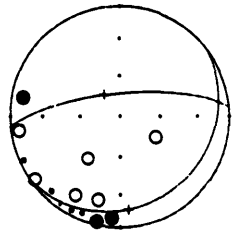

1983. 9.23.21:13:29.71
41 N 42.42
112 W 48.84
Z = 4.39 km Qual I
Planes: (Str, Dip, Rake)
264.8 73.2 260.0
53.3 18.5 238.9

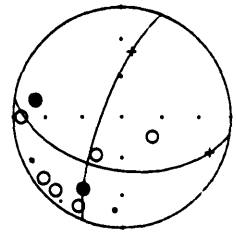

1983. 9.23.21:33:35.66
41 N 42.34
112 W 48.78
Z = 5.29 km Qual I
Planes: (Str, Dip, Rake)
201.7 75.6 221.5
98.3 50.0 341.0

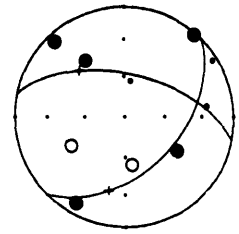

1983. 9.25. 8:39: 2.91
41 N 49.02
112 W 41.34
Z = 3.91 km Qual I
Planes: (Str, Dip, Rake)
−77.6 58.1 308.1
45.4 46.8 224.8

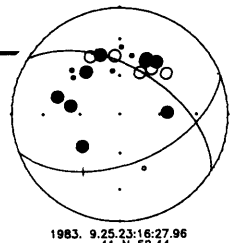

1983. 9.25.23:16:27.96
41 N 52.44
112 W 42.06
Z = 2.65 km Qual H
Planes: (Str, Dip, Rake)
302.0 53.4 128.5
68.9 51.1 50.1

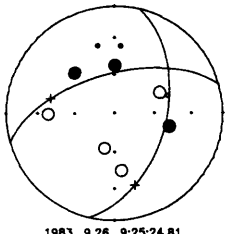

1983. 9.26. 9:25:24.81
41 N 51.12
112 W 39.36
Z = 1.59 km Qual I
Planes: (Str, Dip, Rake)
254.4 59.5 312.3
13.5 50.4 221.2

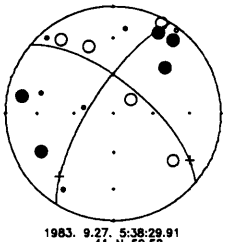

1983. 9.27. 5:38:29.91
41 N 50.52
112 W 42.78
Z = 4.26 km Qual G
Planes: (Str, Dip, Rake)
212.1 72.2 335.0
-49.8 66.3 199.5

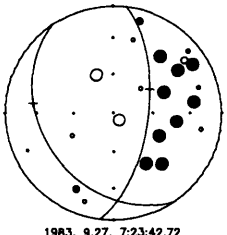

1983. 9.27. 7:23:42.72
41 N 50.88
112 W 36.00
Z = 6.86 km Qual G
Planes: (Str, Dip, Rake)
7.3 63.5 291.0
146.6 33.3 234.3

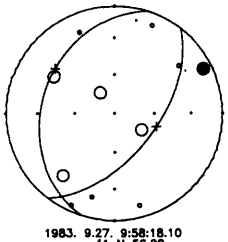

1983. 9.27. 9:58:18.10
41 N 56.22
112 W 35.70
Z = 5.44 km Qual I
Planes: (Str, Dip, Rake)
37.7 58.1 280.8
197.9 33.4 253.3

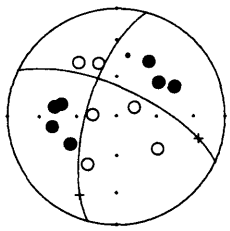

1983. 9.27.13:55:27.72
41 N 50.40
112 W 42.66
Z = 3.16 km Qual I
Planes: (Str, Dip, Rake)
-64.9 68.8 204.8
195.7 67.2 336.9

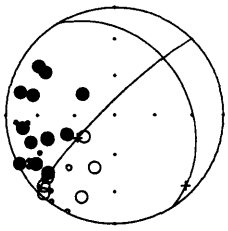

1983. 9.29. 8:59:36.34
41 N 44.94
112 W 49.86
Z = 7.95 km Qual I
Planes: (Str, Dip, Rake)
225.0 81.5 301.8
-31.6 32.8 195.8

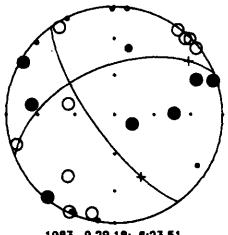

1983. 9.29.18: 8:23.51
41 N 50.10
112 W 40.98
Z = 3.83 km Qual G
Planes: (Str, Dip, Rake)
144.2 73.4 140.9
247.3 52.8 21.0

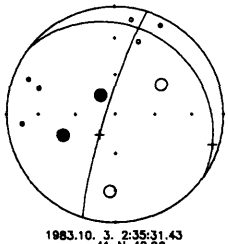

1983.10. 3. 2:35:31.43
41 N 49.26
112 W 46.14
Z = 4.57 km Qual I
Planes: (Str, Dip, Rake)
197.7 83.2 288.5
-52.8 19.8 200.7

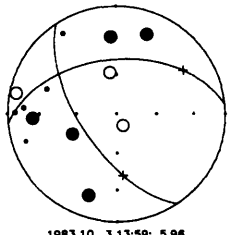

1983.10. 3.13:59: 5.96
41 N 47.82
112 W 47.88
Z = 5.32 km Qual G
Planes: (Str, Dip, Rake)
146.8 82.4 311.1
264.8 48.1 218.5

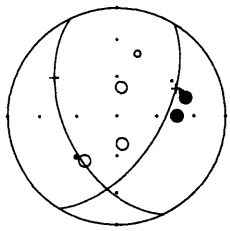

1983. 9. 4. 0:14:30.14
41 N 55.50
112 W 32.04
Z = 2.21 km Qual L
Planes: (Str, Dip, Rake)
31.9 57.2 309.9
154.9 49.8 225.1

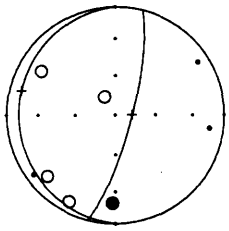

1983. 9. 7. 3:56:59.07
41 N 48.24
112 W 41.70
Z = 0.65 km Qual L
Planes: (Str, Dip, Rake)
14.8 78.0 273.4
178.9 12.5 254.5

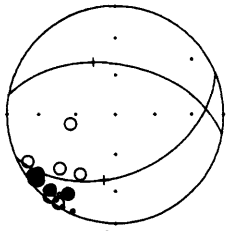

1983. 9. 8.11: 1:10.94
41 N 43.38
112 W 49.74
Z = 5.19 km Qual K
Planes: (Str, Dip, Rake)
-79.5 51.8 292.3
67.0 43.4 244.3

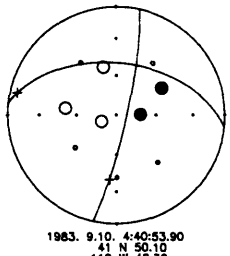

1983. 9.10. 4:40:53.90
41 N 50.10
112 W 42.30
Z = 3.68 km Qual L
Planes: (Str, Dip, Rake)
12.9 82.5 220.3
-83.5 50.1 350.2

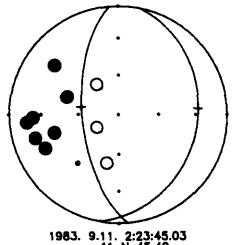

1983. 9.11. 2:23:45.03
41 N 45.42
112 W 49.14
Z = 7.66 km Qual K
Planes: (Str, Dip, Rake)
175.5 62.7 262.5
11.8 28.3 284.3

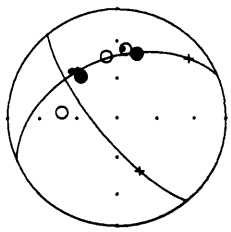

1983. 9.11. 5: 7:38.88
41 N 52.62
112 W 48.44
Z = 3.23 km Qual L
Planes: (Str, Dip, Rake)
140.5 74.3 131.8
247.2 44.2 22.8

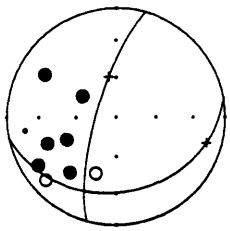

1983. 9.11.17:20:40.47
41 N 44.82
112 W 48.80
Z = 7.13 km Qual K
Planes: (Str, Dip, Rake)
193.8 75.0 242.4
79.5 31.0 329.9

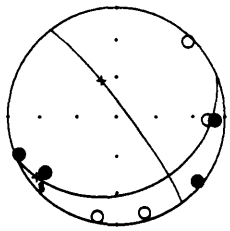

1983. 9.12.17:58:20.03
41 N 46.08
112 W 44.52
Z = 0.16 km Qual J
Planes: (Str, Dip, Rake)
322.8 82.3 118.4
66.8 29.3 16.0

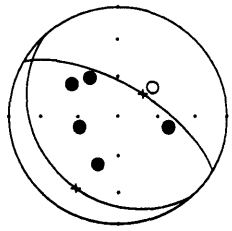

1983. 9.13. 1:27:12.29
41 N 51.80
112 W 41.10
Z = 3.52 km Qual L
Planes: (Str, Dip, Rake)
300.4 86.3 82.5
138.6 24.8 106.5

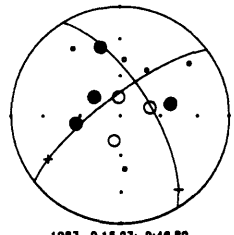

1983. 9.15.23: 9:46.82
41 N 50.78
112 W 38.48
Z = 7.87 km Qual J
Planes: (Str, Dip, Rake)
232.5 84.7 346.0
-31.2 66.8 195.6

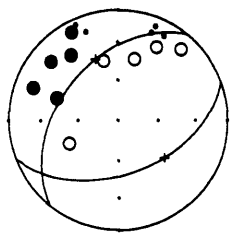

1983. 9.16.14:49:21.87
41 N 52.98
112 W 42.48
Z = 5.29 km Qual J
Planes: (Str, Dip, Rake)
68.8 49.3 291.0
219.1 44.9 247.3

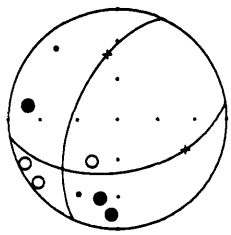

1983. 9.19.12: 5:43.53
41 N 42.24
112 W 48.72
Z = 4.97 km Qual L
Planes: (Str, Dip, Rake)
204.1 57.2 230.1
81.1 48.8 314.9

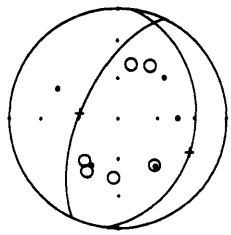

1983. 9.21. 0: 3:19.40
42 N 3.18
112 W 29.10
Z = 2.55 km Qual J
Planes: (Str, Dip, Rake)
205.3 82.7 278.8
7.3 29.1 254.2

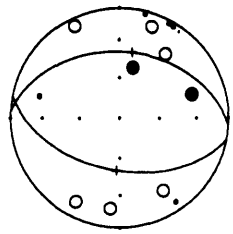

1983. 9.21.23:35:46.57
42 N 2.48
112 W 29.28
Z = 5.14 km Qual K
Planes: (Str, Dip, Rake)
101.3 50.6 84.9
-86.2 39.7 84.1

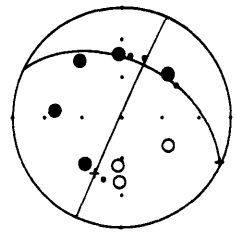

1983. 9.25.19: 0:28.14
41 N 41.88
112 W 47.70
Z = 3.80 km Qual L
Planes: (Str, Dip, Rake)
204.4 88.1 317.2
-63.9 47.3 182.5

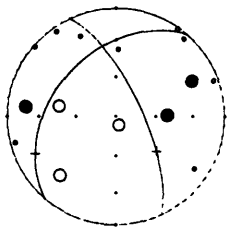

1983. 9.27.13: 4:57.03
41 N 50.10
112 W 41.46
Z = 3.95 km Qual L
Planes: (Str, Dip, Rake)
-25.1 70.8 233.1
221.0 41.0 329.6

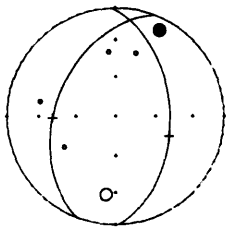

1983.10. 1.10: 2: 8.65
41 N 48.78
112 W 46.38
Z = 4.92 km Qual L
Planes: (Str, Dip, Rake)
-2.0 48.5 254.3
201.0 43.9 287.0

Table 3-A1. Earthquake Parameters Using Structure M3D

event	date	time(Z)	lat N	lon W	x	y	z	stns	rms	dz	dh	ql	pi	pd	ti	td
1	83.09.01.	04:50:34.16	41.797	112.781	-5.14	-15.50	5.80	4	.02	.09	.11					
2	83.09.01.	07:40:31.06	41.813	112.725	-1.22	-12.43	2.19	5	.01	.01	.04					
3	83.09.02.	07:14:14.19	41.835	112.685	1.23	-9.11	4.38	6	.04	.06	.08					
4	83.09.03.	02:01:49.45	41.776	112.701	1.90	-15.76	5.01	5	.08	.14	.26					
5	83.09.03.	02:33:13.79	41.772	112.708	1.47	-16.36	6.10	7	.05	.03	.06					
6	83.09.03.	20:21:28.92	41.905	112.623	3.84	-0.16	5.13	20	.05	.01	.01	G	8	338	62	231
7	83.09.04.	00:14:3.05	41.925	112.529	10.63	4.27	2.72	22	.10	.04	.01	F	63	234	1	141
8	83.09.04.	00:14:30.14	41.925	112.534	10.23	4.15	2.21	10	.04	.03	.01	L	57	358	4	95
9	83.09.04.	02:05:28.54	41.846	112.690	0.47	-8.07	3.82	11	.08	.02	.03	I	38	332	30	90
10	83.09.04.	02:12:43.20	41.784	112.727	-0.43	-15.55	3.51	11	.18	.05	.03					
11	83.09.04.	11:22:53.75	41.797	112.740	-1.89	-14.49	2.42	8	.14	.08	.32					
12	83.09.04.	11:59:38.95	41.785	112.734	-1.02	-15.62	4.48	7	.03	.02	.03					
13	83.09.04.	21:58:15.38	41.917	112.555	8.83	2.78	3.41	20	.09	.02	.01	I	13	65	30	327
14	83.09.05.	06:02:34.89	41.774	112.765	-3.12	-17.54	0.63	6	.02	.01	.01					
15	83.09.05.	06:03:2.15	41.780	112.774	-4.03	-17.13	0.35	6	.05	.04	.09					
16	83.09.05.	21:41:51.10	41.927	112.691	-2.27	.50	2.96	10	.22	.13	.15					
17	83.09.06.	05:27:21.21	41.874	112.731	-3.70	-6.10	2.05	6	.20	.27	.57					
18	83.09.06.	08:41:49.85	42.103	112.330	20.45	28.06	1.58	27	.18	.11	.02					
19	83.09.06.	09:33:6.12	42.006	112.595	2.73	11.23	5.74	9	.05	.03	.04					
20	83.09.06.	09:39:36.19	41.851	112.750	-4.45	-9.01	4.56	15	.09	.04	.04	E	66	100	22	297
21	83.09.06.	10:09:55.19	41.873	112.681	.30	-4.98	5.95	7	.08	.17	.17					
22	83.09.06.	13:36:13.82	41.842	112.698	-0.03	-8.69	1.76	7	.10	.08	.14					
23	83.09.06.	15:39:24.53	41.697	112.894	-10.86	-28.87	8.45	12	.05	.13	.10					
24	83.09.06.	22:23:45.33	41.836	112.708	-0.63	-9.57	3.38	5	.01	.01	.02					
25	83.09.06.	23:57:16.90	41.954	112.418	18.45	10.09	2.75	10	.10	.06	.02					
26	83.09.07.	00:51:28.17	41.782	112.743	-1.63	-16.16	7.53	5	.02	.03	.06					
27	83.09.07.	03:56:59.07	41.804	112.695	1.46	-12.64	0.85	9	.10	.03	.05	L	56	289	32	102
28	83.09.07.	04:12:7.42	42.051	112.498	8.91	18.39	3.68	35	.11	.02	.01					
29	83.09.07.	04:41:24.83	42.053	112.490	9.48	18.80	1.92	7	.04	.02	.10					
30	83.09.07.	06:15:14.48	41.767	112.757	-2.25	-18.09	3.43	11	.13	.06	.13	H	39	321	9	59
31	83.09.07.	06:15:27.97	41.748	112.729	.59	-19.42	3.64	7	.11	.13	.08					
32	83.09.07.	06:26:22.41	42.073	112.461	11.11	21.64	2.55	12	.06	.02	.04					
33	83.09.07.	07:51:56.77	42.034	112.505	8.92	16.42	1.45	6	.06	.03	.09					
34	83.09.07.	09:33:21.34	41.919	112.617	3.86	1.47	3.81	26	.07	.02	.03	H	54	111	22	236
35	83.09.07.	15:03:10.47	41.767	112.817	-7.02	-19.56	5.13	5	.01	.03	.03					
36	83.09.07.	19:53:23.29	41.997	112.497	10.78	12.69	2.85	18	.08	.02	.01	F	40	5	11	104
37	83.09.07.	21:06:23.30	42.021	112.509	9.03	14.94	3.09	16	.15	.03	.02	H	56	57	0	149
38	83.09.07.	21:45:26.02	41.638	112.653	10.25	-29.21	10.12	10	.07	.29	.45					
39	83.09.07.	22:17:30.80	41.733	112.799	-4.48	-22.73	5.59	4	.02	.08	.08					
40	83.09.08.	00:34:51.51	41.833	112.722	-1.64	-10.23	1.41	8	.04	.04	.04					
41	83.09.08.	02:09:17.63	42.057	112.545	5.00	17.87	5.45	9	.07	.02	.04					
42	83.09.08.	11:01:10.94	41.723	112.829	-6.53	-24.52	5.19	22	.11	.11	.06	K	72	250	4	355
43	83.09.08.	12:51:38.17	41.839	112.616	6.57	-6.99	8.06	9	.04	.07	.06					
44	83.09.08.	13:42:13.81	41.885	112.616	5.06	-2.11	4.66	17	.10	.03	.05					
45	83.09.09.	00:08:48.23	41.724	112.831	-6.73	-24.47	6.13	9	.15	.15	.11					
46	83.09.09.	07:51:19.46	41.907	112.631	3.14	-0.15	3.42	12	.23	.11	.03					
47	83.09.09.	08:09:18.95	41.816	112.867	-12.59	-15.58	4.01	8	.07	.23	.51					
48	83.09.09.	08:23:20.91	42.074	112.467	10.60	21.59	3.56	8	.04	.03	.01					
49	83.09.09.	09:07:41.91	42.078	112.458	11.18	22.24	3.57	7	.07	.03	.02					
50	83.09.09.	13:30:11.78	42.081	112.460	10.92	22.51	3.69	10	.03	.01	.01					
51	83.09.09.	16:40:54.92	41.926	112.523	11.07	4.53	2.48	13	.05	.03	.01					
52	83.09.09.	18:03:57.47	41.950	112.558	7.51	6.21	5.13	14	.18	.06	.08	G	24	111	49	234
53	83.09.09.	18:14:13.15	41.950	112.553	7.90	6.33	5.70	17	.05	.01	.01	H	25	66	62	271
54	83.09.09.	18:15:48.56	41.946	112.550	8.27	5.98	5.93	10	.03	.01	.02					

Table 3-A1 (continued). Earthquake parameters

event	date	time(Z)	lat N	lon W	x	y	z	stns	rms	dz	dh	ql	pi	pd	ti	td
55	83.09.09.	18:15:52.74	41.944	112.574	6.44	5.18	6.84	7	.19	.12	.12					
56	83.09.09.	19:41:35.89	41.847	112.685	.84	-7.84	0.43	8	.13	.04	.27					
57	83.09.09.	20:15:57.07	41.949	112.557	7.62	6.13	4.71	15	.07	.03	.04	E	38	130	48	285
58	83.09.09.	20:32:35.23	41.946	112.556	7.80	5.83	4.17	9	.10	.04	.06					
59	83.09.09.	20:57:38.84	41.749	112.784	-3.81	-20.66	2.38	8	.13	.09	.21					
60	83.09.09.	22:37:42.77	41.879	112.725	-3.39	-5.43	6.05	5	.07	.18	.16					
61	83.09.09.	22:38:41.72	42.067	112.461	11.30	21.00	0.14	10	.06	.03	.13					
62	83.09.09.	23:49:53.55	41.855	112.752	-4.74	-8.63	5.96	9	.08	.07	.07					
63	83.09.10.	01:48:18.62	41.870	112.613	5.79	-3.63	4.67	7	.08	.07	.07					
64	83.09.10.	03:01:56.19	41.797	112.823	-8.48	-16.52	6.43	25	.08	.04	.04	F	57	125	28	335
65	83.09.10.	04:36:54.32	41.931	112.532	10.19	4.83	0.10	7	.13	.07	.24					
66	83.09.10.	04:40:53.90	41.835	112.705	-0.36	-9.60	3.68	11	.08	.06	.03	L	33	243	21	138
67	83.09.10.	05:00:53.52	42.061	112.501	8.34	19.38	6.35	10	.04	.03	.06					
68	83.09.10.	08:13:43.99	42.041	112.570	3.55	15.56	4.92	15	.07	.03	.04	G	81	312	8	144
69	83.09.10.	10:45:23.20	41.696	112.834	-6.05	-27.51	6.90	15	.05	.07	.06	G	80	159	9	331
70	83.09.10.	13:38:54.60	41.847	112.654	3.29	-7.08	0.10	9	.29	.12	.64					
71	83.09.10.	15:11:56.44	41.849	112.702	-0.58	-8.04	4.13	11	.04	.02	.03	G	64	245	22	96
72	83.09.10.	18:59:45.85	41.922	112.455	16.58	5.78	2.56	24	.05	.02	.01	E	74	19	3	276
73	83.09.10.	19:10:30.02	41.871	112.750	-5.11	-6.89	1.35	5	.14	.15	.22					
74	83.09.11.	02:23:13.68	41.755	112.830	-7.66	-21.15	8.34	30	.07	.04	.03	D	76	93	10	314
75	83.09.11.	02:23:45.03	41.757	112.819	-6.85	-20.67	7.86	12	.03	.03	.03	K	71	69	17	271
76	83.09.11.	02:23:57.78	41.756	112.824	-7.22	-20.90	8.25	30	.06	.03	.03	D	57	62	11	312
77	83.09.11.	02:34:57.47	41.757	112.818	-6.77	-20.65	7.07	16	.04	.03	.03	C	61	53	7	310
78	83.09.11.	02:48:45.59	41.758	112.827	-7.52	-20.76	8.00	12	.07	.08	.07	G	45	357	41	149
79	83.09.11.	05:07:39.85	41.877	112.774	-7.21	-6.84	3.23	10	.13	.12	.13	L	18	201	44	91
80	83.09.11.	06:08:10.55	41.691	112.814	-4.30	-27.55	6.05	25	.09	.04	.04	E	24	63	20	323
81	83.09.11.	06:10:25.15	41.687	112.812	-4.01	-27.93	6.00	26	.12	.04	.04					
82	83.09.11.	06:10:42.42	41.689	112.819	-4.63	-27.89	5.66	26	.11	.05	.07					
83	83.09.11.	06:29:57.15	41.690	112.816	-4.42	-27.71	6.82	43	.12	.04	.02	C	67	98	21	271
84	83.09.11.	06:34:16.86	41.722	112.766	-1.49	-23.09	0.19	24	.12	.04	.05					
85	83.09.11.	06:47:54.70	41.757	112.832	-7.88	-20.99	7.85	8	.06	.11	.11					
86	83.09.11.	06:53:6.32	41.683	112.823	-4.75	-28.62	5.34	19	.07	.07	.09					
87	83.09.11.	06:59:51.62	41.680	112.823	-4.65	-28.94	5.29	6	.05	.07	.06					
88	83.09.11.	07:35:33.94	41.925	112.454	16.56	6.13	2.37	16	.08	.03	.02					
89	83.09.11.	07:37:21.61	41.677	112.824	-4.63	-29.28	4.87	19	.13	.10	.10					
90	83.09.11.	09:41:9.97	41.711	112.816	-5.11	-25.48	5.48	12	.06	.09	.07					
91	83.09.11.	10:38:43.34	42.158	112.552	1.11	28.40	.10	7	.22	.14	.73					
92	83.09.11.	11:13:37.67	42.071	112.560	3.35	18.98	11.17	14	.18	.06	.10	H	77	82	8	306
93	83.09.11.	17:20:40.47	41.747	112.830	-7.40	-22.00	7.13	10	.04	.03	.03	K	52	74	25	307
94	83.09.11.	18:01:23.89	42.016	112.508	9.28	14.44	3.55	16	.07	.03	.01					
95	83.09.11.	18:15:17.12	42.162	112.545	1.53	29.00	5.02	11	.10	.09	.11	H	67	298	22	126
96	83.09.11.	23:37:24.22	42.052	112.489	9.59	18.72	2.59	8	.23	.09	.26					
97	83.09.11.	23:50:17.90	41.838	112.691	.66	-8.94	.96	7	.05	.03	.04					
98	83.09.12.	01:06:59.14	42.118	112.546	2.91	24.31	2.64	11	.05	.03	.03	F	4	186	72	83
99	83.09.12.	14:03:57.22	41.828	112.702	.11	-10.27	.56	10	.15	.05	.15					
100	83.09.12.	17:57:47.13	41.768	112.739	-0.86	-17.54	.59	9	.05	.02	.04	G	56	45	25	269
101	83.09.12.	17:58:20.03	41.768	112.742	-1.09	-17.62	.16	11	.06	.02	.10	J	31	30	45	261
102	83.09.12.	18:41:39.35	41.767	112.743	-1.14	-17.75	1.73	11	.07	.02	.07					
103	83.09.12.	18:46:.63	41.771	112.745	-1.43	-17.37	.10	14	.13	.03	.16					
104	83.09.12.	19:24:45.79	41.980	112.615	2.01	7.98	.32	14	.15	.05	.18					
105	83.09.12.	19:44:44.85	41.974	112.519	9.80	9.71	1.05	26	.10	.02	.02					
106	83.09.12.	20:22:55.70	41.829	112.665	3.01	-9.26	9.07	14	.05	.04	.05	G	72	280	13	137
107	83.09.12.	21:18:.57	41.843	112.698	-0.06	-8.58	7.79	13	.05	.03	.04	F	52	202	10	305
108	83.09.12.	21:55:33.15	41.843	112.701	-0.30	-8.66	7.18	16	.05	.02	.03	C	86	164	2	24
109	83.09.12.	21:57:21.94	41.844	112.700	-0.25	-8.53	4.37	10	.09	.08	.10					
110	83.09.12.	23:43:46.03	41.841	112.654	3.49	-7.71	6.47	22	.06	.01	.01	B	21	338	46	92

Table 3-A1 (continued). Earthquake parameters

event	date	time(Z)	lat N	lon W	x	y	z	stns	rms	dz	dh	ql	pi	pd	ti	td
111	83.09.13.	00:10:39.74	42.014	112.599	2.15	11.98	.10	9	.09	.03	.14					
112	83.09.13.	01:27:12.29	41.860	112.685	.41	-6.46	3.52	10	.05	.02	.05	L	20	36	67	197
113	83.09.13.	03:15:32.30	41.949	112.601	4.14	5.04	5.24	16	.15	.06	.10					
114	83.09.13.	04:58:21.02	41.861	112.690	-0.02	-6.48	4.04	9	.05	.04	.06					
115	83.09.13.	14:18:28.08	41.842	112.707	-0.74	-8.91	11.40	7	.20	.22	.40					
116	83.09.13.	15:23:23.02	41.924	112.526	10.90	4.24	2.45	30	.09	.02	.01	F	43	254	0	164
117	83.09.13.	16:40:.64	41.659	112.823	-3.97	-31.17	2.31	10	.19	.69	.80					
118	83.09.13.	17:22:54.75	41.703	112.794	-3.10	-25.79	4.31	13	.05	.06	.04					
119	83.09.13.	17:25:27.79	41.697	112.817	-4.73	-26.99	6.78	28	.16	.07	.05	F	38	93	50	288
120	83.09.13.	18:54:53.76	41.976	112.500	11.24	10.39	3.36	11	.09	.03	.03					
121	83.09.13.	20:42:35.93	41.698	112.789	-2.54	-26.20	3.07	13	.07	.05	.02	H	71	104	9	344
122	83.09.14.	00:54:26.58	41.781	112.854	-10.42	-18.98	6.39	12	.05	.08	.06	I	85	129	2	1
123	83.09.14.	04:00:33.24	41.796	112.826	-8.68	-16.70	4.57	10	.04	.05	.04					
124	83.09.14.	10:53:9.08	41.917	112.541	9.94	3.13	.90	15	.21	.06	.09					
125	83.09.14.	11:09:57.86	42.034	112.559	4.65	15.09	6.88	11	.09	.04	.06					
126	83.09.14.	13:08:18.41	41.827	112.697	.54	-10.25	5.91	8	.06	.04	.05					
127	83.09.14.	15:18:37.83	41.842	112.691	.52	-8.52	4.82	8	.10	.05	.06					
128	83.09.14.	20:58:.40	41.904	112.587	6.73	.62	6.26	11	.15	.09	.10					
129	83.09.14.	23:30:18.08	42.049	112.517	7.48	17.71	4.58	27	.10	.02	.05					
130	83.09.15.	06:18:44.08	41.754	112.752	-1.43	-19.35	.62	8	.05	.02	.06					
131	83.09.15.	06:34:6.61	41.815	112.642	5.30	-10.18	5.24	24	.08	.02	.03	C	78	93	12	287
132	83.09.15.	08:00:23.45	41.988	112.616	1.66	8.81	.10	9	.31	.10	.77					
133	83.09.15.	08:18:49.64	42.015	112.562	5.04	13.00	3.51	10	.08	.03	.01	I	31	4	2	273
134	83.09.15.	09:25:19.42	42.016	112.479	11.57	15.15	4.53	9	.06	.03	.04					
135	83.09.15.	14:32:7.81	41.961	112.533	9.12	7.99	3.23	8	.06	.03	.01					
136	83.09.15.	23:09:46.82	41.846	112.658	3.01	-7.28	7.87	14	.05	.03	.04	J	27	189	6	282
137	83.09.16.	00:20:50.91	41.845	112.655	3.28	-7.31	8.04	14	.04	.02	.03	E	50	13	6	276
138	83.09.16.	01:08:12.90	41.844	112.656	3.23	-7.44	6.43	13	.02	.03	.04					
139	83.09.16.	01:20:23.17	41.845	112.638	4.63	-6.89	7.70	11	.05	.09	.13					
140	83.09.16.	05:16:8.71	42.043	112.510	8.23	17.25	7.12	8	.04	.03	.07					
141	83.09.16.	08:44:47.98	41.834	112.670	2.45	-8.85	7.74	19	.07	.03	.04	E	7	181	10	89
142	83.09.16.	09:44:15.95	41.707	112.814	-4.82	-25.85	7.51	44	.09	.03	.02	C	52	121	37	307
143	83.09.16.	12:13:33.50	41.860	112.612	6.20	-4.66	5.30	11	.04	.03	.04					
144	83.09.16.	14:31:48.80	41.879	112.704	-1.72	-4.91	4.73	25	.07	.02	.03	D	66	114	23	303
145	83.09.16.	14:49:21.87	41.883	112.708	-2.17	-4.59	5.29	18	.08	.03	.04	J	74	46	2	145
146	83.09.16.	15:45:27.84	41.706	112.810	-4.47	-25.86	4.60	8	.03	.06	.04					
147	83.09.16.	20:12:25.75	42.066	112.451	12.13	21.14	1.53	8	.05	.02	.06					
148	83.09.16.	21:02:47.88	41.850	112.686	.66	-7.54	2.80	8	.05	.05	.03					
149	83.09.16.	23:56:38.45	41.755	112.750	-1.30	-19.19	1.28	13	.06	.02	.03					
150	83.09.17.	01:22:53.13	42.047	112.518	7.46	17.48	3.79	8	.05	.05	.11					
151	83.09.17.	03:46:50.84	41.880	112.650	2.53	-3.48	5.60	6	.03	.06	.06					
152	83.09.17.	06:31:12.86	41.953	112.598	4.24	5.54	4.01	6	.02	.04	.04					
153	83.09.17.	06:41:8.84	41.961	112.564	6.67	7.23	3.10	11	.10	.04	.02					
154	83.09.17.	11:05:58.02	41.772	112.833	-8.45	-19.42	5.03	9	.04	.04	.04	H	29	324	49	96
155	83.09.17.	12:25:38.60	42.065	112.458	11.61	20.86	3.26	6	.07	.04	.58					
156	83.09.17.	18:42:26.40	42.122	112.455	9.96	26.98	3.33	6	.15	.09	.19					
157	83.09.17.	19:26:12.98	42.128	112.459	9.44	27.51	3.93	4	.03	.10	.10					
158	83.09.17.	20:01:5.30	42.020	112.572	4.09	13.28	5.69	7	.05	.06	.08					
159	83.09.17.	20:28:42.34	42.000	112.601	2.45	10.45	2.40	10	.11	.05	.03					
160	83.09.17.	23:29:7.84	42.072	112.467	10.67	21.38	2.23	19	.23	.05	.03					
161	83.09.18.	03:48:6.56	42.075	112.469	10.41	21.65	3.53	9	.03	.02	.01					
162	83.09.18.	05:27:44.88	41.929	112.538	9.78	4.47	.10	9	.14	.07	.26					
163	83.09.18.	06:10:14.49	41.769	112.817	-7.08	-19.35	7.44	11	.04	.04	.04	I	49	59	0	149
164	83.09.18.	06:30:50.72	42.069	112.450	12.11	21.48	8.00	6	.19	.14	.38					
165	83.09.18.	09:51:9.33	41.832	112.713	-0.89	-10.12	5.20	40	.08	.02	.02	B	73	107	13	250
166	83.09.18.	09:53:43.27	41.827	112.709	-0.41	-10.55	4.76	14	.05	.02	.03	F	66	40	2	304

Table 3-A1 (continued). Earthquake parameters

event	date	time(Z)	lat N	lon W	x	y	z	stns	rms	dz	dh	ql	pi	pd	ti	td
167	83.09.18.	11:28:30.47	42.099	112.365	17.82	26.76	.10	23	.18	.12	.07					
168	83.09.18.	12:05:1.74	41.876	112.589	7.49	-2.40	6.93	17	.09	.06	.06	F	34	178	11	276
169	83.09.18.	12:46:34.62	41.852	112.634	4.72	-6.05	.80	9	.16	.08	.16					
170	83.09.18.	15:05:12.18	42.031	112.510	8.63	15.98	8.23	7	.04	.03	.08					
171	83.09.19.	00:22:55.70	41.858	112.688	.24	-6.75	8.00	7	.08	.16	.19					
172	83.09.19.	00:44:51.71	42.042	112.491	9.76	17.61	4.46	8	.05	.02	.06					
173	83.09.19.	01:47:23.75	42.018	112.506	9.37	14.70	4.03	8	.06	.02	.03	H	44	33	45	208
174	83.09.19.	06:04:15.17	41.887	112.664	1.19	-3.08	1.12	11	.09	.08	.11					
175	83.09.19.	06:46:16.24	41.826	112.570	10.65	-7.23	5.58	11	.10	.06	.07	H	37	338	44	197
176	83.09.19.	12:05:43.53	41.704	112.812	-4.56	-26.12	4.97	9	.03	.03	.03	L	57	58	4	321
177	83.09.19.	16:24:8.34	42.067	112.435	13.36	21.64	5.91	6	.07	.14	.21					
178	83.09.20.	11:16:16.59	41.877	112.744	-4.83	-6.10	2.57	11	.21	.27	.38					
179	83.09.20.	13:58:41.03	42.083	112.465	10.46	22.60	2.88	8	.06	.04	.16					
180	83.09.20.	14:01:44.83	41.809	112.678	2.64	-11.70	3.84	5	.02	.02	.03					
181	83.09.20.	19:37:21.67	41.801	112.695	1.55	-12.96	.10	18	.11	.02	.03	G	80	343	8	143
182	83.09.21.	00:03:19.40	42.053	112.485	9.87	18.92	2.55	14	.10	.04	.02	J	71	134	16	289
183	83.09.21.	00:50:5.46	41.830	112.706	-0.27	-10.16	5.12	4	.03	.07	.09					
184	83.09.21.	03:54:24.74	42.059	112.458	11.81	20.23	3.60	7	.04	.03	.02					
185	83.09.21.	04:05:40.01	41.903	112.559	8.98	1.20	2.83	16	.14	.05	.02	I	1	160	29	69
186	83.09.21.	04:52:42.98	41.855	112.657	2.79	-6.30	.10	6	.09	.07	.25					
187	83.09.21.	04:54:26.04	41.847	112.649	3.69	-6.95	.10	7	.22	.07	.34					
188	83.09.21.	06:21:41.15	42.074	112.467	10.60	21.59	3.49	7	.02	.01	.01					
189	83.09.21.	06:24:3.62	42.097	112.427	12.99	25.02	4.75	5	.01	.04	.06					
190	83.09.21.	08:35:25.62	42.069	112.456	11.63	21.34	.48	9	.05	.02	.32					
191	83.09.21.	08:44:31.66	41.843	112.646	4.06	-7.30	.12	9	.20	.06	.26					
192	83.09.21.	09:49:31.61	42.051	112.467	11.36	19.16	.78	9	.21	.08	.53					
193	83.09.21.	12:00:50.98	41.786	112.819	-7.80	-17.59	4.86	4	.04	.13	.11					
194	83.09.21.	12:35:33.07	41.816	112.704	.35	-11.59	4.74	8	.15	.08	.12					
195	83.09.21.	16:02:25.29	41.719	112.782	-2.67	-23.80	4.15	9	.07	.03	.05					
196	83.09.21.	21:19:47.47	41.828	112.710	-0.52	-10.47	5.06	27	.07	.01	.02	A	57	23	7	281
197	83.09.21.	23:01:5.03	42.025	112.534	6.93	14.75	5.36	6	.03	.04	.07					
198	83.09.21.	23:11:13.35	41.854	112.653	3.14	-6.31	2.98	28	.12	.02	.02	D	5	217	73	108
199	83.09.21.	23:35:46.57	42.041	112.488	10.03	17.58	5.14	15	.08	.02	.05	K	5	188	83	41
200	83.09.22.	00:38:8.28	41.844	112.663	2.68	-7.62	.10	9	.09	.05	.22					
201	83.09.22.	02:58:6.77	41.840	112.668	2.41	-8.16	5.07	7	.04	.04	.08					
202	83.09.22.	09:00:46.48	41.861	112.690	-0.02	-6.48	4.74	30	.06	.02	.02	E	24	25	22	284
203	83.09.22.	09:20:7.34	41.876	112.714	-2.41	-5.48	2.34	6	.03	.04	.14					
204	83.09.22.	09:58:12.16	42.041	112.507	8.53	17.11	2.90	22	.10	.03	.02					
205	83.09.22.	10:55:44.06	42.067	112.473	10.36	20.70	1.90	6	.07	.02	.11					
206	83.09.22.	18:11:42.40	41.706	112.845	-7.25	-26.72	8.00	9	.06	.09	.10					
207	83.09.22.	19:18:37.77	41.857	112.651	3.20	-5.94	3.45	6	.05	.07	.15					
208	83.09.23.	06:32:37.66	41.878	112.636	3.70	-3.35	4.73	4	.01	.04	.03					
209	83.09.23.	06:36:27.16	41.995	112.486	11.71	12.75	1.71	6	.02	.03	.05					
210	83.09.23.	06:57:38.19	41.843	112.658	3.11	-7.60	.10	12	.11	.03	.29					
211	83.09.23.	08:32:37.88	42.041	112.455	12.64	18.39	4.57	7	.08	.06	.15					
212	83.09.23.	10:41:35.18	42.102	112.464	9.91	24.64	3.64	8	.07	.04	.02					
213	83.09.23.	11:27:15.97	41.879	112.754	-5.68	-6.14	5.74	5	.05	.17	.14					
214	83.09.23.	12:34:5.92	41.851	112.655	3.08	-6.68	2.37	26	.07	.01	.03	D	42	231	5	135
215	83.09.23.	21:13:29.71	41.707	112.814	-4.82	-25.85	4.39	17	.10	.06	.07	I	60	189	27	347
216	83.09.23.	21:33:35.68	41.706	112.813	-4.71	-25.94	5.29	13	.04	.03	.04	I	39	69	16	325
217	83.09.23.	23:58:53.71	41.871	112.751	-5.18	-6.91	4.56	7	.04	.12	.13					
218	83.09.24.	04:43:35.87	42.027	112.489	10.42	16.07	3.21	6	.01	.01	.02					
219	83.09.24.	05:20:42.49	42.007	112.489	11.08	13.95	3.75	12	.09	.07	.07					
220	83.09.24.	05:46:25.08	42.088	112.465	10.29	23.13	2.00	8	.06	.03	.11					
221	83.09.24.	09:13:49.49	41.702	112.814	-4.66	-26.38	5.04	11	.06	.05	.05					
222	83.09.24.	14:28:41.63	41.824	112.697	.64	-10.57	1.64	4	.01	.01	.03					

Table 3-A1 (continued). Earthquake parameters

event	date	time(Z)	lat N	lon W	x	y	z	stns	rms	dz	dh	ql	pi	pd	ti	td
223	83.09.24.	17:36:50.22	42.122	112.500	6.40	25.87	5.64	7	.06	.04	.05					
224	83.09.24.	20:26:10.95	41.985	112.581	4.53	9.35	.10	10	.09	.05	.26					
225	83.09.24.	20:27:58.59	41.937	112.598	4.77	3.84	6.69	29	.07	.02	.03	C	55	243	22	116
226	83.09.24.	22:20:26.18	41.984	112.454	14.61	12.38	8.48	43	.08	.02	.02	C	49	180	11	284
227	83.09.24.	22:29:10.48	41.979	112.445	15.49	12.07	6.17	7	.02	.05	.07					
228	83.09.24.	23:00:27.97	41.804	112.750	-2.91	-13.99	4.87	7	.17	.11	.13					
229	83.09.25.	00:40:35.68	41.985	112.454	14.58	12.48	7.28	27	.08	.03	.04	F	18	196	1	286
230	83.09.25.	06:07:7.44	41.974	112.597	3.63	7.79	1.41	7	.07	.04	.08					
231	83.09.25.	08:39:2.91	41.817	112.689	1.50	-11.12	3.91	14	.05	.02	.03	I	57	247	5	346
232	83.09.25.	09:41:56.93	41.973	112.501	11.26	10.05	4.05	6	.07	.09	.12					
233	83.09.25.	10:46:17.71	41.782	112.745	-1.79	-16.21	4.48	28	.10	.02	.02	B	84	333	2	90
234	83.09.25.	13:44:9.87	42.122	112.454	10.03	27.00	3.31	12	.05	.04	.05					
235	83.09.25.	17:18:43.29	42.019	112.548	6.02	13.77	4.68	9	.05	.03	.04					
236	83.09.25.	18:02:34.90	42.046	112.517	7.58	17.39	7.33	7	.05	.07	.08					
237	83.09.25.	19:00:8.93	41.699	112.791	-2.73	-26.14	2.49	15	.05	.02	.07					
238	83.09.25.	19:00:28.14	41.698	112.795	-3.01	-26.34	3.60	16	.05	.02	.01	L	30	151	27	259
239	83.09.25.	21:49:20.71	41.772	112.735	-0.67	-17.02	.92	10	.04	.02	.03					
240	83.09.25.	21:51:12.65	41.879	112.602	6.36	-2.40	2.00	6	.13	.28	.38					
241	83.09.25.	23:16:27.96	41.874	112.701	-1.32	-5.37	2.65	22	.05	.02	.02	H	1	6	60	273
242	83.09.25.	23:43:55.56	41.999	112.500	10.47	12.83	2.93	17	.09	.03	.01					
243	83.09.25.	23:55:8.02	42.120	112.447	10.65	26.96	11.33	8	.17	.14	.22					
244	83.09.26.	03:07:37.59	41.994	112.499	10.72	12.33	2.33	8	.04	.04	.03					
245	83.09.26.	07:02:34.77	41.752	112.813	-6.21	-21.06	4.66	9	.04	.03	.05					
246	83.09.26.	08:23:2.68	42.087	112.440	12.30	23.64	3.78	8	.05	.05	.15					
247	83.09.26.	09:03:19.43	41.990	112.606	2.39	9.27	.14	7	.13	.06	.41					
248	83.09.26.	09:25:24.81	41.852	112.656	2.97	-6.60	1.59	12	.06	.02	.05	I	54	218	5	316
249	83.09.26.	09:45:54.62	41.930	112.590	5.63	3.30	6.90	7	.03	.02	.02					
250	83.09.26.	12:37:48.32	42.024	112.514	8.54	15.13	11.66	8	.07	.07	.13					
251	83.09.26.	12:54:26.97	41.961	112.610	3.03	6.09	5.06	42	.08	.02	.02	C	74	234	10	101
252	83.09.26.	15:01:42.28	42.058	112.519	7.02	18.62	2.38	18	.14	.04	.03					
253	83.09.26.	15:22:59.24	41.991	112.585	4.02	9.89	3.35	40	.09	.02	.01					
254	83.09.26.	20:32:16.78	41.851	112.681	1.02	-7.32	.10	10	.13	.04	.17					
255	83.09.26.	20:32:38.34	41.937	112.595	5.01	3.92	5.95	21	.09	.05	.05	F	75	319	11	104
256	83.09.26.	20:34:44.82	41.929	112.585	6.06	3.32	5.96	30	.08	.02	.02	C	75	253	13	85
257	83.09.27.	04:34:56.21	41.843	112.711	-1.09	-8.90	4.39	23	.07	.02	.02	F	87	51	2	255
258	83.09.27.	05:38:29.91	41.842	112.713	-1.22	-9.06	4.26	17	.06	.02	.04	G	30	170	4	262
259	83.09.27.	07:01:53.85	42.010	112.492	10.74	14.19	3.21	6	.04	.04	.07					
260	83.09.27.	07:23:42.72	41.848	112.600	7.54	-5.64	6.86	27	.07	.02	.02	G	65	314	16	82
261	83.09.27.	09:58:18.10	41.937	112.595	5.01	3.92	5.44	14	.20	.06	.08	I	74	336	12	120
262	83.09.27.	11:04:24.80	41.892	112.543	10.61	.43	2.44	8	.15	.13	.08					
263	83.09.27.	12:32:58.45	41.982	112.492	11.67	11.23	10.97	7	.16	.20	.23					
264	83.09.27.	13:04:57.03	41.835	112.691	.75	-9.26	3.95	15	.10	.03	.04	L	50	204	17	91
265	83.09.27.	13:21:.74	41.981	112.483	12.41	11.34	13.04	6	.12	.15	.20					
266	83.09.27.	13:55:27.72	41.840	112.711	-1.00	-9.22	3.16	17	.06	.01	.02	I	32	156	1	65
267	83.09.27.	13:55:39.62	41.839	112.711	-0.96	-9.33	3.67	15	.06	.02	.01					
268	83.09.27.	14:15:2.59	41.839	112.711	-0.96	-9.33	3.71	6	.02	.02	.02					
269	83.09.27.	14:50:19.25	41.854	112.657	2.83	-6.41	.59	10	.06	.04	.12					
270	83.09.27.	15:11:53.28	41.834	112.710	-0.72	-9.83	2.82	10	.08	.08	.14					
271	83.09.27.	15:33:20.54	41.852	112.661	2.58	-6.72	.97	7	.03	.02	.06					
272	83.09.27.	18:36:42.25	41.958	112.623	2.10	5.46	1.59	34	.24	.04	.06					
273	83.09.28.	00:27:25.64	42.055	112.446	12.89	20.10	.10	4	.03	.03	.09					
274	83.09.28.	02:28:40.04	41.702	112.813	-4.58	-26.36	6.35	41	.13	.04	.03					
275	83.09.28.	03:32:39.30	42.092	112.469	9.84	23.45	.10	13	.16	.04	.20					
276	83.09.28.	03:42:5.31	41.982	112.567	5.74	9.38	1.52	6	.09	.09	.25					
277	83.09.28.	05:26:30.88	41.932	112.425	18.63	7.59	2.43	14	.07	.07	.03					
278	83.09.28.	05:54:50.99	41.828	112.676	2.17	-9.63	3.60	6	.17	.20	.42					

Table 3-A1 (continued). Earthquake parameters

event	date	time(Z)	lat N	lon W	x	y	z	stns	rms	dz	dh	ql	pi	pd	ti	td
279	83.09.28.	06:24:24.61	41.858	112.712	-1.67	-7.33	3.58	15	.06	.04	.02					
280	83.09.28.	06:43:29.14	42.017	112.539	6.80	13.78	5.59	5	.02	.04	.05					
281	83.09.28.	07:06:18.16	41.789	112.593	10.04	-11.72	.30	12	.04	.03	.07					
282	83.09.28.	09:06:20.95	41.775	112.748	-1.80	-17.02	3.00	33	.12	.02	.02	F	85	323	1	77
283	83.09.28.	10:14:48.12	42.021	112.535	6.98	14.30	5.92	5	.05	.08	.11					
284	83.09.28.	13:03:31.87	42.125	112.449	10.33	27.44	3.62	11	.09	.05	.02					
285	83.09.28.	13:26:19.74	41.868	112.640	3.71	-4.51	7.52	36	.11	.03	.03	C	76	174	9	305
286	83.09.28.	13:51:52.51	42.054	112.604	.44	16.10	4.53	18	.13	.07	.11					
287	83.09.28.	14:03:43.43	42.081	112.436	12.81	23.10	2.12	27	.15	.05	.02					
288	83.09.28.	15:15:59.16	41.827	112.685	1.49	-9.96	1.55	8	.05	.04	.15					
289	83.09.28.	19:29:50.20	42.053	112.429	14.30	20.31	.33	15	.17	.10	.06					
290	83.09.28.	22:30:49.10	42.027	112.507	8.99	15.63	9.48	5	.04	.04	.11					
291	83.09.29.	00:12:40.14	41.849	112.656	3.07	-6.91	.54	7	.10	.04	.15					
292	83.09.29.	08:58:39.64	41.728	112.833	-7.02	-24.09	6.85	27	.26	.09	.08	F	38	136	48	344
293	83.09.29.	08:59:6.15	41.749	112.831	-7.54	-21.81	7.87	32	.06	.02	.02	E	43	127	43	330
294	83.09.29.	08:59:36.34	41.749	112.831	-7.54	-21.81	7.95	36	.09	.03	.03	I	44	166	29	290
295	83.09.29.	09:04:51.06	41.733	112.831	-7.02	-23.51	8.00	29	.16	.07	.07	E	43	114	42	321
296	83.09.29.	09:51:23.15	42.040	112.473	11.25	17.84	5.29	8	.03	.03	.06					
297	83.09.29.	17:25:39.62	41.829	112.681	1.74	-9.65	3.58	9	.02	.02	.01					
298	83.09.29.	18:06:23.51	41.835	112.683	1.39	-9.06	3.93	27	.08	.01	.02	G	13	200	39	99
299	83.09.29.	18:06:46.78	41.835	112.682	1.47	-9.04	3.77	18	.06	.03	.03					
300	83.09.29.	19:34:8.46	41.823	112.686	1.55	-10.41	1.46	7	.02	.02	.03					
301	83.09.30.	04:44:5.36	41.896	112.470	16.26	2.66	7.23	37	.13	.03	.04					
302	83.09.30.	04:44:49.38	41.789	112.706	1.07	-14.51	1.85	10	.25	.09	.33					
303	83.09.30.	06:46:2.60	41.781	112.752	-2.31	-16.48	3.12	23	.08	.02	.07	E	43	357	19	106
304	83.09.30.	06:49:46.88	41.779	112.754	-2.41	-16.75	3.58	12	.02	.02	.05					
305	83.09.30.	11:45:13.33	42.061	112.451	12.29	20.61	6.10	8	.03	.03	.07					
306	83.09.30.	12:32:25.60	41.827	112.689	1.18	-10.06	2.30	8	.08	.04	.13					
307	83.09.30.	14:14:57.46	41.798	112.713	.22	-13.72	2.42	6	.24	.17	.41					
308	83.09.30.	23:49:56.72	41.995	112.501	10.53	12.38	2.60	7	.05	.04	.02					
309	83.10.01.	01:27:11.97	41.859	112.706	-1.22	-7.08	2.04	9	.11	.10	.18					
310	83.10.01.	02:33:8.25	41.913	112.651	1.36	0.00	4.20	17	.06	.04	.05					
311	83.10.01.	04:01:53.20	41.861	112.746	-4.46	-7.85	3.54	7	.06	.13	.28					
312	83.10.01.	05:21:13.24	41.937	112.593	5.16	3.97	4.77	11	.11	.06	.10					
313	83.10.01.	07:35:38.81	41.972	112.642	.13	6.47	4.38	5	.05	.10	.15					
314	83.10.01.	08:05:30.36	41.894	112.676	.01	-2.63	5.47	8	.07	.06	.08					
315	83.10.01.	10:02:6.65	41.813	112.773	-5.03	-13.60	4.92	7	.02	.02	.03	L	78	202	2	99
316	83.10.01.	16:04:58.82	42.072	112.467	10.67	21.38	2.68	4	.01	.01	.08					
317	83.10.01.	18:14:29.94	42.076	112.463	10.85	21.91	4.18	5	.01	.03	.14					
318	83.10.01.	19:05:59.56	41.991	112.493	11.29	12.16	4.04	8	.03	.08	.06					
319	83.10.02.	00:14:33.10	41.819	112.706	.09	-11.32	4.19	15	.04	.01	.02	F	69	128	20	306
320	83.10.02.	00:28:55.24	41.846	112.707	-0.88	-8.49	9.97	12	.18	.09	.18					
321	83.10.02.	04:20:25.38	41.763	112.761	-2.44	-18.61	2.14	8	.01	.02	.04					
322	83.10.02.	05:41:13.88	42.041	112.466	11.77	18.12	2.77	6	.06	.09	.05					
323	83.10.02.	11:32:52.32	41.748	112.840	-8.23	-22.14	7.41	11	.02	.02	.02	F	51	84	18	329
324	83.10.02.	16:30:58.46	41.753	112.832	-7.75	-21.41	7.26	8	.02	.02	.03					
325	83.10.02.	23:13:58.20	41.815	112.738	-2.32	-12.53	3.88	6	.03	.03	.05					
326	83.10.03.	02:19:28.55	41.820	112.769	-4.94	-12.76	5.50	31	.12	.03	.04	E	32	173	2	265
327	83.10.03.	02:35:31.43	41.821	112.769	-4.97	-12.66	4.57	12	.05	.03	.05	I	48	127	35	272
328	83.10.03.	07:14:4.63	41.818	112.703	.36	-11.36	2.14	5	.01	.01	.02					
329	83.10.03.	07:54:11.07	41.857	112.701	-0.76	-7.17	7.34	31	.10	.02	.02	E	36	27	7	291
330	83.10.03.	10:45:26.72	41.846	112.656	3.17	-7.23	1.65	9	.10	.06	.16					
331	83.10.03.	10:45:34.04	41.859	112.620	5.60	-4.97	9.28	7	.11	.14	.20					
332	83.10.03.	11:11:55.37	41.851	112.657	2.93	-6.73	3.69	10	.08	.04	.02					
333	83.10.03.	11:58:1.99	41.775	112.753	-2.20	-17.14	2.35	7	.03	.04	.07					
334	83.10.03.	13:59:5.96	41.797	112.798	-6.49	-15.91	5.32	15	.05	.03	.04	G	53	107	8	209

Table 3-A1 (continued). Earthquake parameters

event	date	time(Z)	lat N	lon W	x	y	z	stns	rms	dz	dh	ql	pi	pd	ti	td

Key: event--earthquake identification number. date (yy.mm.dd)--year-1900 (yy), month (mm), and day (dd) of event origin time. time(Z)--origin time (Coordinated Universal Time), hours:minutes:seconds. lat N--latitude in degrees north. lon W--longitude in degrees W. x and y--distance north and east, respectively, of earthquake from the array center at 41°55'N, 112°45'W, km. z--depth of earthquake, km. stns--number of stations recording the earthquake. rms--root-mean-square of travel-time residuals, s. dz and dh--vertical and horizontal standard errors computed by the relocation routine REL3D, km. ql--focal mechanism grade. pi and pd--inclination and declination, respectively, of the P-axis of the focal mechanism, degrees. ti and td--inclination and declination, respectively, of the T-axis of the focal mechanism, degrees.

CHAPTER 4
IS EXTENSION IN DEATH VALLEY ACCMMODATED BY THINNING OF THE MANTLE LITHOSPHERE BENEATH THE SIERRA NEVADA, CALIFORNIA?[1]

Craig H. Jones

Department of Earth, Atmospheric, and Planetary Sciences,
Massachusetts Institute of Technology, Cambridge

Abstract. While relatively rapid and large-scale extension occurred in the Death Valley region of California during Neogene time, little or no shallow extension occurred in the adjacent Sierra Nevada. This contrast in tectonic history has often been extrapolated to include the entire lithosphere, but geophysical and geologic observations indicate that more extension of the mantle lithosphere has occurred under the Sierra than under the Death Valley region. Upper mantle seismic velocities observed beneath the High Sierra are lower than those observed in other regions with comparable surface heat flow. This discrepancy could be resolved if the mantle lithosphere beneath the High Sierra had become warmer, presumably by tectonic thinning, in the last 10 m.y. Upper mantle seismic velocities, averaged topography, and Bouguer gravity anomalies all are consistent with the presence of thinner mantle lithosphere beneath the High Sierra than beneath the California portion of the Basin and Range Province to the east. This suggests that extension of the crust near Death Valley might be accommodated at a deeper level by thinning of the mantle lithosphere beneath the Sierra Nevada.

The extension in the crust of the California Basin and Range Province and the thinning of the mantle lithosphere under the High Sierra appear to share the same bounds in time and space. The uplift of the High Sierra occurred over the past 9 m.y., which coincides with most of the extension that occurred in the California Basin and Range Province. Because the orientation of extension in the California Basin and Range Province is inferred to be approximately N60°W from geologic, geodetic, and in situ stress measurements, the northern and southern edges of the Death Valley extensional subprovince may extend N60°W from the inferred northern and southern limits of west dipping low-angle normal faults of the Death Valley region. Pronounced changes in the averaged topography and Bouguer gravity

---

[1] Published in *Tectonics*, *6*, 449-473, 1987.

anomaly across these two bounds both in the Basin and Range Province and in the Sierra Nevada support a connection between the tectonics of both regions. The geomorphic history of the southern Sierra suggests an up-to-the-north warp of the Sierra across this southern bound during latest Cenozoic time. Hence extension near Death Valley may be localized in the crust and may be laterally connected to thinning of the mantle lithosphere beneath the Sierra Nevada. This geometry requires extended crust to overlie unextended mantle lithosphere near Death Valley and virtually unextended crust to overlie tectonically thinned mantle lithosphere in the High Sierra Nevada.

INTRODUCTION

In recent years many investigators working to understand the nature and geometry of extension in the Basin and Range Province of western North America have considered deformation of the mantle to mirror deformation of the upper crust: An extended upper mantle underlies an extended crust, and an unextended mantle underlies an unextended crust [e.g., Stewart, 1978; Eaton et al., 1978; Lachenbruch and Sass, 1978; Eaton, 1982]. Deformation of the upper crust has been found to include extension on low-angle normal faults [e.g., Anderson, 1971; Armstrong, 1972; Hunt and Mabey, 1966; Longwell, 1945; Wright and Troxel, 1969, 1973]. If such low-angle normal faults extend deep into the lithosphere as Wernicke [1981] suggests, then the extended portion of the mantle lithosphere might not underlie that portion of the upper crust that is most extended. Geological investigation of exhumed low-angle normal faults has failed to resolve the maximum depth of penetration of such faults [e.g., Bartley and Wernicke, 1984; Brewer and Smythe, 1984; Davis, 1983; Gans et al., 1985; Reynolds and Spencer, 1985]. Although they cannot resolve the style of deformation with depth, geophysical observations can provide crucial bounds to the location of extension in the lower crust and upper mantle in the southwestern Great Basin.

The most rugged terrain in California, the High Sierra, with relief up to about 4 km between 36.2° and 38°N, was formed after the uplift of the area by about 2 km in late Cenozoic time (Figure 4-1 [Christensen, 1966; Huber, 1981]). Over the same time span, that part of the Basin and Range Province between the Sierra and the Spring Mountains underwent extreme extension that may have moved the Sierra Nevada more than 80 km away from the Spring Mountains [Davis and Burchfiel, 1973; Wernicke et al., 1982; Stewart, 1983]. This portion of the Basin and Range Province contains fault block ranges tilted exclusively to the east in Neogene time [Stewart, 1978], suggesting a fairly uniform style of extension throughout the region. This paper considers the source of the uplift of the High Sierra and explores its relationship to the extension to the east. Correlating the shallow and

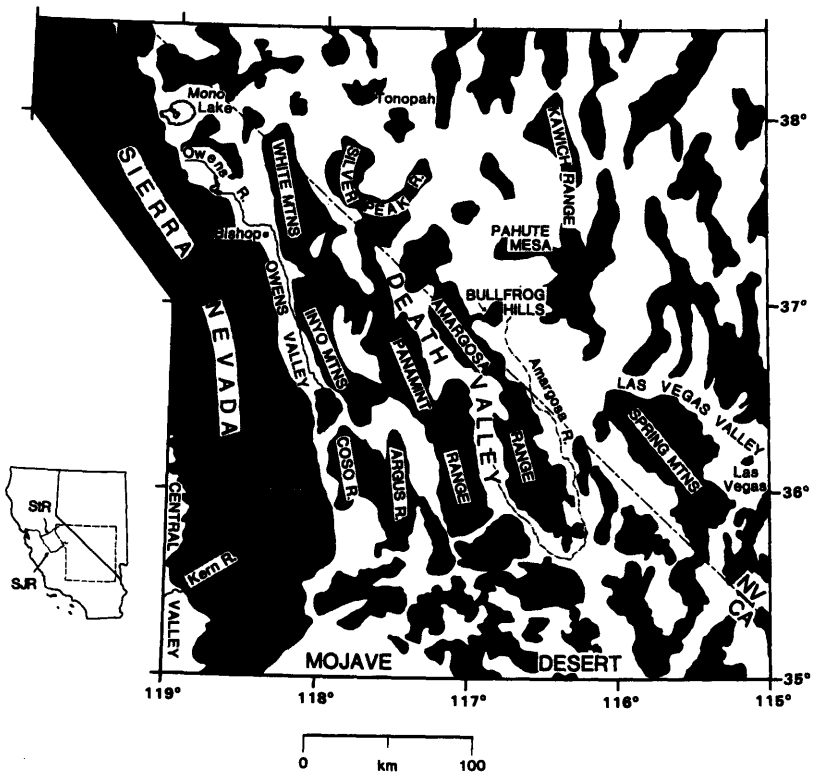

Fig. 4-1. Location map of the southwestern Great Basin. Rivers on inset are the San Joaquin River (SJR) and the Stanislaus River (StR). Ranges are shaded.

deep tectonics in this area is possible because the southwestern part of the Great Basin is both large enough to permit meaningful use of geophysics in determining the gross structure of the crust and mantle and small enough that a single style of deformation probably dominates the tectonics of the entire area.

NEOGENE HISTORY OF THE SIERRA NEVADA

The Sierra Nevada of California is most simply described as a large fault block that has been uplifted and tilted westward in late Cenozoic time [e.g., Christensen, 1966]. The range is underlain by Mesozoic intrusive rocks of the Sierra Nevada batholith and some remaining metamorphic rocks [Bateman and Eaton, 1967]. The only preserved Cenozoic rocks in the High Sierra are some scattered volcanic flows and Quaternary glacial and alluvial deposits [Bateman and Wahrhaftig, 1966]. Beyond the bounds of this area, the Sierra Nevada batholith vanishes beneath sediments of the Great Valley of California to the west and is overlain by Cenozoic volcanic and associated sedimentary rocks to the north. These Cenozoic rocks provide the most detailed information in constraining the history of the Cenozoic uplift of the Sierra Nevada.

Lindgren [1911] first recognized that the gentle valley floors preserved under Miocene volcanic flows in the central Sierran foothills implied that the range had been uplifted and tilted in late Cenozoic time. The wide, flat cross section and even grade of these ancestral channels of the San Joaquin and Stanislaus Rivers (located on Figure 4-1) stand in marked contrast to the less mature channels of their modern successors. Radiometric dates on these volcanic flows (9-10 m.y. ago [Dalrymple, 1964; Huber, 1981]) and younger intracanyon flows in the San Joaquin River drainage allowed Huber [1981] to construct a history of the uplift of the Sierra for the past 9 m.y. He inferred that about 2 km of uplift have occurred at the crest of the range since 9 m.y. ago and that the greatest rate of uplift occurred during the Quaternary period. The incision of some 3-m.y.-old volcanic flows led Christensen [1966] to conclude that the late Cenozoic uplift in the southern High Sierra was somewhat greater than that in the north. Recognition of an influx of clastic debris into the southernmost Great Valley of California starting between 8 and 9 m.y. ago led Bartow [1984] to date the late Cenozoic uplift of the southern Sierra as beginning at that time. Hence the best available estimate for the amount of late Cenozoic uplift of the southern Sierra Nevada is about 2 to 2.5 km over the last 9 m.y.

ORIGIN OF THE SIERRAN UPLIFT

Two main hypotheses have been advanced to explain the Cenozoic uplift of the High Sierra: compensation of the range by a crustal root and uplift caused by a low density anomaly in the upper mantle. Lawson [1936] first suggested that a crustal root accounted for the great elevation of the Sierra. This notion was quickly supported by Byerly [1938], who had observed delays of several seconds in the arrival time of P_n phases from earthquakes west of the Sierra at station TIN east of the Sierra in Owens Valley (Figure 4-4). He interpreted this as an effect of a deep crustal root under the Sierra that delayed the P_n phase from the time it would otherwise arrive. Eaton's [1963, 1966] interpretation of seismic refraction profiles in the Sierra indicated that a crustal root underlies the Sierra. If the lithosphere were in steady-state equilibrium, the extraordinarily low heat flow measured in the Sierra Nevada, less than 1.2 HFU (10^{-3} cal cm^{-3} s^{-1}) with about 0.8 HFU from crustal sources [Roy et al., 1972; Lachenbruch and Sass, 1977], would require a crustal root to counteract the negative buoyancy of the cool, dense mantle that would underlie the Sierra.

Crough and Thompson [1977] detailed several flaws in the crustal root hypothesis. As noted by Bateman and Eaton [1967], any Sierran root probably had formed by late Cretaceous time; the delayed uplift of the range, however, argues against any connection between the root and the uplift in Neogene time. They also suggested that the surface heat

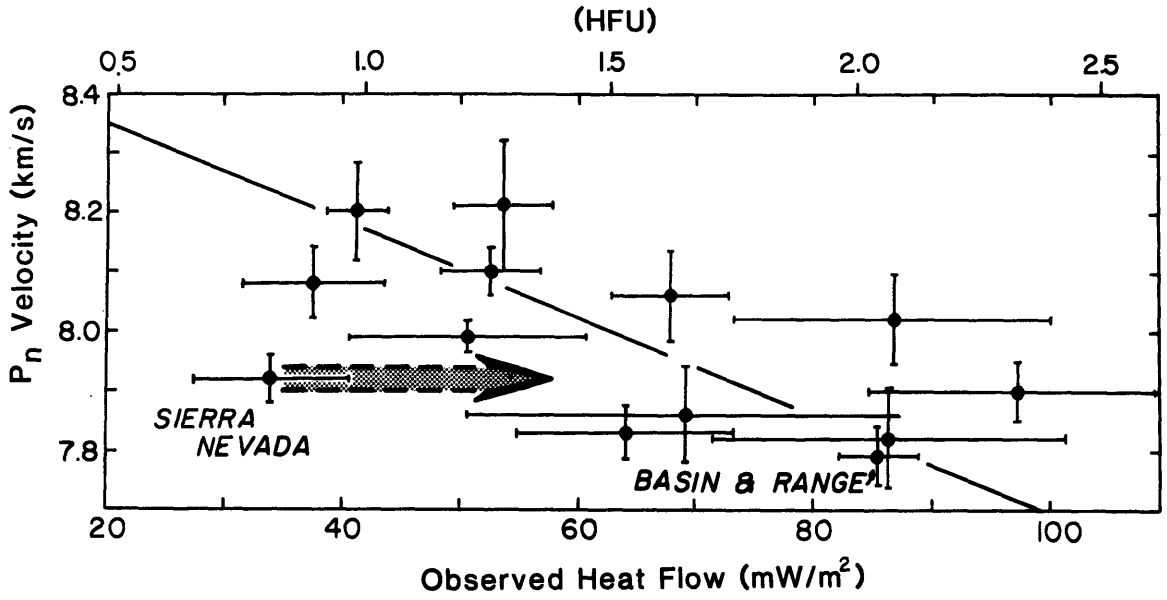

Fig. 4-2. P_n velocity versus surface heat flow for regions of North America, redrawn from Black and Braile [1982]. Arrow indicates possible future values for the Sierra Nevada as it approaches thermal equilibrium.

flow observed in the Sierra was a relic that predated the uplift, for a thermal anomaly placed at the base of the Sierran crust would not change the surface heat flow perceptibly within 10 to 20 m.y. The structure Crough and Thompson [1977] preferred for the Sierra Nevada consists of a thick crust (~50 km) underlain by a low-density anomaly in the mantle, probably caused by a thinned mantle lithosphere.

Black and Braile [1982] found that over most of North America, except for the Sierra Nevada, high P_n velocities correlate with low surface heat flow values (Figure 4-2). They suggested that the correlation reflects a decrease in P_n velocity with increasing temperature at the Moho. This inference assumes that the thermal structure of the crust is in steady state equilibrium. The Sierra Nevada clearly deviates from Black and Braile's inferred relationship but would agree with the other data points in Figure 4-2 if the sub-Sierran mantle were warmed within the last 5 to 10 m.y. Rapid warming of the upper mantle would decrease the observed P_n velocity without changing the surface heat flow; if this Neogene warming under Sierra Nevada were to have occurred in the last 10 m.y., then in the future the data point for the Sierra Nevada would move in the direction indicated by the arrow in Figure 4-2 as the Sierran crust approached thermal equilibrium.

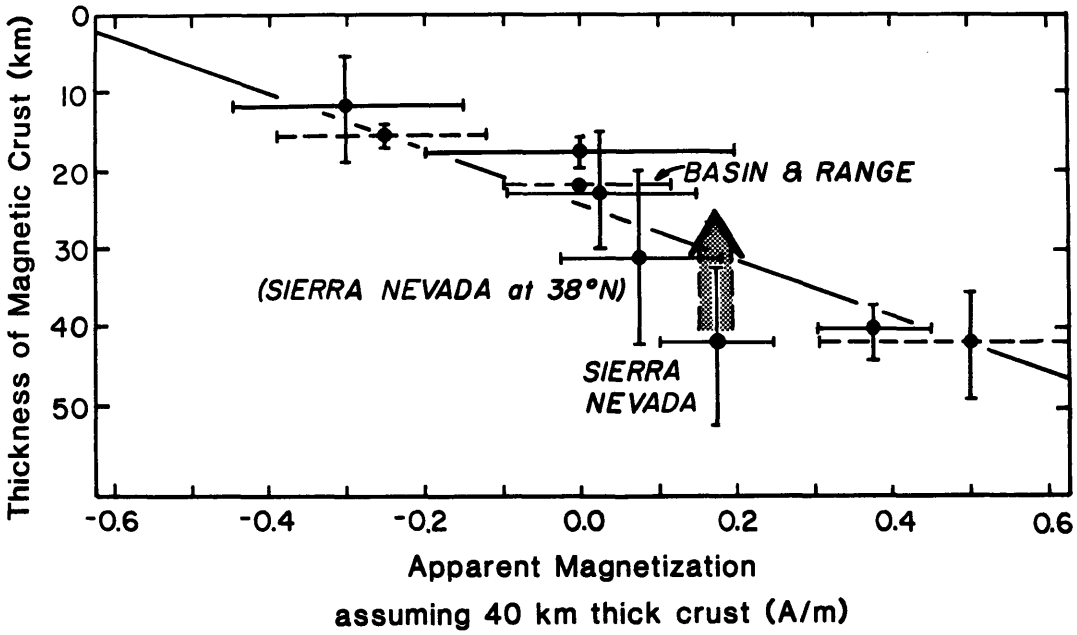

Fig. 4-3. Apparent magnetization of the crust versus depth of the Curie point isotherm inferred by other means, redrawn from Mayhew [1985]. Arrow indicates possible future values for the Sierra Nevada as it approaches thermal equilibrium. Note that application of the "annihilator magnetization" of Harrison et al. [1986] will tend to move Sierran points to the left relative to other regions. The source information used by Mayhew to compute the "Sierra Nevada at 38°N" point is unclear but may partially reflect the high heat flow near the Long Valley Caldera.

Similarly, Mayhew [1985] found a fair correlation for most subregions of the western U.S. between the apparent magnetization of the crust computed from satellite observations and the depth of the Curie isotherm calculated from both the surface heat flux and spectral analysis of aeromagnetic measurements (Figure 4-3). The observation for the Sierra Nevada is somewhat discordant from the overall correlation; this discordance probably would increase if the analysis were repeated using the suggestions made by Harrison et al. [1986]. Because the depth to the Curie point isotherm was calculated from the surface heat flow in the Sierra Nevada, a greater temperature in the lower crust than that computed assuming steady state heat conduction will reduce the inferred depth of the Curie isotherm and so reduce any discrepancy between the Sierran observations and the other data of Figure 4-3.

Late arrival times of teleseismic P waves observed by Mavko and Thompson [1983] at stations in the Sierra between latitude 38°N and the Cascade Range (~40.5°N) also indicate that the mantle lithosphere beneath the Sierra Nevada is anomalously thin. They interpreted an increasing delay of teleseismic arrivals at stations progressively farther south as a result of

a corresponding decrease in the thickness of mantle lithosphere. Noting the correlation of thinner mantle lithosphere with greater surface elevation, they suggested that the thinning of the mantle lithosphere caused the late Cenozoic uplift of the Sierra Nevada. Their interpretation is consistent with but not uniquely required by observations of teleseismic arrivals through the southern Sierra made by Press and Biehler [1964] and Raikes [1980].

Recently Chase and Wallace [1986] proposed that the Cenozoic uplift of the Sierra could be reconciled with Mesozoic emplacement of a crustal root if the root were frozen beneath an elastic plate with an effective elastic plate thickness of 50 km. Rupture of the plate in Neogene time would remove plate stresses restraining the buoyant root and thus produce the modern Sierra. Although they can match most of the observed uplift, their analysis suggests that about 20% of the uplift is due to forces in the mantle if the sub-Sierran Moho is 55 km deep, and it appears that a source in either the crust or the mantle could produce the observed flexure.

UPPER MANTLE STRUCTURE: SIERRA NEVADA VERSUS CALIFORNIA GREAT BASIN

Although uplift of the Sierra Nevada probably occurred over thinned mantle lithosphere, the lateral extent of the anomalous mantle remains poorly constrained. Several workers have assumed that thin mantle lithosphere under the Sierra merely represents an extension to the west of the anomalous mantle structure beneath much of the Great Basin [Crough and Thompson, 1977; Best and Hamblin, 1978; Mavko and Thompson, 1983]. However well founded this assumption may be for ranges abutting the Great Basin elsewhere, it appears to be ill-founded for the region under study.

The only observations of the mantle currently available that differentiate between the Sierra and the Great Basin to the east are P_n velocities observed in seismic refraction experiments (Figure 4-4; Table 4-1). A problem in interpreting these profiles is the discrepancy in velocity structure computed both from different profiles across the Sierra and by different workers studying the same refraction profile. Despite these differences, the P_n velocity beneath the Sierra Nevada is always observed to be equal to or less than that beneath the Great Basin to the east.

The most widely cited interpretation of seismic refraction data in the Sierra Nevada is Eaton's [1966] analysis of the profile between Mono Lake and China Lake along the Sierran axis (profile a, Figure 4-4). The P_n velocity of 7.9 km/s and the crustal thickness of about 50 km are the highest values of each reported from any profile in the Sierra (Table 4-1). When Prodehl [1979] reanalyzed the same data, he was unable to identify any P_n arrival from the

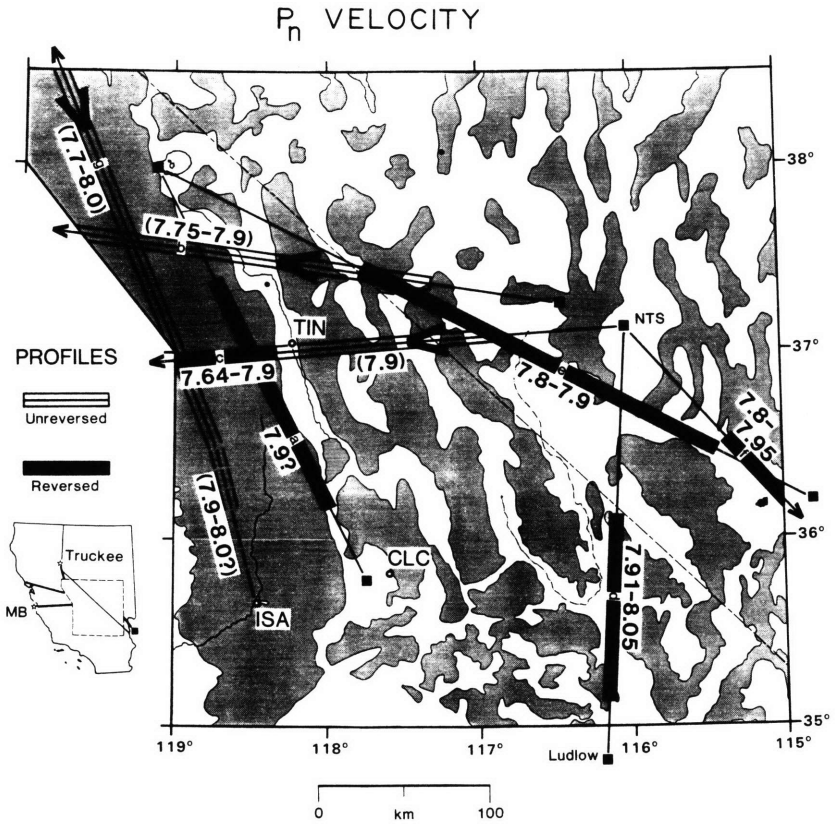

Fig. 4-4. Refraction profiles in the southwestern Great Basin. Thick portion of each profile (either reversed or unreversed) indicates portion of the uppermost mantle sampled by that profile. Letters are keyed to Table 4-1. Sources are blasts (squares) and earthquakes (stars on inset). Permanent seismic stations indicated by circled stars. Arrows on unreversed profiles point away from the single source for these profiles. Earthquake labeled MB is Monterey Bay earthquake of Carder [1973].

northern shot point, and he inferred a different crustal structure with a total thickness less than 42 km. The discrepancy in the identification of the P_n phase apparently stems from an insufficient amount of energy from the chemical explosives used as sources to overcome the high attenuation of the region [Prodehl, 1979]. The differing crustal structures are mostly the result of a disagreement over the presence (Eaton) or absence (Prodehl) of a particular phase in the traveltime curve that would require a thick layer in the lower crust with a high compressional velocity (~6.9 km/s).

The trans-Sierra profiles (b and c in Figure 4-4) both used nuclear explosions and earthquakes as sources, thus greatly diminishing the problem caused by weak arrivals. Unfortunately, these refraction profiles permit many very different interpretations; for instance, Bolt and Gutdeutsch [1982] found two very different structures of the crust and

TABLE 4-1. Upper Mantle P_n Velocities and Crustal Thicknesses From Refraction Profiles in the Southwestern Great Basin

Profile	Source	Observed P_n, km/s, from: North (or West)	South (or East)	Inferred True P_n	Crustal Thickness, km North (or West)	South (or East)
a	Eaton [1966]	8.1	7.7	7.9	54	48
	Prodehl [1979]	n.o.	7.8	---	40.1	33.5
b[a]	Carder et al. [1970]	---	8.7[b]	7.88	~25-30[c]	30
	Pakiser and Brune [1980]	---	"	7.88	>40	~30
	Bolt and Gutdeutsch [1982][d]	---	"	7.75	~25-30[c]	28
	Bolt and Gutdeutsch [1982][e]	---	"	7.88	>50	35
c[a]	Carder [1973]	7.39	7.90	7.64	26	30
	Pakiser and Brune [1980]	"	"	7.9	>50	~30
d	Gibbs and Roller [1966]	8.04	7.76	7.9	34	27
	Prodehl [1979]	8.2	7.9	8.05	35.5	27.5
e	Johnson [1965]	7.8[f]	7.8	7.8	40	32
	Prodehl [1979]	8.0	7.7-7.9	7.9	37.3	33.5
f	Diment et al. [1961]	7.81	---	7.81	28	28
	Roller [1964]	"	7.8[g]	7.8	32	27
	Prodehl [1979]	8.0	7.6-7.9	7.8-7.95	30.7	27.7
g	Pakiser and Brune [1980]	7.7	---	7.9-8.0	53.3[h]	43

Profiles located in Figure 4.

Definitions are as follows: n.o., phase not observed; ---, no data (line not shot in this direction or interpretation not made); " , apparently assumed apparent velocities observed by earlier worker(s).

[a] Western crustal thickness in table is thickness inferred to underlie the Sierran crest; all velocities are for path under the Sierran crest.

[b] Estimated from Carder et al. [1970] for stations TOM to WAL (200 to 265 km from NTS). Apparent P_n from WAL to JAS (265 to 360 km from NTS) is about 7.5 km/s.

[c] Crust immediately to the east beneath the White Mountains inferred to be 38 km thick.

[d] Reinterpreting structure of Carder et al. [1970].

[e] Reinterpreting structure of Pakiser and Brune [1980].

[f] Beyond 260 km from Mono Lake; 8.3 km/s from 170 to 260 km from Mono Lake.

[g] Could be 7.6 km/s if step in P_n branch inferred by Roller is not present.

[h] Maximum thickness under Sierra Nevada; about 40 km near Truckee.

upper mantle of the Sierra Nevada and Great Basin that could be derived from profile b (Table 4-1). In the first structure, modified from that proposed by Carder et al. [1970], the P velocity in the crust is 6.70 km/s, and the P_n velocity in the mantle is 7.75 km/s. The

thickness of the crust decreases westward from almost 40 km beneath the White Mountains to about 23 km just west of the crest of the Sierra. In the second structure, initially proposed by Pakiser and Brune [1980], a crust with two layers (P velocities of 6.1 and 6.9 km/s) overlies a mantle with a P_n velocity of 7.88 km/s. The crust thickens dramatically from 35 km beneath the White Mountains to about 60 km under the crest of the Sierra. Although they found that the modified structure of Carder et al. [1970] fit the observed arrival times better, Bolt and Gutdeutsch concluded that the structure proposed by Pakiser and Brune [1980] could also be correct, especially in view of the observations from profiles a and g along the Sierran axis (Figure 4-4).

Although a large spectrum of seismic structures are permitted by the available refraction profiles, the P_n velocity under the Sierra Nevada in all cases is less than or equal to 7.9 km/s. Moreover, several lines of evidence support a lower velocity. The profile presented by Carder [1973] (profile c, Figure 4-4) was partially reversed by using an earthquake in Monterey Bay as a source. The resulting mean P_n velocity is 7.64 km/s. Pakiser and Brune [1980] claimed that a deep crustal root could account for this low value, but the failure of this structure to predict the observed arrival times over about the same distance of profile b [Bolt and Gutdeutsch, 1982] suggests that the deep crustal root might not account for these arrival times. Unfortunately, there is no analysis for this profile similar to that made by Bolt and Gutdeutsch [1982] for profile b.

The structure of Pakiser and Brune [1980] also requires an eastward dipping Moho under the western foothills of the Sierra to fit the seismic arrivals. However, in an experiment using P_n arrivals from earthquakes and blasts in California and Nevada that was especially designed to detect the dip on the Moho, Oppenheimer and Eaton [1984] found no evidence for any dip on the Moho under or east of the western Sierran foothills north of profile b. This result does agree with the structures of Carder et al. [1970] and Carder [1973], which include P_n velocities less than 7.80 km/s.

The apparent velocity of P_n arrivals north to south along the Sierra Nevada from the Truckee earthquake of September 12, 1966 (M6.5, 39°26.91'N, 120°8.75'W), was 7.7 km/s (profile g, Figure 4-4 [Pakiser and Brune, 1980]). This could be interpreted as the result of a south dipping Moho with a P_n velocity of 7.9 km/s in the upper mantle [Pakiser and Brune, 1980], or it might be fairly close to the true velocity under a relatively flat Moho. This latter possibility is supported by the 7.8 km/s P_n apparent velocity that Prodehl [1979] found for the refraction profile north from China Lake to Mono Lake (profile a, Figure 4-4). Pakiser and Brune found an apparent velocity of 8.6 km/s for P_n along the southernmost portion of their unreversed profile (dashed in Figure 4-4) to station ISA, and the P_n arrival at station CLC was 0.9 s earlier than that at ISA. Unlike the arrivals at stations to the north, these relatively

early arrivals appear inconsistent with an upper mantle velocity less than 7.9 km/s under the High Sierra because the direct paths from Truckee to these stations pass through the High Sierra. The distance of 450 km between Truckee and these stations, however, is sufficient for the raypaths to ISA and CLC to pass through higher-velocity mantle material (~8.0 km/s) west or east of the Sierra Nevada [Mavko and Thompson, 1983; Oppenheimer and Eaton, 1984; Raikes, 1980; Prodehl, 1979]. Hence the early arrivals at stations ISA and CLC do not require a high velocity beneath the High Sierra, and so the best estimate for the P_n velocity under the Sierra Nevada seems to be between 7.65 and 7.9 km/s.

Only one reversed refraction profile crosses the California Basin and Range (profile d, Figure 4-4). This profile was reversed using a nuclear blast at the Nevada Test Site (NTS) and chemical explosives near Ludlow, California, to the south [Gibbs and Roller, 1966]. Gibbs and Roller [1966] inferred a mean P_n velocity of 7.91 km/s with an apparent P_n velocity of 8.04 km/s from the stronger NTS blast. Prodehl [1979] inferred a mean P_n velocity of 8.05 km/s. The two other profiles shown in Figure 4-4 (profiles e and f) cross only the margins of the structural subprovince as described below and probably sample other tectonic subprovinces, but the high apparent P_n velocity observed between 170 and 260 km from Mono Lake on profile e (Table 4-1 [Johnson, 1965]) might indicate the presence of a northward extension of the high-velocity mantle inferred from the Ludlow to NTS refraction profile.

This review of seismic refraction profiles has illustrated the large uncertainty of P_n velocities determined in this area, but a key inference can be drawn from the available evidence: The P_n velocity under the High Sierra Nevada between about 36° and 38°N is at least as low as and quite possibly lower than that under the Basin and Range immediately to the east. From an inversion of arrivals from earthquakes recorded by the Caltech seismic array, Hearn and Clayton [1986] also found lower P_n velocities under the Sierra than to the east. All of these P_n velocities east of the Sierra in the California Basin and Range are higher than in the Great Basin as a whole [Prodehl, 1979]. This suggests a lower temperature in the upper mantle beneath the California Basin and Range [e.g., Black and Braile, 1982] that in turn suggests a denser upper mantle than under the Great Basin in Nevada.

The existence of denser upper mantle would produce lower average elevations and less negative Bouguer gravity anomalies in the California Basin and Range than in the rest of the Great Basin if all else were equal. Since the thickness of the crust is about 30 km in both areas [Gibbs and Roller, 1966; Cheadle et al., 1986; Prodehl, 1979], the 800-m decrease in mean elevation and the roughly 100-mGal-higher Bouguer gravity anomaly in the Death Valley region support the inference that the California Basin and Range overlies relatively cold, high-velocity mantle (Figures 4-7 and 4-8). The lack of an equivalent contrast in

Bouguer gravity anomaly or topography along the axis of the Sierra Nevada supports a southward continuation along the Sierra Nevada of the lower-density mantle that underlies both the northern Great Basin and the northern Sierra Nevada [e.g., Mavko and Thompson, 1983]; hence, the High Sierra south of 38°N overlies warmer mantle with a lower density and P_n velocity than that under the Basin and Range to the east.

GEOLOGY OF THE DEATH VALLEY EXTENSIONAL SUBPROVINCE

If the thinnest mantle lithosphere in this region underlies the High Sierra, then this thinning of mantle lithosphere may be the deeper manifestation of the upper crustal extension known to exist in the Death Valley area. Because available data do not enable us to trace this extension downward through the entire lithosphere, the best test of the possible connection between extension around Death Valley and thinning of the mantle lithosphere under the High Sierra is to compare the temporal and spatial bounds of both deformational events.

The extension in the California Basin and Range and the thinning of the sub-Sierran mantle lithosphere correlate well in time. The low heat flow measured in the Sierra Nevada indicates that the Sierran mantle lithosphere could not have been thinned much before about 10 m.y. ago [Crough and Thompson, 1977]. The geologic evidence cited above indicates that the Sierran uplift dates from about 8-10 m.y. ago. Neogene extension in this part of the Great Basin probably dates back to nearly 20 m.y. ago [Cemen et al., 1982; Wright and Troxel, 1984], but slip on west dipping low-angle normal faults may have begun only 13 to 14 m.y. ago [Stewart, 1983; Burchfiel et al., 1984]. Most of the extension has occurred since that time [Wright et al., 1983; Schweig, 1985], and the expansion of extensional tectonics into Panamint and Owens valleys in the last 4-6 m.y. [Bacon et al., 1982; St. Amand and Roquemore, 1979; Schweig, 1985] occurred as the Sierran uplift accelerated [Huber, 1981]. These data suggest that deformation below the Sierra Nevada and in the California Great Basin occurred simultaneously.

The extensional subprovince of the Great Basin discussed here coincides roughly with a region known to have extended by slip on west dipping low-angle normal faults. Burchfiel et al. [1983] defined its eastern edge to lie near the western edge of the Spring Mountains (Figure 4-5). Much of the southern edge of late Neogene extension coincides with the Garlock Fault [Davis and Burchfiel, 1973; Wernicke et al., 1982], but low-angle normal faults near the Garlock Fault are known only near the southern end of Death Valley and possibly of Panamint Valley (e.g., the "Amargosa Thrust" of Noble [1941] and Wright and Troxel [1984]). The northern boundary is more difficult to locate because of Cenozoic extension farther to the north. The "breakaway" fault of Burchfiel et al. [1983] terminates

against the Las Vegas Valley Shear Zone in the Specter Hills in Nevada. West dipping low-angle normal faults have been recognized as far north as the Bullfrog Hills (Figure 4-1 [Ransome et al., 1910; Cornwall and Kleinhampl, 1964]), so the northern edge of this extensional subprovince probably parallels the Las Vegas Valley Shear Zone and the southern portion of the Walker Lane to the northern end of the White Mountains.

The simplest imaginable geometry for the edges of an extending terrain is a parallelogram with two sides parallel to the extension orientation; these two sides would be analogous to the "intracontinental transform fault" of Davis and Burchfiel [1973]. Orientations of Quaternary extension derived from geologic fault offsets, historic earthquakes, and in situ stress measurements are all very nearly oriented N60°W (Figure 4-5; Table 4-2). By analogy with the idealized geometry discussed above, the northeastern and southwestern edges of this extensional domain should be subparallel to N60°W. Because these two boundaries should truncate features formed within the extensional subprovince, they should provide the best constraint on the lateral extent of the structural subprovince.

The surface geology along the southern boundary of the inferred extensional subprovince is inconsistent with the simple geometry postulated above because of the west-southwest trend of the left-lateral Garlock Fault. For the Garlock Fault to form the idealized boundary between the unextended Mojave Desert and this extensional subprovince, its trend should be parallel to the N60°W extension orientation. The orientation of principal extension within about 10 km of the fault is between N70°W and N75°W [Zellmer et al., 1985; Savage et al., 1981], which is about 35° from the trend of fault. This differs from the situation to the north where the overall orientation of extension is very similar to that of slip vectors on strike-slip faults, as would be expected for intracontinental transform faults (Figure 4-5; Table 4-2). Thus the Garlock Fault may not be the simple intracontinental transform fault that Davis and Burchfiel [1973] envisioned.

Neither Panamint nor Owens valleys continues south to the Garlock Fault; instead, both terminate just north of a region characterized by numerous northwest trending high-angle faults and two less elongate valleys (Figures 4-1 and 4-6 [Duffield and Bacon, 1980; Smith et al., 1968]). This contrast in structural style suggests that this wedge-shaped "accommodation terrain" between the Garlock Fault, the Sierra Nevada, and a line trending about N60°W from the intersection of the Garlock and Death Valley Fault Zones has deformed to absorb the difference in strain between the west-northwest to east-southeast extension to the north and the left-lateral strike-slip motion on the Garlock Fault to the south (Figure 4-6). This geometry requires deformation of the trace of the Garlock Fault because the western segment of the fault must have moved northwestward with the rigid Sierran block with respect to the eastern terminus near Death Valley. Slip on known northwest trending right-lateral faults in

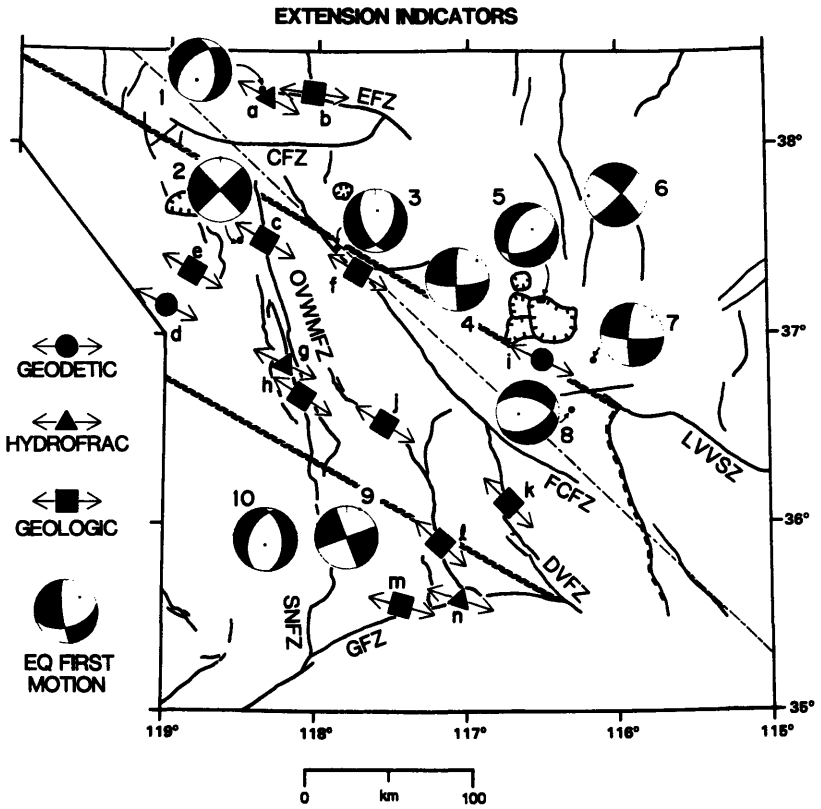

Fig. 4-5. Extension directions in the southwestern Great Basin inferred from geologic, geodetic, and in situ stress measurements. Representative earthquakes shown on lower hemisphere equal area projection; shaded quadrants are compressional. Note that the compressional quadrants of the earthquake mechanisms (except event 6) contain the horizontal vector with the azimuth of N60°W, thus indicating that these events are roughly consistent with a least principal stress of that orientation. Diagonally striped lines on this and later figures trend N60°W from the north and south limits of recognized west dipping low-angle normal faults; these represent the inferred boundaries of an extensional subterrain as discussed in the text. Sources indicated in Table 4-2. Heavy lines are principal faults; boxed line represents eastern extent of west dipping low-angle normal faults of the Death Valley region, after Burchfiel et al. [1983] and Wernicke et al. [1984]. Faults identified are Excelsior Fault Zone (EFZ), Coaldale Fault Zone (CFZ), Owens Valley--White Mountain Fault Zone (OVWMFZ), Sierra Nevada Fault Zone (SNFZ), Furnace Creek Fault Zone (FCFZ), Death Valley Fault Zone (DVFZ), Garlock Fault Zone (GFZ), and the Las Vegas Valley Shear Zone (LVVSZ). The Walker Lane includes the region in Nevada within about 100 km of the California border northwest of the Las Vegas Valley Shear Zone.

the Mojave Desert [e.g., Dokka, 1983] might accommodate at least part of this deformation in a manner similar to that proposed by Garfunkel [1974] for the San Andreas Fault to the south,

TABLE 4-2a. Sources of Nonseismic Extension Indicators Used in Figure 4-5

Label	Source	Orientation	Description
a	Savage and Lisowski [1984]	N63°W	Geodetic array, 1972-1982
b	Speed and Cogbill [1979]	N82°W	Fault striae, Candelaria Fault Zone
c	Russell [1977]	N60°W	Fault striae, White Mountains
d	Haimson [1976], as reported by Zoback and Zoback [1980]	N65°W	Hydrofrac
e	Lockwood and Moore [1979]	N61°W	Finite strain from microfaults
f	B. C. Burchfiel (personal communication, 1984)	N60°W	Pure strike-slip motion, Death Valley Fault Zone
g	Savage and Lisowski [1980]	N66°W	Geodetic array, 1932-1979
h	Zoback and Zoback [1980] from Bateman [1961]	N57°W	Inferred maximum slip of 1872 Owens Valley EQ
i	Stock et al. [1985]	N65°W	Hydrofrac
j	Burchfiel et al. [1987]	N58°W	Slip on Hunter Mountain Fault Zone
k	Wright et al. [1974]	N45°W	Trend of turtlebacks surfaces, Death Valley
l	Maxson [1950]	N48°W	Slickensides, Panamint Valley Fault Zone
m	Zellmer et al. [1985]	N75°W	Tectonic cracks
n	Savage et al. [1981]	N72°W	Geodetic array, 1973-1980

Letters keyed to Figure 4-5.

TABLE 4-2b. Sources of Earthquakes Located in Figure 4-5

Number(s)	Source
1	Ryall and Priestly [1975], composite mechanism
2	Pitt and Steeples [1975] as interpreted by Smith and Lindh [1978], composite mechanism
3, 8, 9	Smith and Lindh [1978], single event mechanisms
4, 7	Rogers et al. [1983], single event mechanism
5	Hamilton and Healy [1969] as interpreted by Smith and Lindh [1978], composite mechanism
6	Smith and Lindh [1978], composite mechanism
10	Jones and Dollar [1986], most prevalent single event mechanism

Numbers keyed to Figure 4-5.

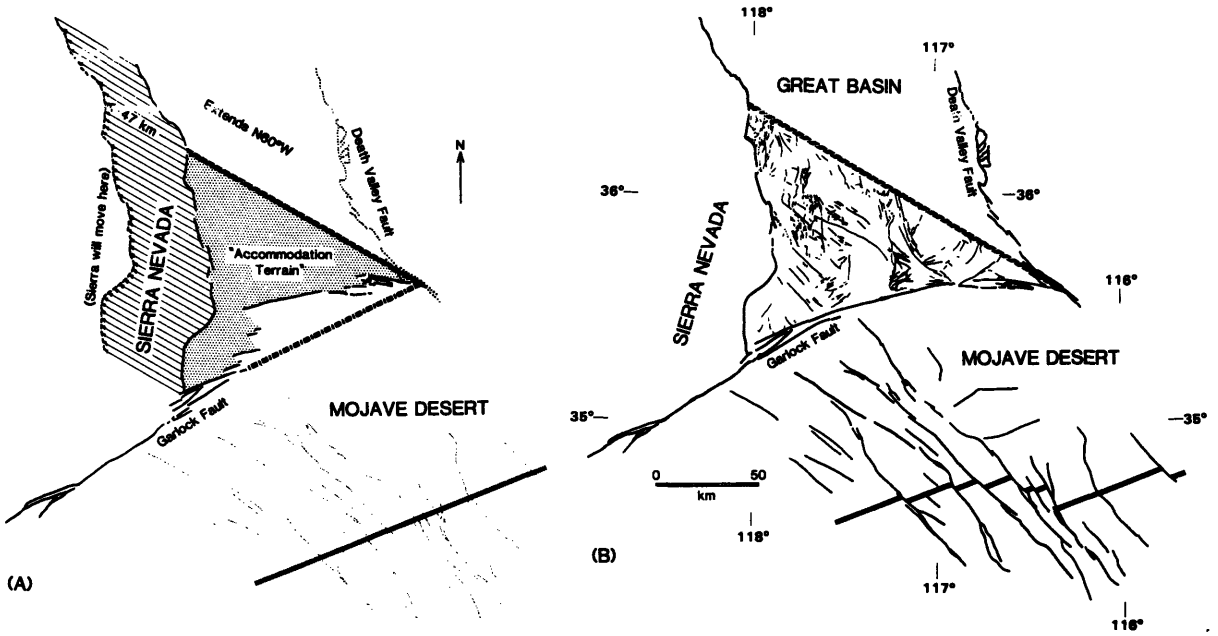

Fig. 4-6. Illustration of possible deformation of the southwesternmost California Basin and Range. Note that the displacements illustrated only reflect motion consistent with documented right slip on faults in the Mojave Desert [Dokka, 1983], and so the total extension across the California Basin and Range is probably underestimated. (a) Southwesternmost Great Basin before movement on right slip faults in the Mojave Desert (small dotted lines). A portion of the short dashed line nearly coincides with the strike-slip portion of the Kane Springs Fault of Dokka [1983]. Garlock Fault has been reconstructed (thin solid line segments) by projecting displacements Dokka [1983] found near the Kane Springs Fault N41°W from the central Mojave. The dash-dot line represents a more probable trace of the ancient Garlock Fault if the right slip in the Mojave becomes more diffuse to the northwest. Lined area represents region vacated by motion of the Sierra Nevada 47 km to N60°W relative to the eastern edge of the map. Proposed "accommodation terrain" deforms internally to reflect the motion of its boundaries. (b) Modern-day southwesternmost Great Basin. Thin lines in the "accommodation terrain" are faults from Jennings [1977]. Note the change in shape of this terrain.

as illustrated in Figure 4-6. Hence the motions of the bounds of the "accommodation terrain" indicate the deformation necessary within this region for the extension oriented N60°W to the north to be compatible with the strike-slip motions documented to the south.

The northern limit of west dipping low-angle normal faults lies in a geologically complex area. Several strike-slip faults lie near this boundary, including the Las Vegas Valley Shear Zone [Burchfiel et al., 1983], the northern Furnace Creek Fault Zone [Stewart, 1983], and the Coaldale and Excelsior faults [Stewart, 1985] (Figure 4-5). A line extending N60°W from

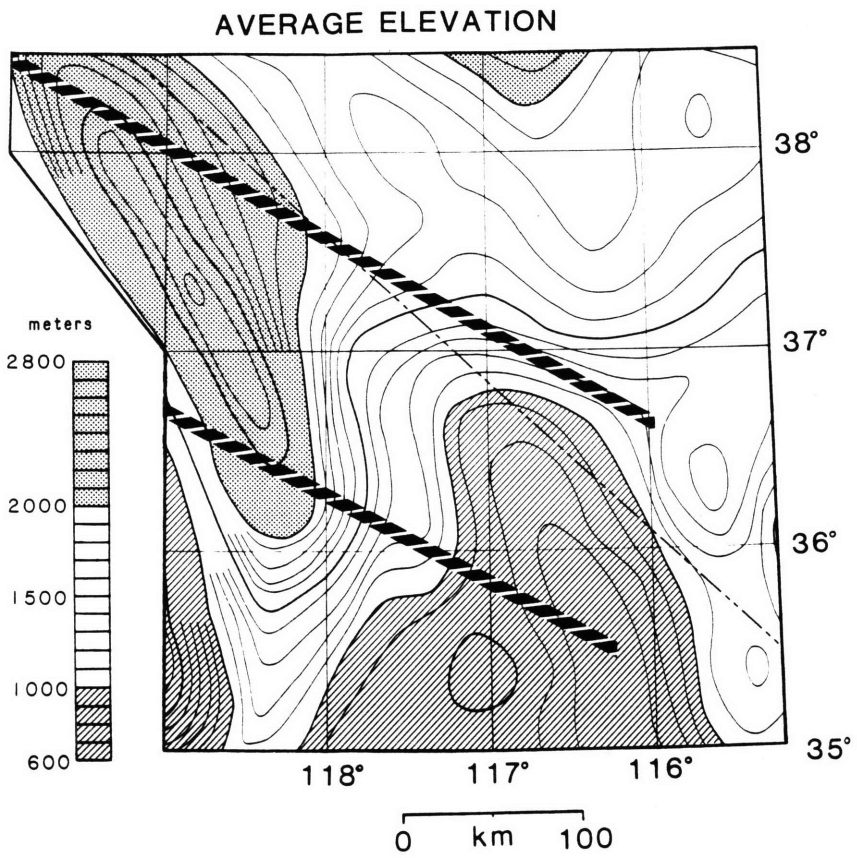

Fig. 4-7. Average elevation of southwestern Great Basin, from Diment and Urban [1981]. Boundaries of the inferred extensional subprovince indicated by the diagonally striped line.

the junction of the eastern limit of the recognized low-angle normal faults with the Las Vegas Valley Shear Zone falls close to all of these structures. The area further north has also extended in late Cenozoic time, but the voluminous silicic volcanism and subdued topography suggest a very different tectonic style [Stewart, 1980]. Although neither the northern nor the southern edges of the extending domain are sharply defined by the surface geology, the geologic structure near both edges might be consistent with N60°W trending bounds to the extensional domain on both sides.

TOPOGRAPHY, GRAVITY, AND GEOMORPHOLOGY: THE CASE FOR WESTWARD OFFSET OF LITHOSPHERIC EXTENSION WITH DEPTH

Data presented above indicate that the Sierra Nevada overlies thinner mantle lithosphere than that under the California Basin and Range and that deformation of both regions has been nearly coeval. The region where the crust has been extended on west dipping low-angle normal faults could be bounded on both the north and south by lines parallel to the extension

orientation of N60°W. This section explores the north-south extent of the mantle anomaly beneath the Sierra and compares it with bounds extended from those inferred for the upper crustal extension by examining the surface topography, gravity anomalies, and geomorphology.

Topography

The existence of extensive pediments in the Spring Mountains [Hewett, 1956], the Panamint Mountains [Maxson, 1950], and the Sierra Nevada [Matthes, 1937] by Miocene time suggests that most of the relief acquired during earlier orogenies had been eliminated. Although other physiographic features are involved, the principal physiographic features acquired or rejuvenated since Miocene time are the Sierra Nevada and Death Valley, which can be identified as the smoothed topographic high and low in Figure 4-7.

The Death Valley area is perhaps the most extended portion of the California Basin and Range [e.g., Davis and Burchfiel, 1973]; therefore it is not surprising that it is also the lowest. The narrow topographic low terminates as a distinct feature at the proposed northern bound of the extensional subprovince and broadens to cover most of the Mojave Desert to the south of the southern bound. This supports the definition of these bounds, for the localization of crustal extension along a line through Death Valley should be a feature unique to this extensional subprovince and should not extend beyond the subprovince's bounds.

The averaged topography along the High Sierra has a nearly constant elevation from near Mono Lake (38°N) southward to a point southwest of Owens Lake (36.2°N) (Figures 4-1 and 4-7). This segment of the crest includes all of the peaks above 4000 m in the Sierra. North from Mono Lake the crest gradually decreases in elevation; south from Owens Lake the averaged elevation along the Sierran crest decreases by more than a kilometer within a lateral distance of 100 km. This suggests that some portion of the forces that created the Sierran uplift are confined to the Sierra between Mono and Owens Lakes. Because the Sierran batholith--and presumably any crustal root associated with it--continues north and south, the best explanation for these topographic variations is that the mantle anomaly inferred to have caused the late Cenozoic uplift of the Sierra is mostly limited to the mantle beneath the High Sierra. The gentle slope to the north of the High Sierra might reflect a transition to an extensional style with a broader mantle anomaly located under the Great Basin and the Sierran crest. The steeper slope to the south probably represents a more abrupt termination of any anomalous mantle. These two gradients in the averaged elevation lie on the western projection of the boundaries of the extensional subprovince east of the Sierra, thus supporting

the inferred connection between crustal extension in Death Valley and thinning of the mantle lithosphere beneath the High Sierra.

Gravity

The Bouguer gravity anomaly over the California Basin and Range largely reflects the features seen in the topography of the region. The anomaly map of Figure 4-8 includes only those measurements of gravity located on pre-Cenozoic bedrock; this eliminates the large negative anomalies associated with low-density sediments in the Cenozoic basins. The remaining anomalies should reflect density contrasts in the middle and lower crust and the upper mantle. Two features dominate this decimated anomaly field: a Bouguer gravity high along Death Valley and a Bouguer gravity low along the Sierra Nevada.

Three sources probably contribute to the Bouguer high along Death Valley: dense crustal rocks, a shallow Moho, and a dense upper mantle. Wright et al. [1981] attributed the gravity high to dense metamorphic rocks such as those exposed in the Panamint and Funeral ranges. Both the large scale of the Bouguer gravity high and its extension into areas just east of Death Valley lacking any exposure of high-density rock suggest that near-surface density contrasts do not entirely explain the observed anomaly. Hunt and Mabey [1966] attributed the high to an anomalously thin crust beneath Death Valley. Although this might explain the lower gravity anomalies to the east and west of Death Valley, the thickness of the crust near Death Valley is similar to that north of about 38°N, where the Bouguer anomaly is about 100 mGal lower (Figure 4-8 [Prodehl, 1979]). This contrast and a parallel contrast in the mean elevation between Death Valley and the Great Basin north of 38°N was interpreted above as reflecting the presence of denser mantle beneath Death Valley. As seen in Figure 4-8, the Death Valley gravity high, like the topographic low, exists as a distinct feature only within the bounds of the extensional subprovince defined from the surface geology, thus reinforcing the importance of these bounds in interpreting the geophysics of the southwestern Great Basin.

The Sierran gravity low also has three possible sources: low density crustal rocks associated with the Sierra Nevada batholith, a crustal root, and a low density anomaly in the upper mantle. The presence of the low-density batholith is undeniable, but the strong correlation between topography and gravity suggests that upper crustal rocks contribute only a small part of the gravity anomaly [Oliver and Robbins, 1982]. Similarly, the correlation of the Bouguer gravity with topography, which was largely acquired in late Tertiary time, suggests that the gravity anomaly is largely a Cenozoic feature, unlike the crustal root, which is probably Mesozoic [Bateman and Eaton, 1967]. Since the ancestral Sierra Nevada

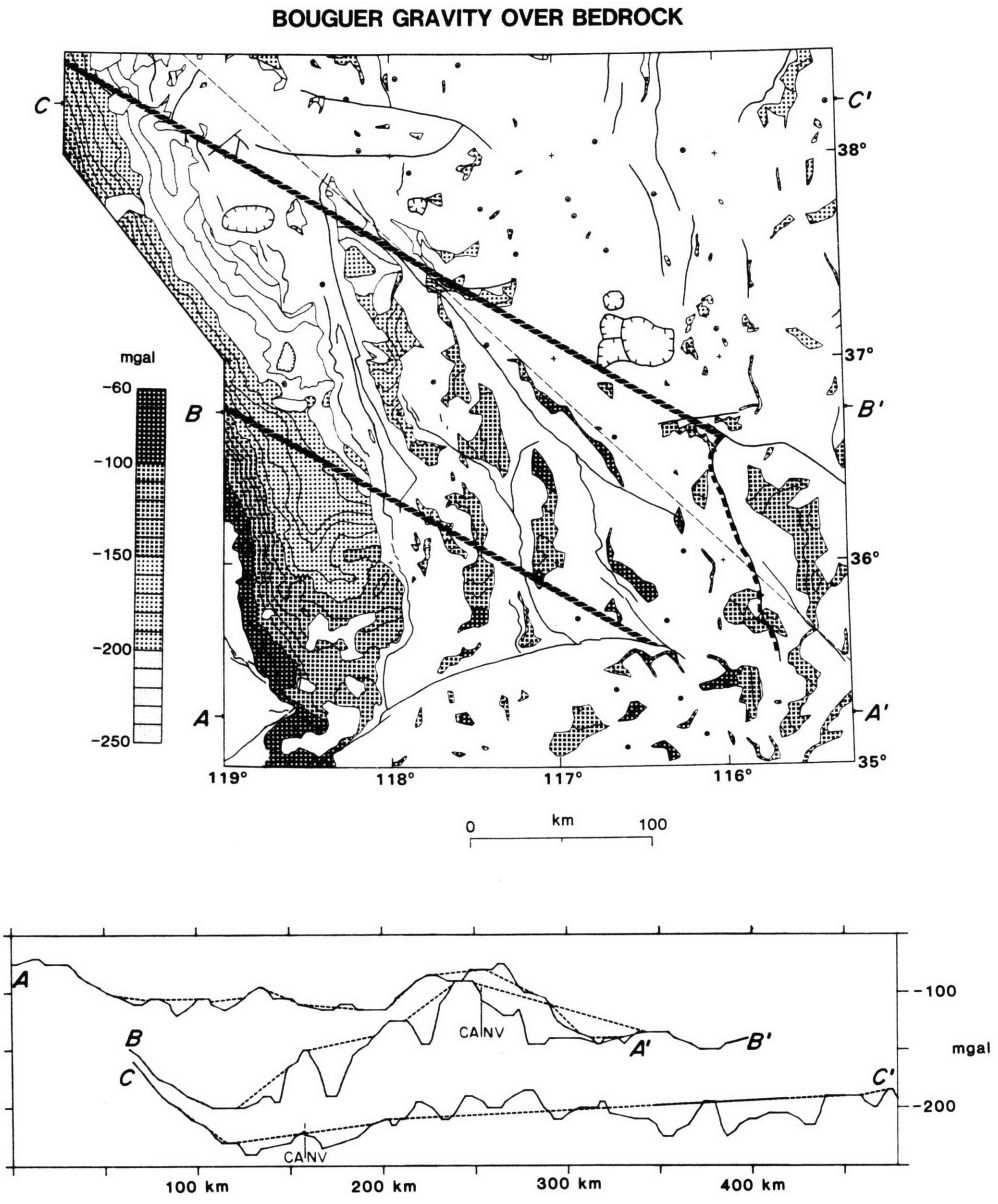

Fig. 4-8. Complete Bouguer gravity anomaly over bedrock. Faults as on Figure 4-5. Profiles A-A', B-B', and C-C' at bottom are roughly aligned by the Sierra Nevada gravity low at left. Dashed lines on profiles connect profile segments on exposures of pre-Cenozoic rock. Measurements included on this map are more than 1 km from any Cenozoic basin. Small circled symbols represent isolated measurements. Compiled from Bracken and Kane [1982], Chapman et al. [1973], Hanna et al. [1982], Healey [1973], Healey et al. [1980a, b, 1981], Kane et al. [1979], Nilsen and Chapman [1974], Oliver and Robbins [1978, 1982], and

occupied much the same area as the modern Sierra [Christensen, 1966], a crustal root that would have supported it might still exist and contribute to the modern gravity anomaly. Thus although much of the Sierra gravity low is probably due to the presence of low-density material responsible for the Neogene uplift of the High Sierra, some part of this low probably is unrelated to the modern tectonic structure.

Within the bounds of the hypothesized extensional subprovince the Bouguer anomaly contours in the Sierra trend roughly north-northwest, and the intensity of the low decreases southward from about -250 to -200 mGal. Along the Sierran crest just southwest of Owens Lake (~36.2°N) the contours trend east-west and the gravity anomaly increases toward the south about 70 mGal in 80 km. A similar gradient exists to the southeast in the Argus Range (Figures 4-1 and 4-8). Neither gradient is easily explained by either a low-density batholith or a crustal root, since both the Mesozoic structural trend and the batholith continue to the south across the gravity gradient. The Mesozoic batholith also continues north beyond Mono Lake (~38°N), yet the distinct Sierran gravity low is reduced, as profiles C-C' and B-B' in Figure 4-8 illustrate. Between Owens and Mono Lakes (profile B-B') the low is a distinct, fairly narrow feature; north of Mono Lake (profile C-C') it appears to be a mere dip on the edge of the vast gravity low of the Great Basin. Hence the gravity low distinctly associated with the Neogene uplift of the High Sierra exists only between Mono Lake and Owens Lake; such a restriction would be inconsistent with a Mesozoic crustal feature. These limits of the Cenozoic Sierran gravity low nearly coincide with a westward extension of the bounds of the Death Valley extensional subprovince. This suggests that the source of this low, inferred to be in the mantle, is structurally related to the extension near Death Valley.

Geomorphology

The foregoing interpretation assumes the creation of the southern edge of the High Sierra in late Cenozoic time by differential uplift of the ancestral Sierra. The geomorphology of the southern Sierra, particularly the Kern River drainage, indicates that the northward increase in the elevation of the Sierra is a late Cenozoic feature and largely unrelated to the ancestral Sierra Nevada. The upper Kern drainage (north of about 36.2°N) has long been known to contain at least two prominent geomorphic surfaces: the Boreal Plateau surface at about 3500 m and the Chagoopa Plateau surface at about 2700 m [Lawson, 1904; Matthes, 1937]. The ages, extent, and deformation of these surfaces provide direct evidence for southward tilting

---

Snyder et al. [1982]. California data reduced to a slightly different datum than the Nevada data.

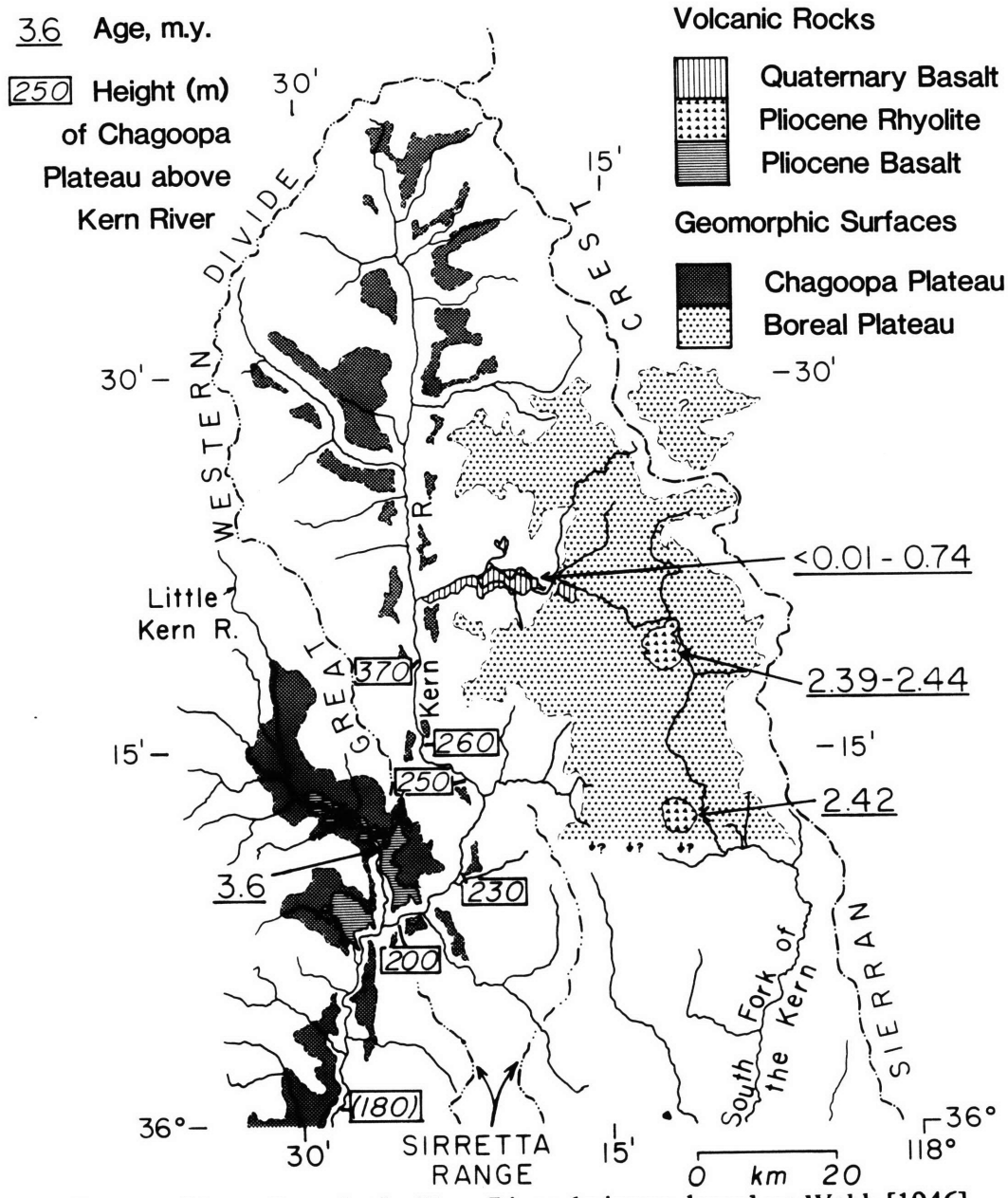

Fig. 4-9. Geomorphic surfaces in the Kern River drainage, based on Webb [1946]. Chagoopa Plateau remnants are gentle benches; Boreal Plateau area includes peaks and uplands adjoining inferred remnants of ancient surface. Dates from Moore and Lanphere [1983], Luedke and Smith [1981], and Dalrymple [1963]. Elevations of Chagoopa Plateau above Kern River from Webb [1946] except for parenthetical value inferred here. Southern edge of Boreal Plateau surface is probably artificial; other remnants likely lie to the south but remain uncorrelated [e.g., Knopf, 1918, Baker, 1912].

of the southern Sierra Nevada.

These geomorphic surfaces are difficult to use in reconstructing both ancient landscapes and their subsequent destruction because of the ambiguities that arise in making correlations between the remnants of these surfaces. Indeed, Wahrhaftig [1965] has questioned the identification of existing benches as remnants of a gentler terrain formed in ancient time. He instead considers these gentle benches to be landforms created in a drainage with relief comparable to that present today. The mechanism he proposed depends on the unique weathering habit of coarse-grained intrusive rock. The presence of similar surfaces on metamorphic and sedimentary rock to the north [Knopf, 1918], east [Maxson, 1950], south [Baker, 1912], and west [Lindgren, 1911], however, suggests a common origin independent of the lithology of the underlying rock for at least some of these High Sierran surfaces. Hence despite Wahrhaftig's misgivings, I assume that the geologic history inferred from these surfaces is approximately correct.

Because of inadequate age control and the likelihood that what now appears as a single geomorphic surface was created and dissected at different times in different places, the chronology of the creation and destruction of the erosional surfaces of the High Sierra is only approximately known. The Boreal Plateau surface is the more poorly constrained, its age being bracketed by the Cretaceous age of the rock it cuts and the 2.4-m.y. age of volcanic rocks erupted on it [Luedke and Smith, 1981; Knopf, 1918]. The Boreal Plateau surface is postdated by the lower Chagoopa Plateau surface, which Webb [1946] correlated with a surface beneath a 3.6 ± 0.1-m.y.-old basalt flow at the confluence of the Kern and Little Kern rivers (Figure 4-9; age date recalculated from Dalrymple [1963] as described by Dalrymple [1979]). The Chagoopa Plateau surface is probably somewhat younger in the northernmost Kern drainage, where Gillespie [1982] considered Pleistocene glacial diamictites to be deposited before significant dissection of the Boreal Plateau surface.

Relations between the Sierran geomorphic surfaces, surfaces to the east, and the ancient drainage divide of the Sierra Nevada suggest southward tilting of the southernmost Sierra. Webb [1946] noted that the Great Western Divide west of the Kern River and the Sirretta Range east of the Kern River probably formed the Sierran crest sometime in the Tertiary Period (Figure 4-9). Webb [1946] inferred that the Kern River breached the paleodivide by the time the Chagoopa Plateau surface formed. Headward erosion of the Kern River across the paleodivide preceded the formation of the entire Chagoopa Plateau surface and suggests that southward tilting of the southernmost Sierra and uplift of the High Sierra caused the rejuvenation of that stream. Hence the present southward warp of the southern Sierra probably started to form before about 4 m.y. ago.

The Chagoopa Plateau surface reflects later southward warping of the southern Sierra. The gentle topography of this surface suggests that the Kern River had a lower gradient when

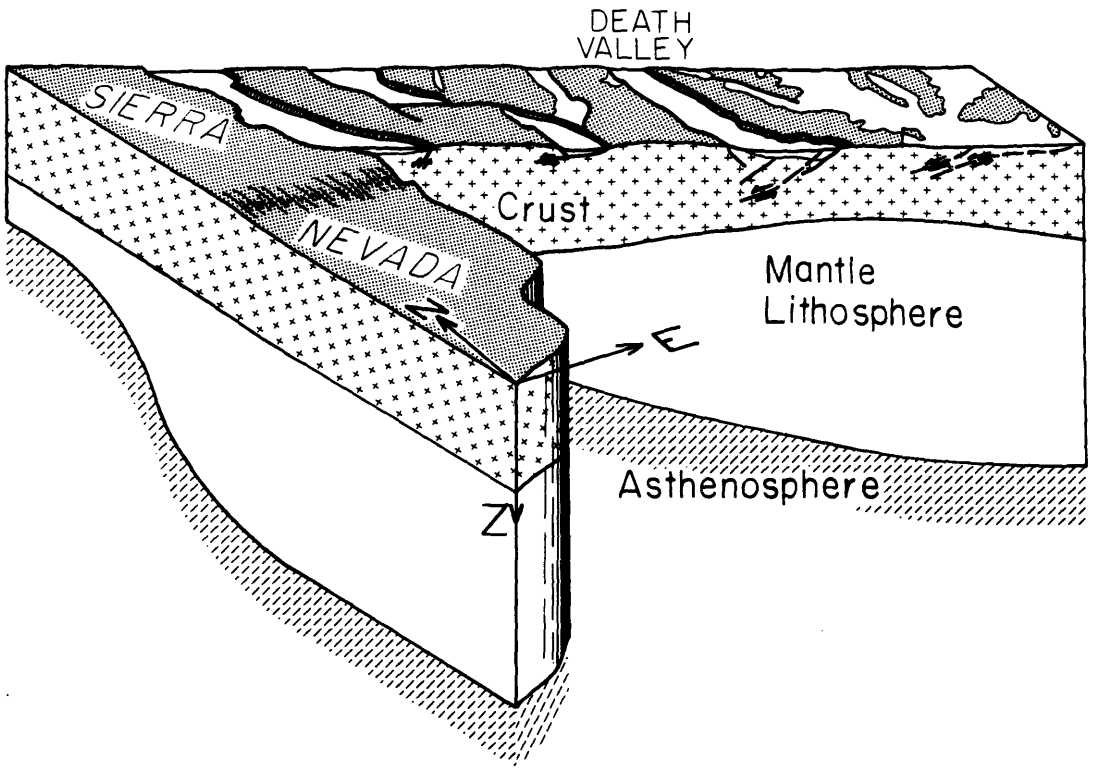

Fig. 4-10. Block diagram illustrating proposed interrelationship of upper crustal and lower lithospheric deformation of the southwestern Great Basin. Note the thinning of the mantle lithosphere both from east to west and south to north. View is toward N30°E. Arrows are 50 km long.

the Chagoopa Plateau formed than it does now, for the modern Kern cuts a deep, narrow canyon through the paleodivide. If Webb [1946] correctly identified the extension of the Chagoopa Plateau surface along the Kern River through the paleodivide, then this surface now dips more steeply to the south than the modern Kern River profile. Thus a substantial southward warping of this area must have occurred since the formation of this surface. This increase of the southward gradient might also be reflected in a series of stream captures in the headwaters of the South Fork of the Kern River [Webb, 1946].

The topography, gravity, and geomorphology reviewed above indicate that the upwarp of the southern High Sierra relative to the very southernmost Sierra occurred in late Cenozoic time. This warp coincides with the inferred southern edge of anomalously thin mantle lithosphere that probably lies beneath the High Sierra. The position of this flexure near the projected southern edge of the extensional subprovince previously defined east of the Sierra is consistent with the inference that the thinning of the mantle lithosphere beneath the Sierra Nevada is the deeper equivalent of the upper crustal extension described in the vicinity of Death Valley (Figure 4-10).

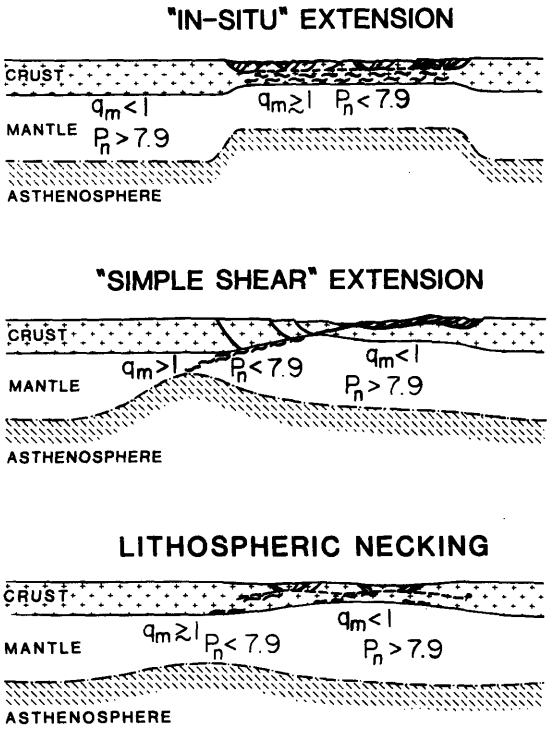

Fig. 4-11. Cartoons illustrating mechanisms proposed for extension of the lithosphere in the Great Basin. Dashed line in the middle crust represents a décollement at the brittle-ductile transition. P_n velocity is in kilometers/second; the heat flow at the Moho in 10^{-3} cal cm^{-3} s^{-1} (HFU) is designated q_m.

CONCLUSIONS

Data from the southern Sierra Nevada and the Basin and Range within about 200 km to the east permit examination of the nature of extension throughout the lithosphere in this region. The Cenozoic sedimentary and physiographic record indicates that the southern Sierra Nevada was uplifted about 2 km in the last 8-10 m.y. This uplift is considered to have been caused by tectonic thinning of the mantle lithosphere beneath the High Sierra because of the anomalously low P_n velocities, delays in teleseimic arrival times, and unexpectedly shallow depth of the Curie point isotherm in the Sierra Nevada [Crough and Thompson, 1977; Mavko and Thompson, 1983]. Sub-Sierran P_n velocities are uniformly less than or equal to 7.9 km/s and possibly as low as 7.6 km/s, and the P_n velocities beneath the Death Valley area are greater than 7.9 km/s. Thus the mantle lithosphere appears to be warmer, and hence thinner, beneath the Sierra than under the Death Valley region to the east. Present-day extension in the Death Valley region is generally subparallel to N60°W, and geologic evidence suggests that the region roughly between the Garlock Fault and the Walker Lane-Las Vegas Valley Shear Zone has extended by slip on west dipping low-angle normal faults. The northern and southern boundaries of this structural subprovince appear to trend about N60°W, parallel to the extension direction. The projection of these bounds into the Sierra Nevada, most particularly the southern boundary, coincides with perceptible changes in the elevation and Bouguer gravity anomaly along the range; these changes are thought to mark

the boundary of the upper mantle anomaly responsible for the uplift of the High Sierra. The near simultaneity of the Sierran uplift and the slip on low-angle normal faults to the east supports the deduction that the tectonic thinning of the mantle lithosphere beneath the Sierra Nevada is a deeper manifestation of the extension of the upper crust near Death Valley (Figure 4-10).

This documentation of possible horizontal offset of extension with depth provides an important test for tectonic theories of the extension of the lithosphere (Figure 4-11). If the amount of extension were vertically uniform [e.g., Stewart, 1978; Eaton et al., 1978; Lachenbruch and Sass, 1978; Eaton, 1982], then the Sierra Nevada would overlie cold mantle with a high P_n velocity, and Death Valley would overlie hot mantle with a low P_n velocity; both of these predictions are opposed to the interpretations detailed in this paper. The concept of a low-angle normal fault through the entire lithosphere [Wernicke, 1981, 1985] correctly predicts these observations but is not unique in so doing. Necking instabilities at different points in the strong upper crust and the strong upper mantle could have different wavelengths and thus provide a possible explanation for vertically offset extension [Zuber et al., 1986; Ricard and Froidevaux, 1986]. The observed anomalies, however, are much larger than currently estimated from those structures (compare Zuber et al. [1986] with Froidevaux [1986]), but the behavior of such necking instabilities after a noninfinitesimal amount of extension remains to be investigated. Although the exact relationship of extension in the upper crust to deformation in the lower crust and mantle must await more detailed investigations, it appears that such deformation need not be vertically uniform; rather the deformation in the upper crust and in the upper mantle can be separated horizontally and are perhaps connected by low-angle or flat zones of deformation.

Acknowledgments. Peter Molnar provided guidance and encouragement in preparing this paper. Comments of and conversations with B. C. Burchfiel, B. Wernicke, and J. D. Walker proved extremely helpful. I thank M. L. Zoback, K. Shedlock, M. Nelson, J. Titilah, L. Pakiser, S. Hickman, and two anonymous reviewers for critical comments.

REFERENCES

Anderson, R. E., Thin skin distension in Tertiary rocks of southeastern Nevada, *Geol. Soc. Am. Bull.*, *82*, 43-58, 1971.

Armstrong, R. L., Low-angle (denudation) faults, hinterland of the Sevier orogenic belt, eastern Nevada and western Utah, *Geol. Soc. Am. Bull.*, *83*, 1729-1754, 1972.

Bacon, C. R., D. M. Giovannetti, W. A. Duffield, G. B. Dalrymple, and R. E. Drake, Age of the Coso Formation, Inyo County, California, *U. S. Geol. Surv. Bull., 1527*, 1-18, 1982.

Baker, C. L., Physiography and structure of the western El Paso Range and the southern Sierra Nevada, *Calif. Univ. Dep. Geol. Bull., 7*, 117-142, 1912.

Bartley, J. M., and B. P. Wernicke, The Snake Range Décollement interpreted as a major extensional shear zone, *Tectonics, 3*, 647-657, 1984.

Bartow, J. A., Geologic map and cross sections of the southeastern margin of the San Joaquin Valley, California, *U. S. Geol. Surv. Misc. Invest. Ser. Map, I-1496*, 2 sheets, 1984.

Bateman, P. C., Willard D. Johnson and the strike-slip component of fault movement in the Owens Valley, California, earthquake of 1872, *Bull. Seismol. Soc. Am., 51*, 483-493, 1961.

Bateman, P. C., and J. P. Eaton, Sierra Nevada Batholith, *Science, 158*, 1407-1417, 1967.

Bateman, P. C., and C. Wahrhaftig, Geology of the Sierra Nevada, in *Geology of Northern California*, edited by E. H. Bailey, *Bull. Calif. Div. Mines Geol., 190*, 107-184, 1966.

Best, M. G., and W. K. Hamblin, Origin of the northern Basin and Range province: Implications from the geology of its eastern boundary, *Mem. Geol. Soc. Am., 152*, 313-340, 1978.

Black, P. R., and L. W. Braile, P_n velocity and cooling of the continental lithosphere, *J. Geophys. Res., 87*, 10557-10568, 1982.

Bolt, B. A., and R. Gutdeutsch, Reinterpretation by ray tracing of a transverse refraction profile through the California Sierra Nevada, part I, *Bull. Seismol. Soc. Am., 72*, 889-900, 1982.

Bracken, R. E., and M. F. Kane, Bouguer gravity map of Nevada: Kingman Sheet, *Nev. Bur. Mines Geol. Map, 75*, 1982.

Brewer, J. A., and D. K. Smythe, MOIST and the continuity of crustal reflector geometry along the Caledonian-Appalachian orogen, *J. Geol. Soc. London, 141*, 105-120, 1984.

Burchfiel, B. C., D. Walker, G. A. Davis, and B. Wernicke, Kingston Range and related detachment faults--A major "breakaway" zone in the southern Great Basin, *Geol. Soc. Am. Abstr. Programs, 15*, 536, 1983.

Burchfiel, B. C., J. D. Walker, D. W. Klepacki, K. V. Hodges, P. G. Tilke, P. D. Crowley, C. H. Jones, and G. A. Davis, The Kingston Range detachment system: Structures at the eastern edge of the Death Valley extensional zone, southeastern California, *Geol. Soc. Am. Abstr. Programs, 17*, p. 345, 1984.

Burchfiel, B. C., K. V. Hodges, and L. H. Royden, Geology of the Panamint Valley--Saline Valley pull-apart system, California: Palinspastic evidence for low-angle geometry of a Neogene range-bounding fault, *J. Geophys. Res., 92*, 10422-10426, 1987.

Byerly, P., Comments on "The Sierra Nevada in the light of isostasy," by A. C. Lawson, *Bull. Seismol. Soc. Am.*, *48*, 2025-2031, 1938.

Carder, D. S., Trans-California seismic profile, Death Valley to Monterey Bay, *Bull. Seismol. Soc. Am.*, *63*, 571-586, 1973.

Carder, D. S., A. Qamar, and T. V. McEvilly, Trans-California seismic profile--Pahute Mesa to San Francisco Bay, *Bull. Seismol. Soc. Am.*, *60*, 1829-1846, 1970.

Cemen, I., R. Drake, and L. A. Wright, Stratigraphy and chronology of the Tertiary sedimentary and volcanic units at the southeastern end of the Funeral Mountains, Death Valley region, California, in *Geology of Selected Areas in the Western Mojave Desert, and Southern Great Basin, California*, edited by J. D. Cooper, B. W. Troxel, and L. A. Wright, Death Valley Publishing Co., Shoshone, Calif., pp. 77-87, 1982.

Chapman, R. H., D. L. Healey, and B. W. Troxel, Bouguer gravity map of California: Death Valley sheet, 8 pp. plus map, Calif. Div. of Mines and Geol., Sacramento, 1973.

Chase, C. G., and T. C. Wallace, Uplift of the Sierra Nevada of California, *Geology*, *14*, 730-733, 1986.

Cheadle, M. J., B. L. Czuchra, T. Byrne, C. J. Ando, J. E. Oliver, L. D. Brown, and S. Kaufman, The deep crustal structure of the Mojave Desert, California, from COCORP seismic reflection data, *Tectonics*, *5*, 293-320, 1986.

Christensen, M. N., Late Cenozoic crustal movements in the Sierra Nevada of California, *Geol. Soc. Am. Bull.*, *77*, 163-182, 1966.

Cornwall, H. R., and F. J. Kleinhampl, Geology of Bullfrog quadrangle and ore deposits related to Bullfrog Hills caldera, Nye County, Nevada, and Inyo County, California, *U. S. Geol. Surv. Prof. Pap.*, *454-J*, 1-25, 1964.

Crough, S. T., and G. A. Thompson, Upper mantle origin of the Sierra Nevada uplift, *Geology*, *5*, 396-399, 1977.

Dalrymple, G. B., Potassium-Argon dates of some Cenozoic volcanic rocks of the Sierra Nevada, *Geol. Soc. Am. Bull.*, *74*, 379-390, 1963.

Dalrymple, G. B., Cenozoic chronology of the Sierra Nevada, California, *Univ. Calif. Publ. Geol. Sci.*, *47*, 1-41, 1964.

Dalrymple, G. B., Critical tables for conversion of K-Ar ages from old to new constants, *Geology*, *7*, 558-560, 1979.

Davis, G. A., and B. C. Burchfiel, Garlock Fault: An intra-continental transform structure, southern California, *Geol. Soc. Am. Bull.*, *84*, 1407-1422, 1973.

Davis, G. H., Shear-zone model for the origin of metamorphic core complexes, *Geology*, *11*, 342-347, 1983.

Diment, W. H., and T. C. Urban, Average elevation map of the conterminous United States (Gilluly averaging method), *U. S. Geol. Surv. Geophys. Invest. Map, GP-933*, 1981.

Diment, W. H., S. W. Stewart, and J. C. Roller, Crustal structure from the Nevada Test Site to Kingman, Arizona, from seismic and gravity observations, *J. Geophys. Res.*, *66*, 201-214, 1961.

Dokka, R. K., Displacements on late Cenozoic strike-slip faults of the central Mojave Desert, California, *Geology*, *11*, 305-308, 1983.

Duffield, W. A., C. R. Bacon, and G. B. Dalrymple, Late Cenozoic volcanism, geochronology, and structure of the Coso Range, Inyo County, California, *J. Geophys. Res.*, *85*, 2381-2404, 1980.

Eaton, G. P., The Basin and Range Province: Origin and tectonic significance, *Annu. Rev. Earth Planet. Sci.*, *10*, 409-440, 1982.

Eaton, G. P., R. R. Wahl, H. J. Prostka, D. R. Mabey, and M. D. Kleinkopf, Regional gravity and tectonic patterns: Their relation to late Cenozoic epeirogeny and lateral spreading in the western Cordillera, *Mem. Geol. Soc. Am.*, *152*, 51-91, 1978.

Eaton, J. P., Crustal structure from San Francisco, California, to Eureka, Nevada from seismic-refraction measurements, *J. Geophys. Res.*, *68*, 5789-5806, 1963.

Eaton, J. P., Crustal structure in northern and central California from seismic evidence, *Bull. Calif. Div. Mines Geol.*, *190*, 419-426, 1966.

Froidevaux, C., Basin and Range large-scale tectonics: Constraints from gravity and reflection seismology, *J. Geophys. Res.*, *91*, 3625-3632, 1986.

Gans, P. B., E. L. Miller, J. McCarthy, and M. L. Ouldcott, Tertiary extensional faulting and evolving brittle-ductile transition zones in the northern Snake Range and vicinity: New insights from seismic data, *Geology*, *13*, 189-193, 1985.

Garfunkel, Z., Model for the late Cenozoic tectonic history of the Mojave Desert, California, and for its relation to adjacent regions, *Geol. Soc. Am. Bull.*, *85*, 1931-1944, 1974.

Gibbs, J. F., and J. C. Roller, Crustal structure determined by seismic-refraction measurements between the Nevada Test Site and Ludlow, California, in *U. S. Geol. Surv. Prof. Pap.*, *550-D*, D125-D131, 1966.

Gillespie, A. R., Quaternary glaciation and tectonism in the southeastern Sierra Nevada, Inyo County, California, Ph.D. thesis, 695 pp., Calif. Inst. of Technol., Pasadena, 1982.

Haimson, B. C., Preexcavation deep-hole stress measurements for design of underground chambers--Case histories, in *Proceedings of the 1976 Rapid Excavation and Tunneling Conference*, edited by R. J. Robins and R. J. Conlin, pp. 699-714, Society of Mining Engineers of AIME, New York, 1976.

Hamilton, R. M., and J. H. Healy, Aftershocks of the Benham nuclear explosion, *Bull. Seismol. Soc. Am.*, *59*, 2271-2281, 1969.

Hanna, W. F., H. W. Oliver, R. F. Sikora, and S. L. Robbins, Bouguer gravity map of California: Bakersfield sheet, Calif. Div. of Mines and Geol., Sacramento, 1982.

Harrison, C. G. A., H. M. Carle, and K. L. Hayling, Interpretation of satellite elevation magnetic anomalies, *J. Geophys. Res.*, 91, 3633-3650, 1986.

Healey, D. L., Bouguer gravity map of California: Kingman sheet, Calif. Div. of Mines and Geol., Sacramento, 1973.

Healey, D. L., R. R. Wahl, and F. E. Currey, Bouguer gravity map of Nevada: Goldfield and Mariposa sheets, *Nev. Bur. Mines Geol. Map*, *68*, 1980a.

Healey, D. L., R. R. Wahl, and H. W. Oliver, Bouguer gravity map of Nevada: Death Valley sheet, *Nev. Bur. Mines Geol. Map*, *69*, 1980b.

Healey, D. L., D. B. Snyder, R. R. Wahl, and F. E. Currey, Bouguer gravity map of Nevada: Caliente sheet, *Nev. Bur. Mines Geol. Map*, *70*, 1981.

Hearn, T. M., and R. W. Clayton, Lateral velocity variations in southern California, II, Results for the lower crust from P_n waves, *Bull. Seismol. Soc. Am.*, *76*, 511-520, 1986.

Hewett, D. F., Geology and mineral resources of the Ivanpah quadrangle, California and Nevada, *U. S. Geol. Surv. Prof. Pap.*, *275*, 1-172, 1956.

Huber, N. K., Amount and timing of late Cenozoic uplift and tilt of the central Sierra Nevada, California--Evidence from the upper San Joaquin River basin, *U. S. Geol. Surv. Prof. Pap.*, *1197*, 1-28, 1981.

Hunt, C. B., and D. R. Mabey, Stratigraphy and structure, Death Valley, California, *U. S. Geol. Surv. Prof. Pap.*, *494-A*, 1-162, 1966.

Jennings, C. W. (compiler), Geologic map of California, *Calif. Div. Mines Geol. Geol. Data Map*, *2*, 1977.

Johnson, L. R., Crustal structure between Lake Mead, Nevada, and Mono Lake, California, *J. Geophys. Res.*, *70*, 2863-2872, 1965.

Jones, L. M., and R. S. Dollar, Evidence of Basin-and-Range extensional tectonics in the Sierra Nevada: The Durrwood Meadows swarm, Tulare County, California (1983-1984), *Bull. Seismol. Soc. Am.*, *76*, 439-461, 1986.

Kane, M. F., D. L. Healey, D. L. Peterson, H. E. Kaufmann, and D. Reidy, Bouguer gravity map of Nevada: Las Vegas sheet, *Nev. Bur. Mines Geol. Map*, *61*, 1979.

Knopf, A., A geologic reconnaissance of the Inyo Range and the eastern slope of the southern Sierra Nevada, California, *U. S. Geol. Surv. Prof. Pap.*, *110*, 1-130, 1918.

Lachenbruch, A. H., and J. H. Sass, Heat flow in the United States and the thermal regime of the crust, in *The Earth's Crust, Its Nature and Physical Properties, Geophys Monogr. Ser.*, vol. 20, edited by J. G. Heacock, pp. 626-675, AGU, Washington, D. C., 1977.

Lachenbruch, A. H., and J. H. Sass, Models of an extending lithosphere and heat flow in the Basin and Range province, *Mem. Geol. Soc. Am., 152*, 209-250, 1978.

Lawson, A. C., The geomorphogeny of the upper Kern Basin, *Calif. Univ. Dep. Geol. Bull., 3*, 291-376, 1904.

Lawson, A. C., The Sierra Nevada in the light of isostasy, *Geol. Soc. Am. Bull., 47*, 1691-1712, 1936.

Lindgren, W., The Tertiary gravels of the Sierra Nevada, *U. S. Geol. Surv. Prof. Pap., 73*, 1-226, 1911.

Lockwood, J. P., and J. G. Moore, Regional deformation of the Sierra Nevada, California, on conjugate microfault sets, *J. Geophys. Res., 84*, 6041-6049, 1979.

Longwell, C. R., Low-angle normal faults in the Basin-and-Range province, *EOS Trans. AGU, 26*, 107-118, 1945.

Luedke, R. G., and R. L. Smith, Map showing distribution, composition, and age of late Cenozoic volcanic centers in California and Nevada, *U. S. Geol. Surv. Misc. Invest. Map, I-1091-C*, 2 sheets, 1981.

Matthes, F. E., The geologic history of Mount Whitney, *Sierra Club Bull., 22*, 1-18, 1937.

Mavko, B. B., and G. A. Thompson, Crustal and upper mantle structure of the northern and central Sierra Nevada, *J. Geophys. Res., 88*, 5874-5892, 1983.

Maxson, J. H., Physiographic features of the Panamint Range, California, *Geol. Soc. Am. Bull., 61*, 99-114, 1950.

Mayhew, M. A., Curie isotherm surfaces inferred from high-altitude magnetic anomaly data, *J. Geophys. Res., 90*, 2647-2654, 1985.

Moore, J. G., and M. Lanphere, Age of the Golden Trout Creek volcanic field, Sierra Nevada, California (abstract), *EOS Trans. AGU, 64*, 895, 1983.

Nilsen, T. H., and R. H. Chapman, Bouguer Gravity Map of California: Trona Sheet, 9 pp., Calif. Div. of Mines and Geol., Sacramento, 1974.

Noble, L. F., Structural features of the Virgin Spring area, Death Valley, California, *Geol. Soc. Am. Bull., 52*, 941-1000, 1941.

Oliver, H. W., Gravity and magnetic investigation of the Sierra Nevada batholith, California, *Geol. Soc. Am. Bull., 88*, p.445-461, 1977.

Oliver, H. W., and S. L. Robbins, Bouguer gravity map of California: Mariposa sheet, Calif. Div. of Mines and Geol., Sacramento, 1978.

Oliver, H. W., and S. L. Robbins, Bouguer gravity map of California: Fresno sheet, Calif. Div. of Mines and Geol., 23 pp., Sacramento, 1982.

Oppenheimer, D. H., and J. P. Eaton, Moho orientation beneath central California from regional earthquake travel times, *J. Geophys. Res.*, *89*, 10267-10282, 1984.

Pakiser, L. C., and J. N. Brune, Seismic models of the root of the Sierra Nevada, *Science*, *210*, 1088-1094, 1980.

Pitt, A. M., and D. W. Steeples, Microearthquakes in the Mono Lake--northern Owens Valley, California, region from September 28 to October 18, 1970, *Bull. Seismol. Soc. Am.*, *65*, 835-844, 1975.

Press, F., and S. Biehler, Inferences on crustal velocities and densities from P wave delays and gravity anomalies, *J. Geophys. Res.*, *69*, 2979-2995, 1964.

Prodehl, C., Crustal structure of the western United States, *U. S. Geol. Surv. Prof. Pap.*, *1034*, 1-74, 1979.

Raikes, S. A., Regional variations in upper mantle structure beneath southern California, *Geophys. J. R. Astron. Soc.*, *63*, 187-216, 1980.

Ransome, F. L., W. H. Emmons, and G. H. Garrey, Geology and ore deposits of the Bullfrog district, Nevada, *U. S. Geol. Surv. Bull.*, *407*, 1-130, 1910.

Reynolds, S. J., and J. E. Spencer, Evidence for large-scale transport on the Bullard detachment fault, west-central Arizona, *Geology*, *13*, 353-356, 1985.

Ricard, Y., and C. Froidevaux, Stretching instabilities and lithospheric boudinage, *J. Geophys. Res.*, *91*, 8314-8324, 1986.

Rogers, A. M., S. C. Harmsen, W. J. Carr, and W. Spence, Southern Great Basin seismological data report for 1981 and preliminary data analysis, *U. S. Geol. Surv. Open File Rep.*, *83-669*, 1-224, 1983.

Roller, J. C., Crustal structure in the vicinity of Las Vegas, Nevada, from seismic and gravity observations, *U. S. Geol. Surv. Prof. Pap.*, *475-D*, D108-D111, 1964.

Roy, R. F., D. D. Blackwell, and E. R. Decker, Continental heat flow, in *The Nature of the Solid Earth*, edited by E. C. Robertson, pp. 506-543, McGraw Hill, New York, 1972.

Russell, B. J., A structural break and kinematics of faulting in the White Mountains, California, *Geol. Soc. Am. Abstr. Programs*, *9*, 491, 1977.

Ryall, A., and K. Priestley, Seismicity, secular strain, and maximum magnitude in the Excelsior Mountains area, western Nevada and eastern California, *Geol. Soc. Am. Bull.*, *86*, 1585-1592, 1975.

Savage, J. C., and M. Lisowski, Deformation in Owens Valley, California, *Bull. Seismol. Soc. Am.*, *70*, 1225-1232, 1980.

Savage, J. C., and M. Lisowski, Deformation in the White Mountain Seismic Gap, California-Nevada 1972-1982, *J. Geophys. Res.*, *89*, 7671-7687, 1984.

Savage, J. C., W. H. Prescott, M. Lisowski, and N. E. King, Strain accumulation in Southern California, 1973-1980, *J. Geophys. Res.*, *86*, 6991-7001, 1981.

Schweig, E. S., III, Neogene tectonics and paleogeography of the southwestern Great Basin, California, Ph.D. thesis, 207 pp., Stanford Univ., Palo Alto, Calif., 1985.

Smith, G. I., B. W. Troxel, C. H. Gray, Jr., and R. von Huene, Geologic reconnaissance of the Slate Range, San Bernadino and Inyo counties, California, *Calif. Div. Mines Geol. Spec. Rep.*, *96*, 1-33, 1968.

Smith, R. B., and A. G. Lindh, Fault-plane solutions of the Western United States: A compilation, *Mem. Geol. Soc. Am.*, *152*, 107-109, 1978.

Snyder, D. B., D. L. Healey, and R. W. Saltus, Bouguer gravity map of Nevada: Lund sheet, *Nev. Bur. Mines Geol. Map*, *80*, 1982.

Speed, R. C., and A. H. Cogbill, Candelaria and other left-oblique slip faults of the Candelaria region, Nevada, *Geol. Soc. Am. Bull.*, *90*, 143-163, 1979.

St.-Amand, P., and G. R. Roquemore, Tertiary and Holocene development of the southern Sierra Nevada and Coso Range, California (abstract), *Tectonophysics*, *52*, 409-410, 1979.

Stewart, J. H., Basin-range structure in western North America: A review, *Mem. Geol. Soc. Am.*, *152*, 1-31, 1978.

Stewart, J. H., Geology of Nevada, *Nev. Bur. Mines Geol. Spec. Publ.*, *4*, 1-136, 1980.

Stewart, J. H., Extensional tectonics in the Death Valley area, California: Transport of the Panamint Range structural block 80 km northwestward, *Geology*, *11*, 153-157, 1983.

Stewart, J. H., East-trending dextral faults in the western Great Basin: An explanation for anomalous trends of pre-Cenozoic strata and Cenozoic faults, *Tectonics*, *4*, 547-564, 1985.

Stock, J. M., J. H. Healy, S. H. Hickman, and M. D. Zoback, Hydraulic fracturing stress measurements at Yucca Mountain, Nevada, and relationship to the regional stress field, *J. Geophys. Res.*, *90*, 8691-8706, 1985.

Wahrhaftig, C., Stepped topography of the southern Sierra Nevada, California, *Geol. Soc. Am. Bull.*, *76*, 1165-1190, 1965.

Webb, R. W., Geomorphology of the middle Kern River basin, southern Sierra Nevada, California, *Geol. Soc. Am. Bull.*, *57*, 355-382, 1946.

Wernicke, B., Low-angle normal faults in the Basin and Range Province--Nappe tectonics in an extending orogen, *Nature*, *291*, 645-648, 1981.

Wernicke, B., Uniform-sense normal simple shear of the continental lithosphere, *Can. J. Earth Sci.*, *22*, 108-125, 1985.

Wernicke, B., J. E. Spencer, B. C. Burchfiel, and P. L. Guth, Magnitude of crustal extension in the southern Great Basin, *Geology*, *10*, 489-502, 1982.

Wernicke, B., P. L. Guth, and G. J. Axen, Tertiary extensional tectonics in the Sevier thrust belt of southern Nevada (field trip 19), in *Western Geological Excursions*, vol. 4, (Geol. Soc. Am. Annu. Mtg.), edited by J. Lintz, Jr., pp. 473-510, Dept. of Geol. Sci. of the Mackay School of Mines, Reno, Nev. 1984.

Wright, L. A., and B. W. Troxel, Chaos structure and basin and range normal faults: Evidence for a genetic relationship, *Geol. Soc. Am. Abstr. Programs*, [*1*], 242, 1969.

Wright, L. A., and B. W. Troxel, Shallow-fault interpretation of basin and range structure, in *Gravity and Tectonics*, edited by K. A. DeJong and R. Scholten, pp. 397-407, John Wiley, New York, 1973.

Wright, L. A., and B. W. Troxel, Geology of the northern half of the Confidence Hills 15-minute quadrangle, Death Valley region, eastern California: The area of the Amargosa Chaos, *Calif. Div. Mines Geol. Map Sheet*, *34*, 31 pp., 1984.

Wright, L. A., J. K. Otton, and B. W. Troxel, Turtleback surfaces of Death Valley viewed as phenomena of extensional tectonics, *Geology*, *2*, 53-54, 1974.

Wright, L. A., B. W. Troxel, B. C. Burchfiel, R. H. Chapman, and T. C. Labotka, Geologic cross section from the Sierra Nevada to the Las Vegas Valley, eastern California to southern Nevada, *Geol. Soc. Am. Map Chart Ser.*, *MC-28M*, 1-15, 1981.

Wright, L. A., B. W. Troxel, and R. E. Drake, Contrasting space-time patterns of extension-related, late Cenozoic faulting, southwestern Great Basin, *Geol. Soc. Am. Abstr. Programs*, *15*, 287, 1983.

Zellmer, J. T., G. R. Roquemore, and B. A. Blackerby, Modern tectonic cracking near the Garlock fault, California, *Geol. Soc. Am. Bull.*, *96*, 1037-1042, 1985.

Zoback, M. L., and M. Zoback, State of stress in the conterminous United States, *J. Geophys. Res.*, *85*, 6113-6156, 1980.

Zuber, M. T., E. M. Parmentier, and R. C. Fletcher, Extension of continental lithosphere: A model for two scales of basin and range deformation, *J. Geophys. Res.*, *91*, 4826-4838, 1986.